



Mars Radiation Environment  
and  
Effects on EEE Components

Ana Oliveira Braga Keating

PhD Thesis

Lisbon, September 2008



UNIVERSIDADE TÉCNICA DE LISBOA  
INSTITUTO SUPERIOR TÉCNICO

# Mars Radiation Environment and Effects on EEE Components

Ana Oliveira Braga Keating  
(Mestre)

Dissertação para obtenção do Grau de Doutor em Física

*Orientador: Doutor Mário João Martins Pimenta<sup>1</sup>*

*Co-Orientador: Doutor Eamonn Joseph Daly<sup>2</sup>*

*Constituição do Júri*

*Presidente: Reitor da Universidade Técnica de Lisboa*

*Vogais :     Doutor Jorge Manuel Rodrigues Crispim Romão<sup>1</sup>*

*Doutor Robert Allen Weller<sup>3</sup>*

*Doutor Mário João Martins Pimenta<sup>1</sup>*

*Doutor Eamonn Joseph Daly<sup>2</sup>*

*Doutor Ali Mohammad Zadeh<sup>2</sup>*

*Doutor Pedro Miguel Félix Brogueira<sup>1</sup>*

*Doutora Ana Maria Vergueiro Monteiro Cidade Mourão<sup>1</sup>*

Lisbon, September 2008

<sup>1</sup> *Instituto Superior Técnico da Universidade Técnica da Lisboa, Portugal*

<sup>2</sup> *European Space Agency, The Netherlands*

<sup>3</sup> *Vanderbilt University, United States of America*

*Ao João, ao David e ao Afonso*

*Porque são quem realmente orchestra a minha vida...*





## *Preface*

*"In the beginning God created the heavens and the earth. And the earth was without form and void, and darkness was upon the face of the deep. And the Spirit of God was moving over the face of the waters." God creates light; the "firmament" separating "the waters which were under the firmament from the waters which were above the firmament;" dry land and seas and plants and trees which grew fruit with seed; the sun, moon and stars in the firmament; air-breathing sea creatures and birds; and on the sixth day, "the beasts of the earth according to their kinds." "Then God said, Let us make man in our image ... in the image of God He created him; male and female He created them." [...]* [Genesis]

*To men and women God gave eyes, brain and an insatiable need for questioning. From the search for answers and new questions Man gave birth to Science and later to Technology. When questions started to be answered Man decided to build a telescope and look outside His world. He found that Earth was just a tiny point in an incredible vast Universe.*

*He believed it was possible to leave Earth limits and fought to search for new solutions and answers.*

*It is not possible to guess if these questions and answers are leading us to new worlds, new universes or anywhere else. It is just possible to follow the faith...*

*Personally I believe that we, Human kind, shall learn from the worlds we have never been in. We need to learn more about habitability and understand if We are able to inhabit inhospitable environments or if We are able to create habitability conditions in other planets.*

*It is in this scenario that, aware of my insignificance in this magnificent Universe I have dedicated my life to learn "God's purposes" and contribute to the Human mission of learning.*

*It is not the aim of this Thesis to reveal unquestionable truths or exceptional secrets. Instead, it aims at explaining and discussing the results of the last four years of research, willing that they may be useful to the reader.*



### *Resumo*

O planeamento de missões espaciais requiere o conhecimento profundo do ambiente de radiação e seus efeitos. Nesta Tese discute-se o transporte da radiação na Heliosfera e seus efeitos em componentes Electrónicos.

Os modelos desenvolvidos, baseados em GEANT4, utilizam técnicas de simulação Monte Carlos. Têm como objectivo a caracterização do ambiente de radiação em Marte e previsão dos seus efeitos. Como produto final devolvem o historial do transporte de partículas, mapas da radiação, doses, descrição do volume sensível do dispositivo. Os resultados mostram que a radiação em Marte depende fortemente da densidade atmosférica e sua pressão à superfície assim como da geologia local e tem um poder ionizante 100 vezes superior ao da Terra.

A abundância relativa de prótons e neutrões pode conduzir a efeitos nefastos para dispositivos semicondutores provocados pelo deslocamento de átomos das estruturas cristalinas ou por excesso de energia ionizante depositada. Nesta tese simularam-se os efeitos induzidos pela radiação ambiente no caso particular da memória AT60142F-ATMEL, utilizando o princípio de existência de um volume sensível, VS. Ajustando o VS reconstruíram-se as secções-eficazes experimentais. Conclui-se que a forma mais adequada para a memória testada é um volume tetraedral e não um paralalipedo rectangulo como sugerido por modelos tradicionais.

Palavras chave: Marte, Ambiente de radiação, efeitos, volume sensíveis, GEANT4, simulação



### *Abstract*

Successful spacecraft design requires in-depth knowledge of the space radiation environment and its effect. This thesis discusses the problem of transport of radiation in the Heliosphere and induced effects on Electric Electromagnetic Electronic components.

Developed models involving Monte Carlo simulation for Martian radiation environment characterization are presented, as well as, a framework to integrate radiation environment predictions and detailed device simulation. The framework employs Geant4 particle transport tool. Final outcome is full particle transport histories, radiation maps, doses, device sensitive volume size and shape.

Martian radiation environment results show an important dependence on atmospheric density, surface pressure and local geology. Ambient dose equivalents predicted are 100 times higher than on Earth.

The relative abundance of protons and neutrons may lead to Displacement Damage and Single Event Effects. Simulation of induced effects based on GEANT4 relies on the principle of existence of a device sensitive volume, SV. The model, tested with ATMEL-AT60142F SRAM, shows that the fit of SV shape enables the reconstruction of experimental effect cross-section curve. Results show best SV shape as tetrahedron-like, instead of traditional rectangle-parallelepiped.

Keywords: Mars, Radiation Environment, effects, sensitive volume, GEANT4, simulation



## *Acknowledgements*

*Those who believed:*

I would like to show my gratitude to Mario, Ali, Petteri, Eamonn and Ralf. Even without official positions for PhD students at ESA they believed it would be possible and helped me to create the conditions to enable a good, constant and close collaboration between LIP, IST and ESA.

*Those who read, discussed, corrected, worked with:*

Pedro and Mario, Ali, Petteri and Eamonn thank you for so many hours of reading, discussions and supervision.

I am thankful to ESA TEC-QCA and TEC-EES people, for all the discussions and work together, for the good environment and collaboration. I am also very grateful to all TEC-QC division at all levels for hosting me in such a good work and friendly environment.

To Sara and Patricia, thank you for your work, collaboration and team spirit. To the GEANT4 groups at LIP, thank you for the different interactions, discussions and the feeling of potential continuity... To LIP for being such a young and trustful institution.

I would like to thank Sérgio for the strong input he gave me in the beginning of my PhD, dealing with databases.

I need as well to express my gratitude to ESTEC Library service.

This work was funded by the Portuguese Foundation for Science and Technology and by the European Space Agency.

*Family and friends:*

Because life is meaningless without you, thank you so much for living with me.

To João, thank you for reviewing the thesis and for all the helpful discussions. In particular, thank you so much for being such a good husband and father, and to David for being such a good son. Thank you both for holding on during all my absent periods and for allowing me to go on my frequent work leaves with the comfort of trusting you were safe and happy together.

To all my friends in the Netherlands for making me feel at home: To the Portuguese because you give me the strong feeling that there is something special in being Portuguese and that is far more than enjoying a good meal of “bacalhau” together. To my friends from all around the world, locals, European, Brazilians, Asian, because we make me feel that there is something special not related to culture, space and time, but else inherent to the fact of being humans. To those who have already left but left deep roots in my heart, for making me feel that the size of the world doesn't really count. To Liz, Heleen, Joep and the kids for turning my Monday mornings into a direct passage to life in the Netherlands and of course for babysitting allowing me to study and dedicate to my thesis.

To my friends from always, in Portugal, thank you because thinking of you is reviewing my life, past, present and future. It is very important to rely on you.

To the rest of my family and relatives I show my gratitude in our mother tongue...

*Há coisas tão importantes que não se agradecem, vivem-se ...*

João e David, Licas, Sérgio, Miguel e Maria Inês, Mãe e Pai que são o meu núcleo duro. Tios e primos, todos juntos formam o manto que envolve e protege o meu núcleo; um a um, reconheço em mim cada movimento das vossas vidas. Avós: Bela e Helena, António e Paddy, exemplos de serenidade, durabilidade, permanência e eficiência de vida. Marcos que viverão para sempre em mim. Mãe Armanda e Pai Fernando, Eduarda e Toni porque é realmente como se de sangue se tratasse. Pedro e Sofia, porque o brilho dos vossos olhos me traz serenidade e é também a ver-vos crescer que caminho.





## *Table of Contents*

<b>0.</b>	<b><u>ABBREVIATIONS.....</u></b>	<b><u>0-1</u></b>
<b>1.</b>	<b><u>INTRODUCTION .....</u></b>	<b><u>1-1</u></b>
1.1.	MOTIVATION AND OBJECTIVES.....	1-1
1.1.1.	MARS EXPLORATION.....	1-3
1.1.2.	RADIATION ENVIRONMENT AND EFFECTS .....	1-5
1.2.	STRUCTURE OF THE THESIS .....	1-6
1.3.	AUTHOR CONTRIBUTION .....	1-8
1.3.1.	SIMULATION METHODS AND TOOLS.....	1-8
1.3.2.	PUBLICATIONS .....	1-9
<b>2.</b>	<b><u>RADIATION ENVIRONMENT IN THE SOLAR SYSTEM.....</u></b>	<b><u>2-1</u></b>
2.1.	THE SUN AND THE HELIOSPHERE .....	2-1
2.1.1.	HELIOSPHERE.....	2-3
2.1.2.	THE SOLAR CYCLE .....	2-6
2.1.3.	FLARES AND CORONAL MASS EJECTIONS (CME) .....	2-6
2.1.4.	COSMIC RAYS.....	2-8
2.2.	MODELS AND TOOLS .....	2-9
2.2.1.	TRAPPED RADIATION.....	2-10
2.2.2.	SOLAR ENERGETIC PARTICLES .....	2-10
2.2.3.	COSMIC RAYS.....	2-12
2.3.	EARTH RADIATION ENVIRONMENT .....	2-13
2.3.1.	MAGNETOSPHERE .....	2-13
2.3.2.	RADIATION BELTS .....	2-14
2.3.3.	TYPICAL SHUTTLE ORBIT AND ENVIRONMENT PREDICTION.....	2-16
2.4.	NEAR EARTH INTERPLANETARY & TRANSPORT.....	2-18
2.4.1.	INTERPLANETARY TRANSPORT .....	2-18
2.4.2.	PROPAGATION TO MARS.....	2-21
2.4.2.1.	NEAR EARTH INTERPLANETARY PROTON SPECTRA.....	2-22
2.4.3.	ATMOSPHERE SHIELDING AND SOIL CONTRIBUTION .....	2-23
2.4.4.	OTHER PLANETS AND MAGNETOSPHERE EFFECTS.....	2-23

<b>3.</b>	<b><u>RADIATION EFFECTS ON EEE COMPONENTS .....</u></b>	<b><u>3-1</u></b>
<b>3.1.</b>	<b>METAL-OXIDE-SEMICONDUCTOR DEVICES.....</b>	<b>3-1</b>
3.1.1.	BASIC DEVICE CHARACTERISTICS .....	3-1
3.1.2.	PRINCIPLES OF OPERATION .....	3-2
3.1.2.1.	EQUILIBRIUM AND NON-EQUILIBRIUM CONDITIONS .....	3-3
3.1.2.2.	THRESHOLD VOLTAGE .....	3-6
3.1.2.3.	DIFFERENT TYPES OF MOS FIELD-EFFECT TRANSISTORS.....	3-7
3.1.2.4.	COMPLEMENTARY MOS .....	3-8
3.1.3.	IONIZATION RELATED SEMICONDUCTOR MECHANISMS .....	3-9
3.1.3.1.	E-H PAIR GENERATION ENERGY THRESHOLD.....	3-10
3.1.3.2.	RECOMBINATION .....	3-13
<b>3.2.</b>	<b>RADIATION-INDUCED EFFECTS .....</b>	<b>3-15</b>
3.2.1.	TOTAL IONIZING DOSE MECHANISMS .....	3-16
3.2.2.	TRANSIENTS MECHANISMS .....	3-20
3.2.2.1.	PHYSICS OF TRANSIENT IONIZATION.....	3-20
3.2.2.2.	APPROACH TO ANALYSIS.....	3-23
3.2.2.3.	SINGLE EVENT EFFECTS IN COMPLEX DEVICES.....	3-25
3.2.3.	DISPLACEMENT DAMAGE MECHANISMS .....	3-28
<b>3.3.</b>	<b>DEGRADATION RATE PREDICTION.....</b>	<b>3-29</b>
<b>3.4.</b>	<b>CONCLUSIONS.....</b>	<b>3-31</b>
<b>4.</b>	<b><u>MARS RADIATION ENVIRONMENT CHARACTERIZATION .....</u></b>	<b><u>4-1</u></b>
<b>4.1.</b>	<b>SIMULATION ARCHITECTURE.....</b>	<b>4-1</b>
<b>4.2.</b>	<b>GEANT4 TOOLKIT .....</b>	<b>4-3</b>
4.2.1.	GENERAL PROPERTIES .....	4-3
4.2.2.	PHYSICS MODELS .....	4-3
<b>4.3.</b>	<b>MARS RADIATION ENVIRONMENT: TWO IMPLEMENTATIONS.....</b>	<b>4-7</b>
4.3.1.	MARSREC .....	4-7
4.3.2.	DMEREM .....	4-8
<b>4.4.</b>	<b>DATABASES AND INTERFACES .....</b>	<b>4-9</b>
4.4.1.	MARS CLIMATE DATABASE.....	4-9
4.4.1.1.	MCD Version 3.0.....	4-11
4.4.1.2.	MCD Version 4.2 and latest .....	4-14
4.4.2.	MARS TOPOLOGY .....	4-15
4.4.3.	MARS SOIL COMPOSITION .....	4-16

<b>4.5. MARS RADIATION ENVIRONMENT CHARACTERIZATION.....</b>	<b>4-25</b>
4.5.1. INPUT RADIATION.....	4-25
4.5.2. SIMULATION SET-UP.....	4-25
4.5.2.1. Different geometries, different location and times of the day.....	4-25
4.5.3. SIMULATION RESULTS.....	4-26
4.5.3.1. Radiation fluxes due to GCR.....	4-26
4.5.3.2. Radiation fluxes due to SEP.....	4-27
4.5.3.3. Boundary conditions considerations.....	4-28
4.5.3.4. Importance of Backscattering.....	4-29
4.5.3.5. Dose due to GCR.....	4-31
4.5.3.6. Radiation Maps.....	4-32
4.5.4. CONCLUSIONS.....	4-33
<b>4.6. VARIABILITY OF RADIATION ENVIRONMENT IN TIME.....</b>	<b>4-34</b>
4.6.1.1. Primary and secondary particles.....	4-34
4.6.1.2. Backscattered Neutrons.....	4-36
4.6.1.3. Integrated fluence as function of Solar Longitude.....	4-36
4.6.2. GCR-INDUCED RADIATION ENVIRONMENT AND TIME.....	4-37
<b>4.7. DOSE EQUIVALENT CALCULATIONS.....</b>	<b>4-38</b>
4.7.1. FLUKA CONVERSION FACTORS.....	4-39
4.7.2. MARSREC FLUENCES CONVERTED TO DOSE EQUIVALENT.....	4-39
<b>4.8. VERIFICATION OF MARS RADIATION ENVIRONMENT SIMULATIONS.....</b>	<b>4-41</b>
4.8.1. COMPARING MARIE OBSERVED DOSES.....	4-41
4.8.1.1. In orbit Dose rate measures.....	4-42
4.8.1.2. MarsREC Dose rate at the surface.....	4-42
4.8.2. COMPARISONS OF DOSE EQUIVALENT RESULTS.....	4-43
4.8.3. COMPARISONS OF FLUENCES.....	4-44
<b>4.9. IMPORTANCE OF THE SOIL COMPOSITION.....</b>	<b>4-46</b>
4.9.1.1. Simulation results: analysis.....	4-48
<b>4.10. IS MARS A NICE PLACE TO LIVE?.....</b>	<b>4-49</b>
<b>4.11. FUTURE DEVELOPMENTS.....</b>	<b>4-51</b>

<b>5. SINGLE EVENT EFFECTS ON EEE COMPONENTS .....</b>	<b>5-1</b>
<b>5.1. SEE ON MEMORY DEVICES .....</b>	<b>5-1</b>
5.1.1. METHODS FOR FITTING DEVICE RESPONSE FUNCTIONING.....	5-3
5.1.1.1. Unique Critical Charge Method .....	5-4
5.1.1.2. The Bendel Method .....	5-4
5.1.1.3. The Weibull Method .....	5-5
5.1.2. TRADITIONAL RPP MODELS.....	5-6
5.1.2.1. Funnelling.....	5-6
5.1.2.2. From step function to smooth curves .....	5-7
5.1.3. NON- RPP MODELS .....	5-7
<b>5.2. SIMULATION FRAMEWORK .....</b>	<b>5-9</b>
5.2.1. GEANT 4 AND DEVICE PHYSICS .....	5-9
5.2.2. COMPONENT DEGRADATION SIMULATION (CODES) FRAMEWORK .....	5-10
<b>5.3. ATMEL DEVICE .....</b>	<b>5-12</b>
<b>5.4. STATISTIC APPROACH .....</b>	<b>5-16</b>
5.4.1. REPRODUCING IRRADIATION TEST DATA .....	5-16
5.4.2. SEU RATE PREDICTIONS .....	5-18
5.4.3. COMPARISONS WITH CREME96 .....	5-20
5.4.4. DISCUSSION .....	5-23
<b>5.5. MICROSCOPIC APPROACH.....</b>	<b>5-24</b>
5.5.1. REDEFINITION OF SENSITIVE VOLUME.....	5-24
5.5.2. EFFICIENCY MATRIX MODULE.....	5-24
5.5.3. PLACEMENT OF SENSITIVE VOLUMES.....	5-25
5.5.4. SENSITIVE VOLUMES THICKNESSES AND SHAPES .....	5-26
5.5.5. SHIELDING.....	5-27
5.5.6. ION COCKTAILS .....	5-28
5.5.7. ANGLING .....	5-29

<b>5.6. SV-FIT .....</b>	<b>5-30</b>
5.6.1. CONSIDERATIONS ON AT60142F SRAM EXPERIMENTAL DATA .....	5-30
5.6.2. GETTING RPP THRESHOLD SENSITIVITY FROM GROUND BASED TEST DATA .....	5-31
5.6.3. REDEFINITION OF CRITICAL LET .....	5-33
5.6.4. FIT SV DIMENSIONS AND SHAPE BY MICRODOSIMETRY CALCULATIONS .....	5-35
5.6.4.1. Rectangle Parallelepiped Sensitive Volume.....	5-36
5.6.4.2. Tetrahedron Sensitive Volume .....	5-38
5.6.4.3. Transversal Area correction .....	5-40
5.6.4.4. Truncated Tetrahedron Sensitive Volume .....	5-41
5.6.5. DISCUSSION: DRIFT AND DIFFUSION MECHANISMS .....	5-43
<b>5.7. FUTURE DEVELOPMENTS.....</b>	<b>5-47</b>
<b><u>6. CONCLUSIONS.....</u></b>	<b><u>6-1</u></b>
6.1. MARSREC AND DMEREM .....	6-1
6.2. CODES .....	6-3
6.2.1. STATISTIC APPROACH .....	6-3
6.2.2. MICROSCOPIC APPROACH .....	6-4
6.3. CONTEXT AND FUTURE .....	6-5
<b><u>7. BIBLIOGRAPHY .....</u></b>	<b><u>7-1</u></b>
<b><u>APPENDIX I:.....</u></b>	<b><u>A- 1</u></b>



## *Table of Figures*

Figure 1-1 - Phase Diagram of water (adapted from [Chaplin, 2007]) .....	1-3
Figure 2-1 – Internal structure of the Sun (adapted from [Kallenrode, 2001]).....	2-2
Figure 2-2 – Photospheric, source surface and interplanetary magnetic field (adapted from [Kallenrode, 2001]).....	2-4
Figure 2-3 – Different population of charged particles in the inner heliosphere and modulation structures (adapted from [Kallenrode, 2001]) .....	2-5
Figure 2-4 –Monthly average of Sunspots since 1749 until today (adapted from [SIDC, 2007]) .....	2-6
Figure 2-5- Relative abundance of elements in cosmic radiation [Keating, 2002] (extracted from [Balebanov, 1990]).....	2-9
Figure 2-6- Comparison between the Integrated Fluences of solar events of October-November 2003 and the Worst Week model from CREME96 based on the solar event of October 1989.....	2-11
Figure 2-7- Earth Magnetosphere modulation by solar wind. [Russel, 1987].....	2-14
Figure 2-8- Movement described by the trapped particle around a force line of the magnetic field [Boezio, 1998].....	2-15
Figure 2-9 - Electron radiation belts. Isoflux map of electron with energies above 1MeV. The radius of the Earth is 6371 km [Holmes-Siedle, 2006] .....	2-16
Figure 2-10- Proton radiation belts. Isoflux map of proton, with energies above 10MeV. The radius of the Earth is 6371 km [Holmes-Siedle, 2006] .....	2-16
Figure 2-11 –Effect of Trapped Protons Flux and GCR protons for a common orbit (28.5°, 450 km) for shuttle missions. ...	2-17
Figure 2-12- Galactic Cosmic Rays for charged particles for a common orbit (28.5°, 450 km) for shuttle missions. Charge number, Z, from protons (Z=1) to Neon (Z=10).....	2-17
Figure 2-13- Worst week SEP fluxes for charged particles for a common orbit (28.5°, 450 km) for shuttle missions. Charge number, Z, from protons (Z=1) to Neon (Z=10).....	2-18
Figure 2-14 - Fluence correction factor for 250-MeV solar protons as a function of distance from the Sun for different mean free paths. Mean free paths of 0.4 and 0.2 AU imply event fluences at Mars about 20% higher than would be predicted from measurements at Earth if only geometrical corrections ( $1/R^2$ ) were used. The dashed line indicates the location of Mars at 1.5 AU.....	2-21
Figure 2-15- GCR proton flux in solar-quiet model in the solar maximum and proton flux from “worst week” model SEP, by CREME96.....	2-22
Figure 3-1– Schematic diagram of a n-channel MOSFET [Sze, 1981] .....	3-2
Figure 3-2 – Energy Bands and charge distribution in a MOS. ....	3-4
Figure 3-3- Two-dimension band diagrams of an n-channel MOSFET. ....	3-5
Figure 3-4- Illustration of the operation of surface field-effect transistor for $V_G > V_T$ .....	3-5
Figure 3-5- MOSFET drain current-voltage relationship for different gate voltages, $V_G$ .....	3-7
Figure 3-6 – Basic types of MOSFET devices.....	3-8
Figure 3-7 – CMOS inverter. ....	3-9
Figure 3-8 – Real energy band structures of Si, including hypothetical impact-ionization process. ....	3-11
Figure 3-9 - Recombination through intermediate centres, or single-level recombination process .....	3-14
Figure 3-10 – Dependence of lifetime upon impurity content: Shockley and Read theoretical prediction.....	3-14

Figure 3-11 – Charge build-up mechanisms & variation of the electric field due to trapped charge.....	3-17
Figure 3-12 – Simple charge sheet model. ....	3-17
Figure 3-13 – Typical variation of CMOS characteristic capacitance curve and drain current with gate voltage. ....	3-18
Figure 3-14 – a) NMOS degradation and failure points; b) PMOS degradation and failure points .....	3-19
Figure 3-15- Graphical view of ion track creating a electron plasma in the semiconductor .....	3-20
Figure 3-16 – Transient distortion of the electric field along the ion track from original depletion region.....	3-21
Figure 3-17- Time dependence of drift current: a) Prompt charge collection, b) Transient current .....	3-21
Figure 3-18 - Charge collected as a function of alpha particle energy depending on substrate resistivity.....	3-22
Figure 3-19 - Charge collected as a function of bias voltage for different substrate resistivity.....	3-22
Figure 3-20 - SEE response function curves for different devices for ion irradiation test data.....	3-27
Figure 3-21 - SEE response function curves for different devices for proton irradiation test data. ....	3-27
Figure 4-1 – Simulation architecture.....	4-2
Figure 4-2– Scheme of the twelve seasons of Mars [Forget, 2001].....	4-10
Figure 4-3- Data organization on MACLIDI.v.3.0 .....	4-14
Figure 4-4- 3D Martian topology map .....	4-16
Figure 4-5- Geological map of Mars [Spohn, 1998] .....	4-17
Figure 4-6 – TES spectra: basalt (top) and andesite (down).....	4-18
Figure 4-7- OMEGA- Mars Express surface maps: Pyroxenes (top) and anhydrous nanophase ferric oxides (down). ....	4-19
Figure 4-8 - Equivalent-weight water found in the regions around the equator of Mars by GRS on board of Mars Odyssey, March 2006 [GRS, 2008]. ....	4-21
Figure 4-9 - Map of Martian Hydrogen at the North Pole, July 2004 [GRS, 2008] .....	4-21
Figure 4-10 – Surface CO <sub>2</sub> layer, solar Longitude 0° to 30°; Map obtained with MCD. ....	4-22
Figure 4-11- Surface CO <sub>2</sub> layer, solar Longitude 180° to 210°: Map obtained with MCD.....	4-22
Figure 4-12- SOILCOMPI.v.2.0 data organization .....	4-23
Figure 4-13- Equivalent-weight of iron found in the regions around the equator of Mars by GRS on board of Mars Odyssey, March 2006 [GRS, 2008] .....	4-24
Figure 4-14 - Radiation Environment at the surface of Mars due to GCR protons for Case A.....	4-27
Figure 4-15- Radiation Environment at the surface of Mars due to SEP protons for Case B .....	4-27
Figure 4-16 - Backscattering component of all particles detected at the surface of Mars due to GCR protons for simulation Case A.....	4-30
Figure 4-17- Backscattering component of all neutrons detected at the surface of Mars due to GCR protons for simulation Case A.....	4-30
Figure 4-18 - Backscattering component of all particles detected at the surface of Mars due to SEP protons for Case B. ....	4-31
Figure 4-19 - Backscattering component of all neutrons detected at the surface of Mars due to SEP protons for simulation Case B. ....	4-31
Figure 4-20 - Total fluence per year of neutrons with energy higher than 30 MeV at the surface of Mars due to GCR protons for simulation Cases C, D E and F, in the vicinity of Tyrrhena Paterae.....	4-32
Figure 4-21 - Pressure at the Viking 1 <sup>1</sup> (bottom curve) and Viking 2 <sup>3</sup> (top curve) sites for 1 year of the MCD Viking dust scenario [Lewis, 1999].....	4-34
Figure 4-22 –Transfer function for integrated fluence of protons at the surface of Mars .....	4-35
Figure 4-23–Transfer function for integrated fluence of secondary particles at the surface of Mars.....	4-35

Figure 4-24 –Impact of surface pressure in the percentage of Backscattered neutrons. ....	4-36
Figure 4-25–Total integrated fluence as function of Solar Longitude for different locations. ....	4-36
Figure 4-26 - MARIE dose rate measurements from May through September 2003; the last SPE observed in this period was May 31-June 3.....	4-42
Figure 4-27 – Dose Equivalents.....	4-43
Figure 4-28 – Proton flux spectra for solar minimum GCR emergent from $\geq 50\text{g/cm}^2$ regolith: In dark blue MarsREC results for Martian Regolith and in red triangle NASA results for Lunar Regolith.....	4-45
Figure 4-29– Neutron flux spectra for solar minimum GCR emergent from $\geq 50\text{g/cm}^2$ regolith: In dark blue MarsREC results for Martian Regolith and in red triangle NASA results for Lunar Regolith.....	4-45
Figure 4-30- Dependence of neutron backscattering on soil composition (top) and density (bottom).....	4-47
Figure 4-31- Dependence of ambient dose equivalent due to neutrons on soil composition (top) and weight percentage of $\text{Fe}_2\text{O}_3$ (down). ....	4-48
Figure 4-32 – Ambient dose Equivalent. ....	4-49
Figure 5-1 – Scheme of a memory cell.....	5-2
Figure 5-2- Logical functioning of a recorded memory cell.....	5-2
Figure 5-3- Scheme of a SEU in a SRAM cell.....	5-3
Figure 5-4- Critical charge method .....	5-4
Figure 5-5 – RPP model scheme.....	5-6
Figure 5-6 - Geometrical explanation of cross-section modulation due to path length distribution .....	5-8
Figure 5-7- CODES Philosophy.....	5-11
Figure 5-8- ATMEL 4-Mbit SRAM – 8 blocks of $512\text{K} \times 1$ .....	5-12
Figure 5-9- Single bit cell .....	5-13
Figure 5-10- Electronic Circuit .....	5-13
Figure 5-11- Ion ranges in the CMOS technology.....	5-14
Figure 5-12- Two possible ways of construct implants geometry into GEANT4. ....	5-15
Figure 5-13 - Reproducing experimental data with Weibull response function .....	5-17
Figure 5-14- Reproducing experimental data with Weibull response function. ....	5-17
Figure 5-15 –Simulation set-up scheme.....	5-18
Figure 5-16- SEU cross-sections for protons and neutrons: MarsREC reconstruction and experimental data.....	5-19
Figure 5-17- SEP- induced simulated SEU rates predictions and CREME96.....	5-22
Figure 5-18- GCR- induced simulated SEU rates predictions and CREME 96.....	5-23
Figure 5-19- Simulated sensitive areas: dimensions and placement.....	5-25
Figure 5-20 – Simulation setup: 4 bit cells with 6 sensitive volumes each. ....	5-25
Figure 5-21- Vertical profile of simulated geometry .....	5-26
Figure 5-22- Simulation scheme: Rectangle Parallelepiped (left) and Tetrahedron (right).....	5-27
Figure 5-23 – Comparison between GEANT4 RPP simulation irradiation test data.....	5-32
Figure 5-24 – SEU cross-section as function of SV thickness .....	5-33
Figure 5-25– Path length distribution: Assumption critical energy by analyses of Nitrogen deposited Energy distribution for a SV thickness of $2\mu\text{m}$ .....	5-34
Figure 5-26- Rpp scheme.....	5-35
Figure 5-27- SEU cross-section curves: Comparison between experimental data and simulation results .....	5-36

Figure 5-28- Energy deposited in MeV for different Nitrogen and Neon travelling through the device with rpp SV of 1 $\mu$ m thick.....	5-37
Figure 5-29 – 2D calculation of SV shape based on reduction postulate III.....	5-38
Figure 5-30 - Deposited energy distribution for Nitrogen, Neon, Silicon, Argon and Krypton with the TRD SV.....	5-39
Figure 5-31- SEU cross-section curves: Comparison between experimental data and simulation results .....	5-39
Figure 5-32- SEU cross-section curves: Comparison between experimental data and simulation results .....	5-41
Figure 5-33- SEU cross-section curves: Comparison between experimental data and simulation results TRD and tTRD.	5-42
Figure 5-34 – P-n-p-n effects in CMOS device after [Holmes-Siedle, 2006] .....	5-43
Figure 5-35 – Influence of ion impact location on transient pulse shape [Bertrand, 2007] .....	5-45

---

## 0. Abbreviations

AM	Analysis Module
ATMEL	Name of Semiconductor manufacturer
BIC	Binary Cascade Model
CIR	Corotating Interaction Region
CME	Coronal Mass Ejections
CMOS	Complementary metal–oxide–semiconductor
CNES	Centre National d'Etudes Spatiales
CODES	Component Degradation Simulation tool
CREME96	Cosmic Rays Effects on Micro Electronics
DD	Displacement Damage
dMEREM	detailed Mars Energetic Radiation Environment Model
DRAM	dynamic random access memories
EEE	Electrical, Electromagnetic and Electronic
EM	Efficiency Matrix
ESA	European Space Agency
ESWW	European Space Weather Week
GCR	Galactic Cosmic Rays
GD	Geometry Description
GEANT4	GEometry ANd Tracking
GRS	Gamma Ray Spectrometer
HEP	High Energy Parameterised
IAA	International Academy of Astronautics
IC	Integrated Circuits
ICRU	International Commission on Radiation Units
IEEE	Institute of Electrical and Electronics Engineers
IEEE TNS	IEE Transactions on Nuclear Science
IMP-8	Interplanetary Monitoring Platform
ISO	International Standards Organization
IST	Istituto Superior Técnico de Lisboa

---

---

LEP	Low Energy Parameterised
LET	Linear Energy Transfer
LHEP	Low and High Energy Parametrized models
LIP	Laboratório de Instrumentação em Física Experimental de Partículas
MACLIDI	Mars Climate Database Interface
MARIE	Mars Radiation Environment Experiment
MarsREC	Mars Radiation Environment Characterization
MarsREM	Mars Radiation Environment Models
MBU	Multiple Bit Upset
MCD	MARS CLIMATE DATABASE
MGS	Mars Global Surveyor
MO	Olympus Mons
MOLA	Mars Orbiter laser altimeter
MOS	Metal-Oxide-Semiconductor
MOSFET	Metal-Oxide-Semiconductor Field-Effect Transistors
NASA	National Aeronautics and Space Administration
NASA/GSFC	NASA Goddard Space Flight Centre
NIEL	Non-Ionising Energy Loss
NIR	Noise Immunity Reduction
NMOS	N-channel Metal-Oxide-Semiconductor
NMRC	National Microelectronics Research Centre
NSREC	Nuclear and Space Radiation Effects Conference
NSSDC	National Space Science Data Centre
NUCFRG1	Nuclear Fragmentation Model
PMOS	P-channel Metal-Oxide-Semiconductor
RADFET	Radiation-sensing Field Effect Transistor
RPP	Rectangle Parallelepiped
SEE	Single Event Effects
SPE	Solar Particle Events
SEP	Solar Energetic Particles
SEU	Single Event Upset
SOILCOMPI	Interface with Soil Composition Database

---

---

SPENVIS	Space Environment Information System
SRAM	Static Random Access Memory
SRH	Shockley-Read-Hall
SRIM	Stopping and Ranges of Ions in Matter
SV	Sensitive Volume
SV-FIT	Sensitive Volume interactive Fit Tool
TES	Thermal Emission Spectrometer
TID	Total Ionizing Dose Effects
TP	Tyrrhena Paterae
TRD	Tetrahedron
tTRD	Truncated Tetrahedron
VS	Volume Sensitive

---







# 1. Introduction

*Science gives mankind inspiration and aspiration. Space science makes us look outwards from our planet, towards the stars.*

*in "ESA Space Science" [ESASS, 2008]*

## *1.1. Motivation and objectives*

Space Exploration and Science is a strategic asset for ESA, NASA and other Space Agencies. It ensures technological development and independence and it supports science-based societies [ESASS, 2008].

Ancient astronomers observed points of light that appeared to move among the stars. They called these objects planets and named them after Roman deities: Jupiter, king of the gods; Mars, the god of war; Mercury, messenger of the gods; Venus, the god of love and beauty, and Saturn, father of Jupiter and god of agriculture. The stargazers also observed comets with sparkling tails, and meteors or shooting stars apparently falling from the sky.

However Man has just reached the ability of operating spacecraft successfully due to advancements in rocketry after World War II enabling our machines to break the grip of Earth's gravity. In 1957 the Russian Sputnik was launched into orbit [Fortescue, 2001]. In a few decades the technology has made progresses, in 1969 Americans sent the first successful manned mission to the Moon, and in little more that 30 years unmanned explorer spacecrafts have flown by the major bodies of the solar system.

Table 1-1 shows the ESA space missions log. It classifies the missions according to their current status and objectives: Study of the Sun, Solar System exploration, Astrophysics and Fundamental physics.

---

 <b>Science &amp; Technology</b>		Science Programme European Space Agency		
	Sun	Solar System	Astrophysics	Fundamental
<b>Operations</b>	SOHO [1995] Ulysses [1990]	Venus Express [2005] Rosetta [2004] Mars Express [2003] Double Star [2003] Cluster [2000] Cassini-Huygens [1997]	INTEGRAL [2002] XMM-Newton [1999] Hubble [1990]	
<b>Implementation</b>		BepiColombo	Herschel [2008] Planck [2008] Gaia JWST	Lisa-Pathfinder [2009]
<b>Assessment</b>	Solar Orbiter			
<b>Completed</b>		SMART-1 [2003] Giotto [1985]	ISO [1995] Hipparcos [1989] EXOSAT [1983] IUE [1978] Cos-B [1975]	
<b>Future Missions</b>	Cosmic Vision 2015 - 2025			

**Table 1-1- ESA Science and technology missions [ESASS, 2008]**

The planetary exploration aims at understanding Earth environment and evolution in the context of the Solar System. Additionally the Solar System exploration is an essential stepping stone for exploring the wider Universe. In the next decade, research will focus on planets around other stars [ESASS, 2008].

The Sun being the star of our Solar System plays an important role at different levels. The study from its deep core, through its outer atmosphere - the corona - and the domain of the solar wind, out to a distance ten times beyond the Earth's orbit, aims at understanding the heliosphere and different mechanisms such as radiation propagation and acceleration in the heliosphere, and pattern of interplanetary magnetic field changes. The study of the Sun is as well a contribution for the comprehension and analysis of Earth's changing climate.

Space Science aims as well at searching for answers regarding the origin of the Universe. By looking into the microwave background of the Universe, space science looks directly into the Universe creation and evolution. The NASA/ESA Hubble Telescope has become one of the most important science projects. Using advanced cameras and spectrometry have observed the Hubble Deep Fields [ESASS, 2008], black holes [Noyola, 2008], looked into the galaxy

formation [Miley, 2006], measured the expansion of the universe [ESASS, 2008] and latest found organic molecules on an extrasolar planet [Swain, 2008].

Studying space science at its largest scale provides as well some of the deepest insights into Fundamental Physics.

### 1.1.1. Mars Exploration

The main motivation for exploring and sending missions to Mars is the search for life and the understanding the evolution of Earth. Figure 1-1 depicts the phase diagram of water [Chaplin, 2007]. It illustrates the surface pressure and temperature ranges for Earth and the closest neighbouring planets Mars and Venus. Martian surface pressure and temperature are very near the triple point where the three phases of water can live together, while Venus lives above the critical point with very high surface temperature and pressure. Different authors [Kahn, 1985], [Melosh, 1989] explain that in the past the temperature and pressure at the surface of Mars should have been higher, of the order of  $3 \times 10^3 \text{ Pa}$ . This is shown in figure 1-1 by a negative time line.

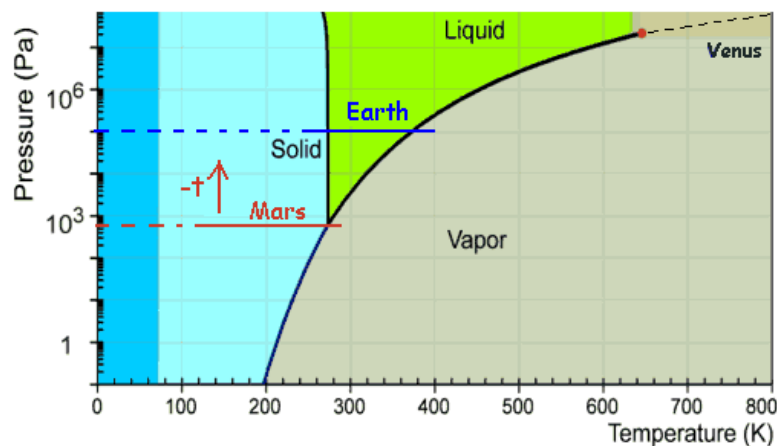


Figure 1-1 - Phase Diagram of water (adapted from [Chaplin, 2007])

This result indicates that in the past Mars might have had conditions for liquid water, hence potentially enabling the creation of life.

The search for evidences of water on Mars is one of the major issues in Mars exploration, since it is the fundamental element in the search for life. Additionally radiation levels expected at the surface of Mars may bring additional information when searching for remaining forms of life on the planet.

Since 1960, ESA, NASA and other Space Agencies have flown more than 35 missions to Mars and its moons of which only 11 were successful, produced or are currently producing data (e.g. Viking 1 and 2, Phobos 2, Mars Express, Mars Exploration Rovers, Odyssey and Phoenix) [NASA, 2006], [ESAST, 2007]. Table 1-2 illustrates the latest 17 missions to Mars describing the purpose and results.

<i>Mission</i>	<i>Country</i>	<i>Launch Date</i>	<i>Purpose</i>	<i>Results</i>
Viking 1	U.S.	8/20/1975	Mars orbiter/lander, orbit 6/19/76-1980, lander 7/20/76-1982	Combined, the Viking orbiters and landers returned 50,000+ photos
Viking 2	U.S.	09/09/1975	Mars orbiter/lander, orbit 8/7/76-1987, lander 9/3/76-1980	combined, the Viking orbiters and landers returned 50,000+ photos
Phobos 1	USSR	07/07/1988	Mars/Phobos orbiter/lander	lost 8/88 en route to Mars
Phobos 2	USSR	07/12/1988	Mars/Phobos orbiter/lander	lost 3/89 near Phobos
Mars Observer	U.S.	9/25/1992	orbiter	lost just before Mars arrival 8/21/93
Mars Global Surveyor	U.S.	11/07/1996	orbiter (MOLA, TES, HR Camera, Magnetometer & Reflectometer), arrived 9/12/97	currently conducting prime mission of science mapping
Mars 96	Russia	11/16/1996	orbiter and landers	launch vehicle failed
Mars Pathfinder	U.S.	12/04/1996	Mars lander and rover (Sojourner), landed 7/4/97	last transmission 9/27/97
Nozomi (Planet-B)	Japan	07/04/1998	Mars orbiter, currently in orbit around the Sun	Mars arrival delayed to 12/03 due to propulsion problem
Mars Climate Orbiter	U.S.	12/11/1998	Orbiter	lost on arrival at Mars 9/23/99
Mars Polar Lander/Deep Space 2	U.S.	01/03/1999	lander/descent probes to explore Martian south pole	lost on arrival 12/3/99
Mars Odyssey	U.S.	04/07/2001	Orbiter (GRS, Neutron Detector, TES, MR Image)	currently conducting mission of science mapping
Mars Express	ESA	02/06/2003	Orbiter (HR colour Image, IRS, Mineralogic Mapping, 2 Atmosp. Spectrometers)	currently conducting mission of science mapping
Spirit (MER1)	U.S.	10/06/2003	Mars Exploration Rovers (Hazcams and Navcams, Mini-TES, Mössbauer, Alpha Particle X-Ray (APXS), Rock Abrasion Tool (RAT), Magnet Array)	currently conducting mission
Opportunity (MER 2)	U.S.	24/01/2004		currently conducting mission
Mars Reconnaissance	U.S.	12/08/2005	Orbiter (Optical Navigation Camera (ONC), a detector on the Mars Climate Sounder (MCS), and the KaBand Telecommunications experiment)	currently conducting mission
Phoenix	U.S.	04/08/2007	Investigate the History of the Water, Determine possibility of microbial life in the northern plains: Chemical lab, oven mass spectrometer	currently conducting mission

The rest of the missions and part of the successful missions have failed. In particular the Mars Radiation Environment instrument on board of Mars Odyssey (MARIE) and Nazomi (Planet-B) failed as a consequence of the intense solar event of October–November 2003 [Cucinotta, 2003] [Barbieri, 2004]. As a result, studies of Martian radiation environment are of increasing importance.

The development of the work of this Thesis was initiated in a period in which Mars Exploration was an ESA priority and later the President of United States of America assumed publicly that Mars Exploration was one of the most important scientific goals of NASA Space Program.

### 1.1.2. *Radiation Environment and effects*

The radiation environment was discovered due to cosmic radiation ionisation power. In the eighteenth's century Elster and Geitel observed that completely airtight electroscopes insulated in dry air containers revealed electric discharges whenever the containers were covered or not by lead layers [Holmes-Siedle, 2005]. Based on these observations they concluded that this ionising radiation has a high penetration power. Only in 1912 Victor Hess, flying an electroscope in one of his balloon experiment, proved that this ionising radiation has an extraterrestrial origin because its intensity increases with altitude.

Before the discovery of cosmic radiation,  $\gamma$ -rays originated from natural radioactivity were the most penetrating radiation already known. This raised the hypothesis that the environment radiation was composed by high frequency  $\gamma$ -rays. Only after the evolution of experimental techniques it was possible to verify that: 1<sup>st</sup>, this radiation consists in a mixture of heavy ions,  $\gamma$ -rays, protons and electrons within a wide range of energies; and 2<sup>nd</sup> this mixture of charged particles is in part due to secondary radiation originated by reactions between primary particles and the atmospheric nucleus. Based on these verifications it can be concluded that there are two kinds of cosmic radiation spectrums: the one composed by particles coming from interplanetary or interstellar medium, the *primary spectrum*; and that composed by the secondary particles, the *secondary spectrum*.

Spacecraft operation is characterized by its remoteness from the Earth protective magnetic shielding and atmosphere [Fortescue, 2001]. Earth atmosphere and magnetosphere provide a suitable environment in which life has been able to evolve. However outside this shielded environment, radiation hazard increases and may adversely affect Electrical, Electromagnetic and Electronic (EEE) components, spacecraft and compromise the entire mission as illustrated in Table 1-2.

Radiation-induced effects on semiconductor devices is a challenging area of increased interest due to increased requirements in space exploration such as, mission duration time, lower power consumption requirements and scaled down technologies.

Semiconductor materials are particularly sensitive to damage caused by high-energy charged and neutral particles. This generally arises due to both the displacement of atoms from crystal lattice sites and to local ionisation, together with an ionisation track caused by penetrating radiation.

---

Depending on the semiconductor technology undesirable radiation-induced effects may be very variable. It is therefore impossible to use theory alone to predict the effects on devices under a given radiation exposure [Holmes-Siedle, 2006]. Irradiation test and simulation are an integral part of the devices and systems evaluation.

Since the 80's many researchers and institutions have worked to build engineering tools to enable the simulation of radiation environment conditions and its effects on EEE components. However 1D, or 2D approximations including elastic and inelastic interactions reveal unsatisfactory results for nowadays scaled technologies, with complex shielding materials. In the latest years many in-house tools start to be developed in order to combine Monte Carlo radiation tracking and interfacing with expensive circuit simulation tools. These frameworks, in particular those applied to the simulation of single event effects, require for an accurate simulation, the full detailed technology description of the device, often not delivered by the vendor. In this domain the development of an integrated tool enabling the prediction of planetary radiation environment, characterization of radiation environment at component level and enabling the fit of sensitive volume properties based on experimental data rather than vendor information is considered greatly beneficial.

## *1.2. Structure of the Thesis*

This thesis aims at describing the context background and the development of novel tools for Martian Radiation environment characterization and the evaluation of radiation induced effects on EEE components.

The thesis is organised into six chapters including this introduction. Chapter 2 aims at characterising the radiation environment in the Solar System from the most important sources to the planetary environments. In particular the Sun and Galactic Cosmic Rays (GCR) being the most important radiation sources in the Solar System are studied. Additionally propagation mechanisms in the heliosphere and solar modulation of GCR spectra are described. Still in Chapter 2 a few models and tools used quantifying and analysing radiation environment are described. Finally planetary radiation environment is considered being highly dependent on planetary magnetic field and atmospheric shielding. Earth radiation environment is explored in particular because it is the most well known and the reference for

---

habitability. Moreover Chapter 2 also aims at passing to the reader the idea of quantities that can be expected under different conditions or user cases.

Chapter 3 aims at explaining how to predict radiation-induced degradation on complex EEE components, and describes the different types of effects that can be expected under hazardous radiation environments, such as those described in Chapter 2. Additionally Chapter 3 aims to introducing the bases for the discussion of the computational tools and results to be presented in Chapter 5. The focus is on description of degradation mechanisms and radiation effects in Metal-Oxide-Semiconductor (MOS) transistors which are the most commonly used devices in modern integrated circuits (IC), and in particular on the specific Static Random Access Memory devices (SRAMs) used for testing the tool proposed and discussed in Chapter 5.

Chapter 4 describes the simulation framework developed in order to simulate radiation Environment at the surface of Mars, presents simulation studies of the GCR and SEP proton as well as albedo neutron induced radiation environment on Mars and finally it discusses radiation environment dependencies and makes some considerations about habitability and radiation damage. Results are compared against others obtained by other simulation tools available in literature and MARIE in orbit measurements before the Solar Event of October-November 2003.

Chapter 5 aims at describing the *Component Degradation Simulation tool (CODES)* and results. CODES [Keating, 2008] was designed as a general framework in order to predict radiation degradation on EEE components when submitted to different radiation environments. As described in Chapter 3, degradation rates can be predicted by convolving the incoming fluence (or flux) spectrum through the device with the damage rate at component level. CODES achieves the goal of generality because it interfaces information on the device with GEANT4 based Monte Carlo application for tracking primary and secondary particles at component level. Additionally it is designed to output information required for degradation analysis. Finally it is able to convolve the information at component level with input radiation in order to predict degradation rates. Detail simulations are also possible by using the developed interactive tool to fit device sensitivity, *Sensitive Volume interactive Fit Tool (SV-FIT)*, based on ground level irradiation tests. Due to the extended range of mechanisms and devices, the full development and application of CODES and SV-FIT were based on the analysis of a specific device. The device selected was the 4Mbit ATMEL

---

AT60142F Static Random Access Memory (SRAM) comprehensively characterised as part of ESA's "Reference SEU Monitor" development activity [Sørensen, 2005].

Chapter 6 recounts the main conclusions of this thesis and assesses the possible directions for future work. Chapter 7 is the list of bibliographic references. Finally the appendix I includes fluence-to-ambient-dose-equivalents coefficients for different particles [Pelliccioni, 2003].

### ***1.3. Author contribution***

#### *1.3.1. Simulation Methods and tools*

The last four years of research lead to the design and development of one integrated engineering tool to predict radiation environment at the surface of Mars and effects. The tool was entitled: "MarsREC, a framework for the prediction of the Martian radiation environment" and developed under a two years ESA contract No. ESA 18121/04/NL/CH (2004-2006).

Later this tool derived in two more specific engineering tools: One specified in the detailed description of the physical environment on Mars and Moons and prediction of radiation environment. Entitled "MarsREM: Mars Radiation Environment Models" was developed under a LIP participation in the consortium with three international institutes/companies, which issued the winning proposal for the ESA ITT/AO/1-4944/05/NL/JD. The 18 month contract with ESA was initiated in July 2006. Aiming at developing the physical understanding of radiation-induced effects on EEE components a new tool is being developed as an extension of ESA activity contract no. ESA 18121/04/NL/CH. Entitled "CODES: Component Degradation Simulation Tool" uses GEANT4 application interfaced with device analysis techniques in order to achieve the simulation of microdosimetry in the device.

The author was the Technical Manager of the MarsREC, CODES and MarsREM work package entitled "*Development of In-Orbit and Surface Radiation Environment Model (dMEREM)*" of LIP responsibility. The author has designed, developed and implemented the entire MarsREC simulation framework and CODES. The author is solely responsible for the GEANT4-based simulation implementation and results. Regarding the developments in the MarsREM project, the author was responsible for the research and design of the soil

---

composition database and initial implementation of interfaces between GEANT4- based application (dMEREM) and databases. The latest format and performance of the GEANT4 application, pre-processor and interfaces, as they are discussed in Chapter 4, are mostly due to the work and collaboration of other members of the group.

### 1.3.2. Publications

During the last four years the author has submitted, published and presented her work in different international meetings, IEEE TNS journal and proceedings as listed below. Her work has been recognized by the international Scientific/Engineering communities. As a result the author was invited to give a GEANT4 tutorial for Space Users, be the chair of a section at the GEANT4 collaboration workshop 2006, to attend the International Standards Organization (ISO) Radiation Working Group meeting as an expert on Mars radiation Environment and be reviewer for IEEE TNS.

- *P.Truscott, F.Lei, **A.Keating**, S.Valente, P.Gonçalves, L.Desorgher, D.Heynderickx, N.Crosby, H.de Witte, G.Degreef, P.Nieminen & G.Santin "The Mars Energetic Radiation Environment Models", accepted to NSREC 2008 (submitted to IEEE TNS December 2008).*
- ***A.Keating**, A.Mohammadzadez, P. Brogueira, M. Pimenta, P. Gonçalves, S.Valente, R. Harboe-Sorensen, "CODES a SEU Prediction Tool", accepted to NSREC 2008 ( submitted to IEEE TNS December 2008).*
- ***A.Keating**, S. Valente, P. Gonçalves, M. Pimenta, P. Nieminen, L. Desorgher, P. Truscott, F. Lei, "Martian Radiation Environment: The Importance of Seasonal variations and Landing Site", European Mars Science and Exploration Conference, ESTEC, Noordwijk, The Netherlands, November 2007.*
- ***A.Keating**, "Radiation Environemtn at the Surface of Mars", 6<sup>th</sup> International Workshop: New Worlds in Astroparticle Physics", Portugal, September 2007.*
- *B. Tomé, P. Brogueira, P.Gonçalves, **A. Keating**, D. Maia, M.Pimenta, "GEANT4 applications in the heliospheric radiation environment", accepted to 30th International Cosmic Ray Conference, July 2007.*
- *P.Gonçalves, **A.Keating**, "Planetary Radiation Environment and Effects (JRA)", EUROPLANET workshop, ESTEC, Noordwijk, The Netherlands, 26-27 February 2007.*
- ***A. Keating**, "Modelling SEE on EEE components", 8<sup>th</sup> QCA Presentation Day, Louvain-la\_Neuve, Belgium, 23<sup>rd</sup> January 2007.*
- ***A. Keating**, M. Pimenta, A. Mohammadzadeh, P. Nieminen and E. Daly, "Mars Radiation Environment Characterization: Results, previous and ongoing activities", Third European Space Weather Week, 16<sup>th</sup> November 2006, Brussels, Belgium.*

- 
- ***A. Keating***, “***MarsREC and Future MarsREM***”, ISO–International Standards Organization: Working group 4 on Radiation Environment and effects, CNES, Paris, France, 26<sup>th</sup> October 2006.
  - E.J. Daly, H. Evans, P. Nieminen, G. Santin, R. Lindberg, J. Sorensen, A. Glover, A. Menicucci, ***A. Keating***, A. Mohammadzadeh, “***Models and Computational Tools for Space Radiation Effects***”, Proceedings RADESA2006– The 7th International Workshop on Radiation Effects on Semiconductor Devices for Space Application, 17<sup>th</sup> October 2006.
  - ***A. Keating***, M. Pimenta, A. Mohammadzadeh, P. Nieminen and E. Daly, “***MarsREC, an integrated tool for Mars Radiation Environment Characterization and Effects***”, GEANT4 users workshop”, IST, Lisbon, Portugal., 9<sup>th</sup> October 2006.
  - ***A. Keating***, M. Pimenta, A. Mohammadzadeh, P. Nieminen and E. Daly, “***MarsREC and SEU predictions at the Surface of Mars***”, RADECS2006, Athens, Greece, 27<sup>th</sup> to 29<sup>th</sup> September 2006.
  - ***A. Keating***, M. Pimenta, A. Mohammadzadeh, P. Nieminen and E. Daly, “***Galactic Cosmic Rays induced Radiation Environment at the surface of Mars***”, Submitted to European Cosmic Rays Symposium, Lisbon, Portugal, 5<sup>th</sup> to 8<sup>th</sup> September 2006.
  - ***A. Keating***, M. Pimenta, A. Mohammadzadeh, P. Nieminen, J.-P. Huot and E. Daly, “***The Effects of Atmospheric Variations On the High Energy Radiation Environment at the Surface of Mars***”, Second workshop on Mars atmosphere modelling and observations, Granada, Spain, 27<sup>th</sup> February to 3<sup>rd</sup> March 2006.
  - ***A. Keating***, A. Mohammadzadeh, P. Nieminen, M. Pimenta and E. Daly, “***A GEANT4 based Model for Mars Radiation Environment Characterization***”, Second European Space Weather Week: ESWW-II, ESTEC, Noordwijk, The Netherlands, 14<sup>th</sup> to 18<sup>th</sup> November, 2005. (Poster)
  - ***A. Keating***, A. Mohammadzadeh, P. Nieminen, D. Maia, S. Coutinho, H. Evans, M. Pimenta, J.-P. Huot, and E. Daly, “***A Model for Mars Radiation Environment Characterization***”, NSREC, Seattle, USA, 12<sup>th</sup> July, 2005 (Keating, A., et al (2005), IEEE TNS 52, 0018-9499).
  - L. Desorgher, S. Duzellier, T. Ersmark, H-H. Fischer, C. Fuglesang, S. Guatelli, M. Gurtner, C. Inguibert, ***A. Keating***, F. Lei, B. Mascialino, A. Mohammadzadeh, P. Nieminen, M. Grazia Pia, G. Santin, K. Thiel, P. Truscott, “***GEANT4 Particle Transport Software Applications to Radiation Shielding and Human Effects Analyses***”, 15<sup>th</sup> [IAA](#) Humans in Space Symposium, 22<sup>nd</sup>–25<sup>th</sup> May, 2005.
  - ***A. Keating***, “***Mars Radiation Environment and Its Effects on Components, inputs for an integrated software tool***”, TOS-EES Final presentation Day, ESTEC, Noordwijk, The Netherlands, 19<sup>th</sup> and 20<sup>th</sup> February 2004.
  - ***A. Keating***, “***GEANT4 applications on Radiation Environment and Components degradation parameters prediction***”, GEANT4 Tutorial Courses, Vanderbilt University, Nashville, Tennessee, USA, 14<sup>th</sup> January 2004.
  - E. Daly, H. Evans, S. Esteve Hoyos, A. Hilgers, ***A.Keating***, A. Mohammadzadeh, P. Nieminen, L. Rosenqvist, G.Santin, J. Sørensen, “***Radiation Environments and Effects Analysis Tools for Future planetary Exploration Missions***”, 37<sup>th</sup> ESLAB Symposium, ESTEC, Noordwijk, The Netherlands, 2<sup>nd</sup>–4<sup>th</sup> December 2003.
-

- ***A.Keating, A.Mohammadzadeh, B.Nickson, A.Jaksic, W. Hajdas; "Modelling packaging effects on proton irradiation response of NMRC RadFETs, New GEANT4 simulations and Co-60 irradiations", Proceedings of 7<sup>th</sup> European Conference RADECS 2003, Noordwijk, The Netherlands, 15<sup>th</sup> to 19<sup>th</sup> September 2003 (IEEE 03TH8776, October 2004).***
-



## 2. Radiation Environment in the solar system

The understanding of radiation environment in the solar system requires knowledge of the heliosphere and radiation transport of galactic cosmic radiation and solar radiation. Moreover the complete description of individual planetary conditions and features that may lead for local radiation environment is required.

While the various planetary radiation environments may have some commonalities with the environment of the Earth, each planet has its own unique features. The important drivers for proper feature modelling are: distance from the Sun, presence of a magnetosphere and/or atmosphere, moons, local geology and topology, and temporal variations.

This chapter will give an overview of the different processes and concepts needed to understand the transport of radiation through the heliosphere to Earth and Mars. Moreover this chapter also aims at passing to the reader the idea of quantities that can be expected under different conditions or user cases.

### 2.1. *The sun and the Heliosphere*

The physics of the Sun and the different processes of generation of accelerated particles and their propagation in the heliosphere are still very controversial today. Searching for answers ESA, NASA and others have sent different missions to observe the Sun and the heliosphere (e.g. SOHO, Ulysses, Hinode).

The Sun consists mainly of hydrogen as the fuel for solar energy production (92% in terms of particle number) and helium (about 8%), partly primordial and partly waste product [Kallenrode, 2001].

The source of Sun's energy is the nuclear fusion occurring in the inner core of the Sun ( $0.3 R_{\odot}$ <sup>1</sup>). This region is surrounded by a radiative region where the energy is transported by radiation reaching very high temperatures and finally surrounded by the convection zone. The visible surface of the Sun sits in the top of the convection zone and is called the *Photosphere*.

---

<sup>1</sup> Radius of the Sun,  $R_{\odot} = 0.696 \times 10^6 \text{ km}$ .

---

Above the photosphere the solar atmosphere consists of three layers: the chromosphere, the transition region and the *Corona*. As illustrated in figure 2-1 the temperature above the photosphere is 5800K while just below it reaches temperatures of the order of  $10^6$ K. The nature of the processes that heat the corona, maintain it at these high temperatures, and accelerate the solar wind are the still big questions today [NASA, 2007].

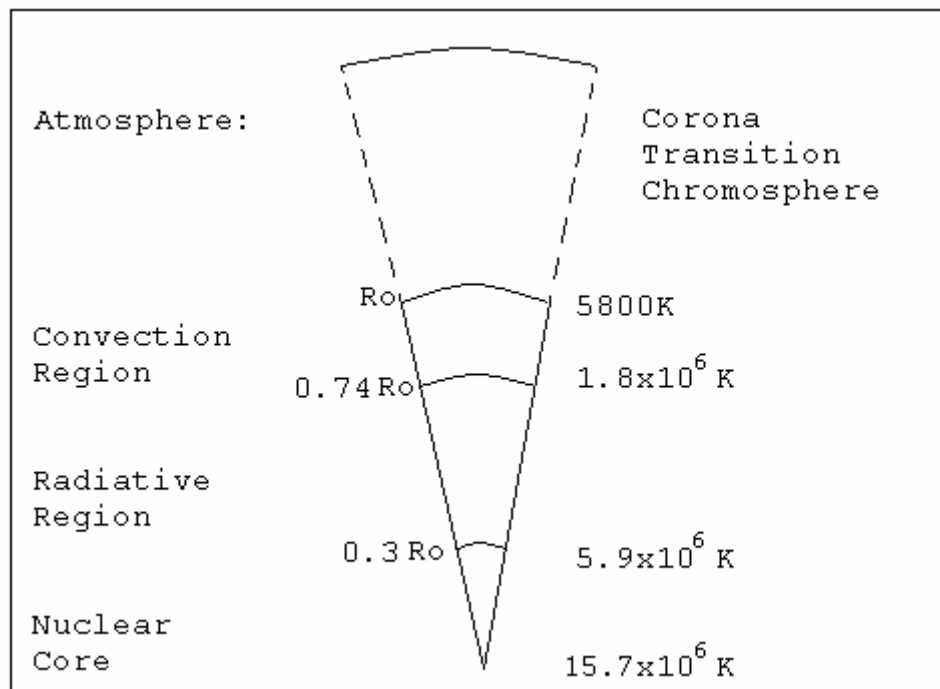


Figure 2-1 – Internal structure of the Sun (adapted from [Kallenrode, 2001])

Independent of the details of the reactions, energy is liberated in the form of electromagnetic radiation, electrons, positrons, neutrinos and accelerated protons and ions.

Most of the Sun's emission is electromagnetic radiation ( $3.86 \times 10^{23}$  kW) consisting of five frequency bands:

- 1) X-ray and extreme ultra-violet with wavelength  $< 180$  nm, contributing to about 0.1% of the total output. This is highly variable depending on the level of solar activity;
- 2) Ultra-violet with wavelength between 180 and 400nm [Hecht, 1987], contributing to about 9% of the solar flux. It is radiated from the photosphere and the corona;
- 3) Visible light with wavelength between 400 and 740nm, varying with the solar cycle contributes to about 40% of the energy flux. Only in extremely strong flares a local brightening can be observed;

- 4) Infrared from 740nm to 1mm (far infrared), gives the maximum energy flux contribution (about 51%) is emitted by the photosphere and reveals no variations with solar activity.
- 5) Radio-emission above 1mm, originated from the corona vary significantly during solar flares, contributes with  $10^{-10}\%$ .

Continuous expansion of the solar corona produces changes and movements on the interstellar plasma. This phenomenon resulting in about 10 protons per  $\text{cm}^3$  to reach the earth orbit is known as *Solar Wind* [Ptuskin, 2001]. Two different types of plasma flow are observed with different velocities: the fast and the slow wind streams. The *fast wind*, which velocity ranges between 400 and 800 km/s, has a low average density of about 3 ions per  $\text{cm}^3$  at  $1\text{AU}^2$ . The average particle flux is about  $2 \times 10^{12} \text{m}^{-2} \text{s}^{-1}$ . The ratio of Helium is of 4% and is very stable over different fast streams. The *slow wind* speeds between 250 and 400 km/s and has a density of about 8 ions per  $\text{cm}^3$  at 1AU and about twice the average flux of the fast stream. The slow wind composition is highly variable with solar activity. Despite their differences, fast and slow solar wind streams have very similar average momentum and total energy fluxes.

### 2.1.1. *Heliosphere*

The solar wind having a high conductivity transports the magnetic field of the Sun through the space creating the *interplanetary magnetic field or Heliosphere*. The photospheric magnetic field discovered due to Zeeman Effect, by Hale in 1902, is of the order of  $1\text{G}^3$  outside and 3000 to 4000 G inside sunspots [Kallenrode, 2001]. Within 2 solar radii this complex and variable field turns into a radial field, as illustrated in figure 2-2. However the Sun's rotation winds up the field lines to an Archimedian spiral [Kallenrode, 2001], also known as the Parker spiral.

---

<sup>2</sup> Medium Earth-Sun distance corresponds to approximately  $150 \times 10^6$  km.

<sup>3</sup> G states Gauss.  $1\text{G} = 10^{-4}\text{T}$ .

---

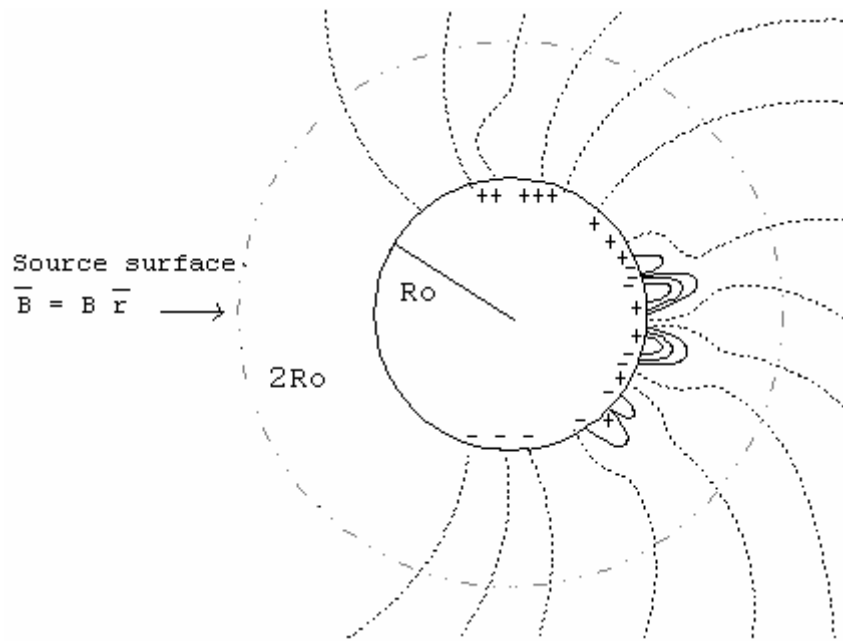


Figure 2-2 – Photospheric, source surface and interplanetary magnetic field (adapted from [Kallenrode, 2001])

For long distances the radial and azimuthal components of the magnetic field,  $B_r$  and  $B_\phi$  respectively, can be derived from the formalism of Archimedes spiral and Gauss's law as:

$$B_r = \frac{B_o r_o}{r^2} \sqrt{1 + \left(\frac{\omega_\odot r}{u_r}\right)^2} \quad \text{and} \quad B_\phi = -\frac{r \omega_\odot B_r}{u_r} \quad (2-1)$$

where  $B_o$  and  $r_o$  are the magnetic field and the radius of the source surface,  $\omega_\odot$  is angular velocity of the Sun and  $u_r$  is the radial component of the momentum. Therefore in a first approximation:

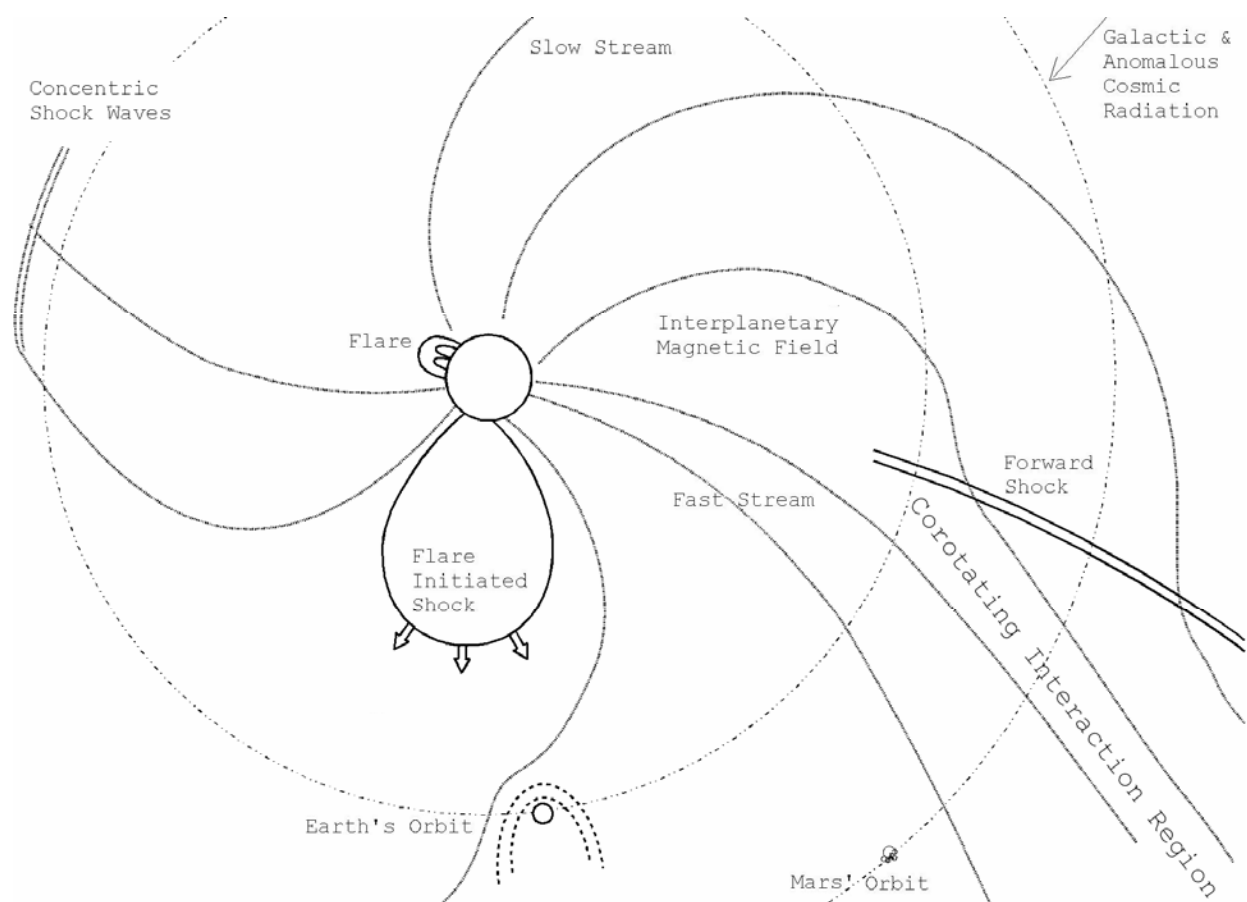
$$B_r \propto \frac{1}{r^2} \quad \text{and} \quad B_\phi \propto \frac{1}{r}. \quad (2-2)$$

Figure 2-2 shows that the interplanetary magnetic field polarity has abrupt changes and large angular region of uniformity [Kallenrode, 2001].

In the slow stream the field line is curved more strongly than in the fast one. Since magnetic field lines are not allowed to intersect, at a certain distance from the Sun an interaction region develops between the two streams. Because this structure rotates with the Sun it is known as the *Corotating Interaction Region* (CIR) [Kallenrode, 2001]. As these streams propagate outwards, flow compression and deflection on both sides of the interface lead to a continuous increase of speed. The presence of such structures tends to distort small-scale fluctuations and

disturbances propagation outwards. In the outer heliosphere the magnetic field and therefore the shock fronts are more azimuthally aligned. Thus the spiral form of the field lines in the inner heliosphere may be converted into a shell of concentric shock waves propagating outward. The interaction between different CIRs or CIRs and interplanetary shocks results in merged interaction regions which play an important role in the modulation of the galactic cosmic radiation.

Figure 2-3 is a sketch of the different populations of energetic charged particles in the inner heliosphere (<5AU) as well as the different modulation structures such as CIR and shock fronts.



**Figure 2-3 – Different population of charged particles in the inner heliosphere and modulation structures (adapted from [Kallenrode, 2001])**

Finally figure 2-3 depicts the modulation of the interplanetary field lines with the planetary magnetic field. In planets with a strong magnetosphere, such as Earth, this magnetic cavity acts sometimes as a shielding trapping particles in the radiation belts. On the other hand for

planets such as Mars, Venus and Mercury that have no magnetosphere or a very weak and localised one, the solar wind particles can penetrate without getting trapped. [See sections 2.3 and 2.4 of this chapter].

### 2.1.2. *The Solar Cycle*

The solar activity follows a cycle with a periodicity of 11 +/- 4 years. The cycle is associated with violent energy and matter releases from the Sun and with the reversal of the solar magnetic polarity. Since 1610 it has been measured using the number of Sunspots, however just from 1749 daily measurements started to be registered. Figure 2-3 shows the monthly average of the number of Sunspots since 1749 until today.

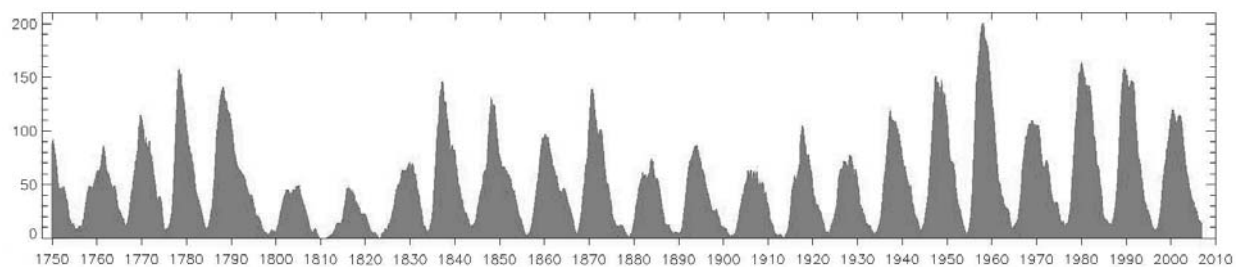


**Figure 2-4 – Monthly average of Sunspots since 1749 until today (adapted from [SIDC, 2007])**

At the solar minimum the Sun is almost spotless. Then spots start to appear at latitudes around 30°. The number of spots increases till solar maximum. During an 11 year cycle the magnetic field reverses its polarity. Thus the complete magnetic cycle is twice as long as the solar cycle (22-year total solar cycle).

The variability of Solar activity and consequently on Sunspots have a strong impact on the photospheric magnetic field. It causes a change in the source surface and tilts the neutral line of the heliosphere leading to temporal and spatial variation of solar wind.

### 2.1.3. *Flares and Coronal Mass Ejections (CME)*

One of the most controversial topics is the relation between solar flares and CMEs and solar energetic particle events [20, 23, 24].

Solar flares are violent explosions on the surface of the Sun. In a few minutes they heat material to many millions of degrees and release an enormous amount of energy. They occur near sunspots, usually along the neutral magnetic field lines between areas of oppositely directed magnetic fields [20, 23].

Flares release energy in many forms - electro-magnetic (Gamma rays and X-rays), energetic particles (protons, neutrons and electrons), and mass flows. Flares are characterized by their X-rays brightness (X-Ray flux) in the wavelength range 1 to 8 Angstroms. There are three main categories: X-class flares are big defined by having power output higher than  $10^{-4}\text{W/m}^2$ ; they are major events that can trigger planet-wide radio blackouts and long-lasting radiation storms. M-class flares are medium-sized; they have a tenth of the energy of the X-class and can cause brief radio blackouts that affect Earth's Polar Regions. Minor radiation storms sometimes follow an M-class flare have a tenth of their flux. Compared to X- and M-class events, C-class flares are small with few noticeable consequences here on Earth [Kallenrode, 2001] [NASA, 2007].

The first warning of a solar flare is given by the electromagnetic radiation component (X-rays, UV-light, etc.) that travels out into space crossing the Earth's orbit approximately 8.5 minutes later [Underwood, 1996].

CMEs are huge bubbles of gas threaded with magnetic field lines that propagate outwards through the corona and drive the delayed component of energy propagation from the Sun [Torsti, 2001].

These dynamical events increase with high solar activity. The propagation of charged solar radiation depends on the magnetic connection between observer and the flare-site on the Sun. If an observer lies in the field line, which is connected to the eruption region on the Sun, the particles will arrive, causing a *Solar Particle Event*.

*Solar Energetic Particles* (SEPs) consist mainly of high-energy protons with energies up to several hundred MeV. However solar energetic electron events are as well observed in interplanetary space. SEPs are associated with flares and/or CME [Klassen, 2002]. It is often hard to decide which of these agents is responsible for the generation of mildly relativistic electrons, because both agents can appear independent of each other or together [Klassen, 2002].

Depending on interplanetary scattering conditions and on the observer's distance from the Sun, SEPs last in the interplanetary space for some hours or a few days. In gradual solar flares SEPs mix with particles accelerated at the interplanetary shocks.

---

Neutrons, being electrically neutral, travel in straight lines from the Sun, decaying mostly into protons and electrons by 1 AU, however very energetic neutrons can propagate to this distance and further [Underwood, 1996].

For example, in October 2003, three giant sunspots unleashed eleven X-class flares in only fourteen days, equalling the total number observed during the previous twelve months. The effects on spacecrafts on orbit of Mars and Earth were many [Barnieri, 2004]: Solar protons penetrated Earth's upper atmosphere, exposing astronauts and some air travellers to radiation doses equal to a medical chest X-ray. Auroras appeared all over the world [Philips, 2003].

#### 2.1.4. *Cosmic rays*

Primary cosmic radiation coming from outside the solar system includes all stable charged particles and nuclei with lifetimes of order  $10^6$  years or longer. It can have different astrophysical sources. In particular they can be originated from the interstellar space, the *galactic cosmic rays*. Secondary cosmic rays are those particles produced in interaction of the primaries with interstellar plasma. Thus electrons, protons and helium, as well as carbon, oxygen, iron, and other nuclei synthesized in stars, are primaries. Nuclei such as lithium, beryllium, and boron (which are not abundant end-products of stellar nucleosynthesis) are secondaries. Antiprotons and positrons are also in large part secondary [Eidelman, 2005].

The spectrum of galactic cosmic radiation observed at the Earth's orbit consists of approximately 83% of protons, 13% alpha particles, 3% of electrons and 1% heavy ion nuclei. The spectrum of energies extends from a few thousands of eV up to some  $10^{20}$  eV.

Figure 2-5 shows the relative abundances of elements in cosmic rays with energies between 70 to 280MeV/nucleon [Holmes-Siedle, 2006].

---

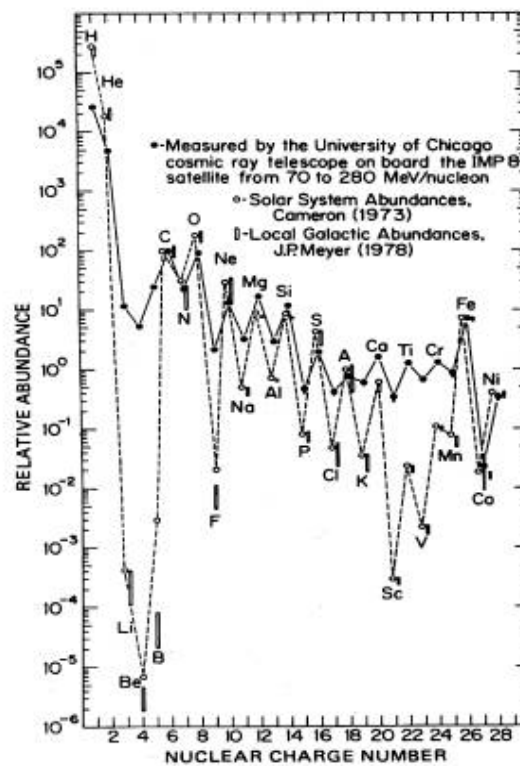


Figure 2-5- Relative abundance of elements in cosmic radiation [Keating, 2002] (extracted from [Balebanov, 1990])

Galactic Cosmic Rays are incident upon the heliosphere uniformly and isotropically [19, 20]. The incoming charged particles are modulated by the solar wind, which decelerates and partially excludes the lower energy galactic cosmic rays from the inner solar system. In the inner heliosphere there is a significant anticorrelation between solar activity and the intensity of the cosmic rays with energies below about 10 GeV.

As neutral particles of the interstellar medium travel through interplanetary space towards the Sun, they become ionized. These new charged particles, also known as the *Anomalous Cosmic Rays* are convected outwards with solar wind and are accelerated at the termination shock. This cosmic rays component is connected with the lower energy range cosmic rays; however it has a different composition, charge states, spectrum and variation with the solar cycle.

Cosmic rays may create in electronic devices Single Event Effects (SEE) [5, 10].

## 2.2. Models and Tools

The importance of quantifying and analysing radiation environment under different conditions and applications lead to the development of different models and tools with web-

interfaces. Most of the up to date tools, such as CREME96 and SPENVIS, predict the radiation environment at Earth or near-earth interplanetary orbits (~1AU).

This chapter aims at introducing the standard models used to quantify radiation environment and predict fluences and particle species due to the different radiation sources.

### 2.2.1. *Trapped radiation*

The de facto standard models for prediction of radiation belt energetic particles are the AE-8 and AP-8 models for electrons and protons respectively [ECSS-E-10-04A]. These models developed at the NSSDC at NASA/GSFC are based on data from satellites flown in the '60s and early '70 and give omni-directional fluxes as functions of idealized geomagnetic dipole coordinates, dependent on the solar cycle phase and altitude. These models present some limitations. In particular, around geostationary orbit fluxes vary by orders of magnitude over short times and exhibit significant diurnal variations not described by the models.

### 2.2.2. *Solar Energetic Particles*

During energetic events on the sun, large fluxes of energetic protons are produced which can reach the Earth. For engineering applications, solar particle events, because of their unpredictability and large variability in magnitude, duration and spectral characteristics, have to be treated statistically [ECSS-E-10-04A].

Feynman et al. [Feynman, 1993] have developed a database and assessment tool for solar protons well known as JPL91. This statistical model is based on data from three solar cycles [Feynman, 1993]. It provides data up to 60MeV. For fluences at energies above this, an exponential fit to the rigidity spectrum is used, where rigidity is defined as:

$$P = (A/Z) (E^2 + 1862 E)^{1/2} / 10^3 \quad (2-3)$$

where  $P$  is in GV and  $E$  is in MeV. According to the ECSS Standards [ECSS-E-10-04A], this is used as the standard model for engineering consideration of time-integrated effects.

Given a confidence level and offset from solar maximum, JPL91 provides spectra of the proton fluence for a selected duration for different confidence levels. Moreover it provides worst-case event fluence during the selected duration.

In CREME96 [Tylka, 2007] SEP models are based on satellite measurements of particles throughout the range of energies and elements relevant for SEU/SEE studies. These

measurements come primarily from GOES (for protons) and the University of Chicago's Cosmic Ray Telescope on IMP-8 (for heavy ions). Specifically, it is based on measurements of the extended episode of solar particle emission which occurred on 19-27 October 1989. This episode is the most severe SEP event observed since at least August 1972. Table 2-1 illustrates a comparison between the SEP of Worst week model given by CREME96 and the real SEP of October November 2003. It shows that the Worst Week based on SEP fluxes averaged over 180 hours beginning at 1300 UT on the 19 October 1989 model gives a much worst prediction than the SEP of October-November 2003.

	FLUENCE [ $10^{10}$ #/CM <sup>2</sup> ]		RELATIVE DIFFERENC E [%]	EVENT DURATION [HOURS]		FLUX [ $10^4$ #/CM <sup>2</sup> /s]		RATIO [%]
	10-11/2003	SEP WW		10-11/2003	SEP WW	10-11/2003	SEP WW	
ALL SPECTRUM	12.3	11.0	11	338	118	10.1	25.9	39
ABOVE 50MEV	0.13	0.18	33			0.10	0.43	23

**Table 2-1 - Comparing SEP Worst Week Model from CREME96 with SEP October-November 2003.**

Figure 2-6 illustrates the integrated fluence for both SEP WW Model and SEP October-November 2003 [ESA, 2007].

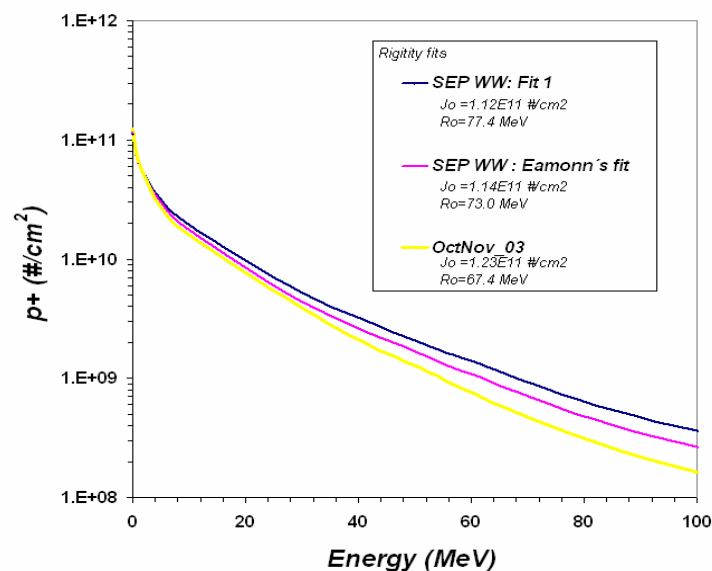


**Figure 2-6- Comparison between the Integrated Fluences of solar events of October-November 2003 and the Worst Week model from CREME96 based on the solar event of October 1989.**

The October 1989 episode qualifies as a "99% confidence-level worst case" in the JPL flare model's three highest proton energies, >10, >30, and >60 MeV [Tylka1, 1997].

Most of current models rely on a description of event fluences and occurrence based on a compound Poisson process for which the parameters are derived from observations. ESA has studied the effect of observation data set size on the prediction of cumulated fluence by such models. This study showed that with the current size of the event data set of Solar Proton Events (about a couple of hundred events) the estimated parameters used as input may lead to significant errors. Furthermore, this work has shown that in order to get significant accuracy improvement, data set shall contain a much larger number of events (typically one thousand), which requires a long-term data acquisition infrastructure [Rosenqvist, 2003].

In parallel space system design and radiation health communities have identified three concerns related to the previously described models: inadequacy of the models for modern applications; data that have become available since the creation of the models are not being fully exploited for modelling purposes; absence of any authorizing organization identified to evaluate the models or their datasets for accuracy and robustness. In this context NASA had sponsored the development of PSYCHIC, a model for energetic solar particle based on satellite data set extended to cover the time period of 1966-2001 and energy range extended to over 300 MeV, including estimates for solar minimum spectra [Xapsos, 2006].

### 2.2.3. *Cosmic rays*

Cosmic-Ray environment and effects models were originally created by Adams and co-workers at the U.S. Naval Research Laboratory [Adams, 1986], under the name CREME. In 1996 improved models including solar-cycle modulation of Cosmic Rays were made available in CREME96 [Tylka2, 1997]. According to the ECSS standards [ECSS-E-10-04A] CREME96 is the standard model for cosmic ray environment assessment.

The solar-quiet model in CREME96 represents the ambient environment which prevails in the absence of solar energetic particle events. This environment, which varies slowly in intensity over the 22-year solar cycle, is the basic environment in which all space systems must operate. It includes galactic cosmic rays spectra above ~50MeV/nuc and extends to very high energies and anomalous cosmic rays. Additional fluxes, which arise from various acceleration processes at the Sun and in interplanetary space, dominate the spectra of most elements below

---

~10MeV/nuc are as well included in CREME96. The dependence of the GCR fluxes on the solar activity is calculated by the semi-empiric MSU model developed at the Skobeltsyn Institute of Nuclear Physics, Moscow State University. The MSU model is the International Standard Galactic cosmic ray model of International Organization for Standardization [ISO 15390:2004(E)], [Nymmik, 2006].

The anomalous cosmic ray model in CREME96 is based on the latest composition, spectra, and charge state measurements from SAMPEX, as well as the historical record of anomalous cosmic ray measurements extending back to 1972 [Tylka2, 1997].

### 2.3. *Earth Radiation Environment*

For Earth-orbiting missions, the radiation environment is due to three main sources of radiation, namely: the radiation belts, cosmic rays and solar events.

This section aims at describing the main sources of radiation at 1AU, giving also an idea of typical values and order of magnitude predicted using CREME96.

#### 2.3.1. *Magnetosphere*

By means of radiative diffusion and convection [Nieminen, 1997] the solar winds modulate the planet dipolar magnetic field as well as the interplanetary radiation environment in shape, particle species, energy and fluence. The cavity created by this distortion and confinement of the planet magnetic field is called *Magnetosphere*. This magnetic cavity acts sometimes as a shielding deflecting the incident charged particles. Other times it acts as an accelerator, creating charge particle beams that hit the neutral upper atmosphere originating the *Polar Aurora* [Russel, 1987].

Figure 2-6 illustrates the interaction of the solar winds with the magnetosphere. The size of the *magnetopause* is dependent on the normal stress exerted by the solar wind dynamic and thermal pressure, and on the tangential stress on the cavity. This drag on the cavity is dependent on the stability of the boundary between the flowing *magnetosheath* plasma and the stationary magnetospheric plasma, and on the direction of the interplanetary magnetic field. The *bow shock* is due to the interaction of charged particles with the magnetic and electric field and is as well dependent on the solar winds conditions [Russel, 1987].

---

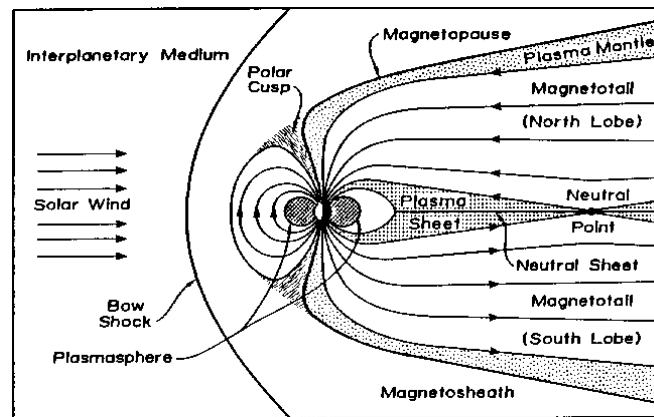


Figure 2-7- Earth Magnetosphere modulation by solar wind. [Russel, 1987]

In conclusion all the magnetosphere parameters are dependent on the solar wind conditions and on the planet magnetic field properties. The modulation of planetary magnetosphere must be based on experimental data and observations of all these parameters.

### 2.3.2. Radiation Belts

Due to radial diffusion, particles from solar wind can penetrate into the magnetosphere. The ability of a particle to enter into the magnetosphere is dependent on its *Magnetic Rigidity* (function of its relativistic momentum, atomic number and charge) [Underwood, 1996].

The Van Allen *Radiation Belts* are regions in the space where these particles are trapped by the Earth's magnetic field. These regions are characterised by their particle species composition [Holmes-Siedle, 2006].

As a result of the first satellite observations it was concluded that the Earth radiation belts leave two empty zones around the Earth magnetic axis. The movement of charged particles in the dipolar electric field originates these polar zones. Considering the time interval of a particle flying trapped in the force line, this field can be considered constant. Consequently the particle magnetic moment is in first approximation given by [Boezio, 1998]:

$$\mu = \frac{p^2(1-\beta^2)^{-1/2} \sin^2 \alpha}{2mB} = \text{const}^e \quad (2-4)$$

where  $\beta=v/c$  is the relative velocity,  $m$  is the particle mass and  $\alpha$  is the angle between the magnetic field  $\vec{B}$  and the particle momentum  $\vec{p}$ . And as  $\vec{p}$  must be considered as a constant,

$$\frac{\sin^2 \alpha}{B} = \text{const}^e \quad (2-5)$$

So the particle oscillates between two points with a geomagnetic coordinate,  $B$ . The constant depends on the particle species and energy. Each particle describes approximately circular motion around the force line in the radiation belt, with a radius inversely proportional to the field intensity. That means that the particle is trapped in a tubular space, as shown in figure 2-8 [Boezio, 1998].

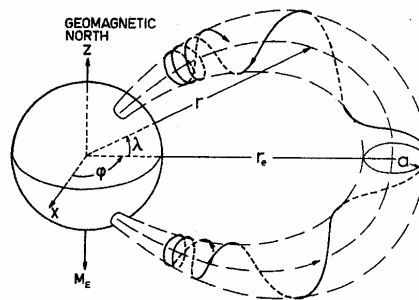


Figure 2-8- Movement described by the trapped particle around a force line of the magnetic field [Boezio, 1998]

The inversion points, known as *Mirror Points*, are located in the polar zones. This is the reason why the particle density is very low in the earth magnetic poles. The region delimited by the force lines between the mirror points is called *Magnetic Shell* [Boezio, 1998].

In addition to the previously described motion, two forces act through a particle moving in the Earth magnetic field: the centrifuge strength due to the tangential velocity, and the Coriolis force. That is the reason why trapped particles move according to Earth rotation and their own charge [Boezio, 1998].

Depending on regions, the number of electron and proton particles trapped in the magnetic field varies. Figures 2-9 and 2-10 show the trapped electron and proton Van Allen radiation belts in the Earth's magnetic field respectively.

The electron belts consist of two distinct zones with high fluxes. The inner zone is centred at approximately 1.4 earth radii and extends to approximately 2.4 earth radii whereas the outer zone is centred at around 5 earth radii and extends to about 12 earth radii. In the first zone, electron energies are lower than 5MeV whereas in the second they are more intense and can be as high as 7 MeV [Holmes-Siedle, 2006].

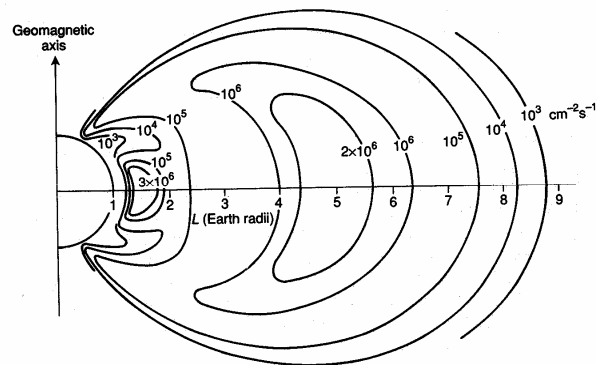


**Figure 2-9 - Electron radiation belts. Isoflux map of electron with energies above 1MeV. The radius of the Earth is 6371 km [Holmes-Siedle, 2006].**

Protons, on the other, hand are restricted to only one zone. The flux varies monotonically with energy and distance with a maximum at around 2 Earth radii. The energy of the trapped protons may vary from  $\sim 1\text{MeV}$  to  $400\text{MeV}$  [Holmes-Siedle, 2006].

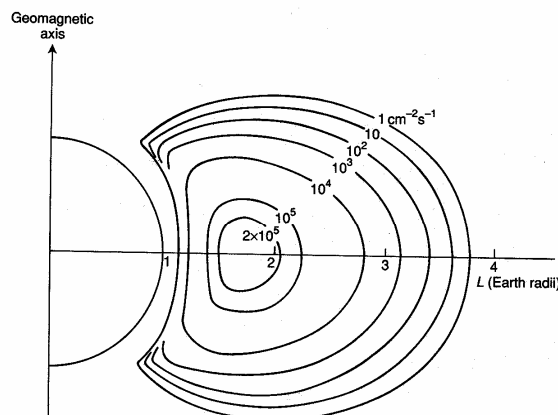
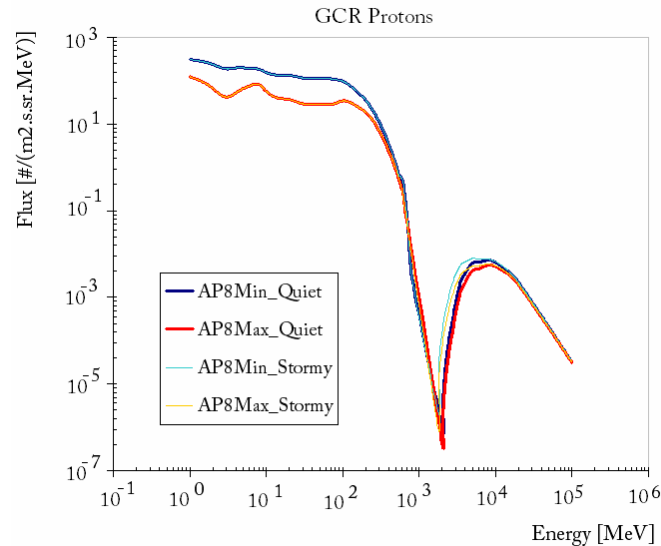


**Figure 2-10- Proton radiation belts. Isoflux map of proton, with energies above 10MeV. The radius of the Earth is 6371 km [Holmes-Siedle, 2006].**

### 2.3.3. *Typical Shuttle orbit and Environment Prediction*

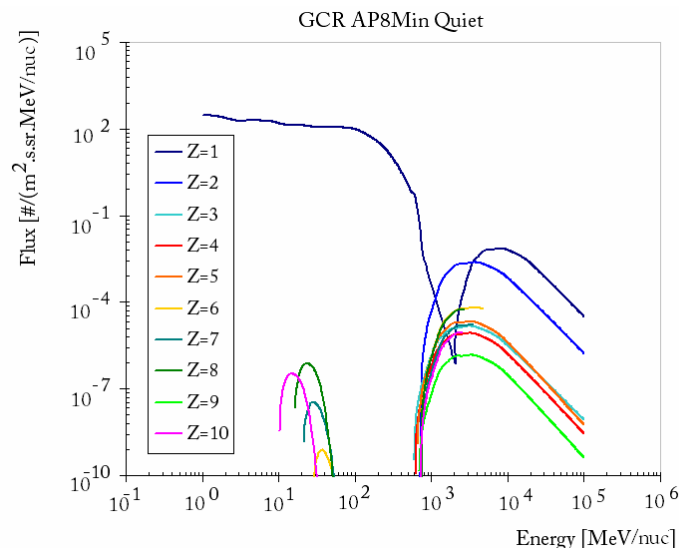
In order to completely evaluate radiation effects and payload life time in a Mars mission the possible orbit and trajectory has to be considered from the launch to the end of mission. The current section presents the typical Shuttle orbit ( $28.5^\circ$ , 450 km) proton and ion radiation environment simulated with CREME96.

Figure 2-11 compares the trapped and GCR protons scenario simulated with AP8 Max and Min with both quiet and stormy models. It can be seen that AP8Min gives higher proton fluxes than AP8Max and for very high energetic particles (above 1GeV) the choice of the stormy and quiet magnetosphere scenario appears to have a slight significance.



**Figure 2-11 –Effect of Trapped Protons Flux and GCR protons for a common orbit (28.5°, 450 km) for shuttle missions.**

According to CREME96 literature [Tylka, 2007] for calculations intended to reflect long-term averages, the quiet condition should be selected. Figure 2-12 shows the charged GCR particles scenario (up to Neon) for solar min in a quiet magnetosphere environment.



**Figure 2-12- Galactic Cosmic Rays for charged particles for a common orbit (28.5°, 450 km) for shuttle missions. Charge number, Z, from protons (Z=1) to Neon (Z=10).**

For “worst case” and “peak rate” calculations, the “stormy” condition should be considered [Tylka, 2007]. Figure 2-13 illustrates the worst week SEP calculations using the stormy magnetosphere model with fluxes for ions with charge number 1 to 10.

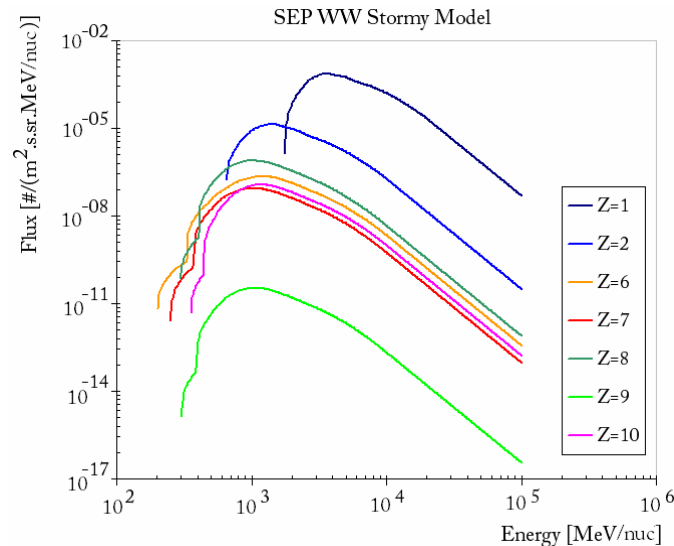


Figure 2-13- Worst week SEP fluxes for charged particles for a common orbit (28.5°, 450 km) for shuttle missions. Charge number,  $Z$ , from protons ( $Z=1$ ) to Neon ( $Z=10$ ).

## 2.4. Near Earth Interplanetary & Transport

This section describes the different transport mechanisms of radiation in the Heliosphere. The proton spectra provided are used for the full simulations of the radiation environment at the surface of Mars described in chapter 4.

### 2.4.1. Interplanetary Transport

Although GCR fluxes may not vary significantly from near-Earth interplanetary locations to Mars [Tylka, 2007], for SEP the interplanetary transport may be very complex and dependent on many factors such as energy, time, and solar wind conditions.

As previously discussed in this chapter, a large amount of data of SEP in the vicinity of the Earth exists. However extrapolating SEP Earth measures to another point in the heliosphere requires different corrections. The most obvious ones being the radial expansion of the solar wind that simplistically suggests a  $1/R^2$  ( $R$  being the distance from the Sun) law as well as effects coming from the spiral nature of the magnetic field.

The heliosphere being a hot plasma has the thermal speed higher than the flow speed [Kallenrode, 2001]. Thus the kinetic theory to describe the particle propagation and the distribution function of particles in the heliosphere needs two different approaches: the microscopic that considers the position and velocity of individual particles, and the macroscopic describing the averaging over a large number of particles, the statistical description of the plasma.

The Fokker-Plank equation [Kallenrode, 2001] of focused transport considers the short-range, local interactions between particles. D. Ruffolo [Ruffolo, 1998], considering that the particle momentum perpendicular to the magnetic field as a constant, rewrote the particle distribution function as shown below. In this form it clearly expresses particle time propagation as a function of interplanetary scattering, adiabatic focusing and solar wind convection and adiabatic deceleration in the form:

$$\begin{aligned}
 \text{Streaming} \quad \frac{\partial F}{\partial t} &= -\frac{\partial}{\partial z} \mu v F \\
 \text{Convection} &-\frac{\partial}{\partial z} \left( 1 - \mu^2 \frac{v^2}{c^2} \right) v_{sw} \sec \psi F \\
 \text{Focusing} &-\frac{\partial}{\partial \mu} \frac{v}{2L} \left( \frac{E'}{E} + \mu \frac{v_{sw}}{v} \sec \psi \right) (1 - \mu^2) F \\
 \text{Differential} &+\frac{\partial}{\partial \mu} v_{sw} \left( \cos \psi \frac{d}{dr} \sec \psi \right) \mu (1 - \mu^2) F \\
 \text{Convection} & \\
 \text{Scattering} &+\frac{\partial}{\partial \mu} \frac{\varphi}{2} \frac{\partial}{\partial \mu} \frac{E'}{E} F \\
 \text{Deceleration} &+\frac{\partial}{\partial p} p v_{sw} \left( \frac{\sec \psi}{2L} (1 - \mu^2) + \cos \psi \frac{d}{dr} (\sec \psi) \mu^2 \right) F
 \end{aligned} \tag{2-6}$$

where  $F(t, \mu, z, p) \equiv d^3N/(dzd\mu dp)$ , the density of particles in a given magnetic flux tube as a function of time,  $t$ , pitch angle cosine in the solar wind frame,  $\mu$ , the distance along the magnetic field,  $z$ , and the momentum in the solar wind frame,  $p$ . Still in the previous equation  $v$  is the particle speed,  $v_{sw}$  is the solar wind speed,  $\psi$  is the angle between the magnetic field and the radial direction,  $L(z) \equiv -B(dB/dz)^{-1}$  is the focusing length in the magnetic field,  $B$ ,  $\varphi(\mu)$  is the pitch angle diffusion coefficient and finally

$E'/E = 1 - v_{sw} v \cdot \sec \psi / c^2$  is the ratio of the total energy in the solar wind frame to that in the fixed frame [Ruffolo, 1995].

On the other hand the pitch angle scattering depending on the wave- particle interaction can be related with the particle mean free path parallel to the magnetic field,  $\lambda_{\parallel}$ , as:

$$\varphi(\mu) \propto \frac{|\mu|^{q-1} (1 - \mu^2) v}{\lambda_{\parallel}} \quad (2-7)$$

Or with the particle mean free path perpendicular to the magnetic field,  $\lambda_{\perp}$ , as:

$$\varphi(\mu) \propto \frac{|\mu|^{q-1} (1 - \mu^2) v}{\lambda_{\perp}} \cdot \cos^2 \psi \quad (2-8)$$

where the index q characterizes the dependence of the scattering rate upon pitch angle.

In sum particle propagation in its simplest form can be modelled by considering three factors: (1) the solar wind speed and solar rotation that lead to a spiral magnetic field, (2) the decrease of the magnetic field that leads to focusing in the pitch angle of particles as they propagate outwards, and (3) pitch-angle scattering due to small-scale irregularities in the magnetic field. Numerical simulations solving the Fokker-Plank equation [Ruffolo, 1998] have shown that: (1) in the absence of the solar wind effect, the evolution of the event fluence is energy independent assuming the mean free path is energy independent; (2) since the solar wind term depends on  $v_{sw}/v$ , the solar wind effect on the evolution of the event fluence as particles propagate outwards decreases for higher energies; (3) correction to focusing and differential convection, affecting the variability of the pitch angle cosine, although important in shaping the flux versus time profiles of particle events has a very small impact in change event fluences; (4) convection and deceleration create an amplified deficit in the intensity with the distance. Moreover Ruffolo [Ruffolo, 1998] alerts for the importance of other effects such as perpendicular drift and diffusion neglected in the previous analysis.

In the next sections the problem of particle propagation to Mars will be discussed. The simulation exercise published in [Keating, 2005] will be described and finally the proton spectra used in the full Mars simulation will be provided.

### 2.4.2. Propagation to Mars

The fluences measured at different points in the heliosphere, for the same injection of particles near the Sun, can differ essentially by (1) re-acceleration or deceleration of the particles as they propagate in the heliosphere, (2) by having some particles propagate backwards, either due to pitch-angle scattering or by mirroring at some magnetic bottleneck in the heliosphere. In order to quantify the importance of these effects, a simulation was performed following the Lintunen and Vainio kinetic approach [Lintunen, 2004]. In this family of models, particle propagation is determined via the mean free path parameter, which controls pitch-angle scattering. Results were obtained by launching a few thousand of test particles in a spiral magnetic field (solar wind speed 400 km/s) for 250 MeV protons. The mean free paths considered were based on the mean free paths of the two of the major SEP events occurred on 14<sup>th</sup> July 2000 and on 15<sup>th</sup> April 2001 of the Solar Cycle 23. The two events had mean free paths of 0.4 and 0.2 AU, respectively [Bieber, 2002], [Bieber, 2004]. As can be seen in figure 2-14, these values of mean free paths imply event fluences at Mars about 20% higher than would be predicted from measurements at Earth if only geometrical corrections ( $1/R^2$ ) were used.

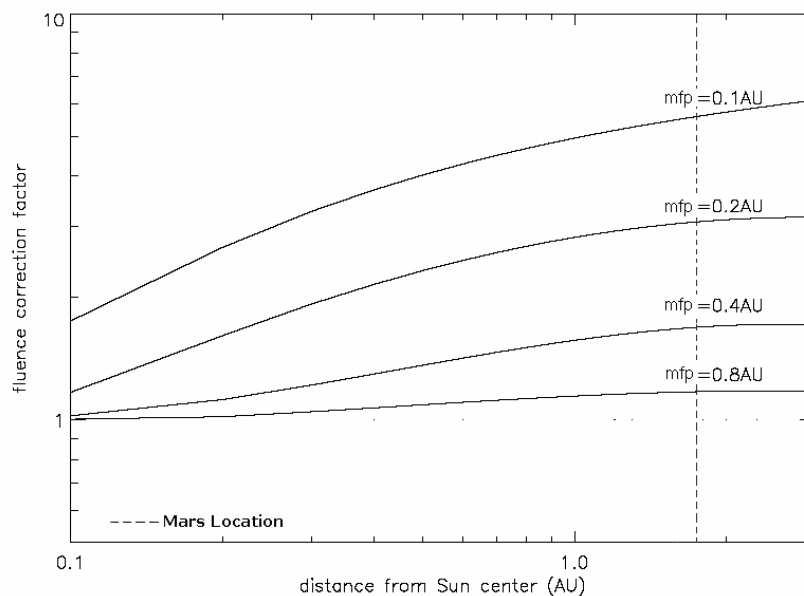


**Figure 2-14 - Fluence correction factor for 250-MeV solar protons as a function of distance from the Sun for different mean free paths. Mean free paths of 0.4 and 0.2 AU imply event fluences at Mars about 20% higher than would be predicted from measurements at Earth if only geometrical corrections ( $1/R^2$ ) were used. The dashed line indicates the location of Mars at 1.5 AU.**

From the discussion on the previous sections it can be inferred that the propagation from SEPs to Mars has to be considered on a case by case basis. In general the use of Near Earth Interplanetary (outside the magnetosphere) predictions from CREME96 should work as a worst case scenario.

#### 2.4.2.1. Near Earth Interplanetary Proton spectra

As previously discussed GCR and SEP protons are the most important radiation inputs to consider when studying the orbital and surface radiation environment of Mars. Therefore most of the results presented in Chapter 4 were obtained for: GCR at solar maximum and SEP generated by CREME96 for near-Earth interplanetary locations [Tylka, 2007]. These interplanetary flux models are based on measurements at Earth (1AU) [Tylka, 2007].

The phasing with respect to the solar cycle corresponds to the foreseen European Mars mission ExoMars [Keating, 2005] expected launched in 2013.

These GCR flux models represent the environment that prevails in the absence of solar energetic particle events. Figure 2-15 shows the solar-quiet proton flux in the solar maximum part of the cycle.

The most severe proton environment corresponds to that from solar energetic protons given by the “worst week” model of CREME96 [Tylka1, 1997] as shown in figure 2-15. This environment can produce very high particle fluxes in near-Earth space persisting for several days. The SEP worst week model is based on SEP fluxes averaged over 180 hours beginning at 1300 UT on the 19 October 1989.

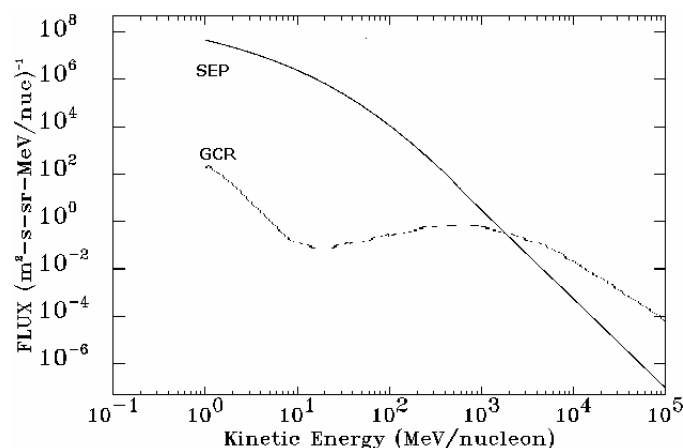


**Figure 2-15- GCR proton flux in solar-quiet model in the solar maximum and proton flux from “worst week” model SEP, by CREME96.**

### 2.4.3. *Atmosphere Shielding and Soil contribution*

As cosmic or solar particles enter in the Martian upper atmosphere they may undergo nuclear reactions resulting in the emission of electrons, neutrons and other subatomic particles. Progressing further into the atmosphere, the increased density increases energy loss of the protons and increases such *secondary particles* production. Mars's geology also plays a very important role in the radiation environment characterization. The Martian atmosphere, being very low density (maximum values of the order of  $10^{-2} \text{ kgm}^{-3}$ ), behaves as a soft attenuator for incoming radiation capable of reaching the Mars surface. This results in an important contribution from secondary particles generated and backscattered at the surface [Keating, 2005].

### 2.4.4. *Other planets and magnetosphere effects*

Space missions to other planets of the solar system have shown that several of them have a significant magnetic field. In particular, the giant planets have a much stronger magnetic field than Earth. Their magnetospheres are furthermore much larger than Earth's, in part because of the stronger dipole moments and because the solar wind becomes increasingly weaker far away from the Sun. Mercury has a magnetic moment only about 1/2000 that of Earth and a very small magnetosphere. The magnitudes of the dipole moments of Mercury, Earth, Jupiter, Saturn, Uranus and Neptune, in units of  $10^{25} \text{ Gauss-cm}^3$ , are 0.004 (approx.), 7.9, 150000, 4300, 420 and 200, respectively [Lepping, 1995].

Venus (as well as Mars) has a very weak magnetic field, probably not generated by dynamo action in the core but possibly due to remnant magnetization of crustal rock acquired earlier from a stronger magnetic field generated by a now dead core dynamo [Spohn, 1998]. A dynamo powered by thermal power alone would have ceased a few billions of years ago as the core cooled to an extent that it became stably stratified [Spohn, 1998].

Mars has no radiation belts of trapped particles, but the presence of the localised magnetic fields may create shielded zones. Work by Laurent Desorgher [Darnell, 2007] has shown that electrons up to 10MeV can experience significant deflection by the magnetic anomalies. The effect of Martian localised magnetic field is of less significance for protons in the range of energy that may concern effects on EEE devices.

---



### 3. Radiation Effects on EEE components

The space radiation environment may adversely affect spacecraft systems, sub-systems and components in the form of functional/parameter degradation or even complete failure. Successful spacecraft design thus requires in-depth knowledge of the space radiation environment and its effect.

This chapter aims at explaining how to predict radiation-induced degradation on complex Electrical, Electromagnetic and Electronic (EEE) components, and describing the different types of effects that can be expected under hazardous radiation environments, such as those described in Chapter 2. Additionally this chapter aims at introducing the bases for the discussion of the computational tools and results to be presented in Chapter 5. The focus is on description of degradation mechanisms and radiation effects in Metal-Oxide-Semiconductor (MOS) transistors which are the most commonly used devices in modern integrated circuits (IC), and in particular on the specific Static Random Access Memory devices (SRAMs) used for testing the tool proposed and discussed in Chapter 5.

The chapter is organised in three subchapters. The first introduces the characteristics, properties and principals of MOS devices. In 3.2 the basic radiation induced degradation mechanisms will be described for complex devices based on MOS technology. Finally, in 3.3 general methods for prediction of the degradation are proposed with particular emphasis on single event effects on EEE components.

#### 3.1. *Metal-Oxide-Semiconductor Devices*

##### 3.1.1. *Basic Device Characteristics*

The n-channel MOSFET, NMOS, represented in figure 3-1, is one of the various kinds of metal-oxide semiconductor field-effect transistors (MOSFET). It is a four-terminal device and consists of a p-type semiconductor substrate in which two n<sup>+</sup> regions, source and drain, are formed for example by ion implantation [Sze, 1981]. Material of n-type is typically produced by doping the silicon with impurities with valence higher than the base material. These impurities, such as phosphorus, are known as *donors* and give electrons to the conduction band of the

---

doped silicon. While p-type may be obtained by doping with impurities with valence lower than the base material. By capturing electrons from the valence band they increase the density of holes. A typical *acceptors* used to create p-type silicon is boron [Grove, 1967]. The metal contact on the insulator is called gate. Generally the gate is heavily doped poly-silicon.

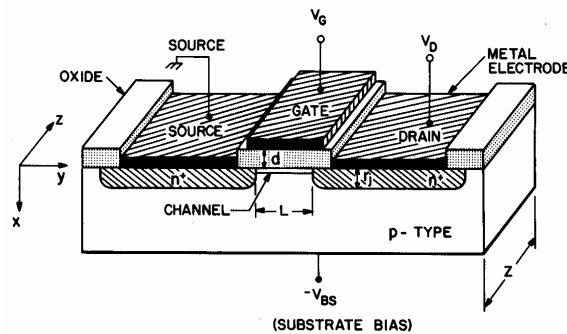


Figure 3-1– Schematic diagram of a n-channel MOSFET [Sze, 1981]

The basic device parameters are:

1. The distance between the two n+-p junctions, i.e. the channel length  $L$ ;
2. The channel width,  $Z$ ;
3. The insulator thickness,  $d$ ;
4. The junction depth,  $r_j$ ;
5. The substrate doping,  $NA$ .

In silicon integrated circuit a MOSFET is surrounded by a thick oxide, called the field oxide, to isolate it from the adjacent devices.

Considering the source contact as the voltage reference, when no voltage is applied to the gate, the source-to-drain electrodes correspond to two p-n junctions connected back to back. In an n-channel MOSFET, the only current that can flow from source to drain is the reverse leakage current. When a sufficiently large positive bias is applied to the gate so that a surface inversion layer (or channel) is formed between the two  $n^+$  regions, the source and the drain are then connected by a conducting-surface n-channel through which a large current can flow. The conductance of this channel can be modulated by varying the gate voltage.

### 3.1.2. Principles of operation

Material presented in the following subsections is based on principles reported in the literature and mainly obtained from three main sources: [Grove, 1967], [Sze, 1981], [Ma, 1989].

### 3.1.2.1. *Equilibrium and Non-equilibrium Conditions*

The energy band diagram of a p-type (n-channel) metal-oxide-semiconductor structure and the associated charge distribution are shown in figure 3-2 for three different gate bias conditions.

Regardless of the gate voltage value, the Fermi level in the bulk semiconductor remains constant since equilibrium is maintained.

When a negative potential is applied to the metal gate, the positive charges in the semiconductor are attracted. In a p-type device, this will create an accumulation of holes (majority carriers) near the oxide-silicon interface. As illustrated in figure 3-2.a.

If a small positive voltage is applied to the gate a negative charge is induced in the semiconductor, because the holes are pushed away from the vicinity of the interface, leaving behind a *depletion region*, consisting of uncompensated acceptor ions (figure 3-2.b).

Increasing the positive potential applied to the gate, the width of the surface depletion zone increases. Consequentially the total electrostatic potential variation in the silicon is as well increased. As the bands are bent further, the conduction band comes eventually closer to the Fermi level. In this case the concentration of electrons (minority carriers) near the interface is increased. After this, most of the additional negative charge induced in the semiconductor will consist in the charge  $Q_n$ , (figure 3-2.c) due to the electrons in a very narrow n-type inversion layer. The thickness of the inversion layer is about 1 to 10 nm. It is much smaller than the depletion region because the concentration of minority carriers drops ten percent of its value over a distance of about  $3kT/qE$  ( $k$  is the Boltzmann constant,  $T$  is the temperature,  $q$  is the carrier unit charge and  $E$  is the electric field at the interface). Once the inversion layer is formed, the width of the surface depletion region tends to a maximum. This is because once the bands are pulled down far enough for strong inversions, even a very small increase in the band bending, corresponding to a very small increase in the depletion region width, results in a very large increase in the charge contained within the inversion layer.

---

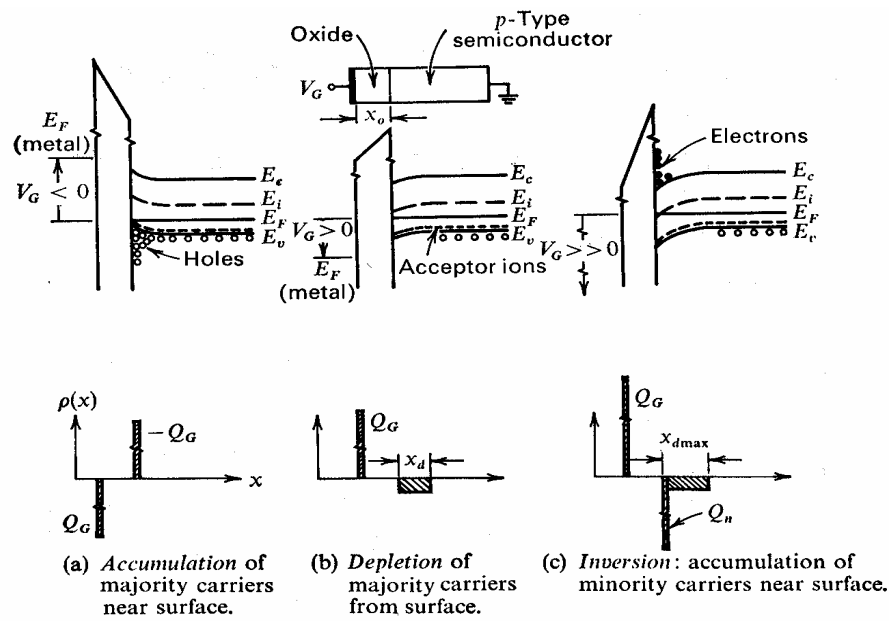
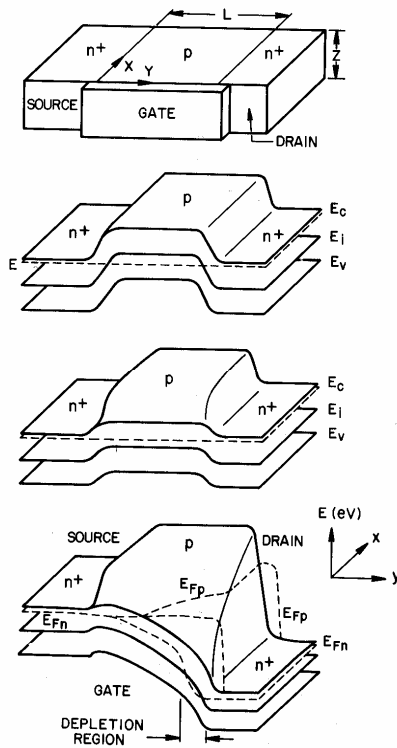


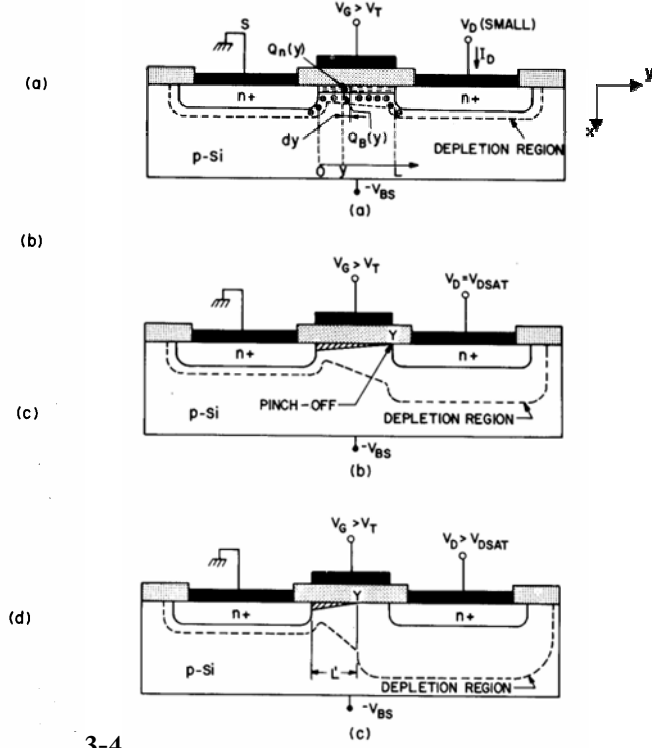
Figure 3-2 – Energy Bands and charge distribution in a MOS structure under various bias conditions, in the absence of surface states and work function difference [Grove, 1967]. In the figure  $E_c$  states for minimum energy of the conduction band,  $E_v$  states for minimum energy of the valence band and  $E_i$  states for the intrinsic Fermi level, ideal case obtained in intrinsic semiconductors where equal density of both carriers.

When a voltage is applied to the source-drain contacts, the MOS structure is in a non-equilibrium condition.

Figure 3-3 illustrates the MOSFET turned 90° (3-3.a), and the energy bands for different equilibrium conditions (3-3.b & c) and for the non-equilibrium condition (3-3.d). As revealed in figure 3-3.d, the non-equilibrium condition with both drain and gate biased shows a separation of the electrons and holes reference energy bands; the holes' Fermi Level,  $E_{Fp}$ , remains at the bulk Fermi level while the electron (minority)  $E_{Fn}$  is lowered towards the drain contact. The applied drain bias lowers the electron reference energy band, and because an inversion layer can only be formed when the potential at the surface crosses over the minority carrier reference energy band, the gate voltage required for inversion at the drain is larger than the equilibrium case.



3-3



3-4

Figure 3-3- Two-dimension band diagrams of an n-channel MOSFET: (a) Device configuration; (b) Flat-band zero-bias equilibrium condition; (c) Equilibrium condition under a gate bias; (d) Non-equilibrium condition under both gate and drain biases [Sze, 1981]. In the figure  $E_c$  states for minimum energy of the conduction band,  $E_v$  states for minimum energy of the valence band and  $E_i$  states for the intrinsic Fermi level, ideal case obtained in intrinsic semiconductors where equal density of both carriers.

Figure 3-4- Illustration of the operation of surface field-effect transistor for  $V_G > V_T$ : (a)  $V_D$  is small; MOSFET operated in the linear region with the channel constant resistance. (b)  $V_D = V_{D,sat}$ ; MOSFET operated at onset of saturation. The  $y$  indicates the pinch-off point (c)  $V_D > V_{D,sat}$ ; MOSFET operated beyond the saturation, no further increase of drain current and the effective channel length is reduced [Sze, 1981]

Figure 3-4 represents the operating principals of an n-channel MOSFET.

Consider that a voltage is applied to the gate, causing an inversion at the semiconductor surface ( $V_G$  higher than the threshold voltage for inversion,  $V_T$ ) as shown in figure 3-4.a. If a small drain voltage is applied, a current will flow from the source to the drain through the conducting channel. Thus the channel acts as a resistance, and the drain current,  $I_D$ , is proportional to the drain voltage  $V_D$ . This is the linear region. Increasing the voltage applied to the drain the channel depth at  $y=L$  can be reduced to zero, as illustrated by figure 3-4.b. This is called the pinch-off point. Beyond the pinch-off point the drain current remains essentially the same, reaching its saturation value,  $V_{D,Sat}$ . The number of carriers arriving at point Y from the source

remains the same, and consequently the current flowing from the source to drain remains constant, apart from the distance  $L$  that decreases to  $L'$  (figure 3-4.c).

Assuming an ideal n-channel MOSFET the characteristics functions can be proved to be a function of gate,  $V_G$ , and drain biases,  $V_D$ , semiconductor bulk potential,  $\psi_B$ , and oxide capacitance per unit area,  $C_i$ , as given in equation 3-1.

$$I_D = \frac{Z}{L} \mu_n C_i \left\{ \left( V_G - 2\psi_B - \frac{V_D}{2} \right) V_D - \frac{2}{3} \frac{\sqrt{2\varepsilon_s q N_A}}{C_i} \left[ (V_D + 2\psi_B)^{3/2} - (2\psi_B)^{3/2} \right] \right\} \quad (3-1)$$

for  $y=L$  and  $V=V_D$ , where  $Z$  is the source-drain depth (figure 3-3),  $\mu_n$  is the mobility of electrons and  $\varepsilon_s$ ,  $q$  and  $N_A$  are respectively the semiconductor permittivity, the magnitude of electronic charge and acceptor impurity density.

### 3.1.2.2. Threshold voltage

As previously defined the threshold voltage,  $V_T$ , is the gate voltage at which the inversion layer forms. According to Sze [Sze, 1981] equation 3-1 can be rewritten for the case of  $V_D$  small (linear region) as

$$I_D \approx \frac{Z}{L} \mu_n C_i (V_G - V_T) V_D \quad (3-2)$$

for  $V_D \ll (V_G - V_T)$  where

$$V_T = 2\psi_B + \frac{\sqrt{2\varepsilon_s q N_A} (2\psi_B)}{C_i} \quad (3-3) \text{ [Sze, 1981]}$$

Equations 3-1 and 3-2 show that for a given  $V_G$  the drain current increases linearly with drain voltage and for  $V_D$  approximately of the order of  $V_G - V_T$  (figure 3-5), drain current gradually levels off approaching its saturation value,  $V_{D \text{ sat}}$ .

Figure 3-5 shows the basic output characteristic of an idealized MOSFET for different gate bias voltages. The dashed line indicates the locus of the drain voltage ( $V_{D \text{ sat}}$ ) at which the current reaches a maximum value. Additionally it shows how the drain current changes for increasing gate biases.

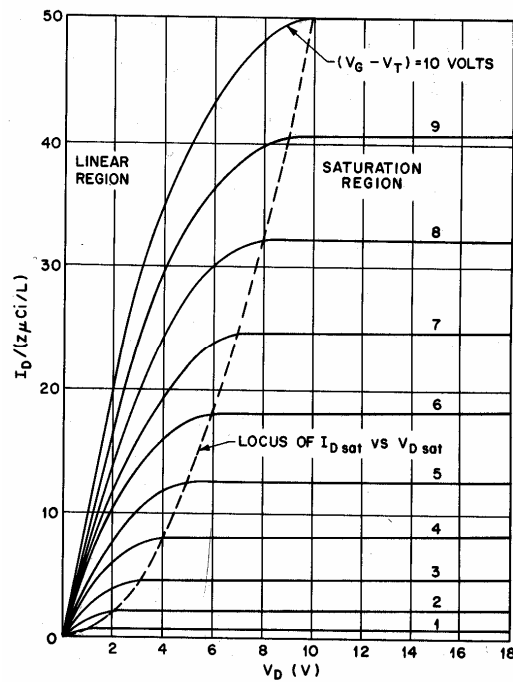


Figure 3-5- MOSFET drain current-voltage relationship for different gate voltages,  $V_G$ : The dashed line indicates the locus of saturation drain voltage ( $V_{D sat}$ ). For  $V_D > V_{D sat}$ , the drain current remains constant [Sze, 1981]

Equation 3-3 shows that threshold voltage of an ideal device is highly dependent on bulk potential, on semiconductor doping density, oxide capacitance and subsequently on oxide thickness. However real MOS capacitors deviate from the ideal either by: a) nonzero metal-semiconductor work function difference,  $\phi_{ms}$ , this term is related to the existence of a built-in field in the oxide interfering with the band bending between the gate metal and the semiconductor; b) presence of trapped charge either in the oxide,  $Q_{ox}$ , or at the interface,  $Q_{it}$ , (discusses in sections 3.1.5 and 3.2.1). Therefore, for real devices the threshold voltage is sensitive to these parameters and is given by equation 3-4.

$$V_T = 2\psi_B + \frac{\sqrt{2\varepsilon_s q N_A (2\psi_B)}}{C_i} - \phi_{ms} - \frac{Q_{ox}}{C_i} - \frac{Q_{it}}{C_i} \quad (3-4) \text{ [Ma, 1989]}$$

### 3.1.2.3. Different types of MOS field-effect transistors.

There are basically four different MOSFETs types, depending on the types of inversion layer. At zero gate bias, the channel conductance is very low. In order to form the n-channel a positive voltage shall be applied to the gate. This type is the normally-off (enhancement) n-channel MOSFET. If an n-channel exists at zero bias, a negative bias shall be applied to the

gate to deplete carriers in the channel to reduce the channel conductance. This is the normally-on (depletion) n-channel MOSFET. In case the MOSFET is processed in a n-type substrate with two p-type well implantations, the minority carriers are holes, the inversion is obtained for negative gate bias and the source-drain current flowing in the p-channel will be induced by negative drain voltages. This type of MOSFET is known as PMOS. Similarly to the normally-on NMOS, if a p-channel exists at zero bias on a PMOS device, it is called normally-on PMOS. Figure 3-6 illustrates the main features and summarizes the characteristic functions for both n and p-channel enhancement MOSFETs.

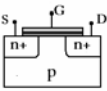
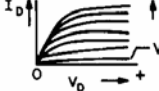
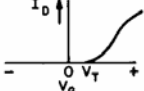
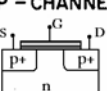
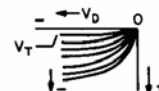
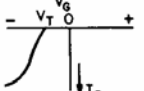
TYPE	ELECTRICAL SYMBOL	OUTPUT CHARACTERISTIC	TRANSFER CHARACTERISTIC
<b>N - CHANNEL</b> 			
<b>P - CHANNEL</b> 			

Figure 3-6 – Basic types of MOSFET devices: (a) n-channel (NMOS): (b) p-channel (PMOS) including electric symbol, transfer characteristics, and output characteristics for the four types of MOSFET devices (adapted from [Sze, 1981])

#### 3.1.2.4. Complementary MOS

Complementary metal-oxide-semiconductor (CMOS) is a major class of integrated circuits. CMOS technology is used in microprocessors, microcontrollers, SRAM, and other digital logic circuits, as well as in a wide variety of analogue circuits such as image sensors, data converters, and highly integrated transceivers for communication applications.

Two important characteristics of CMOS devices are high noise immunity and low static power consumption [Ma, 1989].

CMOS transistors use complementary pairs of p-type and n-type metal oxide semiconductor field effect transistors for logic functions, as illustrated in figure 3-7 a) and b).

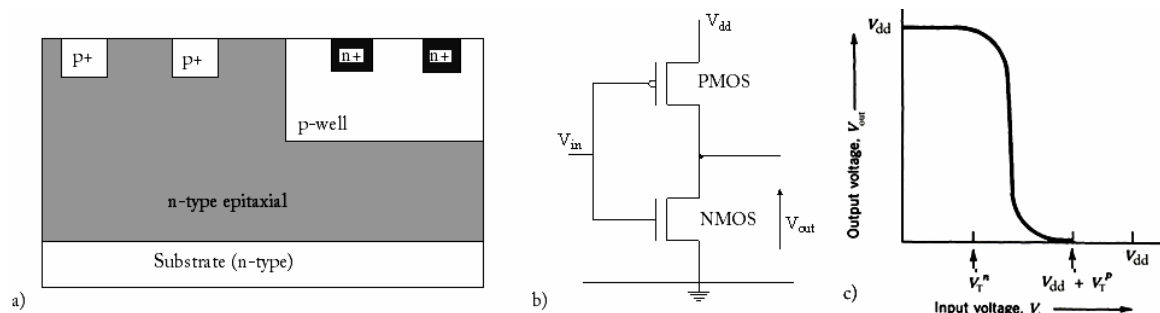


**Figure 3-7 – CMOS inverter: a) schematic diagram; b) circuit; c) Voltage- transfer characteristics of a CMOS inverter [Ma, 1989].**

Figure 3-7 c) shows the voltage-transfer characteristics of a CMOS inverter where the n-channel device has a positive threshold voltage ( $V_{T^n} > 0$ ) and the p-channel has a negative threshold voltage. When the input voltage,  $V_{in}$ , is high ( $\gg V_{T^n}$ , approximately of the order of  $V_{dd}$ ) the NMOS is “on” and PMOS is “off”. Therefore the resistance of the p-channel is much higher than the n-channel and the output voltage,  $V_{out}$ , is low. In case the input voltage is low (approximately of the order of  $V_{T^n}$ ) the NMOS is “off” while the PMOS is “on” and  $V_{out}$ , is high, of the order of  $V_{dd}$ . Thus, CMOS technologies being based on the use of either one or the other individual MOS (P or N) in conduction require less power than chips using just one type of transistor. Significant power is only drawn when the transistors in the CMOS device are switching between on and off states. Consequently, CMOS devices do not produce as much waste heat as other forms of logic. Additionally CMOS also allows a high density of logic functions on a chip.

### 3.1.3. Ionization related semiconductor mechanisms

*Carrier multiplication* through impact ionization and *recombination* of excess carriers are essential mechanisms in the operation of semiconductor devices. The following subsections focuses on

the description of *electron-hole pair generation* by impact ionization and recombination mechanisms.

### 3.1.3.1. *E-h pair generation Energy Threshold*

Most recent publications<sup>1</sup> propose the energy threshold for the generation of an electron-hole pair by impact ionization to be an experimental value with a semi-empirical relationship with the material energy band gap,  $E_g$ . Earlier publications<sup>2</sup>, 1954-1961, provided different theories of statistical interrelation between the threshold energy for ionization, optical phonon energy, ionization mean free path and the mean free path for optical phonon scattering.

This section gives a phenomenological description of the e-h pair generation threshold energy as an intrinsic characteristic of a particular material. While for photon absorption/emission the threshold energy is  $E_g$ , for e-h pair production,  $E_{th}$ , is given by the threshold for the production on an electron,  $E_{th}^e$ , and the energy required for the production of a hole,  $E_{th}^h$ :

$$E_{th} = E_{th}^e + E_{th}^h \quad (3-5)$$

After Ahmad and Khokley (1967) [Ahmad, 1967], in 1972, Anderson and Crowell [Anderson, 1972] published an improved methodology to predict the carrier multiplication through impact ionization based on the realistic band structure of the material. The methodology [Anderson, 1972] allows the determination of  $E_{th}$  as a function of the wave vector by taking into account: a) all possible mechanisms for e-h pair production, including phonon production; b) the electron-energy-wave vector relationship; c) minimization of the energy of the primary particle with respect to small changes of wave vector of any of the final particles; and finally d) by ensuring

---

<sup>1</sup> [Sze, 1981], [Ma, 1989], [Musseau, 1994], [Holmes-Siedle, 2006]

<sup>2</sup> [Wolff, 1954], [Shockley, 1961], [Baraff, 1962]

---

the energy momentum conservation. Figure 3-8 illustrates the real energy band structures of Si, as function of the wave vectors ( $\vec{k}$ ), where  $E_g$  is the energy band gap. Additionally figure 3-8 includes an example of hypothetical impact-ionization process: a) primary particles before ionization where  $E_i(k_i)$  is the initial state of the incoming electron and  $E_v(k_1)$  is the initial state of an electron in the valence band; b) resultant particles immediately after ionization involving the minimization of the incoming electron energy, with  $E_c(k_3)$  final state, the creation of an electron  $E_c(k_2)$  in the conduction band and hole in the valence band.

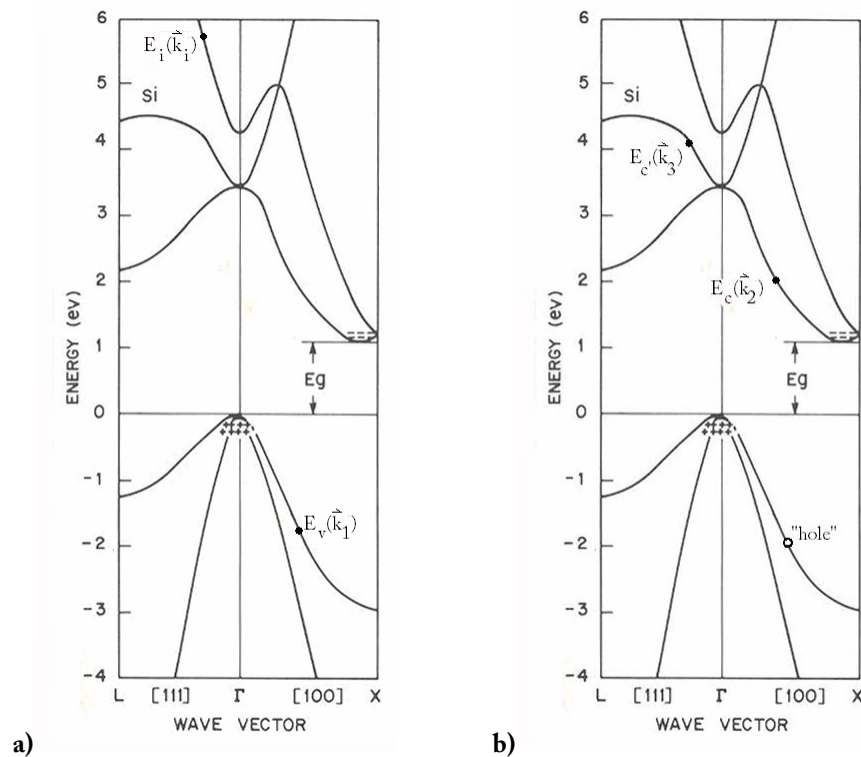


**Figure 3-8 – Real energy band structures of Si, where  $E_g$  is the energy band gap (Adapted from Sze after Chelikowsky and Cohen) [Holmes-Siedle, 2006], including hypothetical impact-ionization process: a) primary particles before ionization; b) resultant particles immediately after ionization [Anderson, 1972].**

In the particular example of phononless mechanisms, assuming spherical constant energy surfaces with exactly the same band dynamic for electrons in the conduction band and holes in the valence band ( $m_v^*/m_c^*=1$ ) the energy required to create an electron-hole pair can be estimated as three times band gap as given in equation 3-6 [Anderson, 1972], [Wolff, 1954]:

$$E_{th} = 3 \cdot E_g \quad (3-6)$$

Lower threshold energies for each initiating carrier from Anderson and Crowell [Anderson, 1972] are given in Table 3-1 as function of orientation. All energies are quoted in eV relative to

the band edge with an estimate accuracy of  $\pm 0.2\text{eV}$ . Additionally Table 3-1 specifies whether the processes are direct (D) or phonon assisted processes (U) and if the initial carrier comes from other than the normal conduction or valence band. Finally it is also indicated when two processes have the same threshold.

Material	Si	Ge	GaAs	GaP	InSb	
Band gap assumed (eV)	1.1	0.7	1.4	2.3	0.2	
Band structure	Indirect	Indirect	Direct	Indirect	Direct	
Direction	Initiation					
$\langle 100 \rangle$	electrons	1.1 U*	0.9 U, D	2.1 D*	2.6 U†	0.2(5) D
		1.5 D	1.0 D*, U	2.3 U*	3.0 D†	1.6 D
		1.6 U*	1.2 D	2.4 D*	3.1 D†	1.7 D*, D*
	holes	1.8 D	1.3 D, D*	1.7 D*	2.4 D <sup>b</sup>	0.2 D*
		2.1 D*	1.7 D*	1.9 D	...	0.6 D
		...	4.5 D*	2.5 D	...	2.2 D*
$\langle 111 \rangle$	electrons	3.1 U*	0.8 U, <sup>b</sup> U <sup>b</sup>	3.2 D†, D†	3.0 D†	0.2(5) D
		3.3 U*	2.5 D <sup>c</sup>	3.6 D†, D†	3.4 D†	...
		3.5 U*	2.6 D*	3.7 D†	3.5 U†, D† <sup>b</sup>	...
	holes	2.9 D*	0.9 D	1.6 D†	2.9 D†	0.4 D*
		4.4 D* <sup>c</sup>	1.0 D*	2.3 D†	3.6 D†	1.5 D*
		4.7 D*	1.4 D*	2.5 D†	...	1.8 D*
$\langle 110 \rangle$	electrons	2.1 U	1.1 D*	1.7 D	2.8 D†	0.2 D
		4.0 D*	1.2 D	1.9 D*	2.9 D†	1.6 D
		4.2 U*	1.3 U	2.2 D	3.3 D†	1.7 D*, D*
	holes	1.8 D	0.9 D*, D*	1.4 D*	2.3 D <sup>b</sup>	0.2 D*, D*
		4.0 D*	1.3 D	1.6 D*	2.6 D*	0.4 D
		4.1 D*	1.8 D*	1.9 D	2.8 D*	1.7 U* <sup>b</sup> , D*

<sup>a</sup>D, direct process (no reciprocal-lattice translation vector involved); U, umklapp process; \*, initiating carrier comes from other than the normal conduction or valence band; †, normal conduction or valence band cannot supply the initiating carrier (even if momentum conservation is neglected) because the energy range of the band is less than the band gap.

<sup>b</sup>The cross section for the process cited is likely to be very small, owing to the existence of an antithreshold within 0.1 eV of the threshold.

<sup>c</sup>This value obtained by a linear extrapolation of the light-hole band slightly beyond the limits of the graph.

**Table 3-1 – Ionization threshold energies as function of the wave-vector direction for different semiconductor materials [Anderson, 1972]**

Consequently, the required energy to produce an electron-hole pair can given by the linear combination of all the possible processes for electron-hole pair generation weighted by the cross-section of each process  $\sigma_{ijk}$  as given by equation 3-7:

$$E_{th} = \sum_{ijk} \sigma_{ijk} E_{th,jk}^i \quad (3-7)$$

where  $i=e, h$ ;  $j$  is the index for all possible processes and  $k$  is the wave vector directions.

Nowadays the energy threshold for electron-hole pair generation by impact ionization can be accurately determined experimentally. Table 3-2 gives the experimental values for Silicon, Germanium, Gallium Arsenide and Silicon Dioxide.

---

	Si	Ge	GaAs	SiO <sub>2</sub>
Ionization Threshold [eV]	3.6 <sup>3</sup>	2.9 <sup>1</sup>	4.8 <sup>4</sup>	18 <sup>5</sup>
Accuracy [eV]	----	----	----	± 3 or (17 ± 1) <sup>6</sup>

---

**Table 3-2 – Ionization energy threshold for Silicon, Gallium Arsenide and Silicon Dioxide**

### 3.1.3.2. *Recombination*

Whenever the thermal-equilibrium condition of a physical system is disturbed, processes exist to restore the system to equilibrium. For example, in the case of electron-hole pair generation by impact ionization the density of carriers is increased and *recombination processes* work in the material (either in the oxide or in the semiconductor) to restore the equilibrium conditions. Different processes may hold the recombination of minority carriers, namely: *Band-to-band* recombination process [Kerra, 2002] and *trap assisted recombination* through intermediate centres [Shockley, 1952] [Hall, 1952] by either single-level (figure 3-9) or multi-level interstitial traps.

The *band-to-band* recombination happens when electrons in the conduction band and holes in the valence band recombine directly. Thus the rate of recombination for this process is proportional to both the concentration of electrons and holes. Also known as *Auger recombination*, this process dominates when the concentration of carriers is very high, such as under irradiation conditions.

---

<sup>3</sup> [McKay, 1953]

<sup>4</sup> [Ma, 1989]

<sup>5</sup> [Ausmann, 1957]

<sup>6</sup> [Benedetto, 1986]

---

Imperfections on the manufacture process of MOS devices may cause different defect centres in the oxide, at the surface or in the bulk semiconductor. These defects add interstitial energy levels to their band structure that, depending on the relationship between the lifetime of the trapping and carriers' mobility, may work as potential centres for charge trapping or recombination.

Shockley and Read [Shockley, 1952] have worked out the *trapped assisted recombination* generated through intermediate centres, as depicted in figure 3-9. Hall [Hall, 1952] has experimentally verified Shockley and Read's predictions. The *Shockley-Read-Hall (SRH)* rate depends crucially on the defect density, the defect energy levels in the gap, and the electron and hole scattering cross-sections.

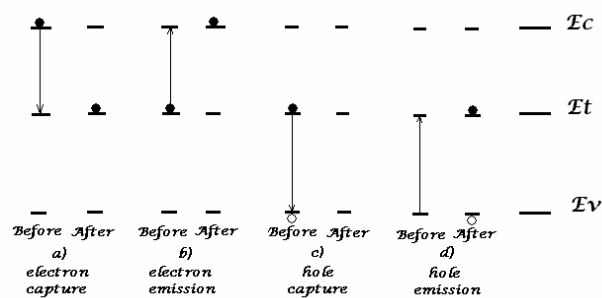
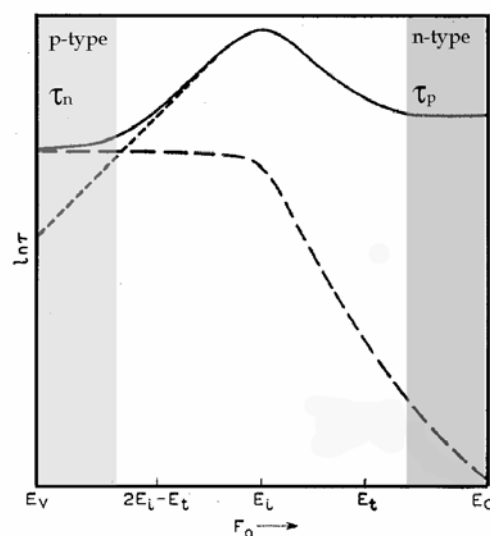


Figure 3-9 - Recombination through intermediate centres, or single-level recombination process

Figure 3-10 illustrates the carrier lifetime,  $\tau \equiv \delta n / \delta R$ , calculated by Shockley and Read based on the excess carriers' density,  $\delta n$ , and on recombination rates,  $\delta R$ , as a function of the impurity contents. The composition of the specimens is represented by Fermi level for thermal equilibrium conditions,  $F_0$ .



**Figure 3-10 – Dependence of lifetime upon impurity content: Shockley and Read theoretical prediction [Shockley, 1952]**

Figure 3-10 depicts the quantitative result for carriers' lifetime as a sum of terms depending on recombination of holes injected into high doped n-type semiconductor and electrons into highly doped p-type semiconductor. Different behaviours of  $\tau$  can be identified: Starting from a strongly doped p-type semiconductor with Fermi level close to the top of valence band, with empty trap levels. Here carriers' lifetime is due to immediate recombination of every injected and trapped electron, by electron capture. On the other extreme, a strongly doped n-type semiconductor with the Fermi level close to the bottom of the conduction band, with full trap levels, where by hole capture, electrons recombine with every trapped hole. Intermediate behaviours are dominated or limited by the ratio of holes in trap levels and electrons in the conduction band. Whenever electrons cannot recombine they are re-emitted into the conduction band and hole capture may not be possible into empty trap levels.

### 3.2. *Radiation-Induced Effects*

When high energy particles traverse a MOS device, various types of effects occur either in the oxide or in the semiconductor. Depending on the particle charge and mass, the effects may involve processes with enough energy to break atomic bonds and create electron-hole pairs, *ionization*; or processes in which the atoms are displaced from their original positions in the crystal, *displacement damage*. Displacement damage affects primarily minority carriers' lifetime in the semiconductor substrate. These processes are briefly discussed in section 3.3.3.

Ionization may be manifested as long-lived/cumulative or transients effects. Basically when a charged particle crosses a MOS device, electron-hole pairs are created in the materials of the device. In the metal the mobility of carriers is so high, around  $10^5 \text{m}^2\text{V}^{-1}\text{s}^{-1}$ , that we may assume instantaneous return to equilibrium, therefore the metal effects are negligible. In the oxide electron mobility is much lower, around  $10^{-4}$  to  $10^{-3} \text{m}^2\text{V}^{-1}\text{s}^{-1}$ , being even lower for holes (of the order of  $10^{-5}$ – $10^{-12} \text{m}^2\text{V}^{-1}\text{s}^{-1}$ ) [Ma, 1989]. As will be explained in section 3.3.1 these mechanisms being very slow result in long-lived cumulative effects, also known as *Total Ionizing Dose Effects (TID)*. While in the bulk semiconductor where both types of carrier mobility are of the order of  $10^{-1}$  to  $1 \text{m}^2\text{V}^{-1}\text{s}^{-1}$ , charged particles can create ionization-induced currents that will tend to

---

return to equilibrium in a few picoseconds. These mechanisms can cause transient effects such as *Single Event Effects (SEE)* as described in section 3.3.2 under very high dose rate conditions.

### 3.2.1. Total Ionizing Dose Mechanisms

The insulator layer of the MOS device is the oxide. In a quasi infinite dielectric medium at room temperature any generated charge is expected to be immobile. However the oxide layer is in contact with the metal gate under an electric field. For this reason when a charged particle travels through the oxide with energy enough to create e-h pairs, 18eV for SiO<sub>2</sub> (table 3-2), electrons and holes are separated by the electric field across the oxide. When the gate is unbiased, most e-h pairs are recombined. Electron-hole pairs are initially recombined mostly via band-to-band recombination process. Initial recombination is expected to occur in a few picoseconds after injection [Ma, 1989]. Those electrons that escape recombination having a mobility of around  $10^{-4}\text{m}^2\text{V}^{-1}\text{s}^{-1}$  at room temperature will drift to the gate in a few microseconds [Ma, 1989], depending on the gate biasing. Holes having mobility lower than  $10^{-8}\text{m}^2\text{V}^{-1}\text{s}^{-1}$  will remain approximately immobile near their point of generation in the oxide. Figure 3-11 illustrates a general picture of charge built-up processes occurring simultaneously in an oxide with a steady dose rate. Over a period of time of the order of seconds at room temperature [Ma, 1989], holes execute a relatively slow transport activated by temperature and field toward the negative electrode (the semiconductor substrate under a positive gate bias). This dispersive mechanism is also called *holes hopping* as illustrated in figure 3-11. *Deep oxide interface trapping* sites, also known as *oxide traps* are mostly associated to deficient bonding between silicon and oxygen and oxygen vacancies. During the hopping process, holes may be collected or captured in deep oxide trapping sites. They are asymmetrically located in the oxide generating an asymmetric distribution of excess positive charge. When oxide traps are located near the interface new recombination of electron-hole pairs can occur near the oxide/semiconductor interface due to either radiation-induced carriers' generation or electron injection from the semiconductor. Moreover by increasing the oxide field as illustrated in the bottom of figure 3-11, holes can be tunnelled into the semiconductor where they can be captured at *interface traps*. This process reduces the oxide trap charge accumulated and increases positive trapped charge at the interface. Other mechanisms such as hydrogen release, drift and trapping at the interface are also described in the literature [Holmes-Siedle, 2006], however it will be considered of lesser concern in the discussion of this chapter.

---

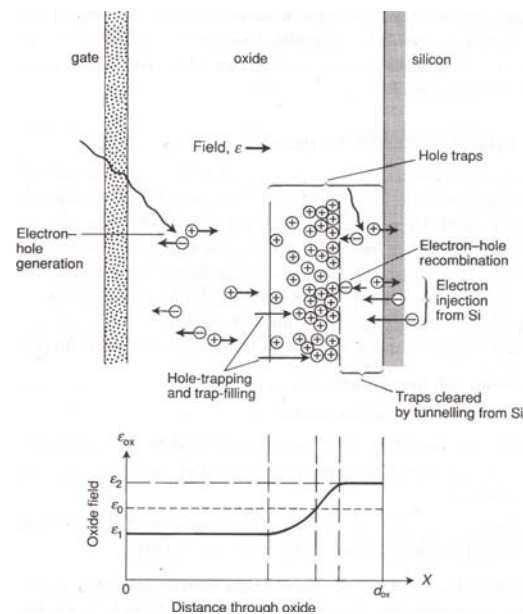


**Figure 3-11 – Charge build-up mechanisms: charge build-up and removal processes in a MOS structure. Top: Sketch of processes taking place under irradiation. Bottom: Strong variation of the electric field in the region of the sheet of trapped charge [Holmes-Siedle, 2006].**

Under a positive gate voltage, holes generated in the Collection region 2 of figure 3-12 are swept by hopping towards the silicon, as previously described. Positive trapped charge in the oxide,  $Q_{ot}$ , is collected in a thin sheet of density, at a distance  $x_1$  from the silicon. If the voltage applied to the gate is negative, the charge is collected from region 1. The thickness of region 1,  $x_1$ , is in general much smaller than the thickness of region 2,  $x_2$  [Holmes-Siedle, 2006].

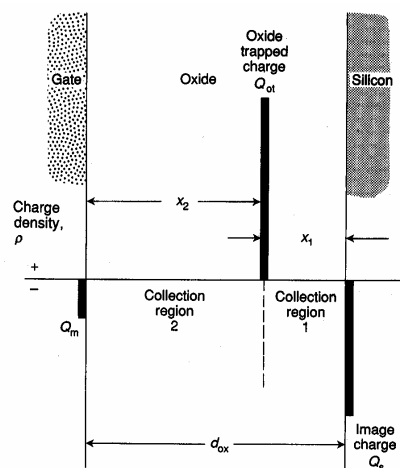


**Figure 3-12 – Simple charge sheet model: the very thin sheet of charge,  $Q_{ot}$ , is produced when holes generated in regions 1 or 2 are swept towards it by the applied field.  $Q_s$  is the image charge in the semiconductor, and determines the threshold voltage [Holmes-Siedle, 2006].**

By incrementing oxide and interface charge radiation-induced ionizing dose effects may cause a change in the oxide capacitance and as shown in equation 3-4 may affect the threshold voltage.

In an n-channel transistor, trapped holes induced by ionisation in the oxide layer have the same qualitative effect on the potential in the silicon as the positive gate bias. It bends the energy bands further downwards and tend to induce inversion in the p-type substrate. This effect leads to Noise Immunity Reduction (NIR). The charge near the interface will cause a small threshold shift. Given a sufficient trapped charge, inversion may be established by the trapped charge alone and a “leakage current” will flow in the channel even in the absence of a gate voltage which will cause  $V_T$  of n-channel to cross zero (VTNZ). In other words, simple trapped charge accumulation results in a parallel shift  $I_D$ - $V_G$  and in typical variation of the capacitance as well, dependent on the transistor material parameters of the insulator layer, as shown in figure 3-13 [Holmes-Siedle, 2006].

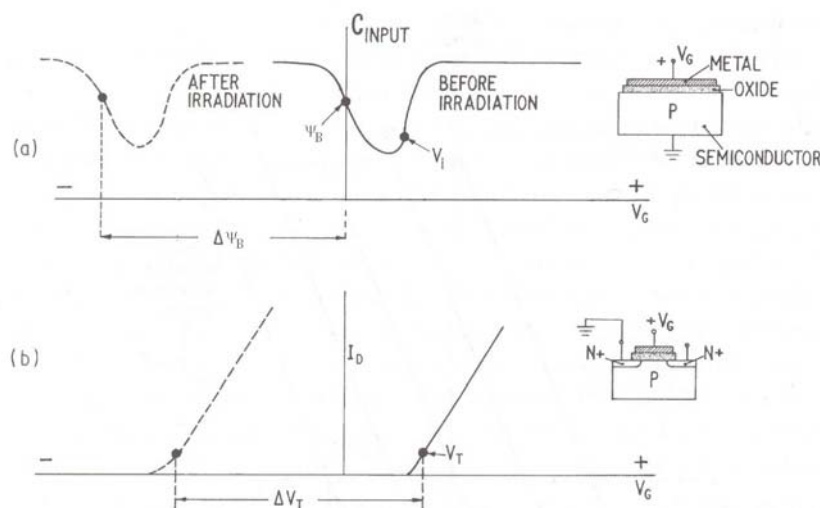


**Figure 3-13 – Typical variation of (a) CMOS characteristic capacitance curve and (b) drain current with gate voltage by effect of ionizing radiation [Holmes-Siedle, 2006].**

A p-channel transistor, as described before, requires a negative gate bias to make the channel conduct. The parallel shift in the  $I_D$ - $V_G$  characteristic caused by the trapped charge means that an increasing negative bias is needed to operate the device. At high radiation doses, it may therefore become impossible to switch the device “ON” [Holmes-Siedle, 2006]. Furthermore, the creation of interface states must always turn matters worse, as shown by the dotted line of figure 3-14.

Figure 3-14 a) and b) show a series of parallel curves of drain current,  $I_D$ , as a function of the gate voltage, for successively increased doses for n and p-channel MOSFETs [Holmes-Siedle, 2006].

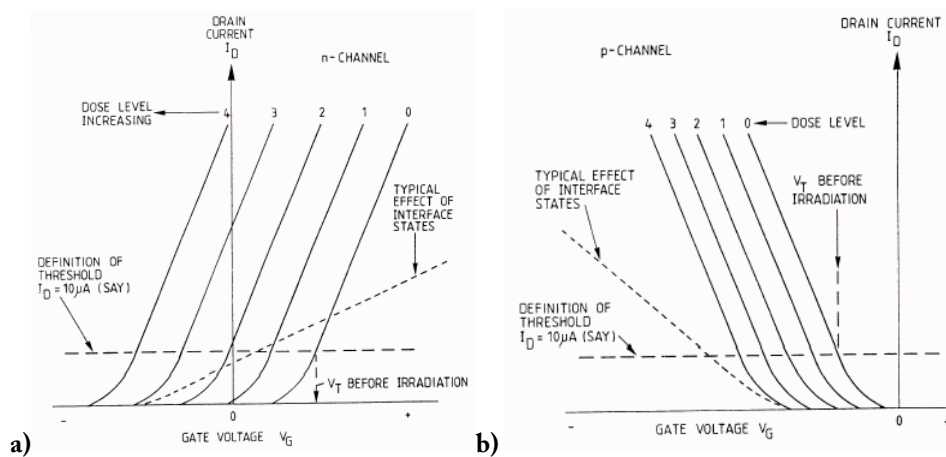


**Figure 3-14 – a) NMOS degradation and failure points; b) PMOS degradation and failure points [Holmes-Siedle, 2006]**

These typical  $I_D$ - $V_G$  curves illustrate an example given by Holmes-Siedle and Len Adams [Holmes-Siedle, 2006] for the progressive effect of increasing radiation dose. Curves 1 to 4 identify the typical threshold voltage shift correspondent to the applied dose and a consequent failure mechanism as described in Table 3-3 [Holmes-Siedle, 2006]:

Curve	Threshold Voltage Shift $-\Delta V_T$ [V]	Dose [KRad(Si)]	Main degradation Mechanism	Symbol
1	0.2	0.8	Noise immunity reduction	NIR
2	1	5	Sharp quiescent current increase due to $V_T$ of n-channel crossing zero (NMOS)	VTNZ
3	2	10	Switching speed reduction	SSR
4	4	30	Logic Failure	LF

**Table 3-3- Ionizing effects on MOS devices, due to long-term ionization of the oxide**

From the analysis of figure 3-14 and Table 3-3 it can be seen that for a threshold voltage shift of  $-4V$  the characteristic curve  $I_D$ - $V_G$  reaches saturation with  $V_G$  equal to zero. As previously discussed under subchapter 3.1, the n-channel of an enhancement NMOS device is closed for  $V_G$  negative or null. In conclusion this cumulative ionizing dose, *Total Ionizing Dose Effects*

(TID), by increasing oxide and interface traps induce a shift in the  $I_D-V_G$  that for high doses can turn the channel definitely off inducing a logical failure of the device.

### 3.2.2. Transients Mechanisms

#### 3.2.2.1. Physics of transient ionization

As discussed at the beginning of this chapter, transient ionization, phenomena decaying with time, occur in the semiconductor. When an incident ion crosses a device with energy higher than the  $e-h$  pair generation threshold in the target material (see table 3-1), *quasi-free electrons are ejected* with large energy and the *ion trajectory* remains approximately in a *straight line*. In analogy to what happens in a metal the ion track creates a transient  $e-h$  plasma. These hot electrons, *plasmons* [Musseau, 1994], generate an electron cascade until secondary electrons have lower energy than  $e-h$  pair generation threshold. Along the ion track the density of  $e-h$  pairs is proportional to the linear energy transfer ( $LET=1/\rho dE/dx$ ,  $\rho$  is the density of the target material). In the radial direction, the density is supposed to have a Gaussian variation from the core, where carriers' density can peak at  $10^{20} \text{cm}^{-3}$ , decaying to the local dopant concentration, as represented in figure 3-15 [Musseau, 1994].

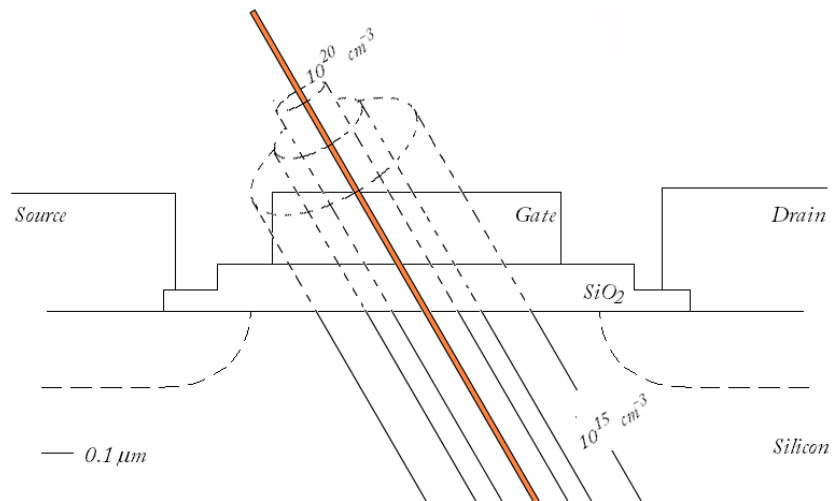


Figure 3-15- Graphical view of ion track creating an electron plasma in the semiconductor

Electron and holes may recombine. Those escaping recombination are later separated and transported by the electric field (drift) and by diffusion. The total carrier current is then given by equation 3-8.

$$J_i = \underbrace{qn_i m_i E}_{\text{drift}} + \underbrace{qD_i \nabla n_i}_{\text{Diffusion}} \quad i = e, h \quad (3-8)$$

The electrical field in standard devices, before irradiation, is limited to the depletion region. After an ion penetrates a pn-junction, the generated carriers drastically distort the junction field and it extends far down into the bulk silicon along the length of the ion track and funnels a large number of carriers into the junction [Hsieh, 1981]. This mechanism is known as *Funnelling*. Figure 3-16 shows the transient distortion of the electric field along the ion track according to results published by Hsieh et al. [Hsieh, 1981] due to alpha particles with 4.8MeV. The charge collected by drift in the funnelled field is called *prompt charge*. Prompt charge collection occurs in the 0.5ns immediately after ionization as illustrated in figure 3-17. If the track is long enough (10 $\mu$ m) excess charge generated beyond the *funnelling length* is left to be transported by diffusion [Hsieh, 1981]. Additionally figure 3-17 shows that the funnelling field is substrate concentration dependent.

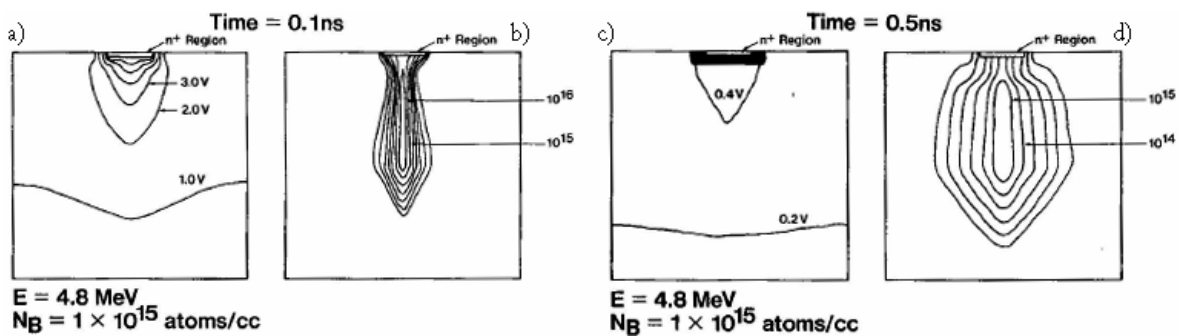


Figure 3-16 – Transient distortion of the electric field along the ion track from original depletion region: equipotential lines a) at 0.1ns after irradiation with counter interval of 0.1V, c) at 0.5ns with counter interval of 0.2V; electron concentration distributions b) at 0.1ns, d) at 0.5ns [Hsieh, 1981].

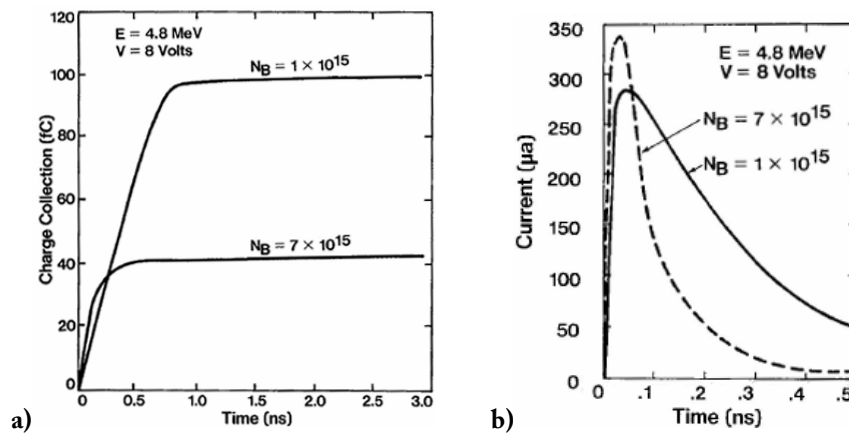


Figure 3-17- Time dependence of drift current: a) Prompt charge collection, b) Transient current [Hsieh, 1981]

Moreover in figure 3-18 and 3-19, it can be seen that the drift component increases with increasing resistivity and gate biasing. Combining these two effects one can conclude that the funnelling length is an inverse function of substrate concentration, while it increases with increasing bias voltage [Hsieh, 1981].

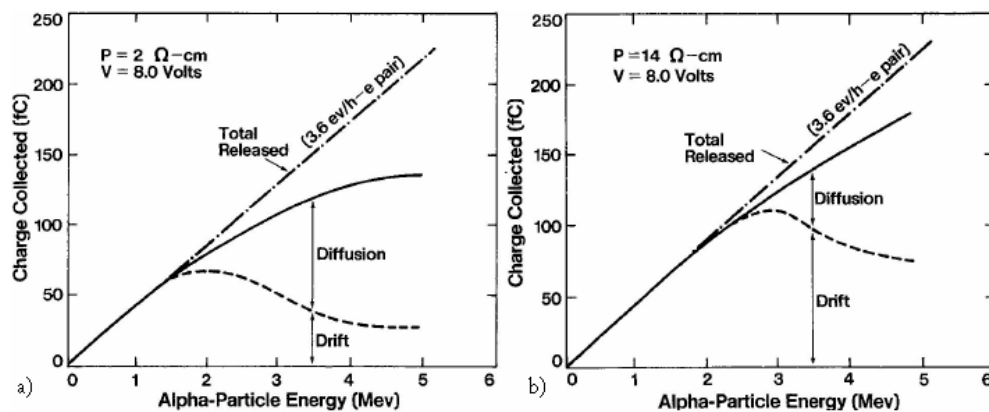


Figure 3-18 - Charge collected as a function of alpha particle energy for a substrate with a resistivity of a) 2 ohm-cm and b) 14 ohm-cm, with a bias voltage of 8.0 volts: (solid line) measurements shown for the total charge collected and (dotted line) for the drift component [Hsieh, 1981].

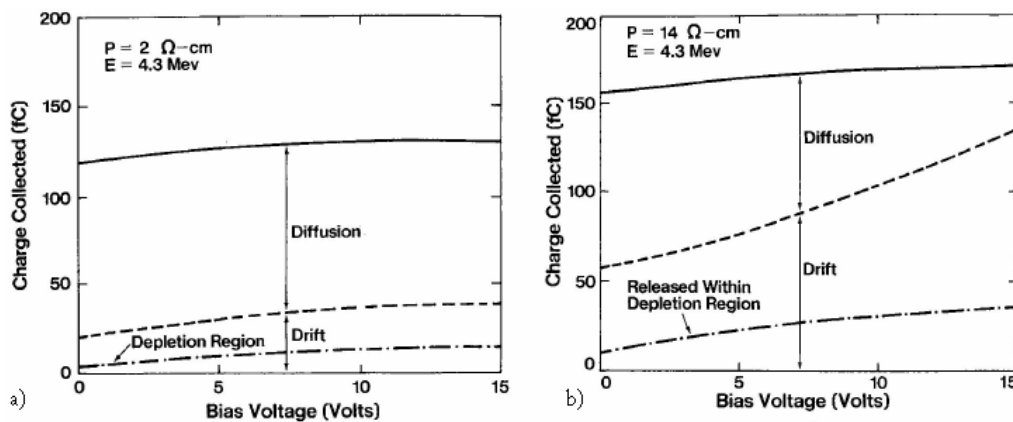


Figure 3-19 - Charge collected as a function of bias voltage for a substrate with a resistivity of (a) 2 ohm-cm and (b) 14 ohm-cm, with an alpha-particle energy of 4.3 MeV: (solid line) measurements shown for the total charge collected and for the drift component (dotted line); (dash-dot lines) are the calculated equivalent charge generated within the original depletion layer before the field distortion [Hsieh, 1981].

The theoretical description of funnelling results from non-linear coupling of Poisson's equation, current and continuity differential equations and there is no generic analytic solution for the problem. Many different semi-empirical models have been proposed to give a comprehensive picture of funnelling field effects in pn junctions [Ma, 1989]. In particular Hu [Hu, 1982] and

Edmonds [Edmonds, 1991] predict that the funnelling length,  $l_F$ , and funnelling charge collection,  $Q_F$ , could be derived from depletion length,  $l_D$ , and charge collected in the depletion region,  $Q_D$ , as given by equations 3-9 and 3-10.

$$l_F = \left(1 + \frac{\mu_n}{\mu_p}\right) \frac{l_D}{\cos \theta} \quad (3-9)$$

$$Q_F = \left(1 + \frac{\mu_n}{\mu_p}\right) Q_D \quad (3-10)$$

where  $\mu_n$  and  $\mu_p$  are the mobility of electrons and holes in the material and  $\theta$  is the angle of incidence. However carriers' mobility depend on substrate concentration and voltage bias therefore it is expected that equations 3-9 and 3-10 can be rewritten as

$$l_F(E) = \left(1 + \frac{\mu_n(E)}{\mu_p}\right) \frac{l_D(E)}{\cos \theta} \quad (3-11)$$

$$Q_F(E) = \left(1 + \frac{\mu_n(E)}{\mu_p}\right) Q_D(E) \quad (3-12)$$

In particular, for example, in silicon at a voltage biasing of  $1V/\mu m$ , electron mobility is of the order of 2.5 times higher than holes mobility [Grove, 1967], which means that  $l_F \approx 3.5 \cdot l_D / \cos \theta$  and  $Q_F = 3.5 \cdot Q_D$ .

This transient charge collection induced by a single ionizing particle may be able to create a state alteration in an integrated circuit. In that case we refer to this effect as a *Single Event Effect* (SEE).

#### 3.2.2.2. Approach to analysis

Whether a single event is able to upset a device depends mostly on the duration of the particle induced transient or pulse compared to device response time, noise margins of the electrical node and the total charge collected. The sensitivity of most complex devices can be estimated by measuring or predicting the sensitivity threshold (*critical charge*), sensitive area (*cross-section*) and the *sensitive volume*.

The sensitivity threshold is determined by the smallest perturbation (charge collection) that induces a detectable error on the output of the device. This sensitivity is called critical charge,  $Q_c$ , or when expressed in unit of energy is known as critical energy,  $E_c$ . It is given by the

integration of the energy transferred from the incoming ion to the target along its track,  $x$ , as expressed by equation 3-13 [Musseau, 1994]

$$E_c = \frac{E_{th} Q_c}{q} = \int_{x=0}^{x=l} \frac{dE}{dx} \eta_c(x) dx \quad (3-13)$$

By definition the charge is converted to energy simply by multiplying the number of e-h pairs generated by the ionization threshold. In equation 3-13,  $\eta_c(x)$  is the differential collection yield,  $\eta_c(x)$  is equal to 1 in case recombination is neglected and charge collection is just due to funnelling, for  $0 < l < l_F$ .

This means that an SEE may occur if the charge/energy deposited by the incoming particle and collected by the target device is greater than the sensitivity threshold. While heavy ions due to their high electronic stopping power can create a SEEs by *direct ionisation*, energetic protons (and clearly neutrons) mainly induce SEEs by means of secondary particles produced by nuclear reactions, *indirect ionisation*.

For this reason the capacity of a single event protons and neutrons to induce an upset (SEU), i.e., the SEU cross-section by protons and neutrons is a function of their capability to create recoils and consequently is a function of energy. While for ions to a first approach this is directly a function of their Linear Energy Transfer, LET [Keating, 2006]. The LET is then the measure of ionizing energy transferred by the ion to the material.

Therefore for ions it make sense to divide and multiply equation 3-13 by the density of the target material,  $\rho$ , and rewrite it as function of the critical energy transferred,  $LET_c$ , and the effective sensitive depth,  $l_{eff}$ :

$$E_c = \rho \int_{x=0}^{x=L} \frac{1}{\rho} \frac{dE}{dx} \eta_c(x) dx = \rho \cdot LET_c \cdot l_{eff} \quad (3-14)$$

The effective sensitive depth and the sensitive area define the *sensitive volume*,  $SV$ , which is the region of the target where charge collection may occur in time to upset the device. The sensitive volume shape is modulated by the shape of the depletion region and funnelling.

Concepts such as funnelling, sensitive volume and critical charge, are important elements of irradiation-induced charge collection mechanism possibly leading to device upset. However, experimentally, device sensitivity is given by the probability of a SEE to occur per unit surface, also known as SEE cross-section,  $\sigma$ . It is measured as the number of events recorded per unit

fluence, corrected by the incidence angle of the beam,  $\theta$ , with respect to the perpendicular to the chip, as given by equation 3-15.

$$\sigma [cm^2 / device] = \frac{\# events / device}{fluence [particle / cm^2] \cdot \cos \theta} \quad (3-15)$$

### 3.2.2.3. Single Event Effects in complex devices

Complex devices result from the assembly of a very large number of individual transistor or sets of transistors such as CMOS units. The minimum unit cell of the device is known as *bit*. In modern MOS microelectronic devices, information is stored as quantities of charge. This information can be stored in a single node, as in dynamic random access memories (DRAM), or in a subcircuit with a stable, latched state, as in static random access memory (SRAM).

SEEs manifest themselves in many different ways depending on the device type. Table 3-4 illustrates SEE types and effects. However this subsection only focuses on *Single Event Upset* (SEU) effect and principals required for understanding modelling concept.

ERROR	NAME		DESCRIPTION		EFFECT/CONDITIONS
Non Destructive	SEU	MBU	Single Event Upset	Multiple Bit	Corruption of the information stored in a memory cell
		SBU		Single Bit	
	SET	Transient		Impulse response for a certain duration and amplitude	
	SEFI	Functional Interruption		Loss of normal operation	
	SED	Disturb		Momentary of the information stored in a bit	
	SHE	Hard Error		Unalterable change of state in a memory element	
Destructive	SEL	Latch-up		High current conditions	
	SEB	Burnout		Destructive burnout	
	SESB	Snapback		High current conditions	
	SEGR	Gate	Rupture	Destructive rupture	
	SEDR	Dielectric			

**Table 3-4- Single event effects types and failure mechanisms (adapted from [Duzellier, 2003]).**

For SEUs the cross-section,  $\sigma$ , is usually expressed in units of  $cm^2/device$  or  $cm^2/bit$ . This cross-section depends on the characteristics of the incident particle and details of the sensitive

volume. In an ideal case the cross-section reaches saturation equal to the area of the irradiated bit, and all ions with LET higher than the critical LET will cause an upset. In real devices the process is mostly continuous and SEU cross-section increases with ions ionizing capability (LET) until it reaches the maximum sensitive area,  $\sigma_{\text{sat}}$ . This LET-dependent (energy-dependent in case of protons and neutrons) behaviour of SEU response on complex EEE devices can be expressed as function of the ion LET. While for protons and neutrons SEU response is a function of particle energy. This is also known as the device *SEE response function*.

Independently from the particle type, the SEE response function is believed to be represented by a smooth function. Therefore data are often presented in logarithmic scale so that discontinuities are obscured [Petersen, 1993]. As a consequence of the logarithmic representation SEE response data increase from the sensitivity threshold to saturation passing through a knee shaped region. It is also common to interpret the SEE response function as the distribution of cell sensitivities. Translated in units of area it is common to assume that a data point at 20% of the saturation cross-section indicates that 20% of the total sensitive area is irradiated and the saturation cross-section itself gives a measure of the total sensitive area of the device.

Figure 3-20 is extracted from literature [Xapsos, 1993] and illustrates SEU response function to heavy ion irradiation for different SRAM devices. It shows that different devices can have different sensitivities (with different sensitivity thresholds and saturation cross-sections). In the example it can be seen that the 93L422 bipolar SRAM [Nichols, 1988] having saturation cross-section of  $2.5 \times 10^{-5} \text{cm}^2/\text{bit}$  is much more vulnerable than the TCS130S CMOS/SOS SRAM [Kolasinski, 1982]. The second device does not show saturation up to  $120 \text{MeV}/(\text{mg}/\text{cm}^2)$ .

---

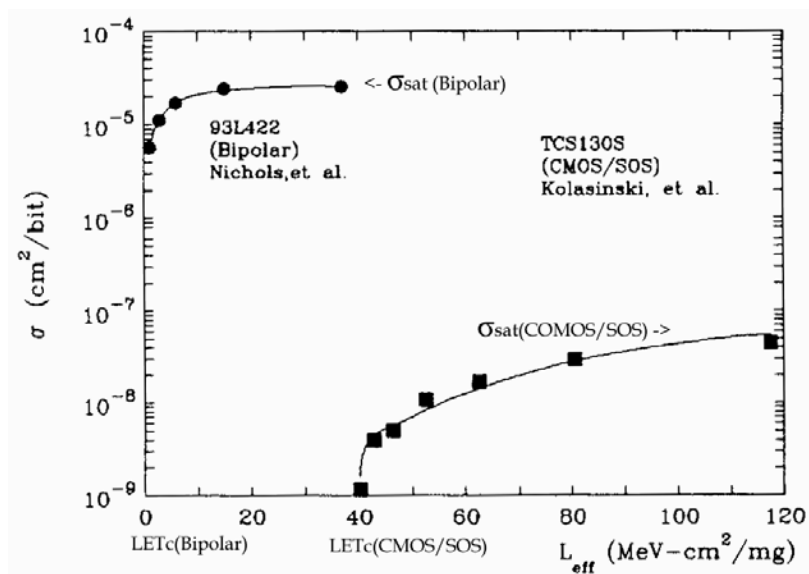


Figure 3-20 - SEE response function curves for different devices for ion irradiation test data: Cross-section as function of LET [Xapsos, 1993];

Figure 3-21 depicts three examples of SEU response function to proton ionization for different modern devices with submicron dimensions (KM41C4000Z-8, 62832H and IBM 01G9274) [Barak, 2001]. Cross-section curves are presented as function of proton energy. All three devices show a very similar critical energy, but very different saturation cross-sections.

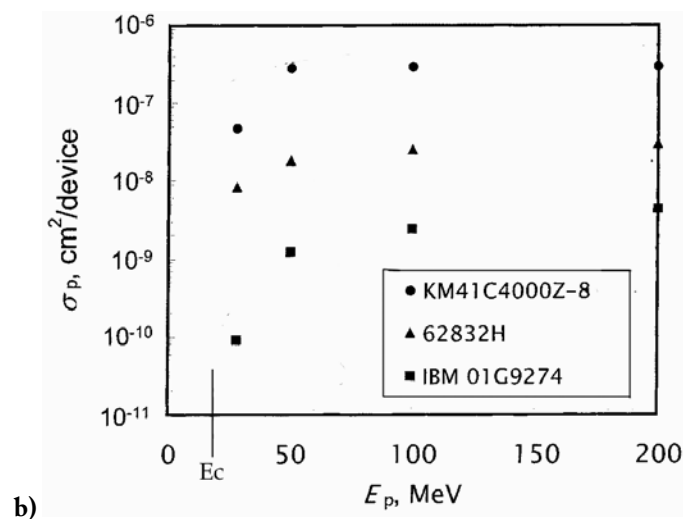


Figure 3-21 - SEE response function curves for different devices for proton irradiation test data: cross-section as function of proton energy [Barak, 2001].

### 3.2.3. *Displacement Damage Mechanisms*

Crystalline materials, such as silicon and gallium arsenide, ideally have a regular lattice structure. Energetic particles passing through matter by means of elastic and inelastic interaction can remove an atom from its lattice position, if the energy transferred is higher than the threshold energy for displacement. This disruption in the lattice structure, which in turn may alter the electrical properties of the device, is called *Displacement Damage* [Holmes-Siedle, 2006], [Holmes, 1962]. The space remaining from the displaced atom is called a *vacancy*. The resulting mobile atom is called an *interstitial*. The ejected atom (called the Primary Knock on Atom, PKA) may have enough energy to knock out a second atom creating a second vacancy. Depending on the energy of the primary particle a cascade of displaced atoms may occur. Vacancies and interstitials are mobile and may recombine or react with impurities in the bulk semiconductor creating stable defect centres. Stable defect centres may be electrically active and act as a source or traps of carriers, decreasing the mobility of mobile charge. As discussed in sections 3.1.4.2, 3.2.1 and 3.2.2, increasing the number of trapping centres either in the oxide, at the interface or in the bulk semiconductor, may lead to devices electrical parameter degradation or increase the sensitivity of the device to ionizing (long-term or transient) effects.

For a good approximation, assuming that those defects act independently and there are no co-operative or multi-level effects, displacement damage is proportional to the Non-Ionising Energy Losses (NIEL). NIEL is the measure of the non-ionising energy transferred to the struck nucleus [Holmes-Siedle, 2006]. The displacement damage depends on many variables such as: incoming particle species, radiation energy, semiconductor resistivity, device geometry, material properties such as oxygen-richness and phosphorous and boron doping, recombination parameters, biasing conditions applied, and nature of technology production (diffused or ion-implanted devices) [Musseau, 1994].

---

### 3.3. Degradation rate prediction

It is the goal of the final chapter to describe the principals for predicting EEE component degradation given a radiation environment as described in Chapter 2.

In general for all the described radiation-induced effects the degradation rate is dependent on the damage rate that is a function of the incoming particle energy or stopping power, angle of incidence and material; and on the radiation environment differential spectra,  $d\Phi/dE$ , as given in equation 3-16

$$\text{Degradation Rate} = \int_{\theta \text{ E min}}^{\theta \text{ E max}} \int_{E \text{ min}}^{E \text{ max}} \text{Damage}(E, \theta) \cdot \frac{d\Phi(E, \theta)}{dE} dE d\theta \quad (3-16)$$

The units of equation 3-16 are defined by both the environment spectrum (in units of  $\text{cm}^{-2} \cdot \text{s}^{-1}$  or  $\text{cm}^{-2}$ ) and the  $\text{Damage}(E, \theta)$  for each one of the three kinds of radiation induced effects: TID, DD and SEE.

In the case of TID effects, the degradation is measured by the threshold voltage shift that is a function of the cumulative ionizing dose,  $D$ , as discussed in section 3.2.1. Therefore the Degradation rate is the dose rate and the  $\text{Damage}(E, \theta)$  is the linear energy transferred, in units of  $\text{MeV}/(\text{mg}/\text{cm}^2)$ , and equation 3-16 comes in the form of

$$\dot{D} = 1.6 \times 10^{-8} \int_{\theta \text{ E min}}^{\theta \text{ E max}} \int_{E \text{ min}}^{E \text{ max}} \text{LET}(E, \theta) \cdot \frac{d\Phi(E, \theta)}{dE} dE d\theta \quad (3-17)$$

Table 3-5 indicates typical dose rates in units of rad/day, calculated in space [Holmes-Siedle, 2006].

Source	Dose rate
Galactic radiation	0.01 - 0.05rad/day
Radiation belts	Protons: 1 - 10rad/day [Behind 1cmAl] Electrons: $10^2$ - $10^3$ rad/day
Solar flares	12 - 350rad/event

Mean dose on Earth= 25 - 30rad/day

**Table 3-5– Radiation dose in space-laboratory-type orbits in free space (extracted from [Holmes-Siedle, 2006])**

As discussed in section 3.2.3 Displacement Damage (DD) is for a good approximation proportional to the Non-Ionising Energy Losses (NIEL), in units of MeV/(mg/cm<sup>2</sup>), therefore

$$Degradation\ Rate\ (DD) = \int_{\theta} \int_{E_{min}}^{E_{max}} NIEL(E, \theta) \cdot \frac{d\Phi(E, \theta)}{dE} dE d\theta \quad (3-18)$$

A detailed discussion of predicting DD degradation rate is beyond the scope of this chapter. However for the understanding of the general capabilities of the tool proposed and discussed in Chapter 5 it is important to verify that the prediction of degradation rate follows the same structure for all the different mechanisms.

As previously discussed an SEE may occur if the charge deposited by the incoming particle and collected at a sensitive node is greater than charge threshold to create an SEE. In general SEE rate are presented in number of events per unit of time.

The probability of an event being caused by an ion is measured by the SEE cross-section,  $\sigma$  [in units of cm<sup>2</sup>/bit or cm<sup>2</sup>/device], and is a direct function of its ionization capability, LET. The degradation rate is the SEE rate,  $N$ . It is given by the integration over the path length and LET ranges of the SEE cross-section convoluted by the path length distribution,  $P(l)$ , and the differential fluence as function of the LET as illustrated in equation 3-19 [ECSS-E-HB-10-12]

$$N_{ions} = \int_{E_c / LET_{max}}^{l_{max}} P(l) \int_{E_c / l}^{LET_{max}} \sigma_{ion}(LET) \cdot \frac{d\Phi}{d(LET)} \cdot d(LET) \cdot dl \quad (3-19)$$

In the ideal case of, as previously described, the cross-section is  $\sigma_{sat}$  above the threshold and 0 below the critical LET and the SEE rate is then given by:

$$N_{ions} = \frac{\sigma_{sat}}{4} \int_{E_c / LET_{max}}^{l_{max}} P(l) \int_{E_c / l}^{LET_{max}} \frac{d\Phi}{d(LET)} \cdot d(LET) \cdot dl \quad (3-20)$$

In case LET is considered in units of deposited charge,  $Q$ , equation 3-19 comes in the form of equation 3-21 [Keating, 2006].

$$N_{ions} = \int_{Q_{min}}^{Q_{max}} \sigma_{ion}(Q) \cdot \frac{d\Phi}{d(Q)} \cdot d(Q) \quad (3-21)$$

On the other hand, for protons and neutrons the SEE rate is a function of their capability to create recoils and consequently is a function of their energy [Keating, 2006], as given in equation 3-22.

$$N_{\substack{\text{protons} \\ \text{neutrons}}} = \int_{E_{\min}}^{E_{\max}} \sigma_p(E) \cdot \frac{d\Phi}{dE}(E) \cdot dE \quad (3-22)$$

Discussions in Chapter 5 will mainly refer to SEU rate predictions based on equations 3-21 and 3-22.

### 3.4. Conclusions

In summary when radiation crosses a complex device, induced effects may occur at different levels in the different regions. Effects may involve *ionization* or *displacement* processes according to the mass, energy and charge of the incoming particles. Degradation induced by displacement damage is, for a good approximation, proportional to NIEL. DD may in certain conditions increase the sensitivity of the device to ionizing (long-term or transient) effects. Depending on the material properties such as carrier mobility and conductivity, metals, insulators and semiconductors handle radiation induced charge differently. In the metal the mobility of carriers is so high, around  $10^5 \text{m}^2 \text{V}^{-1} \text{s}^{-1}$ , that we may assume instantaneous return to equilibrium. In MOS technology electrons and holes generated in the oxide behave differently due to their different carrier mobility, leading to an asymmetric accumulation of positive charge inducing a threshold voltage shift. This effect is proportional to the total energy loss in the oxide. While in the semiconductor, where the mobility of both type carriers are of the order of  $10^{-1}$  to  $1 \text{m}^2 \text{V}^{-1} \text{s}^{-1}$ , charged particles can create transient ionization-induced currents that will tend to return to equilibrium in a few nanoseconds. In complex devices information is stored as quantities of charge. The collected charge induced, if higher than the threshold may create a state alteration in an integrated circuit.

Finally given a specific radiation environment the degradation rate induced by each one of the described effects may be calculated by the integration of the damage over the environment. Degradation rate is then a function of the incoming particle energy or stopping power, angle of incidence and material and on the radiation environment differential spectra.



## 4. Mars Radiation Environment Characterization

This chapter describes the simulation framework developed in order to predict radiation Environment at the surface of Mars due to GCR and SEP proton as well as the expected neutron albedo induced radiation environment on Mars.

Subchapter 4.1 describes the Simulation Architecture. In subchapter 4.2 two implementations of the simulation are presented. Subchapter 4.3 gives a brief description of GEANT4 in the context of the simulation of Mars Radiation Environment. Subchapter 4.4 refers to the atmosphere and soil databases and correspondent interfaces with GEANT4 application. In subchapter 4.5 Martian radiation environment considering a fixed soil composition for different locations on Mars is discussed. Subchapter 4.6 examines the dependency with the season of the year and time of the day. Subchapter 4.7 describes the method used to compute ambient dose equivalents using FLUKA conversion factors and compares surface values with MARIE predictions. Subchapter 4.8 shows results of the comparison of MarsREC results with other software and experimental results. Subchapter 4.9 explores the radiation environment dependence on soil composition and density. Finally on section 4.10 considerations about radiation damage and inhabitability are discussed.

### *4.1. Simulation Architecture*

As cosmic or solar particles enter in the Martian upper atmosphere they may undergo nuclear reactions resulting in the emission of electrons, neutrons and other subatomic particles. Progressing further into the atmosphere, the increased density increases energy loss of the protons and increases such secondary particles production, as introduced in Chapter 2. Mars's geology also plays a very important role in the radiation environment characterization. The Martian atmosphere, being very low density (maximum values of the order of  $10^{-2}$  kgm<sup>-3</sup>), behaves as a soft attenuator for incoming radiation capable of reaching the Martian surface. This results in an important contribution from secondary particles generated at and backscattered from the surface [Keating, 2005].

The important drivers for proper Martian radiation environment modelling are: atmosphere, local geology and topology as well as their temporal variations. The simulation architecture is

---

represented in figure 4-1. Basically it consists of interfacing atmospheric and soil descriptions with the developed GEANT4 application enabling the tracking of primary and secondary particles produced both in the atmosphere and soil. The models output: radiation maps, doses, radiological doses, article species history, fluences and spectra.

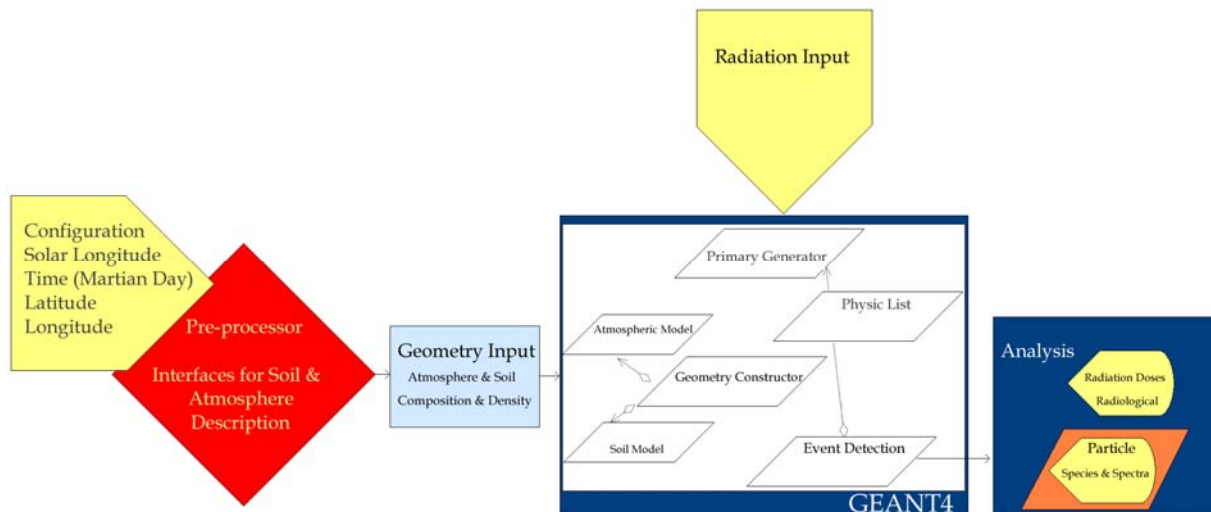


**Figure 4-1 – Simulation architecture**

The following sections describe the tools and databases used in the developed framework. Beginning with a brief description of GEANT4 Monte Carlo particle transport toolkit in the context of the simulation of Mars Radiation Environment and the main GEANT4 physics models used for the results presented in this thesis. Later an overview of the atmospheric and soil databases is given. Finally the developed interfaces are presented.

## 4.2. *GEANT4 toolkit*

GEANT4 is a new-generation open source simulation toolkit for particle transport and interaction through matter across a wide energy range from a few eV to PeV and to thermal energies for neutrons [GEANT4, 2008], [Agostinelli, 2003], [Allison, 2006]. Primarily a toolkit designed to simulate High Energy Physics experiments. In the past years a large effort from the GEANT4 collaboration and users has been done in order to adapt and develop GEANT4 application for space related issues [Keating, 2005], [Keating, 2008], [Allison, 2006], [REAT], [DESIRE], [SEPTIMESS], [GEANT4\_SUH], [Santin, 2005].

This section is based on information from [GEANT4, 2008], [Agostinelli, 2003], [Allison, 2006], [G4Phys, 2008], [G4PMan, 2008].

### 4.2.1. *General properties*

GEANT4 being a Monte Carlo tool is able to track each particle entering the simulation, from its generation point to the moment it is killed or leaves the geometry. The solution for the particle energy, momentum and position is given by using appropriate physic cross-sections and random numbers. The *step* is the minimum distance crossed by a particle in the medium before an interaction occurs. Some physical processes, such as ionization, are assumed to be *continuous* because they continuously modify the particle energy and cross-section during a step.

GEANT4 follows an Object-Oriented design which allows for the development of flexible simulation applications. GEANT4 includes an extensive set of electromagnetic, hadronic and optics physics processes and tracking capabilities in 3D geometries of arbitrary complexity and materials and to define “sensitive” elements where the particle information is recorded (hits).

Design requirements of GEANT4 are that it is modular and flexible and that its implementation of physics is transparent and open to user validation.

### 4.2.2. *Physics models*

The physics configuration, called physics list, of a user application is done in C++ code. In the physics list processes can be assigned to particles and models to processes [G4Phys, 2008]. There are different models for different physics categories. The electromagnetic physics

---

category covers the energy range from 250 eV to 10 TeV (up to 1000 PeV for muons). The optical physics process category allows the simulation of scintillation, Cherenkov or transition radiation based detectors. In the particular case hadronic physics there are also different models available span over 15 orders of magnitude in energy, starting from neutron thermal energies. Therefore the user shall choose according to model validity for the required energy range. Tore Ersmark aiming at simulating the International Space Station Radiation Environment has extensively tested different hadronic physics lists [Ersmark, 2006] and validated them for space radiation shielding applications.

In the physics list used for the Martian radiation environment characterization electromagnetic interactions have been treated by the “Standard” electromagnetic model, and hadronic physics has been treated by employing the Low and High Energy Parametrized models (LHEP), Binary Cascade Model (BIC) [Folger, 2004], low energy neutron physics and ion physics.

Simulations have been performed with different versions of GEANT4. MarsREC simulations used GEANT4.7.0, while dMEREM of MARSREM was designed to run with GEANT4.8.2, GEANT4.8.3 and GEANT4.9.1.

*a. Electromagnetic interaction model*

The Standard GEANT4 electromagnetic physics processes, described in [G4Phys, 2008] and [Agostinelli, 2003], provides a variety of implementations of electron, positron, photon and charged hadron interactions.

Electron/positron processes handle bremsstrahlung, ionisation and  $\delta$ -ray production, positron annihilation and synchrotron radiation. Photon processes include Compton scattering,  $\gamma$ -conversion into electron and muon pairs and the photo-electric effect. The energy loss process manages the continuous energy loss of particles due to ionisation and bremsstrahlung. A significant feature of this is an algorithm which can generate low energy  $\delta$ -rays only near the boundaries of volumes, which can lead to an improved performance while keeping the quality of physics. The ionisation and energy loss of hadrons has several models to choose from, including photo-absorption interaction. The GEANT4 multiple scattering process can handle all charged particles. It is based on a new model that simulates the scattering of the particle after a step, computes the mean path length correction and the mean lateral

---

displacement. Standard electromagnetic processes average the effects of the shell structure of atoms and cannot be expected to simulate details below 1 keV.

*b. LHEP Parameterized Driven Models*

The LHEP Physics lists are based on a parameterized modelling for all hadronic interactions for all particles. The parametrised model is an improved version of the Gheisha model. These lists combine the high energy parameterised (HEP), from 10-20GeV up to 10TeV, and low energy parameterised (LEP), up to 25 GeV, models describing inelastic interactions for all hadrons. The modelling of elastic scattering off a nucleus and of capture of negative stopped particles and neutrons are processed via parameterised models. Cross-sections used are based on Gheisha parameterisations [G4Phys, 2008].

*c. Binary cascade*

The GEANT4 Binary Cascade is an intranuclear cascade propagating primary and secondary particles in a nucleus. Interactions are between a primary or secondary particle and an individual nucleon of the nucleus, leading to the name Binary Cascade. Cross-section data are used to select collisions. Binary cascade models handle hadronic interactions in the energy range of 10MeV to a few GeV. Experimental cross-sections, when available, are used by the simulation. Propagating of particles in the nuclear field is done by numerically solving the equation of motion. The cascade terminates when the average and maximum energy of secondaries is below threshold for further interactions. The low energy coverage of the model is provided by the implementation of precompound model. The remaining fragment is then treated by precompound and de-excitation models documented in [G4PMan, 2008].

*d. Low Energy neutrons*

In GEANT4 the neutron transport class library provides data-driven description neutrons with kinetic energies from thermal energies up to 20MeV. The interactions of neutrons at low energies are split into four parts in analogy to the other hadronic processes in GEANT4: Radiative capture, elastic scattering, fission, and inelastic scattering as separate models. Parameterized models are used instead of data driven high-precision models in case information on a specific element is not available [G4PMan, 2008].

Neutron High Precision Models of GEANT4 use a thermal treatment based on the free gas approximation. However, in molecules and crystalline solids, atomic translational motion as

---

well as vibration and rotation of the bound atoms also significantly affect the cross-sections and final states. Data files were prepared and data-driven models included into GEANT4 to account for vibration and rotation of the bound atoms [Koi, 2006].

*e. Ion Physics*

Big improvements have been done to ion physics in the latest versions of GEANT4. MarsREC developments were done employing GEANT4.7. At the time GEANT4 ion physics was able to treat Elastic and inelastic processes as well as ionization and multiple scattering only light ions such as Deuteron, Triton, Alpha and He3. After version 4.8 GEANT4 enables the use of data-driven models based on ion cross-sections for heavier ions. Improvements are still needed to the generic treatment of ion physics however efforts are being done in that direction.

*f. Interfaces with external codes*

There are also many well-established reaction codes currently used in the same fields where GEANT4 is applied. In order to take advantage of these codes, the GEANT4 collaboration has created interfaces with those codes. The first codes chosen were the Jaeri Quantum Molecular Dynamics (JQMD) and Jet AA Microscopic Transport action Model (JAM) codes. JQMD is a QMD model code which is widely used to analyze various aspects of heavy ion reactions. JAM is a hadronic cascade model code which explicitly treats all established hadronic states, including resonances with explicit spin and isospin, as well as their anti-particles [Koi, 2003].

Lately an interface between the DPMJET II.5 [Ranft, 2008] dual parton model and the GEANT4 has been developed [Truscott, 2008]. This provides the ability to simulate at the microscopic level nuclear-nuclear interactions from 5GeV/nuc to 1PeV/nuc. The European Space Agency, which has sponsored the development of this interface, intends to apply these new models to assess the radiation environment experienced by flight crews and systems for future interplanetary missions. DPMJET-II.5 is freely available from the website of one of the authors at the University of Siegen [Ranft, 2008].

In the implementation of DPMJET-II.5 into GEANT4, the FORTRAN code is used to treat only the fast interaction of the collision. The subsequent de-excitation of the nuclear pre-fragments from the projectile and target can be treated using a G4VPreCompoundModel

---

or G4DeexcitationHandler type, depending upon the user. By default, if the user does not specify any model or specifically requests that no de-excitation physics be applied, the same precompound model used by G4BinaryCascade is applied.

### *4.3. Mars Radiation Environment: two implementations*

As discussed in Chapter 2 the quantitative description of the radiation environment of Mars in terms of particle species and energy spectra relies on the careful modelling of: a) atmosphere climatic variables (pressure, temperature, density, composition, dust storms); b) local geology/topology; c) distance from the Sun and d) any local magnetosphere [Deshorger, 2008].

Initially in the context of MarsREC, an ESA project with LIP from 2004 to 2006, a methodology and computational framework based on a GEANT4 application for simulation of the radiation environment at the surface of Mars was developed, including interfaces with GEANT4, the European Martian Climate Database (MCD) [Jussier, 2008] and the Mars Orbiter laser altimeter (MOLA) [Abshire, 1999] database. At a different stage this tool was improved and detailed in order to allow the prediction of the radiation environment at the surface of Mars and moons and create radiation profiles at different altitudes in the atmosphere of Mars. These last developments were performed under an ESA project with a consortium with four international institutes/companies, in which LIP was responsible for the physical environment description and specifications and the development of the detailed GEANT4 modelling of Mars radiation Environment, dMEREM (detailed Mars Energetic Radiation Environment Model).

The differences between MarsREC and dMEREM are clearly discussed in the following subsections.

#### *4.3.1. MarsREC*

MarsREC is an integrated simulation tool for Mars Radiation Environment and Radiation induced Effect in EEE Components. It aims at predicting the radiation environment and its effect on EEE components in missions to Mars according to the landing locations, time and season of the Martian year. MarsREC consists of two Modules: the Radiation Environment Characterization Module already presented in the literature [Keating, 2005], and the

---

Radiation Effects Module. These modules are integrated in a framework where GEANT4 is used to describe the geometry and the physics of interaction between particles and matter. The physics includes hadronic and ion physics models enabling accurate energy deposition calculations, sensitive volume definition and tracking of particles such as protons, ions and neutrons.

The Radiation Effects Module and results will be described in detail in Chapter 5. In the current chapter MarsREC architecture will be described and results obtained with Radiation Environment Characterization Module will be discussed.

MarsREC features include input solar cycle modulated cosmic ray and solar particle event spectra, based both on CREME-96, the transport of this radiation in the Martian atmosphere and regolith, including creation of secondaries, using the GEANT4 Monte-Carlo toolkit. Details of the atmosphere are derived from the European Mars Climate Database with a dense topological grid and layering of the atmosphere. Seasonal and diurnal variations are considered. Surface topology is derived from the Mars Orbiter laser altimeter (MOLA). The outputs are full particle transport histories, maps of radiation fluxes and doses. Post-processing analysis enabled the evaluation of the variability of the Martian radiation environment with time. MarsREC was developed to work with GEANT4 version 7.

#### 4.3.2. *dMEREM*

dMEREM was developed with the objective of integrating an engineering user friendly tool with web-interface under SPENVIS [Heynderickx, 2004]. The software aims at providing full detailed simulation in the GEANT4 radiation transport toolkit for Mars mapping and Moons Surface Radiation Environment. It is intended to be used with GEANT4 v8.2 or later. The main differences between dMEREM and MarsREC consisted in the fact dMEREM is designed to:

- a. Be interfaced with Mars Climate Database version 4.2 or later [MCD, 2008] instead of version 3.0, enabling the use of different atmospheric compositions in altitude, location at the surface and time;
  - b. Be interfaced with a developed tool to define soil composition and density for different locations at the surface of Mars and time, based on Gamma Ray Spectrometer (GRS) and MCD databases;
-

- c. Use magnetic field class developed by Laurent Desorgher for Planetocosmics;
- d. Be user friendly and openly accessible via SPENVIS web-page.

The interface of dMEREM with physical environment description is done by a developed pre-processor. The pre-processor is a Python tool developed to specify the atmospheric and surface specifications for Mars and Moons geology description. It extracts data from MCD, MOLA and the GRS [GRS, 2006] on board of Mars Odyssey. It outputs the soil and atmosphere descriptions in the format of ASCII tables. These tables are read into dMEREM and integrated into GEANT4 by two specific classes the dMEREMAtmosphericModel and dMEREMSoil Model.

#### ***4.4. Databases and interfaces***

##### *4.4.1. Mars Climate Database*

The European Mars Climate Database contains data on temperature, wind, density, pressure, radiative heat fluxes, and other parameters, resulting from global circulation model simulations. Two different versions of MCD were used in the current work. MarsREC was interfaced with MCD V3.0 while dMEREM was interfaced with MCD 4.2 and later. Main differences consist of: grid map resolution, atmospheric composition dependence on altitude, location and time of the day and season of the year (in the latest versions).

Fields are averaged and stored 12 times a day, for 12 Martian “seasons” to give a comprehensive representation of the annual and diurnal cycles. Each season covers 30° in solar longitude ( $L_s$ ), and is typically 50-70 days long, as illustrated in figure 4-2 and table 4-1. In other words, at every grid-point, the database contains 12 “typical” days, one for each season. In addition, information on the variability of the data within one season or within one grid-point are also stored in the database.

For each Season, fields (wind, temperature, pressure...) are averaged and stored 12 times a day (at 0:00, 2:00, 4:00... 22:00). This time is given in Mars Universal Time, the local time at longitude 0.

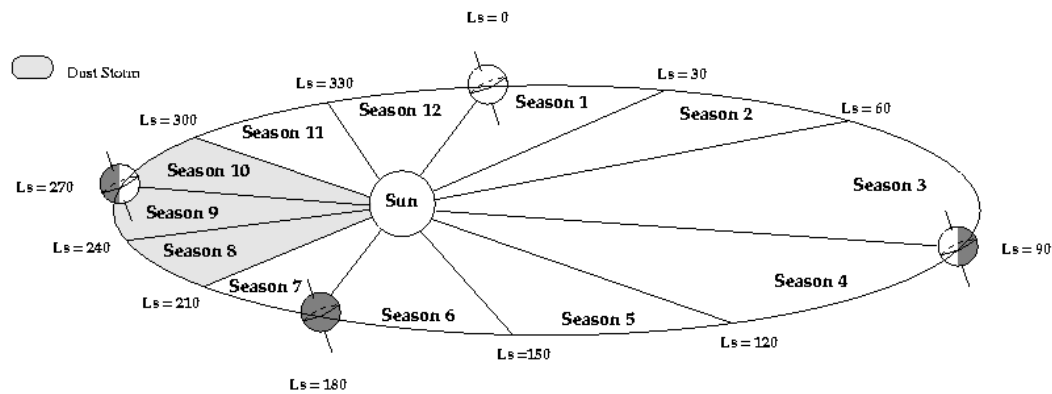


Figure 4-2– Scheme of the twelve seasons of Mars [Forget, 2001]

Solar Longitude	Season	Mars solar days	from day - to day	
Ls = 0 - 30	Season 1	61	0 - 61	
Ls = 30 - 60	Season 2	66	61 - 127	
Ls = 60 - 90	Season 3	66	127 - 193	
Ls = 90 - 120	Season 4	65	193 - 258	
Ls = 120 - 150	Season 5	60	258 - 318	
Ls = 150 - 180	Season 6	54	318 - 372	
Ls = 180 - 210	Season 7	50	372 - 422	
Ls = 210 - 240	Season 8	46	422 - 468	Dust Storm
Ls = 240 - 270	Season 9	47	468 - 515	Dust Storm
Ls = 270 - 300	Season 10	47	515 - 562	Dust Storm
Ls = 300 - 330	Season 11	51	562 - 613	
Ls = 330 - 360	Season 12	56	613 - 669	

Table 4-1- Relationship between seasons and time [Forget, 2001]

Various dust annual scenarios are provided by MCD, corresponding to different datasets which can be selected. MCD version 3.0 allows the use of a maximum of 5 scenarios and MCD version 4.2 uses 4 dust scenarios. In both versions MCD provides an advised dust scenario that includes dust variations along the Martian year modelled according Mars Global Surveyor data between 1999 to June 2001. The dust fields were derived from MGS TES observations using data assimilation technique [Forget, 2001].

Additionally different combination of solar scenarios with dust scenarios are possible, however all the simulations described later in this chapter were performed using the advised dust scenario with the average solar flux scenario.

#### 4.4.1.1. MCD Version 3.0

MCD 3.0 [Forget, 2001] contains simulated data (temperature, wind, density, pressure, radiative fluxes, etc. as shown in the table 4-2) stored on a 5°x5°, longitude-latitude grid from the surface up to an approximate altitude of 120km (above 120 km, pressure and density can be estimated using the database access software).

Mean variable	units	2-D or 3-D
Atmospheric temperature	K	3-D
Zonal (East-West) wind	m s <sup>-1</sup>	3-D
Meridional (North-South) wind	m s <sup>-1</sup>	3-D
Atmospheric density	kg m <sup>-3</sup>	3-D
Boundary layer eddy kinetic energy	m <sup>2</sup> s <sup>-2</sup>	3-D
Surface pressure	Pa	2-D
Surface temperature	K	2-D
LW (thermal IR) radiative flux to surface	W m <sup>-2</sup>	2-D
SW (solar) radiative flux to surface	W m <sup>-2</sup>	2-D
LW (thermal IR) radiative flux to space	W m <sup>-2</sup>	2-D
SW (solar) radiative flux to space	W m <sup>-2</sup>	2-D
CO <sub>2</sub> ice cover	kg m <sup>-2</sup>	2-D
Surface emissivity	none	2-D

**Table 4-2- Variables stored in MCD 3.0 mean data files [Forget, 2001]**

Altitudes are defined with respect to local topological elevations. The vertical coordinate for the 3D spatial variables is defined as  $\sigma = p/p_0$ , where  $p$  is the atmospheric pressure and  $p_0$  is the local surface pressure, also stored in the database. Thus  $\sigma$  is 1 at the surface and 0 at infinity and the  $\sigma$  levels follow the model topography. There are 32  $\sigma$  levels from 5m up to around 120km delineating atmospheric layers.

The altitude of each layer can be computed by integrating the hydrostatic balance equation:

$$g \cdot dz = -RT \cdot d(\ln p) \quad (4-1)$$

and considering a constant temperature inside each layer:

$$z_t - z_b = -\frac{RT}{g} \ln\left(\frac{p_b}{p_t}\right) \quad (4-2)$$

where  $z_b$  is the altitude of the bottom of the layer,  $z_t$  is the altitude of the top of the layer (similarly  $p_b$  and  $p_t$ , refer to the pressure at the bottom and top of a layer),  $g=3.7 \text{ m s}^{-2}$  is the

Martian gravitational acceleration and  $R=191 \text{ J K}^{-1} \text{ Kg}^{-1}$  is the Martian gas constant [Andrews, 2000].

Wind, temperature, pressure and other fields are averaged and stored for 12 Martian Universal Times at longitude  $0^\circ$ , for 12 Martian “seasons” to give a comprehensive representation of the annual and diurnal cycles. Each season covers  $30^\circ$  in solar longitude ( $L_s$ ), and is typically 50-70 Martian days. Information on the variability of the data within one season or within one grid-point is also stored in the database.

An interface, called MACLIDIV1.0, has been built in order to read MCD data as input for the GEANT4 simulation Geometry Construction class, for each location, time and solar longitude. Table 4-3 exemplifies the input atmospheric table for a solar longitude 180-210, at 12:00 hours (Martian longitude  $0^\circ$ ), at location (80E, 7.5S) where the surface elevation is 1.746 km.

MCD V3.0 doesn't provide an atmospheric composition. Therefore in MarsREC implementation the atmospheric composition was considered as suggested by [Boyce, 2002] as a combination of:  $\text{CO}_2$ ,  $\text{N}_2$ , Ar,  $\text{O}_2$ , CO and  $\text{H}_2\text{O}$ .

---

Atmospheric Altitude (Km)	Atmospheric Density (Kg/m <sup>3</sup> )	Atmospheric Temperature (K)	Atmospheric Pressure (Pascal)
0.01	9.47 x10 <sup>-3</sup>	250.1	4.53 x10 <sup>2</sup>
0.03	9.46 x10 <sup>-3</sup>	250.1	4.52 x10 <sup>2</sup>
0.07	9.44 x10 <sup>-3</sup>	249.9	4.51 x10 <sup>2</sup>
0.14	9.39 x10 <sup>-3</sup>	249.6	4.48 x10 <sup>2</sup>
0.30	9.31 x10 <sup>-3</sup>	248.9	4.43 x10 <sup>2</sup>
0.59	9.14 x10 <sup>-3</sup>	247.5	4.33 x10 <sup>2</sup>
1.16	8.84 x10 <sup>-3</sup>	245.0	4.14 x10 <sup>2</sup>
2.20	8.29 x10 <sup>-3</sup>	240.3	3.81 x10 <sup>2</sup>
3.96	7.41 x10 <sup>-3</sup>	232.3	3.29 x10 <sup>2</sup>
6.65	6.18 x10 <sup>-3</sup>	220.5	2.60 x10 <sup>2</sup>
10.37	4.63 x10 <sup>-3</sup>	208.4	1.85 x10 <sup>2</sup>
15.01	3.12 x10 <sup>-3</sup>	197.0	1.17 x10 <sup>2</sup>
20.33	1.90 x10 <sup>-3</sup>	187.5	6.80 x10 <sup>1</sup>
25.94	1.09 x10 <sup>-3</sup>	177.2	3.70 x10 <sup>1</sup>
31.72	5.90 x10 <sup>-4</sup>	171.2	1.93 x10 <sup>1</sup>
37.61	3.06 x10 <sup>-4</sup>	169.0	9.88 x10 <sup>0</sup>
43.58	1.55 x10 <sup>-4</sup>	168.2	4.99 x10 <sup>0</sup>
49.63	7.75 x10 <sup>-5</sup>	169.0	2.51 x10 <sup>0</sup>
55.56	3.98 x10 <sup>-5</sup>	164.9	1.25 x10 <sup>0</sup>
61.35	2.04 x10 <sup>-5</sup>	160.6	6.27 x10 <sup>-1</sup>
67.25	1.00 x10 <sup>-5</sup>	163.5	3.13 x10 <sup>-1</sup>
72.96	5.17 x10 <sup>-6</sup>	158.4	1.56 x10 <sup>-1</sup>
78.41	2.71 x10 <sup>-6</sup>	150.8	7.80 x10 <sup>-2</sup>
83.76	1.38 x10 <sup>-6</sup>	148.1	3.90 x10 <sup>-2</sup>
89.18	6.80 x10 <sup>-7</sup>	150.2	1.94 x10 <sup>-2</sup>
94.45	3.49 x10 <sup>-7</sup>	146.0	9.71 x10 <sup>-3</sup>
99.54	1.80 x10 <sup>-7</sup>	140.9	4.84 x10 <sup>-3</sup>
104.44	9.34 x10 <sup>-8</sup>	135.7	2.42 x10 <sup>-3</sup>
109.05	4.96 x10 <sup>-8</sup>	127.5	1.21 x10 <sup>-3</sup>
113.29	2.69 x10 <sup>-8</sup>	117.4	6.02 x10 <sup>-4</sup>
117.02	1.52 x10 <sup>-8</sup>	103.4	3.01 x10 <sup>-4</sup>
121.97	6.06 x10 <sup>-9</sup>	86.6	1.00 x10 <sup>-4</sup>

Table 4-3– MACLIDiv1.0 Atmospheric Table Input to MarsREC

#### 4.4.1.2. MCD Version 4.2 and latest

The latest versions of MCD calculate and store atmospheric properties stored on a  $5.675^\circ \times 3.75^\circ$ , longitude-latitude grid from the surface up to an approximate altitude of 150km. The 3D spatial coordinate is no longer defined by the sigma levels being directly defined by the elevation above local surface. Additionally it includes atmospheric composition as a 3D variable. MACLIDI was improved in order to be able to read atmospheric composition and additional soil information such as surface pressure, temperature and dry-ice layer. Finally the surface altitude is also extracted from the MOLA files by MACLIDI.v.3.0.

Figure 4-3 shows the data organization on MACLIDI.v.3.0.

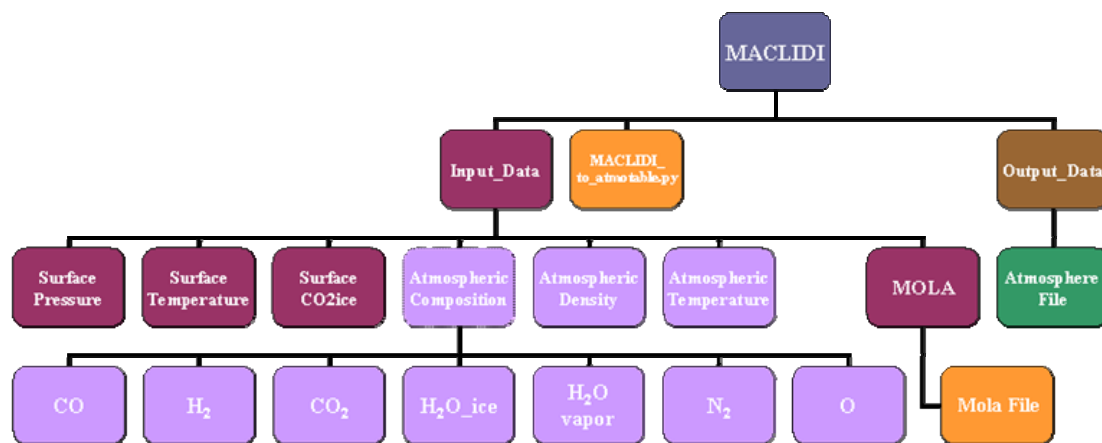


Figure 4-3- Data organization on MACLIDI.v.3.0

For each one of the atmospheric parameters there are 12 folders storing data for each one of the 12 typical Martian seasons (12 solar longitudes). For each solar longitude there are two folders storing data for day and night files (instead of 22 hours per day, MACLIDIv3.0 enables a day/night accuracy for all the locations on the Martian map). Finally for day or night there are files storing parameters for different atmospheric altitudes (maximum 50 atmospheric layers). This means a maximum of 120 stored files.

On the other hand for each one of the surface parameters there are 12 folders, one for each solar longitude. For each solar longitude data are stored for day and night, leading to a maximum of 24 stored files.

Table 4-4 illustrates the much more complex format of atmospheric table with additional information on surface pressure, temperature and dry-ice layer produced by MACLIDIv3.0.

Lat	Long	Solar Long	Time [Hour]	Height [Km]	Density [Kg/m3]	Atoms Temp [kelvin]	CO [mol/mol]	CO2 [mol/mol]	H2 [mol/mol]	H2O_ice [mol/mol]	H2O_v [mol/mol]	N2 [mol/mol]	O [mol/mol]	Surface Pressure [Pascal]	Surface Tem. [Kelvin]	Surface CO2 ice [Kg/m2]	Surface Altitude [Km]
90S	180E	180_210	02:00	0.01	1.3E-02	147.2	8.8E-04	9.5E-01	1.6E-05	1.0E-04	1.1E-08	2.9E-02	5.9E-10	366.5	144.2	69.5	2647.4
90S	180E	180_210	02:00	0.02	1.3E-02	149.4	5.6E-04	9.7E-01	1.0E-05	6.3E-05	2.4E-08	1.8E-02	6.2E-10	366.5	144.2	69.5	2647.4
90S	180E	180_210	02:00	0.05	1.2E-02	153.8	4.6E-04	9.7E-01	8.4E-06	6.6E-05	8.1E-08	1.5E-02	6.5E-10	366.5	144.2	69.5	2647.4
90S	180E	180_210	02:00	0.12	1.2E-02	158.3	4.6E-04	9.8E-01	8.3E-06	6.7E-05	2.1E-07	1.5E-02	6.7E-10	366.5	144.2	69.5	2647.4
90S	180E	180_210	02:00	0.25	1.2E-02	161.0	4.8E-04	9.7E-01	8.7E-06	6.6E-05	3.9E-07	1.6E-02	6.5E-10	366.5	144.2	69.5	2647.4
90S	180E	180_210	02:00	0.5	1.1E-02	163.3	5.4E-04	9.7E-01	9.7E-06	6.3E-05	7.3E-07	1.7E-02	5.4E-10	366.5	144.2	69.5	2647.4
90S	180E	180_210	02:00	1	1.0E-02	167.1	6.6E-04	9.6E-01	1.2E-05	5.9E-05	1.5E-06	2.1E-02	4.3E-10	366.5	144.2	69.5	2647.4
90S	180E	180_210	02:00	2	9.0E-03	168.2	8.0E-04	9.6E-01	1.4E-05	5.0E-05	1.9E-06	2.5E-02	4.1E-10	366.5	144.2	69.5	2647.4
90S	180E	180_210	02:00	3.2	7.9E-03	166.5	8.9E-04	9.5E-01	1.5E-05	4.1E-05	1.5E-06	2.7E-02	5.0E-10	366.5	144.2	69.5	2647.4
90S	180E	180_210	02:00	5	6.5E-03	164.2	9.8E-04	9.5E-01	1.6E-05	2.9E-05	1.1E-06	2.9E-02	7.6E-10	366.5	144.2	69.5	2647.4
90S	180E	180_210	02:00	7	5.2E-03	161.9	1.1E-03	9.5E-01	1.7E-05	1.8E-05	8.0E-07	3.1E-02	1.3E-09	366.5	144.2	69.5	2647.4
90S	180E	180_210	02:00	10	3.7E-03	157.7	1.2E-03	9.5E-01	1.8E-05	7.0E-06	4.3E-07	3.2E-02	2.9E-09	366.5	144.2	69.5	2647.4
90S	180E	180_210	02:00	14	2.4E-03	151.6	1.3E-03	9.5E-01	1.8E-05	1.5E-06	1.6E-07	3.2E-02	8.4E-09	366.5	144.2	69.5	2647.4
90S	180E	180_210	02:00	18	1.5E-03	145.7	1.5E-03	9.5E-01	1.8E-05	2.6E-07	5.7E-08	3.2E-02	2.5E-08	366.5	144.2	69.5	2647.4
90S	180E	180_210	02:00	22	8.9E-04	142.3	1.7E-03	9.5E-01	1.8E-05	3.8E-08	3.4E-08	3.2E-02	8.0E-08	366.5	144.2	69.5	2647.4
90S	180E	180_210	02:00	27	4.4E-04	142.6	2.1E-03	9.5E-01	1.7E-05	9.7E-11	4.1E-08	3.1E-02	2.5E-07	366.5	144.2	69.5	2647.4
90S	180E	180_210	02:00	32	2.3E-04	148.0	2.6E-03	9.5E-01	1.7E-05	5.0E-21	3.9E-08	3.1E-02	5.1E-06	366.5	144.2	69.5	2647.4
90S	180E	180_210	02:00	38	1.0E-04	155.7	3.2E-03	9.4E-01	1.7E-05	2.0E-25	2.7E-08	3.1E-02	1.4E-04	366.5	144.2	69.5	2647.4
90S	180E	180_210	02:00	44	4.9E-05	162.3	3.8E-03	9.4E-01	1.7E-05	5.0E-30	1.5E-08	3.2E-02	6.9E-04	366.5	144.2	69.5	2647.4
90S	180E	180_210	02:00	50	2.4E-05	166.8	4.2E-03	9.4E-01	1.8E-05	-5.0E-35	8.9E-09	3.2E-02	1.8E-03	366.5	144.2	69.5	2647.4
90S	180E	180_210	02:00	56	1.2E-05	169.4	4.6E-03	9.4E-01	1.8E-05	1.0E-38	7.2E-09	3.2E-02	3.0E-03	366.5	144.2	69.5	2647.4
90S	180E	180_210	02:00	62	6.1E-06	170.5	4.9E-03	9.4E-01	1.8E-05	3.0E-38	6.5E-09	3.2E-02	3.8E-03	366.5	144.2	69.5	2647.4
90S	180E	180_210	02:00	68	3.1E-06	171.1	5.0E-03	9.4E-01	1.8E-05	3.0E-38	6.2E-09	3.2E-02	4.1E-03	366.5	144.2	69.5	2647.4
90S	180E	180_210	02:00	74	1.6E-06	170.8	5.5E-03	9.4E-01	1.8E-05	3.0E-38	5.1E-09	3.3E-02	4.8E-03	366.5	144.2	69.5	2647.4
90S	180E	180_210	02:00	80	8.2E-07	171.7	6.8E-03	9.3E-01	1.8E-05	3.0E-38	3.3E-09	3.3E-02	6.2E-03	366.5	144.2	69.5	2647.4
90S	180E	180_210	02:00	86	4.4E-07	162.9	9.5E-03	9.3E-01	1.8E-05	3.0E-38	1.7E-09	3.5E-02	9.1E-03	366.5	144.2	69.5	2647.4
90S	180E	180_210	02:00	92	2.3E-07	163.0	1.2E-02	9.2E-01	1.8E-05	2.0E-38	1.2E-09	3.7E-02	1.2E-02	366.5	144.2	69.5	2647.4
90S	180E	180_210	02:00	98	1.2E-07	164.6	1.4E-02	9.1E-01	1.8E-05	1.0E-38	1.4E-09	3.9E-02	1.5E-02	366.5	144.2	69.5	2647.4
90S	180E	180_210	02:00	104	6.1E-08	166.1	1.7E-02	9.0E-01	1.9E-05	5.0E-38	1.8E-09	4.2E-02	1.8E-02	366.5	144.2	69.5	2647.4
90S	180E	180_210	02:00	110	3.2E-08	168.4	2.0E-02	8.9E-01	1.9E-05	4.0E-38	2.3E-09	4.6E-02	2.3E-02	366.5	144.2	69.5	2647.4
90S	180E	180_210	02:00	116	1.7E-08	171.9	2.4E-02	8.8E-01	1.9E-05	3.0E-38	2.8E-09	4.9E-02	2.8E-02	366.5	144.2	69.5	2647.4
90S	180E	180_210	02:00	122	8.8E-09	178.7	2.6E-02	8.7E-01	2.0E-05	3.0E-38	3.2E-09	5.3E-02	3.3E-02	366.5	144.2	69.5	2647.4
90S	180E	180_210	02:00	128	4.6E-09	190.2	3.0E-02	8.5E-01	2.0E-05	3.0E-38	3.7E-09	5.7E-02	3.8E-02	366.5	144.2	69.5	2647.4
90S	180E	180_210	02:00	134	2.4E-09	206.0	3.3E-02	8.4E-01	2.1E-05	3.0E-38	4.2E-09	6.1E-02	4.4E-02	366.5	144.2	69.5	2647.4
90S	180E	180_210	02:00	140	1.4E-09	221.3	3.8E-02	8.2E-01	2.1E-05	3.0E-38	4.9E-09	6.7E-02	5.3E-02	366.5	144.2	69.5	2647.4
90S	180E	180_210	02:00	146	8.6E-10	234.1	4.3E-02	8.0E-01	2.2E-05	3.0E-38	5.8E-09	7.5E-02	6.6E-02	366.5	144.2	69.5	2647.4
90S	180E	180_210	02:00	152	5.1E-10	245.3	4.7E-02	7.8E-01	2.2E-05	3.0E-38	6.9E-09	8.1E-02	7.6E-02	366.5	144.2	69.5	2647.4
90S	180E	180_210	02:00	158	3.5E-10	252.2	5.4E-02	7.4E-01	2.3E-05	3.0E-38	8.4E-09	9.1E-02	9.7E-02	366.5	144.2	69.5	2647.4
90S	180E	180_210	02:00	164	2.1E-10	258.5	5.9E-02	7.1E-01	2.3E-05	3.0E-38	1.0E-08	9.8E-02	1.1E-01	366.5	144.2	69.5	2647.4
90S	180E	180_210	02:00	170	1.5E-10	262.0	6.6E-02	6.7E-01	2.4E-05	3.0E-38	1.2E-08	1.1E-01	1.4E-01	366.5	144.2	69.5	2647.4
90S	180E	180_210	02:00	176	9.9E-11	265.4	7.0E-02	6.4E-01	2.4E-05	3.0E-38	1.5E-08	1.2E-01	1.6E-01	366.5	144.2	69.5	2647.4
90S	180E	180_210	02:00	182	7.3E-11	268.2	7.7E-02	5.9E-01	2.5E-05	3.0E-38	1.8E-08	1.3E-01	2.0E-01	366.5	144.2	69.5	2647.4
90S	180E	180_210	02:00	188	4.8E-11	270.9	8.0E-02	5.6E-01	2.6E-05	3.0E-38	2.1E-08	1.3E-01	2.2E-01	366.5	144.2	69.5	2647.4
90S	180E	180_210	02:00	194	3.6E-11	271.5	8.6E-02	5.0E-01	2.7E-05	3.0E-38	2.6E-08	1.4E-01	2.7E-01	366.5	144.2	69.5	2647.4
90S	180E	180_210	02:00	200	2.6E-11	272.0	8.9E-02	4.6E-01	2.7E-05	3.0E-38	3.0E-08	1.5E-01	2.9E-01	366.5	144.2	69.5	2647.4
90S	180E	180_210	02:00	206	1.9E-11	272.3	9.1E-02	4.1E-01	2.8E-05	3.0E-38	3.5E-08	1.5E-01	3.4E-01	366.5	144.2	69.5	2647.4
90S	180E	180_210	02:00	212	1.4E-11	272.5	9.3E-02	3.7E-01	2.9E-05	3.0E-38	4.1E-08	1.5E-01	3.8E-01	366.5	144.2	69.5	2647.4
90S	180E	180_210	02:00	218	9.7E-12	272.7	9.4E-02	3.4E-01	3.0E-05	3.0E-38	4.6E-08	1.5E-01	4.0E-01	366.5	144.2	69.5	2647.4
90S	180E	180_210	02:00	224	7.8E-12	272.7	9.3E-02	2.8E-01	3.1E-05	3.0E-38	5.2E-08	1.5E-01	4.7E-01	366.5	144.2	69.5	2647.4
90S	180E	180_210	02:00	230	6.0E-12	272.8	9.3E-02	2.5E-01	3.2E-05	3.0E-38	5.8E-08	1.5E-01	5.0E-01	366.5	144.2	69.5	2647.4

Table 4-4 – MACLIDIV3.0 Atmospheric Table input to dMEREM

#### 4.4.2. Mars Topology

The built interfaces extract the Martian surface altitude from the MOLA instrument on board NASA's Mars Global Surveyor (MGS) spacecraft [Abshire, 1999]. Figure 4-4 depicts the 3D averaged Martian topology map with a 5°x5° resolution.

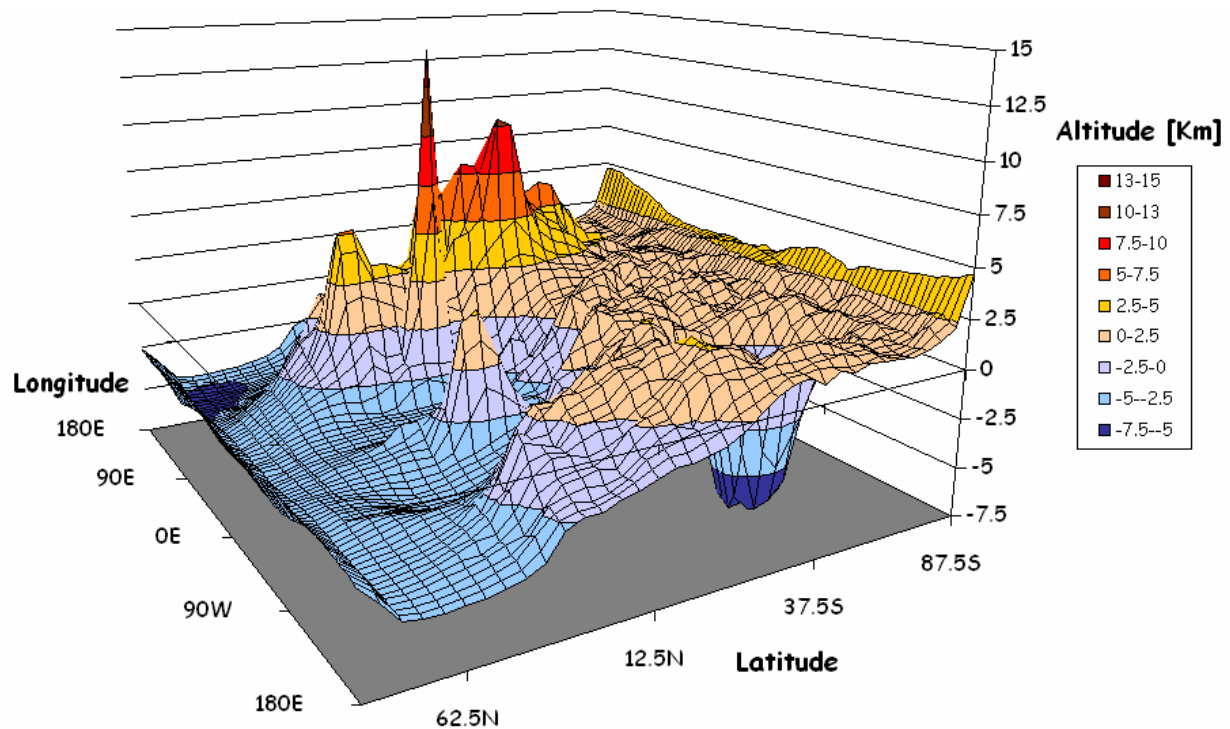
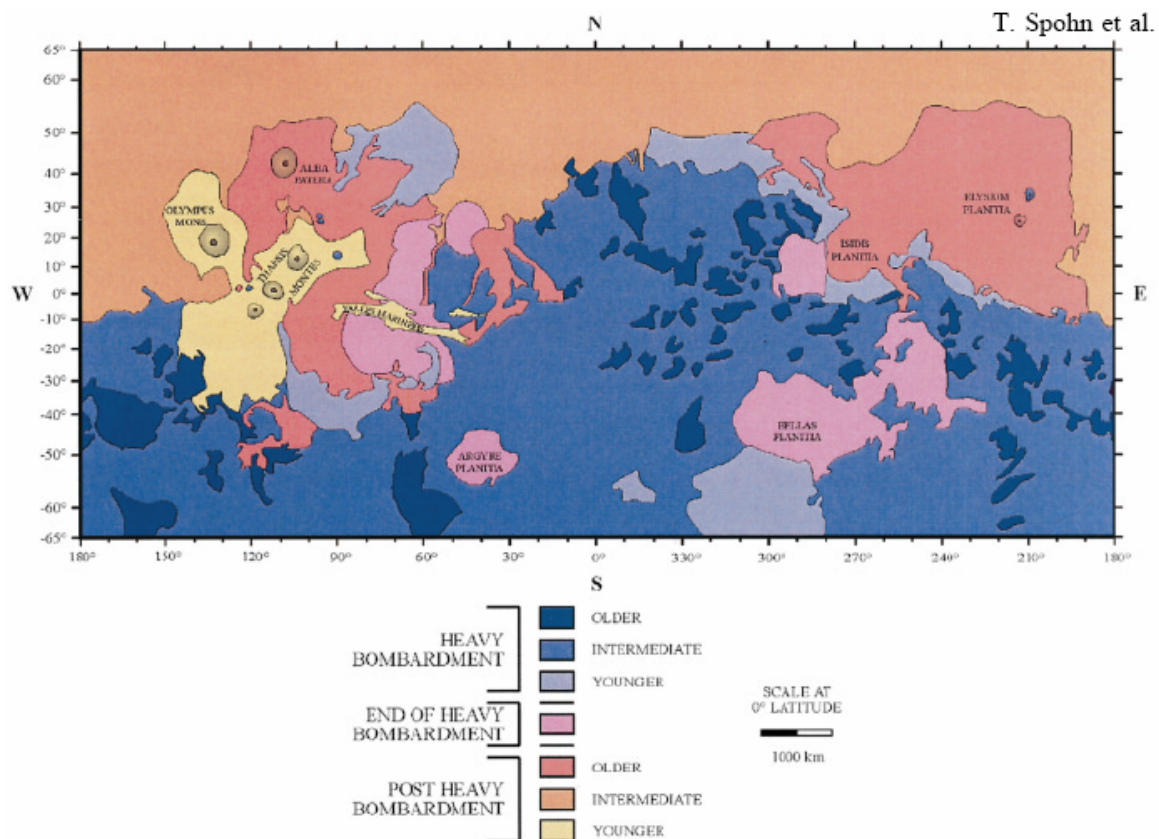


Figure 4-4- 3D Martian topology map

#### 4.4.3. Mars Soil composition

Mars' geology also plays a very important role in the radiation environment characterization. The Martian atmosphere, being very low density (maximum values of the order of  $10^{-2} \text{ kgm}^{-3}$ ), behaves as a soft attenuator for incoming radiation capable of reaching the Mars surface. Thus, resulting in an important contribution from secondary particles generated and backscattered at the surface.

Since the second half of 19<sup>th</sup> century Mars has been known for its dichotomy [Boyce, 2002], [Harland, 2005]. The “line of dichotomy” is the major division of Mars' surface and is due to the clear hemispheric asymmetry. The cause of such asymmetry is unknown. Planetary scientists justify it by defining different meteoritic bombarding periods [Spohn, 1998]. Figure 4-5 shows the Martian surface dichotomy and illustrates the different geological periods of the surface.



**Figure 4-5- Geological map of Mars [Spohn, 1998]**

The line of dichotomy has its most northerly point at about 50° latitude [Harland, 2005]. The southern hemisphere is densely crated and therefore older than the sparsely crated northern hemisphere. The northern lowlands hemisphere is believed to have suffered a resurfacing by volcanic activity early in the Martian history or it might have been the site of an early ocean [Spohn, 1998].

Nowadays, observations from remote sensing to the different landers' measurements suggest that there are compositional differences across the surface of Mars [Boyce, 2002]. However, after TES (from Mars Global Surveyor) spectra analysis, it was found that the composition of Mars volcanic materials varies from basalt in the ancient southern hemisphere highlands to andesite in the younger northern lowlands (Figure 4-6). This conclusion is also being confirmed by the different landers' measurements.

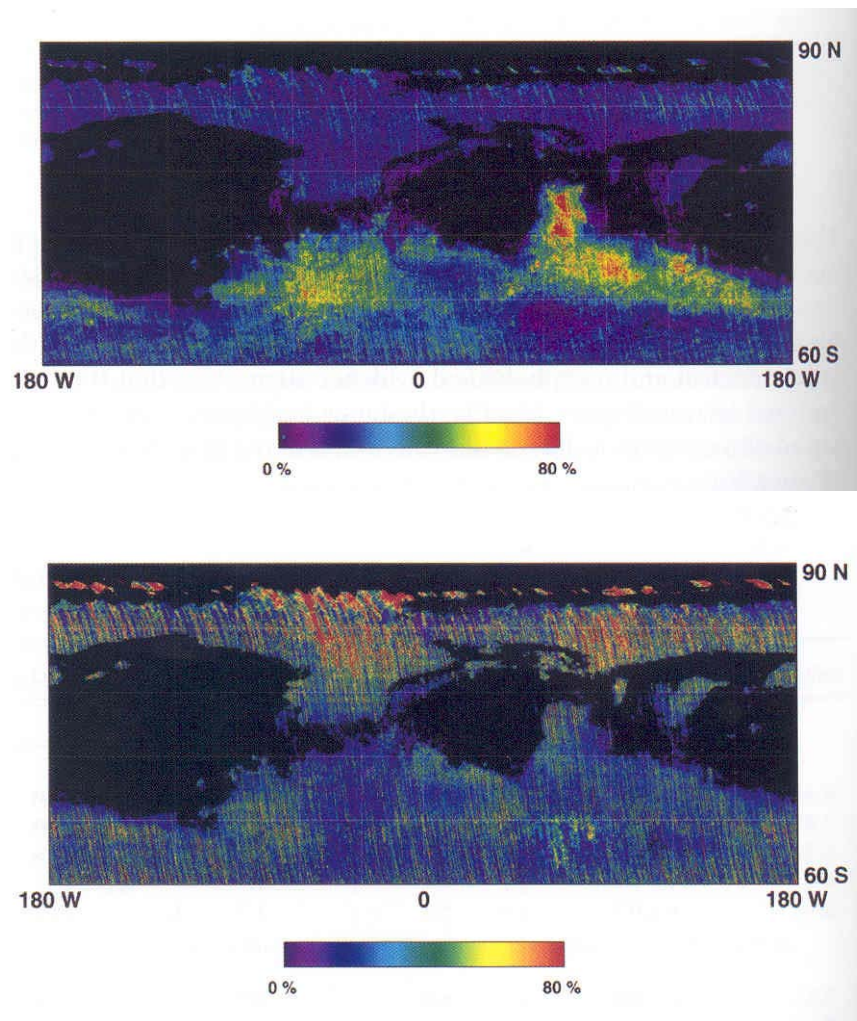


**Figure 4-6 – TES spectra: basalt (top) and andesite (down).**

The major composition distinction between basalt and andesite is characterized by the weight percentage of  $\text{SiO}_2$ : about 45% to 52% in basalt and 52% to 63% in andesite.

Mars Express published the same aspects of the surface of Mars in terms of Pyroxenes and anhydrous nanophase ferric oxides, as illustrated in figure 4-7 [ESA, 2007]. Note that the Pyroxenes are minerals commonly present in basalts and anhydrous nanophase ferric oxides are forms of altered minerals.

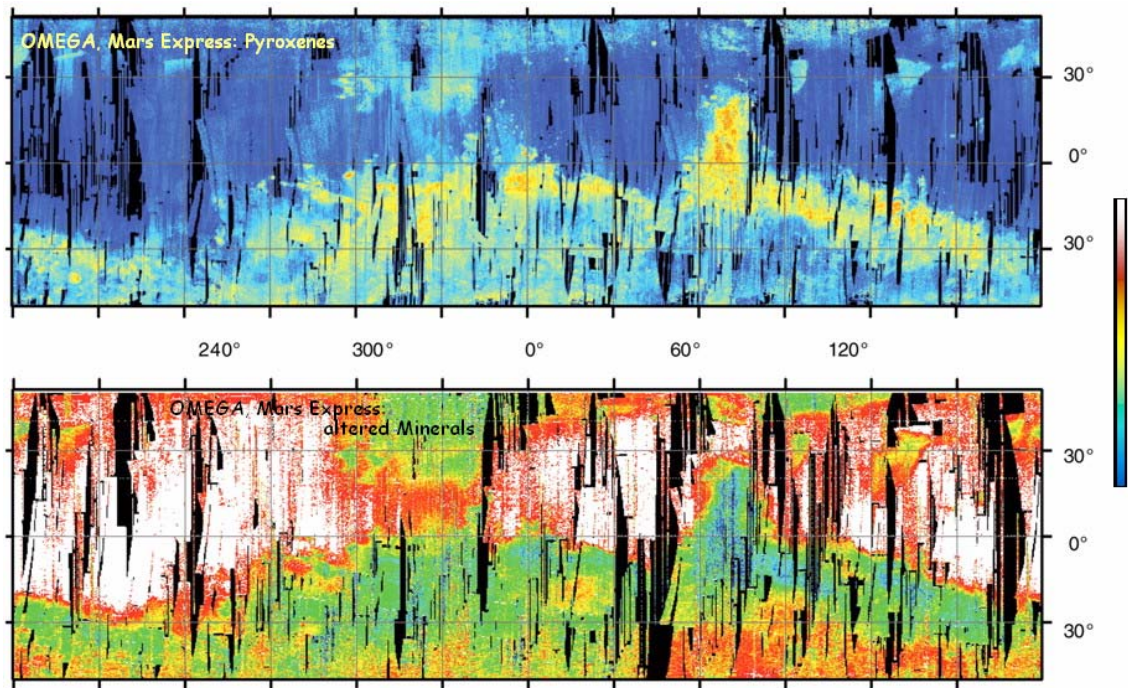


**Figure 4-7- OMEGA- Mars Express surface maps: Pyroxenes (top) and anhydrous nanophase ferric oxides (down).**

Olivine is other mineral detected by the Mars rovers such as Opportunity. It is found in basic and ultra basic igneous rock, formed in warm and wet environments.

Table 4-5 shows a general composition for basalt, andesite, basalt-andesite, Olivine, Pyroxenes and finally a mean composition obtained by the average over the Viking 1 and Mars Pathfinder Landers' soil analysis. Note that results of Table 4-5 were converted from literature results in order to give a total weight percentage of 100%. The averages and conversions shown here may not be as mineralogically significant as the original results. However the creation of this table aims at summarising the most significant elements to input into GEANT4 simulation. On the other hand the user choosing a specific composition can solve the problem of "mineralogical significance".

Composition	Basalt	Andesite	Basalt-Andesite	Olivine	Pyroxenes		Viking 1	Sojourner
	(Generic)	(Generic)	(Generic)		LCP	HCP		(PF)
SiO	50.2	59.7	53.9	39.2	53.0	45.1	56.4	55.3
FeO	6.0	8.3	8.6	18.8	18.8	10.1	20.4	17.8
Al <sub>2</sub> O <sub>3</sub>	17.0	17.2	17.1	0.0	0.8	6.5	8.2	8.8
MgO	10.6	3.9	7.2	42.1	24.0	12.5	6.9	7.7
MnO	0.0	0.0	0.0	0.0	0.3	0.4	0.0	0.0
CaO	14.7	5.8	9.6	0.0	2.0	19.9	6.6	6.4
Na <sub>2</sub> O	1.5	3.5	2.7	0.0	0.0	0.0	0.0	2.3
K <sub>2</sub> O	0.0	1.6	1.0	0.0	0.0	0.0	0.8	0.5
TiO <sub>2</sub>	0.0	0.0	0.0	0.0	0.7	5.3	0.7	1.3
Cr <sub>2</sub> O <sub>3</sub>	0.0	0.0	0.0	0.0	0.4	0.3	0.0	0.0
FeS	0.0	0.0	0.0	0.0	0.0	0.0	0.0	0.0
CoO	0.0	0.0	0.0	0.0	0.0	0.0	0.0	0.0
NiO	0.0	0.0	0.0	0.0	0.0	0.0	0.0	0.0
P <sub>2</sub> O <sub>3</sub>	0.0	0.0	0.0	0.0	0.0	0.0	0.0	0.0
<b>Total</b>	<b>100.0</b>	<b>100.0</b>	<b>100.0</b>	<b>100.0</b>	<b>100.0</b>	<b>100.0</b>	<b>100.0</b>	<b>100.0</b>

**Table 4-5- General compositions of important minerals and soil samples of Mars**

The search for water on Mars is one of the major issues in Mars exploration, since it is the fundamental element in the search for life.

The presence of water in the Martian atmosphere is already known from atmospheric circulation models and already validated by different instruments on board of the multiple missions to the planet. However, the surface morphology gives several indications of past existence of liquid water at the surface and/or in the underground.

At the surface water can be found mostly in ice-states or in the form of mineral hydration.

Figure 4-8 provides result from Gamma Ray Spectrometer, on board of Mars Odyssey, for data collected for the element hydrogen [GRS, 2008]. GRS studies assume these data as water -equivalent maps. The map shows concentration estimates of equivalent-weight water found in the regions around the equator of Mars. Regions of high water-equivalent concentration are shown in red while regions of low water-equivalent concentration are shown in blue.

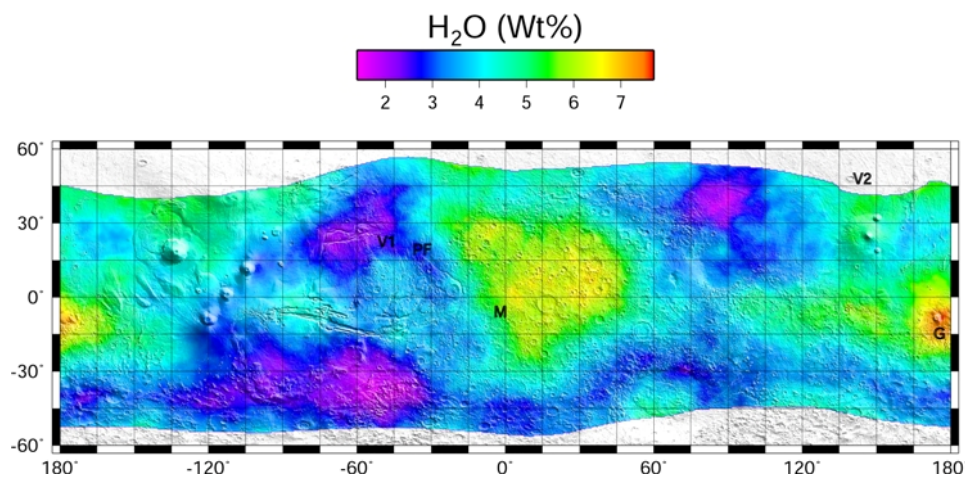


Figure 4-8 - Equivalent-weight water found in the regions around the equator of Mars by GRS on board of Mars Odyssey, March 2006 [GRS, 2008].

Similarly, figure 4-9 shows concentration estimates of equivalent-weight water found in the region of North Pole.

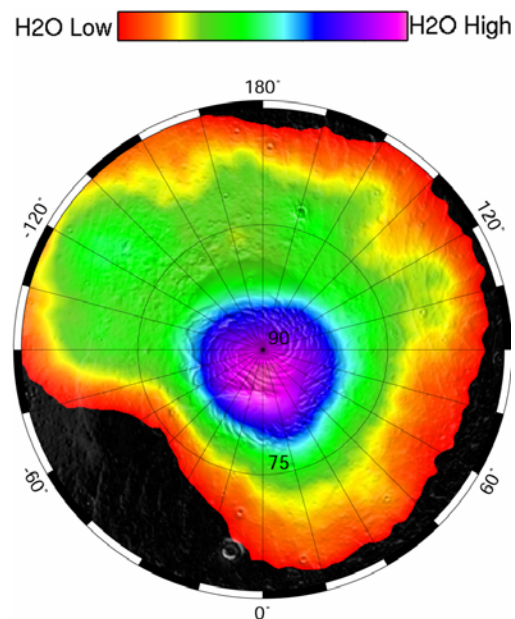


Figure 4-9 - Map of Martian Hydrogen at the North Pole, July 2004 [GRS, 2008]

CO<sub>2</sub> is basically present in the Polar Caps and the thickness of ice varies strongly with solar longitude as depicted in figures 4-15 and 4-16 [Forget, 2001]. As previously discussed the CO<sub>2</sub> map is given by the MCD.

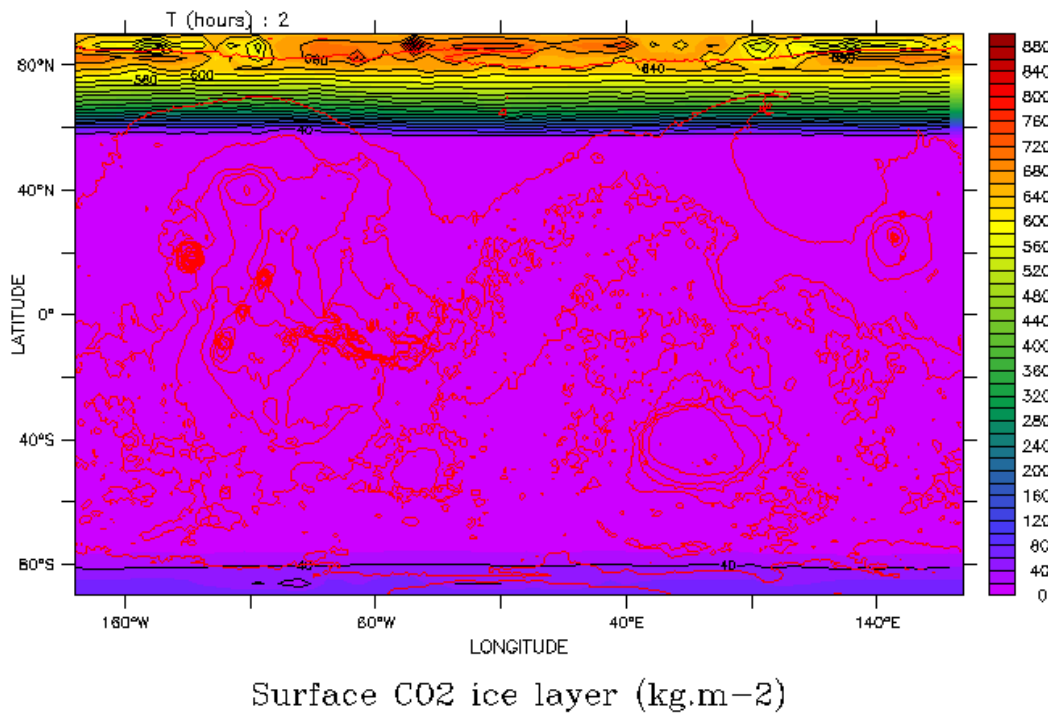


Figure 4-10 – Surface CO<sub>2</sub> layer, solar Longitude 0° to 30°; Map obtained with MCD.

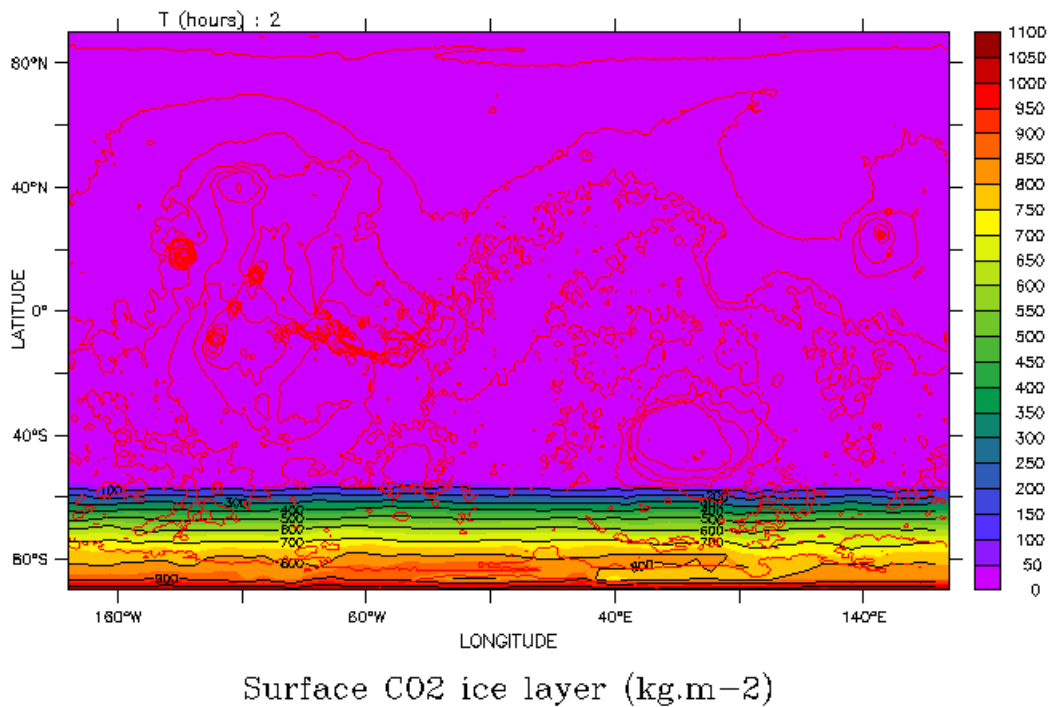


Figure 4-11- Surface CO<sub>2</sub> layer, solar Longitude 180° to 210°: Map obtained with MCD.

MarsREC simulations presented in subchapter 4.5, 4.6, 4.7 and 4.9 of this thesis were simulated assuming a constant average soil density of 3.75gcm<sup>-3</sup> and a composition consist mainly of silicon dioxide and iron oxides as discussed suggested by [Boyce, 2002]. Subchapter

4.8 describes simulations performed to evaluate the importance of different soil compositions in Martian radiation environment.

A tool has been developed in order to determine Martian local soil composition and density. This tool extracts data from GRS soil composition maps, CO<sub>2</sub> ice thickness from MCD and assumes default composition based on the mineralogical study previously described, assumed for locations with no data available. Finally this tool has an algorithm that calculates the soil density taking into account the final local composition, physic state and porosity. The interface with the GEANT4 application, called SOILCOMPI as illustrated in figure 4-12, is integrated into the dMEREM pre-processor.

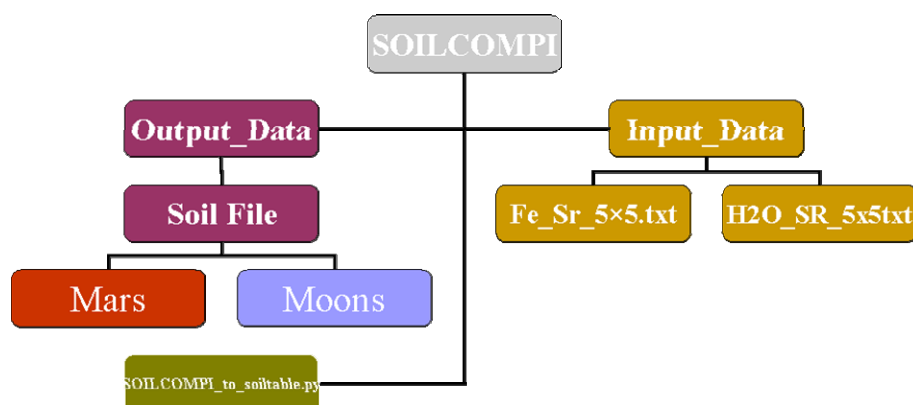


Figure 4-12- SOILCOMPI.v.2.0 data organization

Table 4-6 illustrates the default compositions for Mars surface and Moons.

Composition	Basalt-Andesite (adapted from Generic) [Weight percentage (%)]	Moons
Si <sub>2</sub> O	51.2	38.7
Fe <sub>2</sub> O <sub>3</sub>	9.3	23.2
Bulk (Al <sub>2</sub> MgCa Na <sub>2</sub> K <sub>2</sub> O <sub>7</sub> )	32.1	31.8
FeS	0.0	6.3
H <sub>2</sub> O	7.4	0.0
<b>Total</b>	<b>100.0</b>	<b>100.0</b>

Table 4-6– Default surface composition

For the Martian surface the Pre-processor reads iron and water-equivalent maps (as shown in figures 4-8, 4-9 and 4-13) extracted from the Gamma Ray Spectrometer, on board of Mars Odyssey.

Since these elements in nature appear mostly in the form of oxides in particular iron is commonly found combined with oxygen in the form of  $\text{Fe}_2\text{O}_3$ , SOILCOMPI assumes GRS iron data as the weight percentage of  $\text{Fe}_2\text{O}_3$ .

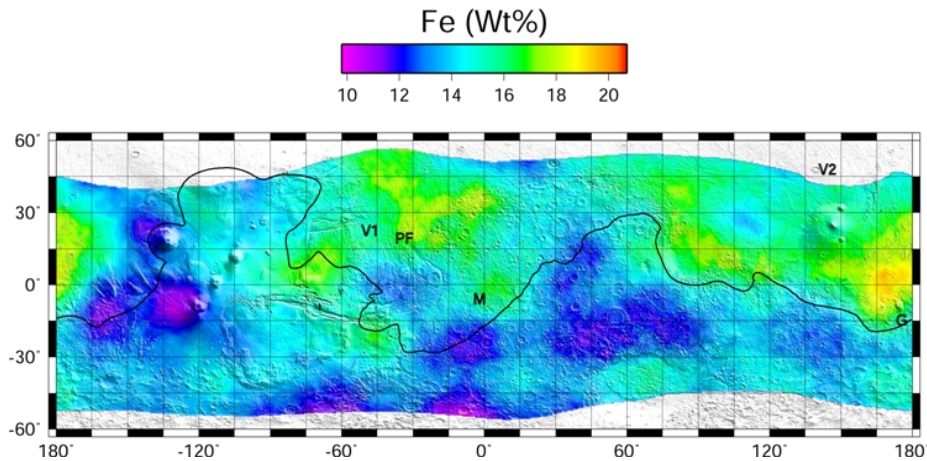


**Figure 4-13- Equivalent-weight of iron found in the regions around the equator of Mars by GRS on board of Mars Odyssey, March 2006 [GRS, 2008]**

The Pre-processor reads the  $\text{Fe}_2\text{O}_3$  and  $\text{H}_2\text{O}$  weight percentages from the map files for the specific (latitude, longitude) position. In case one of these values is not defined in the map files the Pre-processor computation is based on an algorithm that considers the other readable value, the total and the default composition.

The density is calculated according to the weight percentages of each material. The densities used by the density calculator are SRIM [Ziegler, 2006] densities for solid materials,  $\text{CO}_2$  ice and  $\text{H}_2\text{O}$  ice densities are calculated accounting for 9% volume increase from liquid to ice, which means an 9% decrease in density from SRIM values.

Table 4-7 gives the output soil composition for Mars from SOILCOMPI for different locations.

Latitude	Longitude	H2O [%]	Fe2O3 [%]	SiO2 [%]	Bulk [%]	Density [g/cm3]	FeS [%]
90S	180E	7.4	9.3	51.2	32.1	1.68949	0.0
41.2S	84.4E	2.6	13.8	51.5	32.1	1.80065	0.0
48.8S	135W	3.5	13.4	51.0	32.1	1.78542	0.0
22.5S	50.6E	3.6	12.9	51.3	32.1	1.77833	0.0

**Table 4-7- Martian soil description for different locations**

## 4.5. Mars Radiation Environment Characterization

Results discussed in the current subchapter were published in 2005 [Keating, 2005].

### 4.5.1. Input radiation

In this work the following radiation inputs were considered: GCR at solar maximum and SEP generated by CREME96 for near-Earth interplanetary locations [Nymmik, 1992], [Tylka, 2007]. These interplanetary flux models are based on measurements at Earth (1AU\*) [Tylka, 2007].

The phasing with respect to the solar cycle corresponds to the foreseen European Mars mission ExoMars [ESA, 2005].

The GCR fluxes were obtained from the solar-quiet mode in CREME96 while the most severe environment considered corresponds to that from solar energetic protons given by the “worst week” model of CREME96 [Tylka2, 1997] as shown in figure 2-15 in Chapter 2.

### 4.5.2. Simulation Set-up

The geometry implemented takes into account: a) The geographical grid size given by the  $5^{\circ} \times 5^{\circ}$  resolution of MCD; b) The average composition of the soil of 30%  $\text{Fe}_2\text{O}_3$  and 70%  $\text{SiO}_2$ , with density  $3.75 \text{ g cm}^{-3}$ ; c) The thickness of the soil is calculated according to the proton total penetration depth and the MOLA surface elevation; d) The thickness of the 32 atmospheric layers given by the  $\sigma$  levels of MCD, e) A fixed atmospheric composition consisting of:  $\text{CO}_2$ ,  $\text{N}_2$ , Ar,  $\text{O}_2$ , CO and  $\text{H}_2\text{O}$ ; f) The density, temperature and pressure of the 32 atmospheric layers computed from MCD.

#### 4.5.2.1. Different geometries, different location and times of the day

Each location (Longitude, Latitude) on the Martian surface, each phase of the Martian year (solar longitude) or each time of the Martian day corresponds to a specific set of atmospheric properties. For this reason each of them corresponds to specific simulation geometry. All simulation cases (Cases A to H) referred to in the subsequent sections are defined in Table 4-8.

The simulated cases are located in two different areas of the planet, the cliff of Olympus Mons (MO) volcano (700 km across and 25 km high) and Tyrrhena Paterae (TP), one of the

---

\*Medium Earth-Sun distance corresponds to approximately  $150 \times 10^6$  km.

three large, ancient, low relief broad mountain of volcanic origin that have developed along faults that surrounds Hellas Basins[Abshire, 1999]. These locations were chosen because they are diametrically opposed, the first Northwest and the second Southeast of the planet, and possible landing sites for ExoMars.

Case	Radiation Input	Mom Dist. <sup>1</sup>	Long (E)	Lat (N)	Name <sup>2</sup>	Elevation (Km)	Solar Longitude	Time <sup>3</sup> (Hours)
A	GCR	Cos $\theta$	-140	22.5	OM	1.3	180°-210°	12
B	SEP	0°	-140	22.5	OM	1.3	180°-210°	12
C	GCR	Cos $\theta$	80	-7.5	TP	1.7	180°-210°	12
D	GCR	Cos $\theta$	75	-7.5	TP	1.2	180°-210°	12
E	GCR	Cos $\theta$	80	-12.5	TP	2.4	180°-210°	12
F	GCR	Cos $\theta$	75	-12.5	TP	1.2	180°-210°	12
G	GCR	Cos $\theta$	80	-7.5	TP	1.7	180°-210°	2
H	GCR	Cos $\theta$	80	-7.5	TP	1.7	180°-210°	22

<sup>1</sup>Momentum Distribution: Cos  $\theta$ =isotropic; 0°=perpendicular. <sup>2</sup>OM= Olympus Mons and TP=Tyrrhena Paterae. <sup>3</sup>Time of the Martian Day at Longitude 0°

**Table 4-8- Simulation cases**

#### 4.5.3. Simulation Results

The Monte-Carlo transport of  $10^5$  protons through the Martian atmosphere and surface has been incorporated into the simulation. Particles are generated at the top of a column of the atmosphere of  $5^\circ \times 5^\circ$ . All primary and secondary particles are tracked from the generation point until they are absorbed, reach geometry tracking limits, it is abandoned by the tracking or its energy is forced to be zero by a flag (the particle is “killed”). Killing flags were set to reduce computation time by avoiding tracking particles in the atmosphere that do not contribute to the radiation environment. Systematic studies of these were performed in order to optimize the running time and simulation results.

##### 4.5.3.1. Radiation fluxes due to GCR

The radiation environment at the surface of Mars due to GCR simulated in Case A is shown in figure 4-14. In the higher energy range (above 100MeV), the radiation environment is mostly due to protons (circles) while at lower energies there is a high contribution from secondary neutrons (dots), photons (triangles) and electrons (squares). Ions, whose energy spectrum is indicated by boxes, constitute 0.3% of the secondary particles.

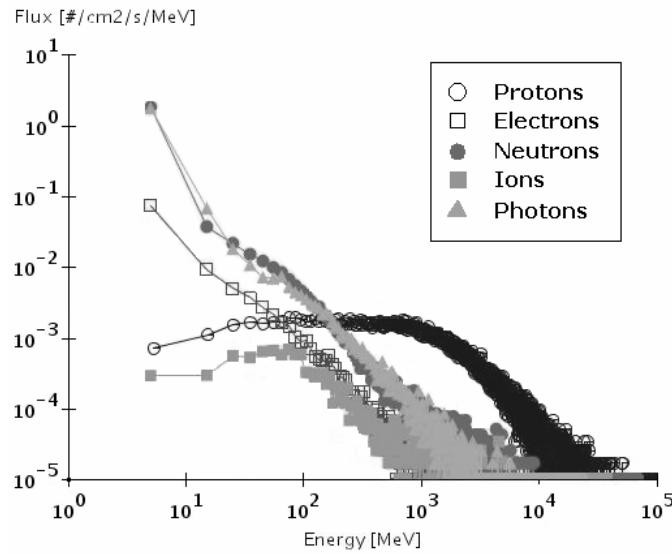


Figure 4-14 - Radiation Environment at the surface of Mars due to GCR protons for Case A

4.5.3.2. Radiation fluxes due to SEP

Figure 4-15 illustrates the radiation environment at the surface of Mars due to SEP simulated in Case B. It can be seen that the energy range is much lower than for GCR. However the fluxes are much higher. For energies above 30 MeV the radiation environment is mostly due to protons (circles) and neutrons (triangles) while at lower energies there is a high contribution from neutrons (triangles), photons (boxes) and electrons (squares). The signature for ions is not very significant.

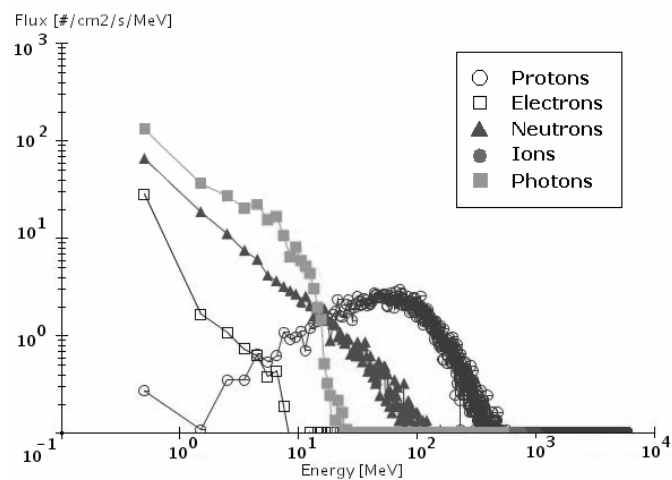


Figure 4-15- Radiation Environment at the surface of Mars due to SEP protons for Case B

### 4.5.3.3. Boundary conditions considerations

The study of boundary conditions is done according to [Seltzer, 1979].

The galactic cosmic ray flux is calculated taking into account a complete  $4\pi$  measurement of the environment flux:

$$\phi_{4\pi}^{GCR} = 4\pi \int_{E1}^{E2} dE \frac{d\phi^{GCR}(E)}{dE} \quad (4-3)$$

where  $d\phi^{GCR}(E)$  is the differential flux spectrum and the integration in energy is performed over the energy range considered in the simulation, E1 to E2.

However the flux received at the surface of Mars is due to the flux generated in the hemisphere above the surface:

$$\phi_{2\pi}^{GCR} = 2\pi \int_{E1}^{E2} dE \frac{d\phi^{GCR}(E)}{dE} \quad (4-4)$$

Besides, considering that the flux was generated with an isotropic momentum distribution ( $\cos\theta$ ) from a source point, the *simulated* differential flux, also known as the current, is:

$$j_{GCR}(E, \theta) = \frac{d\phi^{GCR}(E, \theta)}{dE} \cdot \cos\theta, \quad 0 < \theta < \pi/2 \quad (4-5)$$

The total incident galactic cosmic ray current ( $\Phi^{GCR}$ ) entering the simulation is then given by the integration of the current over energy and angle:

$$\Phi^{GCR} = 2\pi \int_{E1}^{E2} dE \int_0^{\pi/2} \frac{d\phi^{GCR}(E)}{dE} \cdot \cos\theta \cdot \sin\theta \cdot d\theta \quad (4-6)$$

Or,

$$\Phi^{GCR} = \pi \int_{E1}^{E2} dE \frac{d\phi^{GCR}(E)}{dE}. \quad (4-7)$$

Equations (4-3) and (4-7) lead to the conclusion that the current to consider,  $\Phi^{GCR}$ , is:

$$\Phi^{GCR} = \frac{1}{4} \phi_{4\pi}^{GCR} \quad (4-8)$$

Finally a last boundary consideration may be referred. In the isotropic distribution, particles leaving the simulation geometry through the sides are disregarded and do not contribute to

the simulation results. Calculations show that results should increase by an estimated factor of 10 to 20%.

Table 4-9 shows the fluences due to both GCR fluxes during one year and SEP fluxes considering a worst-case scenario of a 338 hours event such as the 2003 October –November [ESA2, 2005]. However since for SEP the event generation was perpendicular to the surface, it was considered that in such a low-density atmosphere it is similar to generating radiation input with isotropic distribution in the acceptance angle. This recalculation gives a correction factor of 1/8 instead of 1/4.

Particles Species	GCR	SEP*
	Fluence per year [x10 <sup>8</sup> #/cm <sup>2</sup> ]	Fluence per event [x10 <sup>8</sup> #/cm <sup>2</sup> ]
Protons	0.333	7.425
Electrons	0.088	0.663
Neutrons	1.555	3.475
Ions	0.013	0.001
Photons	1.514	6.262

\*Considered event duration of 338 hours.

**Table 4-9- Fluences due to GCR and SEP**

#### 4.5.3.4. Importance of Backscattering

The importance of the backscattered component was verified for both GCR and SEP simulations.

Figures 4-16 and 4-17 evaluate the population of backscattered particles detected at the surface of Mars at (140W, 22.5N) location due to GCR input radiation (Case A). It can be seen that 58% of all detected particles (figure 4-16) and in particular 95% of all neutrons (figure 4-17) are backscattered.

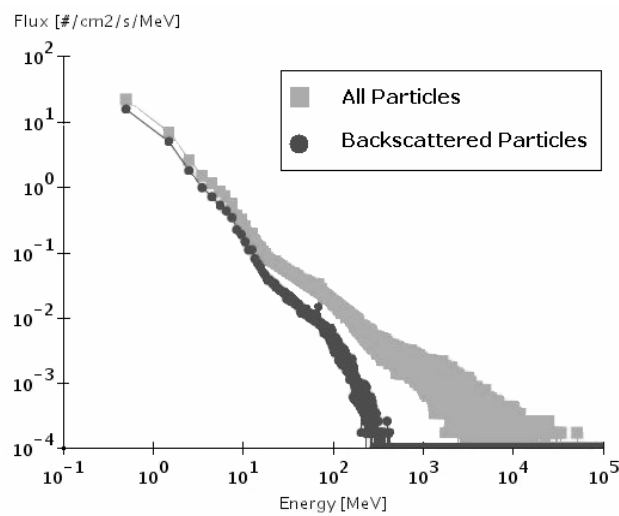


**Figure 4-16 - Backscattering component of all particles detected at the surface of Mars due to GCR protons for simulation Case A.**

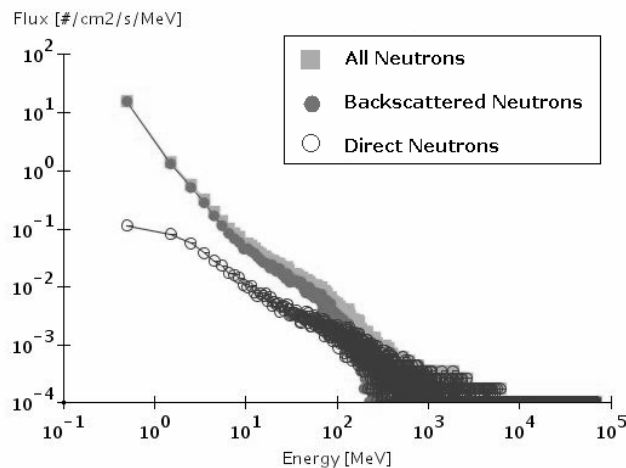


**Figure 4-17- Backscattering component of all neutrons detected at the surface of Mars due to GCR protons for simulation Case A.**

Figures 4-18 and 4-19 compare the population of backscattered and direct particles detected at the surface of Mars at (140W, 22.5N) location due to SEP input radiation (Case B). It can be seen that 19% of all detected particles (figure 4-18) and in particular 51% of all neutrons (figure 4-19) are backscattered.

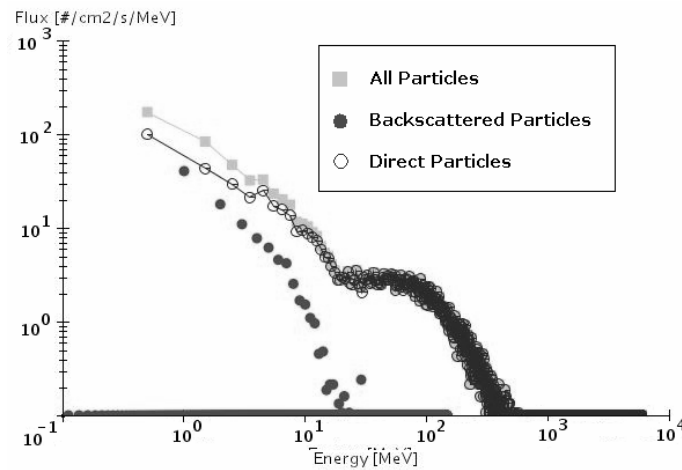


Figure 4-18 - Backscattering component of all particles detected at the surface of Mars due to SEP protons for Case B.

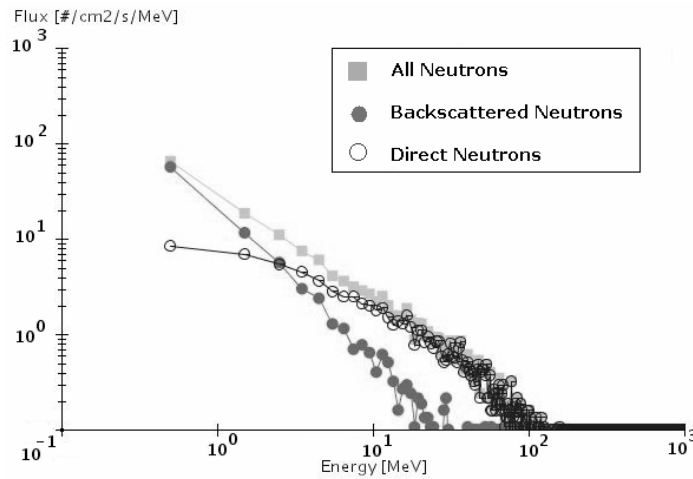


Figure 4-19 - Backscattering component of all neutrons detected at the surface of Mars due to SEP protons for simulation Case B.

4.5.3.5. Dose due to GCR

Doses at the surface of Mars due to GCR protons generated with an isotropic momentum distribution were computed for (80E, 7.5S), Case C, and are illustrated in Table 4-10.

Results of total ionizing energy loss were converted to rads according to the equivalence between flux and dose rate, at a uniform deposited dose given by Equation (4-9).

$$TID = \frac{1}{m} \frac{\Delta E}{N_{evt}} \cdot 1.602 \times 10^{-8} \cdot \frac{1}{4} \phi_{4\pi}^{GCR} \quad (4-9)$$

where

- $m$  = mass density of the sensitive volume made of SiO<sub>2</sub>  $m = \rho \cdot dx$  in kg cm<sup>-2</sup>;
- $\Delta E$  is the total energy deposition in SiO<sub>2</sub> for the overall simulated events in MeV;

- $N_{evt} = 10^5$  is the number of generated primary particles in the simulation;
- $dx = 1$  cm is the elementary abscissa;
- $\rho = 2.32$  g.cm<sup>-3</sup> is the simulated density of SiO<sub>2</sub>;
- $\phi_{4\pi}^{GCR}$  is given by equation (4-3).

Particles Species	Dose per year [Rad(SiO <sub>2</sub> )]
All	2.00
Protons	1.48
Electrons	0.25
Ions	0.18

Table 4-10- Doses due to GCR

4.5.3.6. Radiation Maps

One of the advantages of this modeling framework is the capability of generating maps for visualization of the radiation environment at different altitudes above the surface of Mars.

An example radiation map, figure 4-20, illustrates the total fluence per year of high-energy neutrons at the surface of Mars for Cases C, D, E and F. The visualization enables immediate knowledge of locations potentially of concern to technologies sensitive to radiation. Future more complete maps will be of major importance for scientific and engineering missions in the selection of possible landing locations.

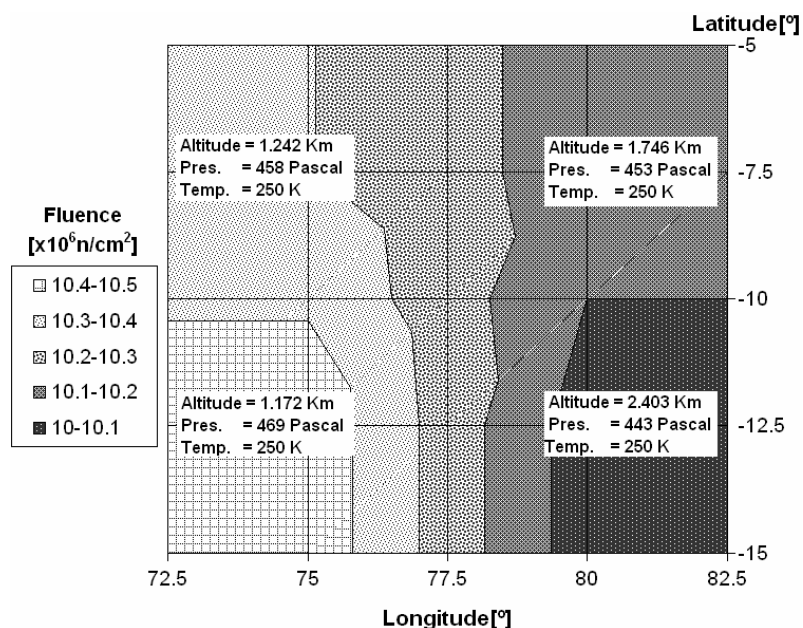


Figure 4-20 - Total fluence per year of neutrons with energy higher than 30 MeV at the surface of Mars due to GCR protons for simulation Cases C, D E and F, in the vicinity of Tyrrhena Paterae.

#### *4.5.4. Conclusions*

The Mars radiation environment modeling framework and its development has been described. It employs the GEANT4 particle transport tool and includes parameters such as Martian time, detection position, solar longitude, solar cycle modulated cosmic ray and solar particle event spectra, 4-D MCD atmosphere, geology and MOLA topology.

Results presented here show that the framework is capable of calculating the energy spectra and particle species at any location on Mars with a resolution of  $5^{\circ} \times 5^{\circ}$ . The model also shows the relative importance of the backscattered component of the radiation environment. While the total ionizing dose at the surface is of lesser concern to EEE components, the relative abundance of protons and neutrons may result in Displacement Damage and Single Event Effects.

The model is developed for ease of future upgrades:

- The methodology can be expanded to evaluate dose equivalents and induced degradation on components;
  - The methodology may be easily adapted to future improved knowledge of geology and atmosphere. For instance, local water ice content in the soil can easily be implemented;
  - The methodology is directly adaptable to other planets and moons such as Mercury and Europa.
-

#### 4.6. Variability of Radiation Environment in time

Figure 4-21 shows the MCD Viking dust scenario daily-averaged pressure from the Viking sites. An estimate of the variability due to weather systems, with the seasonal trend component of the MCD variance removed, is also shown. The seasonal cycle is due largely to the condensation and sublimation of CO<sub>2</sub>, although there is an important dynamical component, while the high-frequency oscillations are due to weather systems passing over the Landers [Lewis, 1999].

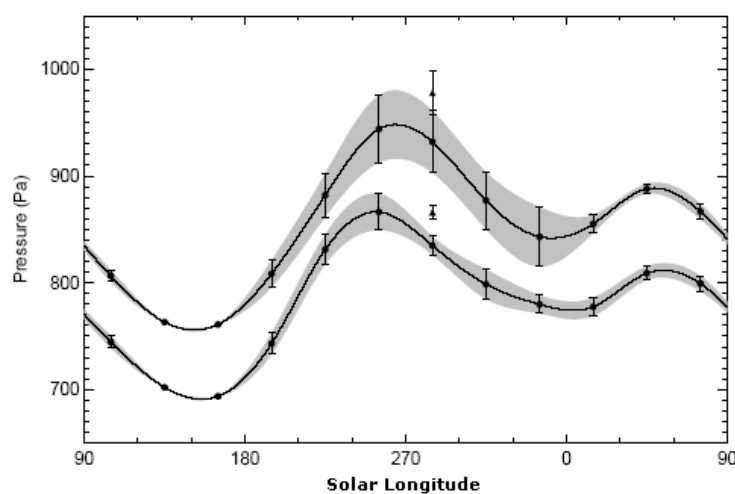


Figure 4-21 - Pressure at the Viking 1<sup>1</sup> (bottom curve) and Viking 2<sup>3</sup> (top curve) sites for 1 year of the MCD Viking dust scenario [Lewis, 1999]

The Following results were published in March 2006 [Keating2, 2006].

##### 4.6.1.1. Primary and secondary particles

The dependence of radiation environment at the surface of Mars due to GCR protons with surface pressure was analysed. Fluence results are presented in units of particles per square centimetre per year.

Figure 4-22 illustrates how the fluence of protons at the surface of Mars varies with the surface pressure. It can be seen that the primary proton fluence at the surface decreases with the atmospheric pressure at the surface. On the other hand the fluence of secondary protons is expected to increase with increasing surface pressure. This result is attributed to the denser air column that primary particles travel through for higher mean surface pressure. Consequently the probability of interaction, absorption and spallation in the atmosphere increases with

<sup>1</sup>Viking lander 1 was situated at 22°N, 48°W. <sup>3</sup> Viking lander 2 was situated at 48°N, 226°W.

increasing surface pressure. For the same reason the fluence of secondary particles is expected to increase with increasing surface pressure. This can also be verified in the in figure 4-23.

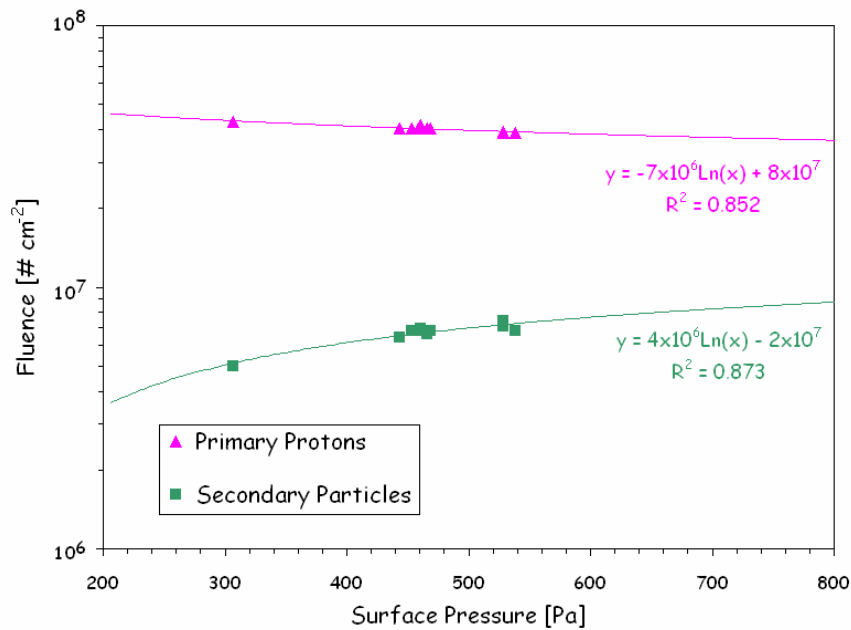


Figure 4-22 –Transfer function for integrated fluence of protons at the surface of Mars

Figure 4-23 shows the dependence of the fluence of secondary electrons at the surface of Mars; direct incident secondary neutrons; ions and photons with the surface pressure.

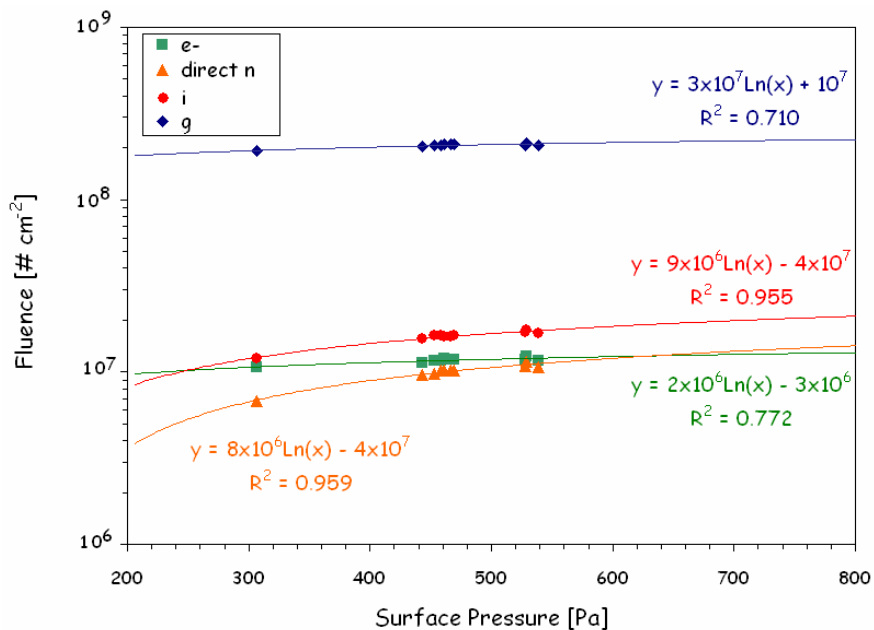


Figure 4-23–Transfer function for integrated fluence of secondary particles at the surface of Mars

#### 4.6.1.2. Backscattered Neutrons

Figure 4-24 illustrates the important contribution from backscattered neutrons at the surface and shows the inverse relationship between surface pressure and the relative importance of backscattered neutrons detected at the surface of Mars.

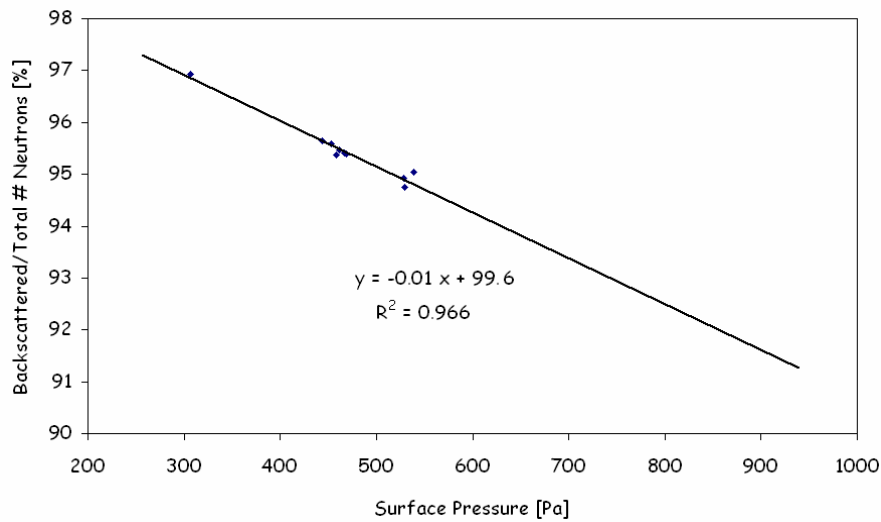


Figure 4-24–Impact of surface pressure in the percentage of Backscattered neutrons.

#### 4.6.1.3. Integrated fluence as function of Solar Longitude

Figure 4-25 illustrates the total integrated fluence of all detected particles at the surface of Mars expected at Viking1 and 2 sites (thick solid curve) and the estimated average integrated fluence of all detected particles at the surface of Mars (dashed curve).

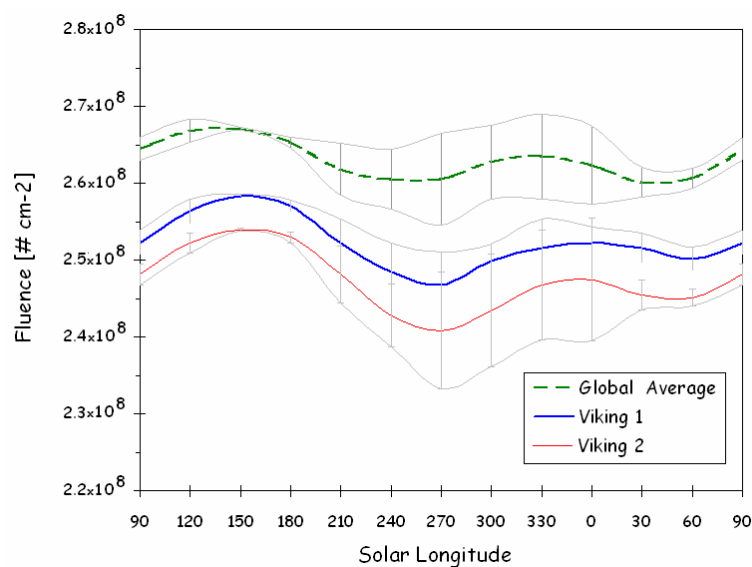


Figure 4-25–Total integrated fluence as function of Solar Longitude for different locations.

#### 4.6.2. GCR-induced Radiation environment and time

Table 4-11 summarizes the dependence of GCR-induced radiation environment with solar longitude, LS.

LS	60°-90°	150°-180°	240°-270°	Max-Min	
Particles Species	Fluence per year [x10 <sup>7</sup> #/cm <sup>2</sup> ]	Fluence per year [x10 <sup>7</sup> #/cm <sup>2</sup> ]	Fluence per event [x10 <sup>7</sup> #/cm <sup>2</sup> ]	Relative difference [%]	
Protons	Primary	3.450	3.604	3.425	5
	Secondary	0.6002	0.5117	0.6145	-18
Electrons	1.000	0.9559	1.007	-5	
Neutrons	19.09	19.97	18.91	5	
Photons	20.50	19.84	20.61	-4	
Other	1.850	1.651	1.883	-13	

**Table 4-11- Seasonal changes at 12:00 hours at Longitude 0°: Fluences due to GCR protons**

Differences obtained due to GCR protons using MarREC for different hours of the Martian day according to the simulated cases C, G and H of table 4-8 are illustrated in table 4-12.

Time	02	12	22	Max-Min	
Particles Species	Fluence per year [x10 <sup>7</sup> #/cm <sup>2</sup> ]	Fluence per year [x10 <sup>7</sup> #/cm <sup>2</sup> ]	Fluence per event [x10 <sup>7</sup> #/cm <sup>2</sup> ]	Relative difference [%]	
Protons	Primary	3.549	3.553	3.557	0.23
	Secondary	0.5435	0.5412	0.5386	-0.91
Electrons	0.9717	0.9706	0.9693	-0.25	
Neutrons	19.72	19.74	19.76	0.20	
Photons	20.08	20.06	20.04	0.20	
Other	1.723	1.718	1.712	0.64	

**Table 4-12- Diurnal changes at Longitude 0°: Fluences due to GCR protons**

While diurnal variations are of the order of 1% or lower, seasonal changes are of the order of 10 to 20%. Tables 4-11 and 4-12 also show that an increase of the primary spectra at the surface is complemented by an increase in the fluence of neutrons and photons and a decrease of electrons and ions and others. This observation can be easily explained by the fact that neutrons and photons (detected at the surface) are mostly created by primary particles interaction with the surface while electrons, ions and other particles are mostly due to the interactions and spallation in the atmosphere. This conclusion is supported by results published by the author [Keating, 2005] [Keating2, 2006].

#### 4.7. Dose Equivalent Calculations

The ambient dose equivalent measures the capability of different radiation environment to ionize or produce damage in organic materials. According to the International Commission on Radiation Units, [ICRU51, 1993] the dose equivalent, H, is the product of the absorbed dose at a given LET, in tissue, D, and a quality factor for that LET, Q:

$$H(\text{LET}) = Q(\text{LET}) D(\text{LET}) \quad (4-10)$$

The unit is  $\text{J kg}^{-1}$ , the special name for the unit of dose equivalent is sievert (Sv). Occasionally the former unit name rem is used. 1Sv is equal to 100rem.

Table 4-13 gives the values of radiation weighting factors as recommended by ICRP [Pelliccioni, 2003] [ICRP74, 1996] [ICRU57, 1998] [ICRP60, 1991] [ICRU51, 1993] [ICRU39, 1985] [Pelliccioni, 1999] [Kramer, 1982] [Pelliccioni, 2000].

RADIATION		WEIGHTING FACTOR
Photons		1
Electrons and muons		1
Neutrons	E > 10 keV	5
	10 keV > E > 100 keV	10
	100 keV > E > 2 MeV	20
	2 MeV > E > 20 MeV	10
	E > 20 MeV	5
Protons, other than recoil protons (E >2 MeV)		5
Alpha particles, fission fragments, heavy nuclei		20

**Table 4-13 - Values for radiation weighting factors recommended by ICRP**

#### 4.7.1. FLUKA conversion factors

ICRP and ICRU<sup>3</sup> recommended conversion coefficients for use in radiological protection for electrons and photons of energies up to 10 MeV and for neutrons up to 180 MeV. Pelliccioni using the FLUKA code [Pelliccioni, 2003] has calculated fluence-to-ambient dose equivalent conversion coefficients for higher energies (up to 10 TeV) for different kinds of radiation (photons, electrons, positrons, protons, neutrons, muons, charged pions and kaons). The calculated conversion coefficients given in Appendix I can be found on FLUKA web site (<http://www.fluka.org/pickup/DoseCoeff/>).

#### 4.7.2. MarsREC Fluences converted to Dose Equivalent

Software macros have been created to evaluate the fluences of particles in the energy ranges identified in Tables 2-4 to 12-7 for each protons, neutrons, electrons and photons. These macro files were run for all the simulated cases illustrated in Table 4-14.

After fluences were computed for each particle,  $i$ , conversion factors were multiplied by the fluences to obtain the ambient dose equivalent.

CASE	LONG [E]	LAT [N]	NAME	SOLAR LONGITUDE	Time <sup>1</sup> [HOURS]
A	75	-7.5	(TP)	180°-210°	12
B	75	-12.5	(TP)	180°-210°	12
C	80	-7.5	(TP)	180°-210°	02
D	80	-7.5	(TP)	180°-210°	12
E	80	-7.5	(TP)	180°-210°	22
F	80	-12.5	(TP)	180°-210°	12
G	-105	22.5	(OM)	180°-210°	12
H	-140	22.5	(OM)	180°-210°	02
I	-140	22.5	(OM)	180°-210°	12
J	-140	22.5	(OM)	180°-210°	22

**Table 4-14- Simulated Cases used for dose equivalent calculations**

Then for each kind of particle the total dose equivalent,  $H_i$ , was obtained by adding the contributions from all energy ranges

$$H_i = \sum_E f^i_{H^*(E)} \cdot \Phi_i(E) \quad (4-11)$$

Finally the total ambient dose equivalent,  $H$ , was obtained by adding all the contributions from the different particles.

$$H = \sum_i H_i \quad (4-12)$$

For the particular case of ions, FLUKA does not give conversion factors. Since ions are heavy particles with charge, and fluence-to-dose equivalent conversion spectra binning for ions was assumed to be similar to protons. However according to Table 4-13 protons' weighting factor,  $W_R$ , is 5 while the weighting factor,  $W_R$ , for Alpha particles, fission fragments and heavy nuclei is 20. Therefore, for each energy binning, the fluence-to-dose equivalent conversion factor for ions was considered to be given by the correspondent proton fluence-to-dose equivalent conversion factor multiplied by four.

Table 4-15 shows dose equivalent obtained for different particles at different locations

Simulation case	depth	Dose Equivalent [cSv/yr]					Total Solar Minimum
		Protons	Neutrons	Electrons	Photons		
G	9.60	2.84	6.20	0.20	0.08	9.90	
F	13.65	2.78	6.17	0.21	0.08	9.80	
D	13.95	2.82	6.19	0.22	0.08	9.90	
A	14.12	2.82	6.15	0.22	0.08	9.87	
E	14.46	2.88	6.32	0.22	0.08	10.16	
B	14.46	2.80	6.19	0.22	0.09	9.89	
C	14.63	2.82	6.27	0.22	0.08	10.00	
H	16.46	2.74	6.00	0.22	0.08	9.61	
I	16.63	2.80	6.13	0.23	0.08	9.85	
J	17.44	2.95	6.06	0.22	0.08	9.90	

**Table 4-15- Dose equivalent calculations for different simulated cases**

#### *4.8. Verification of Mars Radiation Environment simulations*

This subchapter aims at evaluating MarsREC predictions in comparison with other predictions and experimental data.

It is important to notice that none of the available results, neither the experimental data nor the software predictions, were obtained exactly in the same conditions of the MarsREC simulation results. For that reason this subchapter intends to get an evaluation of orders of magnitude instead of accurate validation.

##### *4.8.1. Comparing MARIE observed Doses*

The MARIE experiment [MARIE, 2003] is a payload on the 2001 Mars Odyssey Orbiter; the orbiter is part of an ongoing series of unmanned missions to Mars under the Jet Propulsion Laboratory's Mars Exploration Program. MARIE is one of three instrument packages aboard the orbiter, and it is designed to collect data on the radiation environment to help assess potential risks to any future human explorers. The MARIE team has also performed simulations.

The Mars Odyssey Orbiter was launched from the Kennedy Space Center on April 7, 2001 using a Delta II launch vehicle, and it reached Mars on October 24, 2001. Once it was captured in Mars orbit, an aerobraking technique was employed which used the Martian atmosphere to slow the spacecraft and adjust it to a circular science orbit with an altitude of about 400 km. The orbit adjustment process ended in January 2002, and the science mapping began in February of that same year. The primary science mission intended to continue through August 2004.

The focus of MARIE was to determine the galactic cosmic ray energy spectra during the maximum of the 24th solar cycle, and to study the dynamics of solar energetic particle events and their radial dependence during both the cruise phase and the orbit phase around Mars.

MARIE was constructed to measure particles with energies in the range of 15MeV to 500MeV per nucleon.

The MARIE instrument provided radiation data continuously until Oct. 28. At that time, immediately following a 4-hour period in which DSN coverage was unavailable, MARIE's

---

DC-DC converter was found to be well over its temperature limit. MARIE was not responsive and was turned off. Some 12 hours after MARIE was turned off, Odyssey entered safe mode, likely due to the intense solar activity.

#### 4.8.1.1. *In orbit Dose rate measures*

MARIE measured doses in orbit of Mars are published [MARIE, 2003] from December 2002 to October 2003.

Figure 4-26 illustrates the dose rate in units of mrad/day measured in orbit of Mars Planet (400km height) from May 2003 to September 2003.

It is described in MARIE scientific reports that during solar quiet GCR period the dose rate may vary between 15 to 22mrad/day. In the presence of SEP enhanced dose rate can vary between 20mrad/day and 30mrad/day and can also show larger peak values that can exceed 1000mrad/day.

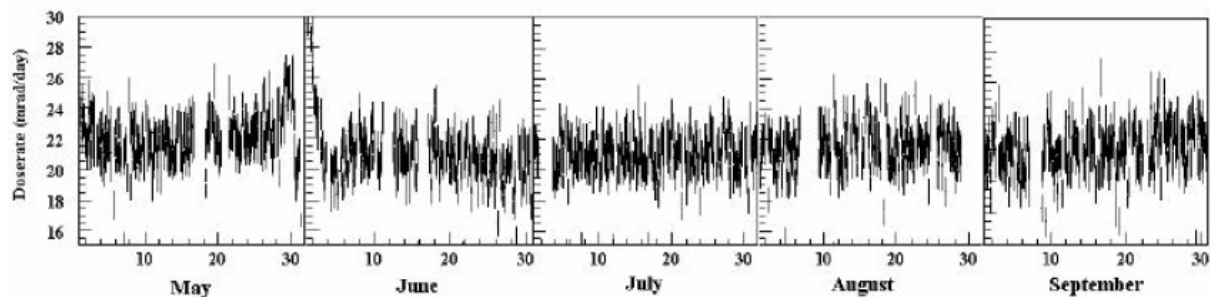


Figure 4-26 - MARIE dose rate measurements from May through September 2003; the last SPE observed in this period was May 31-June 3.

#### 4.8.1.2. *MarsREC Dose rate at the surface*

Dose rates at the surface of Mars have been computed using MarsREC for one location in Tyrrhena Paterae at 12h Martian Universal time at longitude 0°. Results show that dose rates at the surface can vary from around 10mrad/day due to GCR protons, to around 50mrad/day in the presence of strong SEP. Dose rates of the order of 1000mrad/day are estimated due to peak fluences of SEP based on the solar event of October 1989 (See Table 4-16).

Table 4-16

DATA/MARSREC	GCR	SEP	PEAK SEP
MARIE (in orbit)	15 – 22	20 – 30	> 1000
MARSREC (at the Surface)	10	5 -50*	100 – 1000*

\* Depending on the Solar Event intensity

#### 4.8.2. Comparisons of Dose Equivalent results

During the design phase of Mars Radiation Environment Experiment (MARIE) the team has performed simulation work using HZETRN code.

Figure 4-27 shows MarsREC converted dose equivalents both with and without ions (blue and magenta triangles) and MARIE predictions (red dot). It can be seen that the maximum relative difference is obtained for the total dose equivalent considering the MarsREC conversion for all particles including ions and it is as much as 3%.

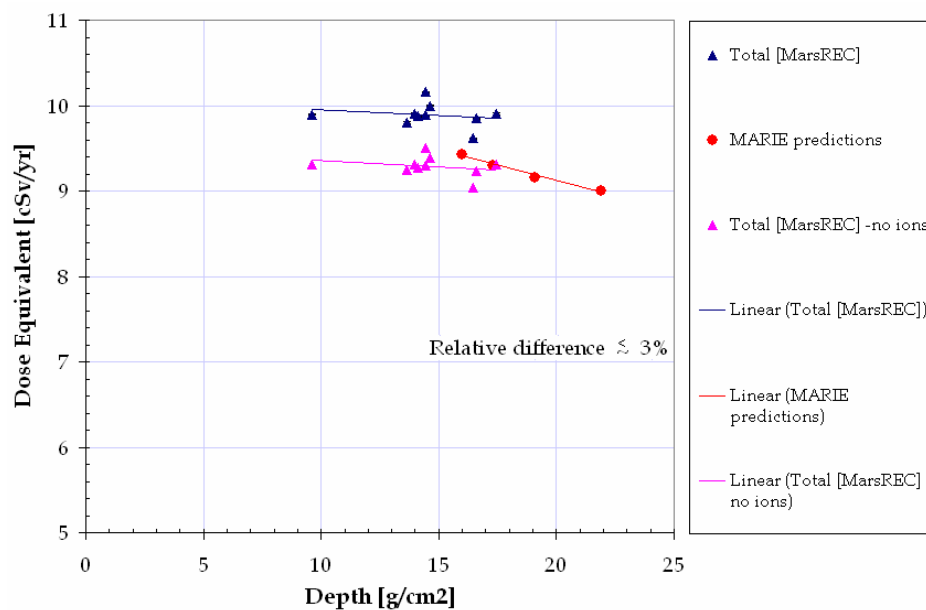


Figure 4-27 – Dose Equivalents

### 4.8.3. Comparisons of Fluences

In 1997 NASA published a study for Shielding strategies for Human Space Exploration [Wilson, 1997]. Presented results were obtained using HZETRN code with the first nuclear fragmentation database NUCFRG1.

Among several other results they publish the energetic particle flux spectra for solar minimum GCR emergent from 50g/cm<sup>2</sup> of lunar regolith.

Table 4-17 illustrates the soils composition and densities considered by this study for both the Moon and Mars.

**Table 4-17**

REGOLITH	COMPOSITION	DENSITY [g/cm <sup>3</sup> ]
LUNAR	52.6% SiO <sub>2</sub> 19.8% FeO 17.5% Al <sub>2</sub> O <sub>3</sub> 10.0% MgO	0.8-2.15
MARTIAN	58.2% SiO <sub>2</sub> 23.7% Fe <sub>2</sub> O <sub>3</sub> 10.8% MgO 7.3% CaO	1.0-1.8
MARSREC	70% SiO <sub>2</sub> 30% Fe <sub>2</sub> O <sub>3</sub>	3.75

Figures 4-28 and 4-29 show the parallel between the MarsREC backscattering protons and neutrons (respectively) for different times and locations at the surface of Mars and NASA results for lunar regolith for depth of about 50g/cm<sup>2</sup>.

Note that the assumed compositions and densities for both soils are slightly different and for this reason this comparison shall work as an evaluation of orders of magnitude instead of a validation. Moreover in the MarsREC simulation there is still the atmospheric shielding while in NASA results are obtained without atmosphere.

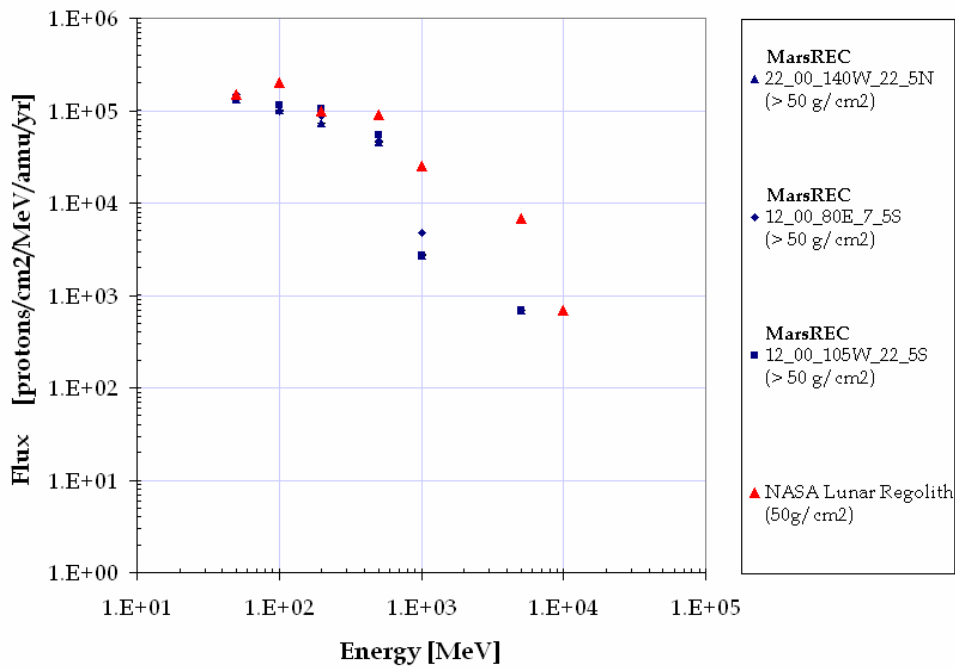


Figure 4-28 – Proton flux spectra for solar minimum GCR emergent from  $\geq 50\text{g}/\text{cm}^2$  regolith: In dark blue MarsREC results for Martian Regolith and in red triangle NASA results for Lunar Regolith.

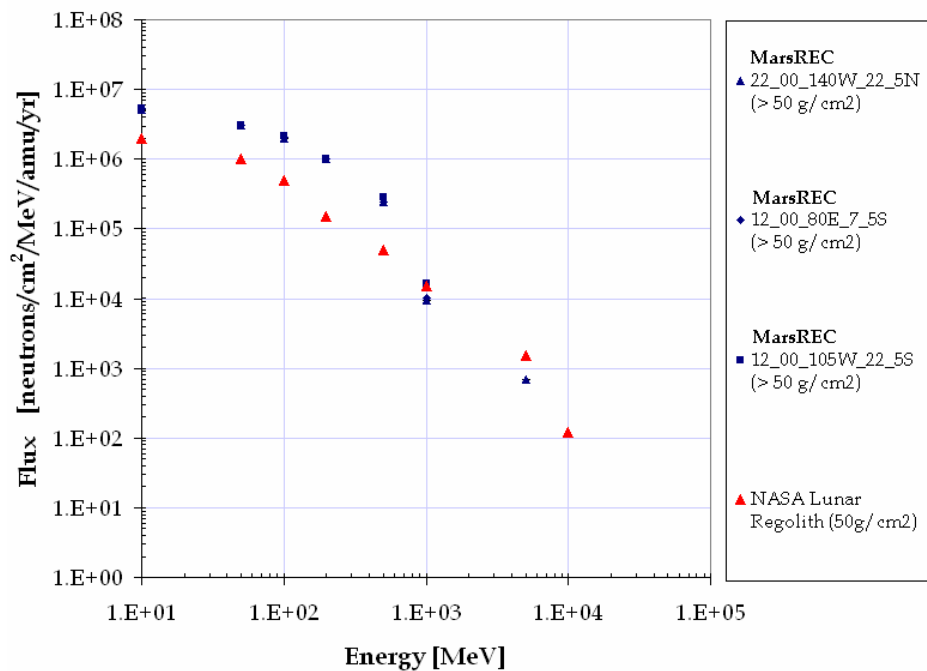


Figure 4-29– Neutron flux spectra for solar minimum GCR emergent from  $\geq 50\text{g}/\text{cm}^2$  regolith: In dark blue MarsREC results for Martian Regolith and in red triangle NASA results for Lunar Regolith.

#### 4.9. *Importance of the soil composition*

MarsREC was used to estimate the impact of soil composition and density in the surface radiation environment.

Table 4-18 shows the different composition simulated, correspondent densities and data label from *a* to *e*.

Composition	Data	Density [g/cm <sup>3</sup> ]
Fe <sub>2</sub> O <sub>3</sub> +SiO <sub>2</sub>	a	1.16 & 3.37
H <sub>2</sub> O <small>(surface)</small>	b	1.00
RealSoil	c	2.12
RealSoil+H <sub>2</sub> O <small>(50 m)</small>	d	2.12
CO <sub>2</sub>	e	1.70

**Table 4-18- Simulated soil compositions**

Simulated data on neutrons' backscattering and ambient dose equivalent was collected and analysed.

Figure 4-30 shows the dependence of backscattering radiation on the soil composition and soil density. It can be seen that the presence of water is very important.

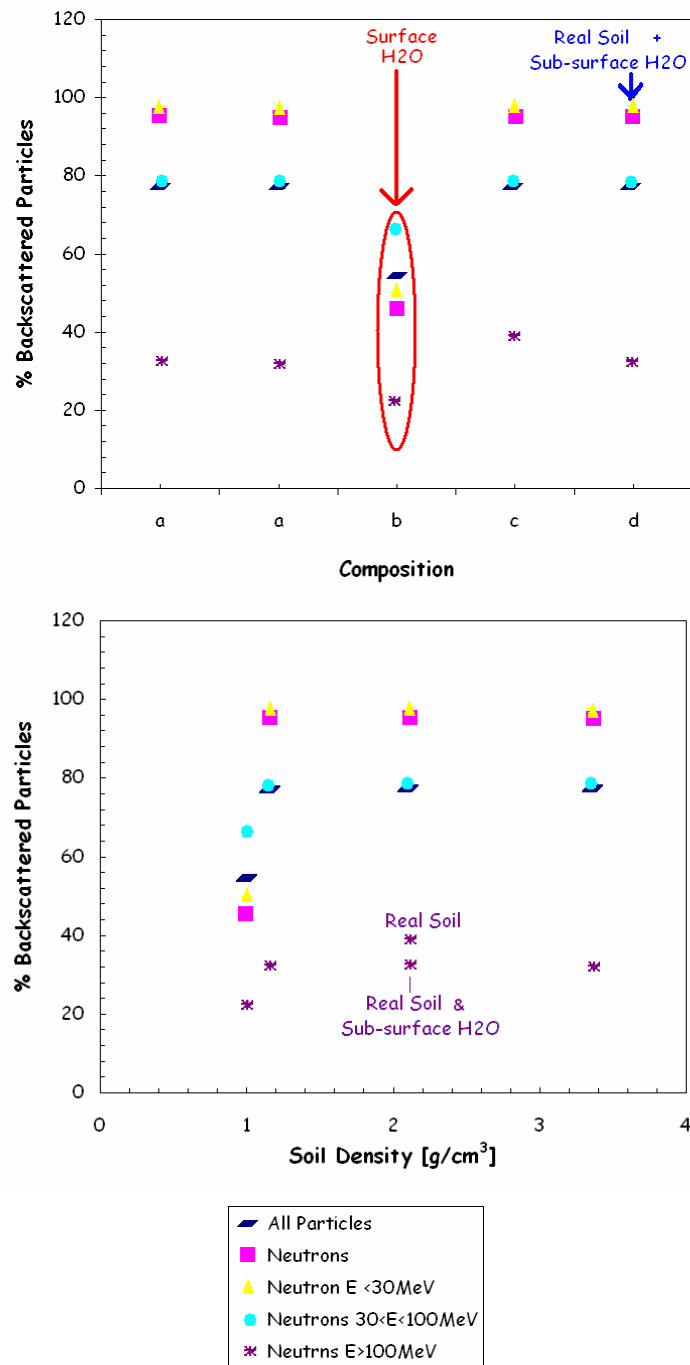


Figure 4-30- Dependence of neutron backscattering on soil composition (top) and density (bottom)

Figure 4-31 shows ambient dose equivalent due to neutrons as a function of composition and weight percentage of Fe<sub>2</sub>O<sub>3</sub>.

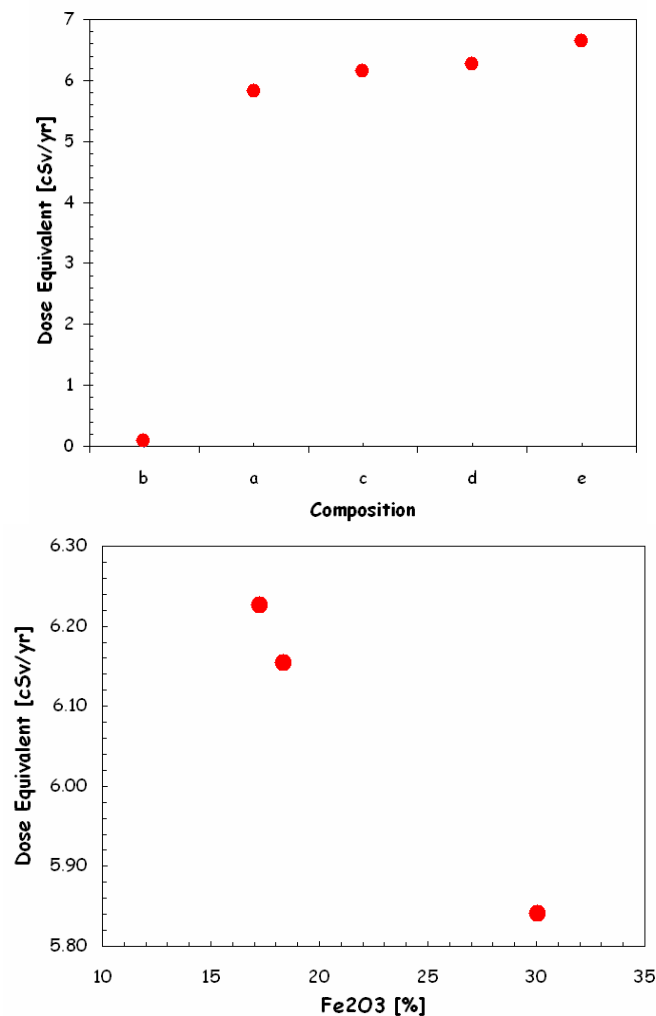


Figure 4-31- Dependence of ambient dose equivalent due to neutrons on soil composition (top) and weight percentage of Fe<sub>2</sub>O<sub>3</sub> (down).

#### 4.9.1.1. Simulation results: analysis

From the analysis of MarsREC simulation results it can be inferred that:

- The presence of water at the surface is the most significant parameter to affect surface radiation environment.
- Changes of 10 to 20% in soil density in the range of 1 g/cm<sup>3</sup> can give differences of 60% percent on neutron backscattering or 30% on general backscattering radiation.
- CO<sub>2</sub> simulation shows a slightly increased ambient dose equivalent (~10%).
- Changes of Fe<sub>2</sub>O<sub>3</sub> weight percentage also induce 10% changes in neutron ambient dose equivalent.

#### 4.10. *Is Mars a nice place to live?*

MarsREC has shown [Keating, 2005], [Keating2, 2006] that GCR and SEP proton-induced total fluxes at the surface of the order of the  $10^3$  particles/cm<sup>2</sup>/s. Table 4-19 gives mean typical individual particle fluxes expected due to GCR and worst case scenario of SEP.

Particles Species	SEP [# /cm <sup>2</sup> /s]	GCR [# /cm <sup>2</sup> /s]
Protons	610	1.58
Electrons	55	0.42
Neutrons	286	8.87
Ions	0.12	0.06
Photons	515	6.70

**Table 4-19 - mean typical individual particle fluxes expected due to GCR and worst case scenario of SEP**

Most of the published studies concerning the effects of radiation in manned missions for space exploration, present results in units of dose equivalent.

Figure 4-32 illustrates MarsREC ambient dose equivalent results obtained for GCR protons: in different location on the surface of Mars in red triangles and for the interplanetary environment in cyan circle. Dark blue triangles are MARIE [MarsOdyssey, 2006] ambient dose equivalent predictions for the surface of Mars and typical values at Earth ( $\sim 0.1\mu\text{Sv}/\text{hour}$ ) are given by the orange degraded mark.

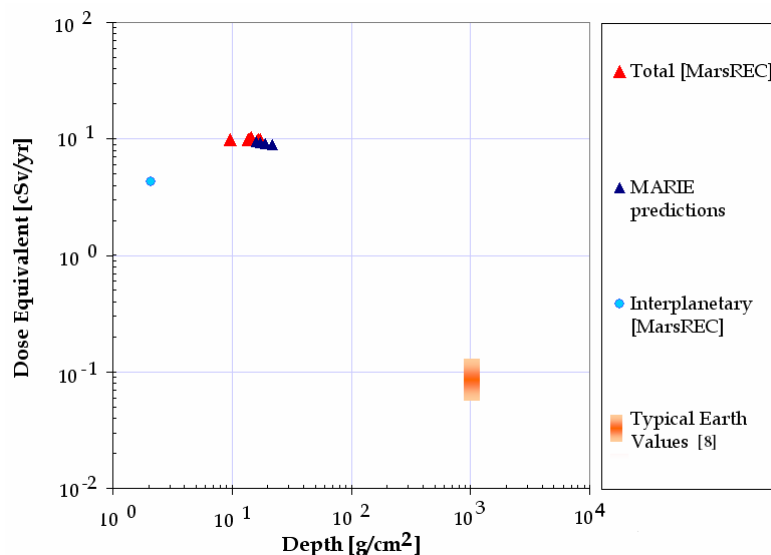


**Figure 4-32 – Ambient dose Equivalent.**

Table 4-20 shows ambient dose equivalents obtained by MarsREC Monte-Carlo calculations and values for Primordial Mars and present-day Earth dose equivalents estimated by other simulation software [Schneider, 2005].

Particles Species	Dose [cGy/yr]
Present-day Mars [MarsREC]	8.01
Primordial Mars <sup>1</sup>	0.10
Present-day Earth <sup>1</sup>	0.05

**Table 4-20 – Ambient Doses Equivalents due to GCR**

From the analysis of figure 4-32 and Table 4-19 it can be seen that Mars is expected to have a much more severe radiation environment than typically at Earth.

Such big differences between Earth and Mars are mainly explained by the presence of the Earth magnetosphere. The magnetosphere strongly shields Earth from incoming and secondary protons and electrons. Inner and outer belts prevent protons with energies around 50 to a few hundred MeV to travel through Earth's dense atmosphere, interact and generate secondary radiation that would reach the surface contributing to higher radiation levels. In contrast Mars magnet field is remanent and localized with maximum intensity of 100nT (~less than  $10^{-3}$  of the Earth's surface magnetic field intensity). Studies have been published showing that the Martian magnetic field works as a localized shielding only for low energy electrons [Desorgher, 2005] not preventing proton transport and spallation through the atmosphere and soil.

Predictions show that ambient dose equivalents at present Mars surface are expected to be more than two orders of magnitude higher than that on Earth. In other words, nowadays Mars presents a hostile radiation environment for the development of earth-like life. Therefore the design of manned missions to Mars shall take in special consideration its severe radiation environment.

### *4.11. Future Developments*

As discussed in this chapter the developed tools have been verified with previous existent tools and some MARIE data, showing that the framework is capable of calculating the energy spectra and particle species at any location on Mars with a resolution of  $5^\circ \times 5^\circ$ . The models also show the relative importance of the backscattered component of the radiation environment and the importance of the soil composition. While the total ionizing dose at the surface is of lesser concern to EEE components, the design of manned missions to Mars should take in special consideration the severe radiation environment. Moreover the relative abundance of protons and neutrons may result in Displacement Damage and Single Event Effects on EEE components.

The model is developed for ease of future upgrades. Therefore work can still be done at different levels, namely: a) GCR Ion; b) Validation of developed tools; c) Implementation of new data from space missions; and d) Extrapolation for other planets.

#### a) GCR ions

The latest GEANT4 versions allow a reasonable performance simulating ion interaction with materials, from around 70MeV/nuc to 5GeV/nuc. Additionally a new interface with DPMJET [DPMJET, 2000] is available for the GEANT4 community and is included in the dMEREM physics list, enabling a better handling of hadronic processes above 5GeV/nuc. A list of applications of dMEREM is already planned for the future month and includes the simulation of Martian radiation environment due GCR ions.

#### b) Validation of developed tools

NASA has lately supported the development of new tools and improvement of previous existent tools. It is now important to validate the developed models with other up to date tools.

#### c) Implementation of new data from space missions

New databases, improved and updated versions of current are continuously being created based on current space missions. It is of major importance to analyze new data, improve the models in order to take account of the state of art knowledge and validate with real radiation-monitors data if applicable.

---

#### d) Extrapolation for other planets

As discussed in Chapter 2, Space missions to other planets of the solar system have shown that several of them have a significant magnetic field. In particular, the giant planets have a much stronger magnetic field than Earth. Their magnetospheres are furthermore much larger than Earth's, in part because of the stronger dipole moments and because the solar wind becomes increasingly weaker far away from the Sun. Mercury has a magnetic moment only about 1/2000 that of Earth and a very small magnetosphere. The magnitudes of the dipole moments of Mercury, Earth, Jupiter, Saturn, Uranus and Neptune, in units of  $10^{25}$  Gauss-cm<sup>3</sup>, are 0.004 (approx.), 7.9, 150.000, 4300, 420 and 200, respectively [Lepping, 1995] .

Venus (as well as Mars) has a very weak magnetic field, probably not generated by dynamo action in the core but possibly due to remnant magnetization of crustal rock acquired earlier from a stronger magnetic field generated by a now dead core dynamo [Spohn, 1998] . A dynamo powered by thermal power alone would have ceased a few billions of years ago as the core cooled to an extent that it became stably stratified [Spohn, 1998] .

Mars has no radiation belts of trapped particles, but the presence of the localised magnetic fields may create shielded zones. Work by Laurent Desorgher [Darnell, 2007] has shown that electrons up to 10MeV can experience significant deflection by the anomalies. The effect of Martian localized magnetic field is of less significance for protons in the range of energy that may concern effects on EEE devices.

Each Planet has its own features; however the most important drivers are the distance to the Sun, presence of magnetospheres and atmospheres. By studying and implementing planetary particularities it is possible to generalize and improve the tools developed for Mars in order to adapt to other planets and moons.

---

## 5. Single Event Effects on EEE components

This Chapter aims at describing the *Component Degradation Simulation tool (CODES)* and results. CODES [Keating, 2008] was designed as a general framework in order to predict radiation degradation on EEE components when submitted to different radiation environments. As described by equation 3-16 in Chapter 3, degradation rates can be predicted by convolving the incoming fluence (or flux) spectrum through the device with a damage function at component level. CODES achieves the goal of generality because it interfaces information on the device with GEANT4 based Monte Carlo application for tracking primary and secondary particles at component level. Additionally it is designed to output information required for degradation analysis. Finally it is able to convolve the information at component level with input radiation spectrum in order to predict degradation rates. Detailed simulations are also possible by using an interactive tool developed to fit device sensitivity, *Sensitive Volume interactive Fit Tool (SV-FIT)*, based on ground irradiation tests.

Due to the extended range of mechanisms and devices, the development and application of CODES and SV-FIT were based on the analysis of a specific device. The device selected was the 4Mbit ATMEL AT60142F Static Random Access Memory (SRAM) comprehensively characterised as part of ESA's "Reference SEU Monitor" development activity [Sørensen, 2005].

The methodology and framework developed in order to predict radiation-induced degradation on EEE components is herein described with detailed explanation of its different modules. However to introduce nomenclature and to provide background material for discussion, this chapter begins with a brief introduction to the problem of predicting Single Event Effects (SEE) on Memory devices.

### 5.1. SEE on Memory devices

A SRAM cell consists of two inverse back-to-back CMOS inverters (described in Chapter 3).

In each memory cell there is a word line selection, which gives the address of each memory cell to be written or read, and a bit line (and inverse bit line) via which the data is written or read, as illustrated in figure 5-1. From simplicity of notation N refers to NMOS and P refers

---

to PMOS, therefore CMOS1 consists of MOS devices N1 and P1, while CMOS2 consists of N2 and P2.

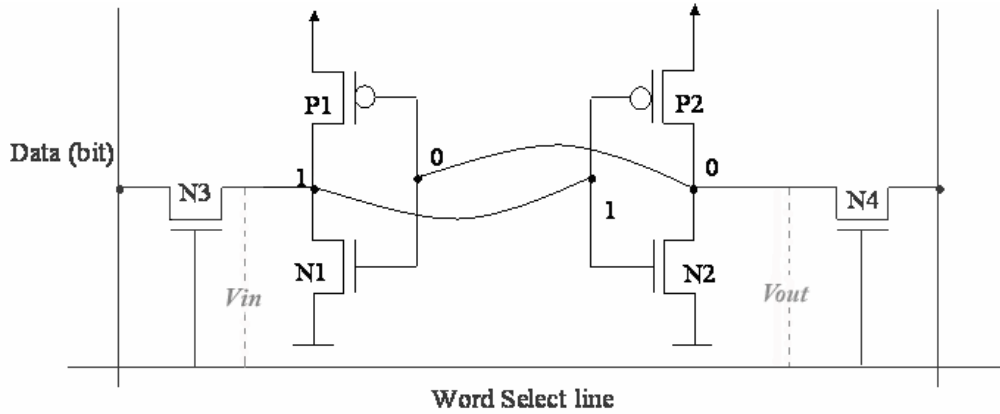


**Figure 5-1 – Scheme of a memory cell**

According to the description of Chapter 3, if the logical input at the left node is “1”, it means that gate voltage at N2 is  $V_{GS}^n = V_{dd}$ . Therefore according to its transfer function N2 is on. At the same time  $V_{GS}^p$  at P2 is off and  $V_{out}$  (NMOS Drain-Source voltage) is equal to 0V, i.e., the logical output will be “0”. This value is transferred to the input of CMOS1 as 0V, thus,  $V_{GS}^n$  of N1 equals 0 and N1 is off. P1 gets  $V_{in}=0V$ , then  $V_{GS}^p$  is  $V_{dd}$ . This means that P1 is on. As a consequence  $V_{out}$  is equal to  $V_{dd}$ , which means that it returns the logical value “1”.

The functioning of a memory cell, where two inverse CMOS ensure that the information loops continuously [Baumann, 2005], is illustrated in figure 5-2. N3 (in the left node) and N4 (in the right node) are read/write NMOS devices, and ensure the flow of information in a continuous loop.

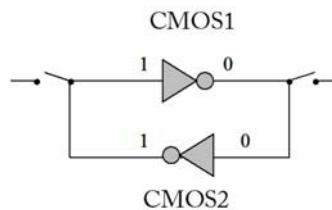


**Figure 5-2- Logical functioning of a recorded memory cell**

Assuming that “0” is stored in the left node, CMOS2 would have “0” at the gate. If the logical value “1” was written in the same node, the gate voltage was set to  $V_{GS}^n = V_{dd}$ , which would tend to get N2 on and P2 off. The provided current would cause the cell to flip. However, the system needs a time to respond to the overwriting process [Baumann, 2005]. This time corresponds to the feedback response of the system.

A sensitive node is defined as any region in a device where collected charge may lead to the upset of the normal functioning of the device. When an ion crosses a sensitive node with the logical value “1” in a SRAM (Figure 5-3), an e-h pair plasma is generated as described in Chapter 3. Part of the carriers is separated and transported due to either funnelling drift or further diffusion. The additional current in N1 causes the drop of the  $V_{\text{storage}}$ . At P1 a hole current starts to compensate. If the collected charge is higher than the critical charge, an error occurs. The SRAM flips if P1 can supply enough current to compensate the additional charge [Baumann, 2005]. Consequently P1 tends to turn-off and N1 on. The voltage drop in CMOS1 starts to turn-on P2 and turn N2 off.

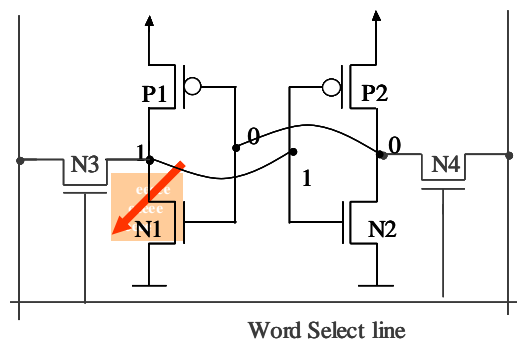


**Figure 5-3- Scheme of a SEU in a SRAM cell**

In a SRAM the effective critical charge described in Chapter 3 consists of a cooperation between two terms: a capacitive term related to the sensitive node,  $C_{\text{node}} \cdot V_{\text{node}}$ , and a term dependent on the system feedback response time,  $\tau_{\text{switch}} \cdot I_{\text{restore}}$ , as described in Equation 5-1.

$$Q_{\text{crit}} = C_{\text{node}} \cdot V_{\text{node}} + \tau_{\text{switch}} \cdot I_{\text{restore}} \quad (5-1) \text{ [Baumann, 2005]}$$

I.e., if the charge collection time of the charge induced by the incoming particle is shorter than the switching time of the system,  $\tau_{\text{switch}}$ , the charge deposited may not be enough to create an error [Baumann, 2005].

### 5.1.1. *Methods for Fitting Device Response functioning*

As described in Chapter 3 and illustrated by figures 3-20 and 3-21, the response function of a device gives the probability of upset, as function of ion linear energy transfer,  $\sigma_{\text{ion}}(LET)$ , or in case of proton and neutrons as function of particle energy,  $\sigma_p(E)$ .

Several fit-functions described in the literature [Tylka, 2007] can be used to represent the measured SEU cross-section data. The following subsections describe the Critical charge, Weibull and Bendel methods.

### 5.1.1.1. Unique Critical Charge Method

If all cells within a memory device are identical with SVs of constant depth, SEU measurements made with monoenergetic ion beams will produce a cross-section curve which is a step function. Every ion above threshold,  $LET_c$ , hitting the volume will cause an upset. In this case the cross-section is  $\sigma_{sat}$ . Ions below the threshold will not upset the device therefore the cross-section is 0, as illustrated in figure 5-5.

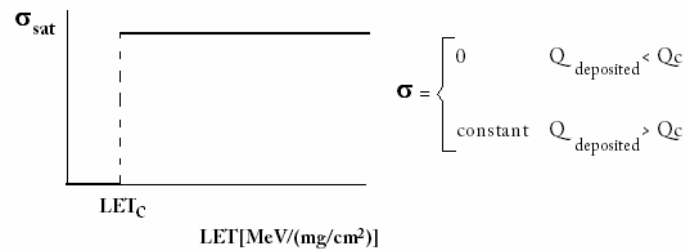


**Figure 5-4- Critical charge method**

Combining equations 3-13, 3-14 the critical charge can be expressed as function of the critical linear energy transfer,  $LET_c$ , and the effective sensitive depth,  $l_{eff}$ .

$$Q_c = \frac{q \cdot \rho \cdot LET_c \cdot l_{eff}}{E_{th}} \quad (5-2)$$

In particular for silicon, with a density,  $\rho$ , of  $2.32 \text{ g/cm}^3$ , this formula yields

$$Q_c = 1.03 \times 10^{-2} LET_c \cdot l_{eff} \text{ pC} \quad (5-3)$$

where  $LET_c$  is expressed in  $\text{MeV}/(\text{mg}/\text{cm}^2)$  and  $l_{eff}$  is expressed in microns.

However step functions are very simplistic descriptions of real device response functions. As described in Chapter 3 real devices show cross-section curves which smoothly vary with LET. Other functions with more parameters, as described in the following subsections, give better description of experimental curves.

### 5.1.1.2. The Bendel Method

As discussed in Chapter 3, proton induced upsets depend on the probability of nuclear reactions, rather than the number of particle directly depositing energy. Therefore the response curve is a function of proton energy.

The Bendel method is often used to describe proton irradiation test data because it gives a good description of proton-induced nuclear reaction.

There are two Bendel functions. The Bendel-1 form was first introduced by W.L. Bendel in 1983. It provides a convenient and widely used single-parameter description of proton-induced SEUs cross-section data [Tylka, 2007]. The Bendel-1 parameter function is described by a single parameter, traditionally called effective threshold "A". Its simplified form may be written as follows:

$$\sigma(E) = \left(24/A\right)^{14} \left[1 - e^{(-0.18y^{0.5})}\right]^4 \quad (5-4)$$

where

$$y(E) = \begin{cases} (E - A)\left(18/A\right)^{0.5} & \text{if } E > A \\ = 0 & \text{otherwise} \end{cases} \quad (5-5)$$

On the other hand Bendel-2 is a modification of Bendel 1-parameter fit. It is a purely empirical functional form, and it has been shown to provide a better description of the cross-section data than the 1-parameter fit for many devices. The Bendel-2 parameter function is described by two parameters, traditionally called "A" and "B". The functional form is somewhat complicated but may be written as follows:

$$\sigma(E) = \left(B/A\right)^{14} \left[1 - e^{(-0.18y^{0.5})}\right]^4 \quad (5-6)$$

where

$$y(E) = \begin{cases} (E - A)\left(18/A\right)^{0.5} & \text{if } E > A \\ = 0 & \text{otherwise} \end{cases} \quad (5-7)$$

For easier treatment of Bendel-2 fit function  $B^{14}=C$  since in fact  $C/A^{14}$ =Limiting cross-section. These functions are often used only for application to proton-induced SEUs, E is the proton energy in MeV and  $\sigma(E)$  is the cross-section in units of  $10^{-12}$  cm<sup>2</sup>/bit.

### 5.1.1.3. The Weibull Method

The Weibull function [Tylka, 2007] may be used to reproduce ions, protons and neutrons SEE cross-section experimental curves. Having four free parameters the Weibull function allows the fit of the cross-section with a smooth single curve. It is given by equation 5-8:

$$\sigma(x) = A \left(1 - e^{-[(x-x_0)/w]^s}\right) \quad (5-8)$$

In particular it is assumed that devices have similar behaviour to proton and neutron irradiation as referred to in Chapter 3. Table 5-1 describes the Weibull parameters required to fit proton, neutron and ion-irradiation test data.

Weibull Method Parameters		Description	
		Protons/Neutrons	Ions
Variable	x	Energy [MeV]	LET [MeV/(mg/cm <sup>2</sup> )]
Plateau	A	$\times 10^{-12}$ [cm <sup>2</sup> /bit]	[m <sup>2</sup> /bit]
Limiting $\sigma$			
Onset parameter, $\sigma(x) = 0$ for $x < x_0$	$x_0$	Threshold Energy [MeV]	Threshold LET [MeV/(mg/cm <sup>2</sup> )]
Width	W	With Parameter [MeV]	With Parameter [MeV/(mg/cm <sup>2</sup> )]
Exponent	s	Dimensionless parameter	

**Table 5-1 – Weibull method parameters for fit of proton, neutrons and ions**

### 5.1.2. Traditional RPP Models

Traditionally, models to predict SEE effects due to direct ionization in complex devices assume that the SV is a Rectangle Parallelepiped (RPP). Furthermore these models assume uniformity of SVs and unique critical charges as described in section 5.1.1.1. Standard tools for SEE prediction due to GCR or SEP, such as CREME96 [Tylka, 1997] use the RPP model.

#### 5.1.2.1. Funnelling

The basis of RPP models is that promptly collected charge is mainly deposited by direct ionization in a RPP sensitive volume and that funnelling (outside of the SV) is considered to be negligible or is even considered to decrease SEU rate [Tylka, 2007]. Those models may only represent funnelling as a fine tuning of the model. Others [Petersen, 1992] consider an overall RPP SV that already accounts for average funnelling dimensions.

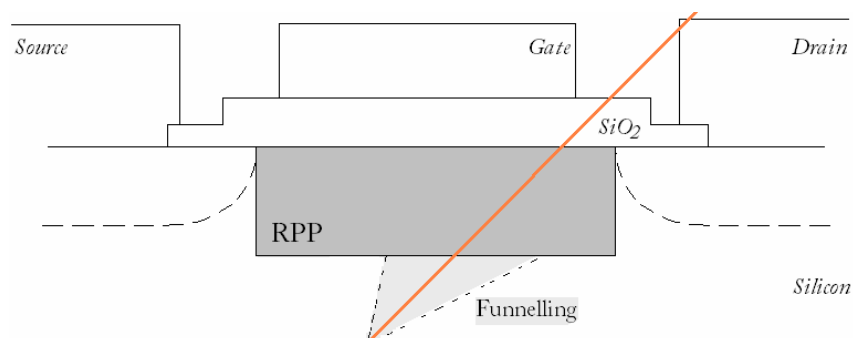


**Figure 5-5 – RPP model scheme**

---

### 5.1.2.2. *From step function to smooth curves*

As already discussed in section 5.1.1.1 the assumption of uniformity of SVs and unique critical charge leads to a step cross-section curve. However authors tend to assume that stochastic variations of deposited charge and statistic fluctuations of sensitivity may justify the smoothed shape of experimental SEE curves. Regarding transversal dimensions of the SV, some authors assume the sensitive transversal area as LET-dependent, others assume fixed sensitive area. These assumptions give two different interpretations of SEE cross-section curves obtained from experimental data (discussed in Chapter 3). The LET-dependent sensitive area describes the cross-section curve as the increase of the sensitive area in the device cell, while the second leads to the statistical interpretation of the curve as the variation of number of upset cells.

RPP models usually neglect scattering effects in the sensitive volume, they assume the incoming *ion trajectory* remains approximately in a *straight line* in the sensitive volume, as discusses in section 3.2.2. These assumptions reveal behaviours not compatible with real processes in modern devices. They appear to fail for modern devices with different shielding configurations, complicated SV shapes, several SVs, small features, and consequently depletion sizes. Furthermore, contrary to the GCR for which high-energy ions predominate, in case of SEP, the contribution from low LET heavy ions is important [Inguibert, 2004]. It is therefore necessary to accurately model the transport of particles through the shielding and accurately understand the real shape of the SV and the physical mechanisms leading to charge collection.

### 5.1.3. *Non-RPP models*

Other different models, known as non-RPP models<sup>1</sup>, have been developed aimed at understanding and modelling SEE cross-section data. For example the model developed by Langworthy defines the cross-section curve as SV shape-dependent and assumes that the path length distribution is responsible for the cross-section curve shape [Langworthy, 1989]. Figure 5-6 depicts a simplified geometrical explanation of cross-section curve modulation due to path length distribution. In case the SV is a RPP the path length distribution is given by a

---

<sup>1</sup> [Langworthy, 1989], [Petersen, 1993], [Petersen, 1998]

---

Dirac delta function which argument is the RPP thickness corrected by the cosine of the incident angle, plus plateau at low path length values. This path length distribution leads to cross-section curves that are step functions [Xapsos, 1993]. In the bottom of figure 5-6 it can be seen that for a non-RPP volume the path length distribution is a continuous function between the maximum and minimum thicknesses of the volume, plus a plateau at low path length values due to the angle effect. In this case the cross-section distribution is a function of the LET. Minimum LET value is given by the critical charge divided by the maximum path length and saturation is reached for high LET ions, depositing charge above the critical charge.

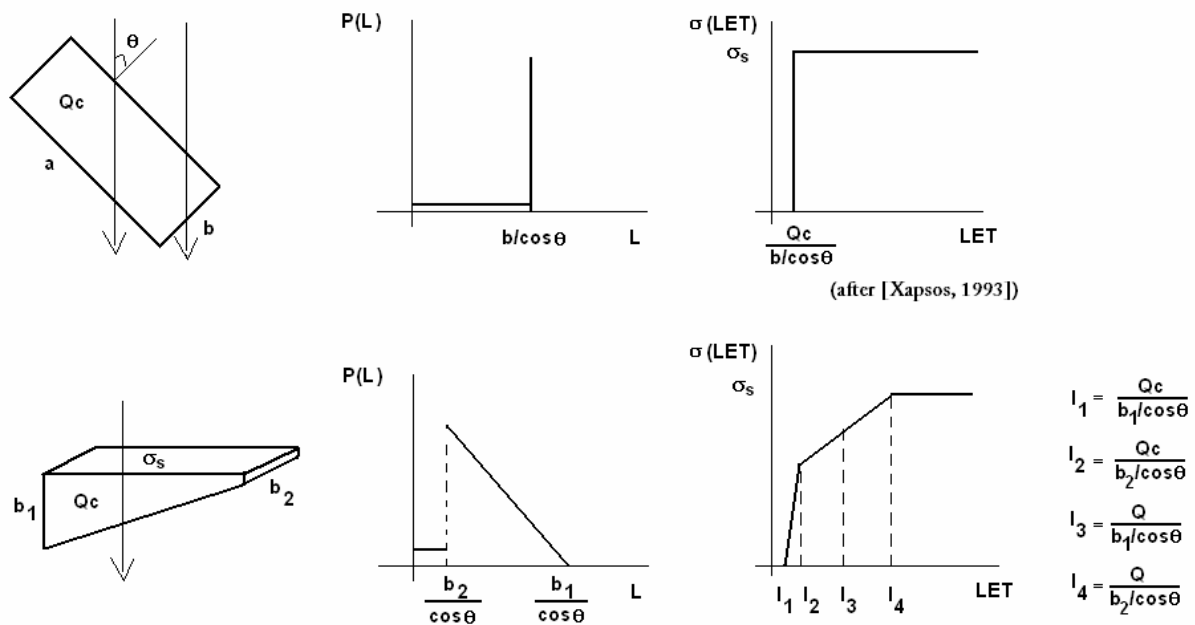


**Figure 5-6 - Geometrical explanation of cross-section modulation due to path length distribution**

In fact many authors, even those that use RPP models, believe that the solution for the understanding of the SEE cross-section curve is to calculate the shape of the sensitive volume and then the distribution of ion path lengths through the sensitive region [Xapsos, 1993].

In particular the non-RPP model investigated this chapter assumes that the sensitive volume is modulated directly by the physical mechanisms leading to charge collection and contributing to upset the device. This will help to analyse the question: to what extent can the departure from a step function be explained by physics of particle interaction, without considering geometrical or sensitivity variation.

---

## 5.2. *Simulation framework*

### 5.2.1. *GEANT 4 and device physics*

As described in Chapter 4, GEANT4 is a toolkit primarily designed to simulate High Energy Physics experiments [Agostinelli, 2003]. In the past years a large effort from the GEANT4 collaboration and users has been done in order to adapt and develop GEANT4 application for space related issues<sup>2</sup>.

GEANT4 being a Monte Carlo toolkit enables the track of primary and secondary radiation from the generation point until they are absorbed, exit the device or interact. These features bring an important contribution for device physics simulation. Some recent developments have been done in order to improve GEANT4 capabilities such as including screened Coulomb scattering to compute the nonionizing component of energy deposited in semiconductor materials by energetic protons and other forms of radiation [Weller, 2004]. This is an essential aspect for previous NIEL computations [Inguibert, 2006]. Other recent applications include as well modelling of TID effects [Butt, 2007].

However the use of GEANT4 in predicting components degradation and failure mechanisms is still a quite novel application. Therefore GEANT4 does not take into account the complexity of crystalline structures of materials neither mechanisms such as electron-holes transportation, recombination and trapping, leading to single event effects.

Since 1996 many researchers and institutions<sup>3</sup> are working in building tools that combine Monte Carlo radiation tracking with expensive circuit simulation tools. These integrated frameworks are often in-house tools developed for specific in-house applications, not available for public use. Furthermore these tools often require detailed technology description of the device, for an accurate simulation, often not delivered by the vendor. The development of a flexible integrated tool enabling the fit of sensitive volume properties as well as the path length distribution based on experimental data or/and on vendor information is therefore considered of great benefit.

---

<sup>2</sup> [Keating, 2005], [Keating, 2008], [Allison, 2006], [REAT], [DESIRE], [SEPTINESS], [GEANT4\_SUH], [Santin, 2005]

<sup>3</sup> [Murley, 1996], [Makoto, 2005], [Weller, 2006], [Warren, 2006], [Butt, 2007], [Inguibert, 2007].

---

### 5.2.2. *Component Degradation Simulation (CODES) Framework*

The developed framework aims at predicting radiation-induced degradation on EEE components and enabling verification with other software such as CREME96. Figure 5-7 gives an overview of CODES' philosophy. By combining as much information as possible the framework is capable of predict radiation induced degradation on EEE components. Additionally it is interfaced with the GEANT4 applications. CODES involves two different approaches to the quantitative algorithms namely: The *Statistic* and *Microscopic* approaches.

Under the *Statistic approach*, illustrated on the left side of figure 5-7, GEANT4 is just used to simulate the energy spectra and particle species at component level. The simulated primary and secondary spectra above the threshold are then convolved with the experimental SEE cross-section curves. This approach is described in detail and compared with CREME96 simulations in subchapter 5.4.

On the right side of the diagram of figure 5-7, the *Microscopic approach* is described. This approach uses GEANT4 application interfaced with device analysis techniques in order to achieve the simulation of microdosimetry in the device. Aiming at the fit of sensitive volume shape and dimensions, as well as the path length distribution, the microscopic approach consists of three main modules to perform SEU rate prediction of memory devices. The three modules are Geometry Description (GD), Efficiency Matrix (EM), and Analysis Module (AM). The SV-FIT module is an iterative process that by employing the three modules GD, EM and AM, calculates a function for the Sensitive Volume and subsequently calculates the cross-section versus LET curve required to predict SEU rates. The framework is developed with flexibility in mind such that SEU rate prediction may be achieved employing vendor technology details, semiconductor/circuits simulation data, laser mapping data or irradiation test data. The device physics input into the main GEANT4 application can be done by the efficiency matrix module.

Ultimately CODES aims at being optimized as an engineering user friendly tool. Under this environment CODES may allow the user to simulate device degradation response with the minimal information available. Therefore CODES may be able to estimate simulation accuracy and SV volume shape and dimensions whenever used without device vendor information based only on ground based test data. Finally it shall be noted that this work is in progress in order to complete the CODES designed capabilities.

---

Subchapter 5.5 will focus on describing the concept and development of SV-FIT. Final discussion will be held in order to describe additional corrections that need to be implemented to optimize the tool’s capabilities.

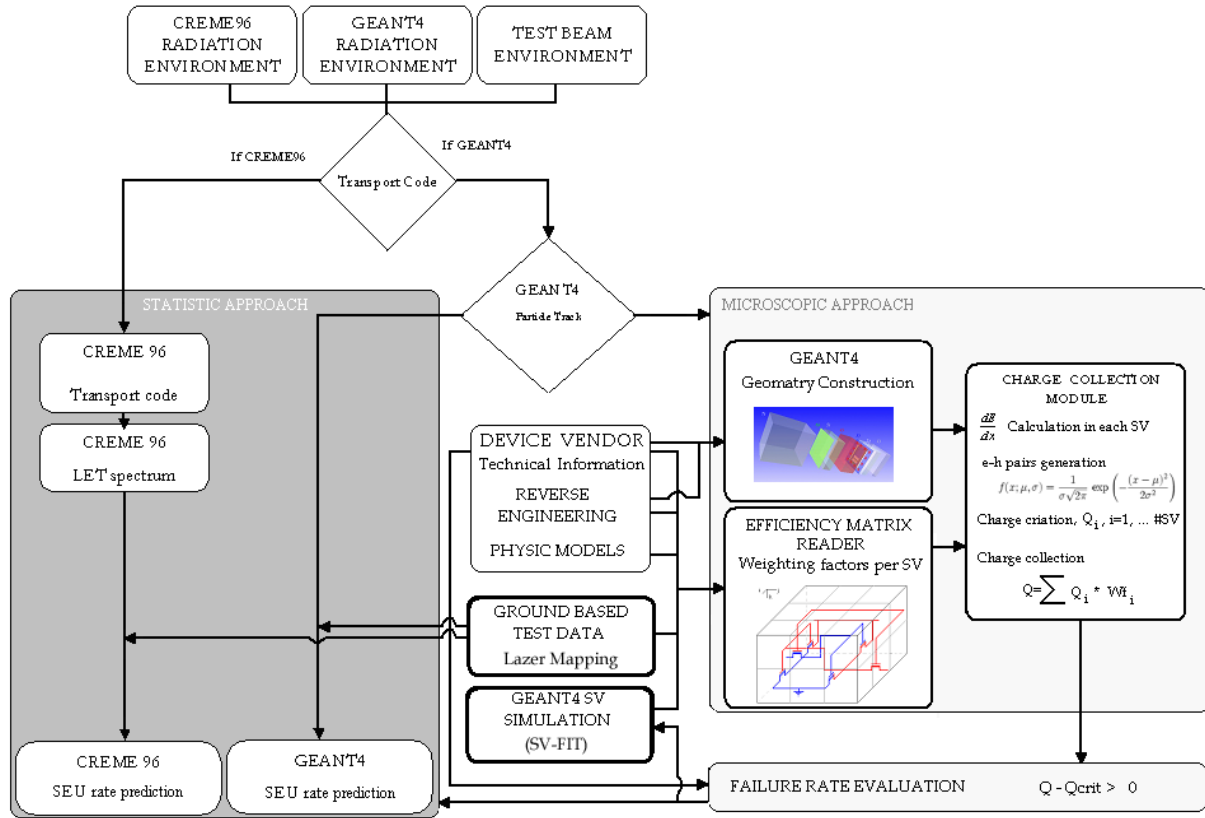


Figure 5-7- CODES Philosophy

### 5.3. ATMEL Device

The AT60142F is a very fast low power Static RAM organized as 512K x 8 bits. It is produced on a radiation hardened 0.25  $\mu\text{m}$  CMOS process having an access time of 15ns. The device is specified for 3.3V with a 6-transistor memory cell. The die is 6.1 x 11.2 mm resulting in a 68.3  $\text{mm}^2$  size with a memory cell size of 9.765  $\mu\text{m}^2$ . To prevent the occurrence of multiple SEU in a byte, ATMEL has organised the memory plan in eight parallel blocks of 512K x 1 with the control and voltage regulation block in the lower middle position. The layout of the 8 blocks is clearly visible on the die photo shown in figure 5-8 [Sørensen, 2005].

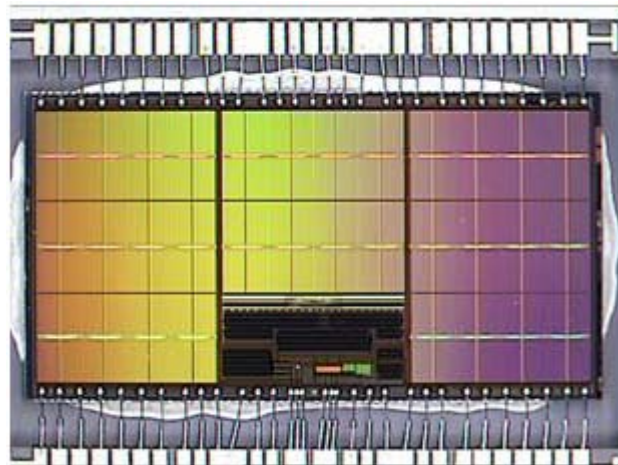


Figure 5-8- ATMEL 4-Mbit SRAM – 8 blocks of 512K x 1

The technology details delivered by ATMEL on the 4Mbit AT60142 device were carefully studied. The details on doping species, implantation energy and doses were combined with layering geometry and discussed with experts at the Components Division of ESA. SRIM [Ziegler, 2006] was used to calculate implantation depths and doping distribution. Moreover a gds2 file viewer was used to extract all the dimensions of the device layers.

The ATMEL single bit cell scheme is analysed in figure 5-9 giving information on the bit line, word line and Vdd and Vss. The painted areas correspond to the Field Oxide (Gates) in red, the Metallization 2 in dark grey and the Metallization 3 in cyan.

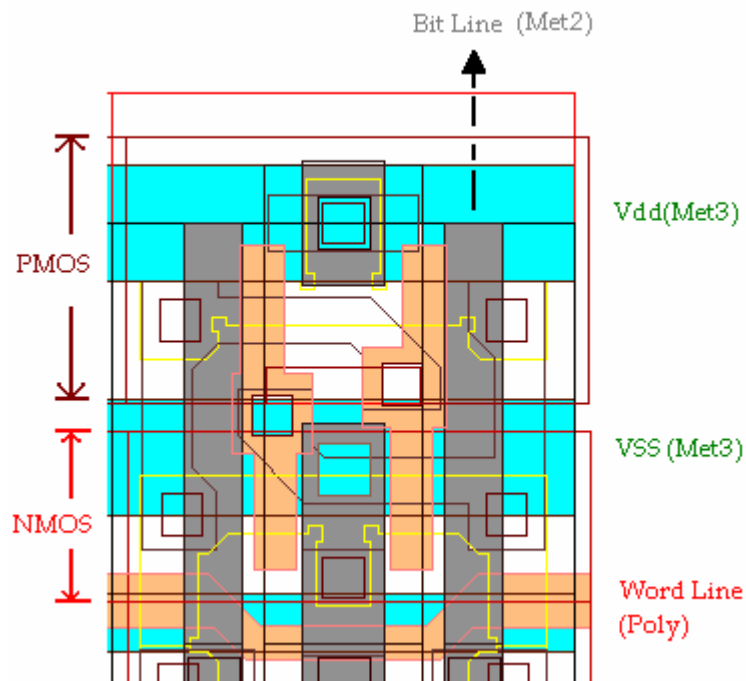
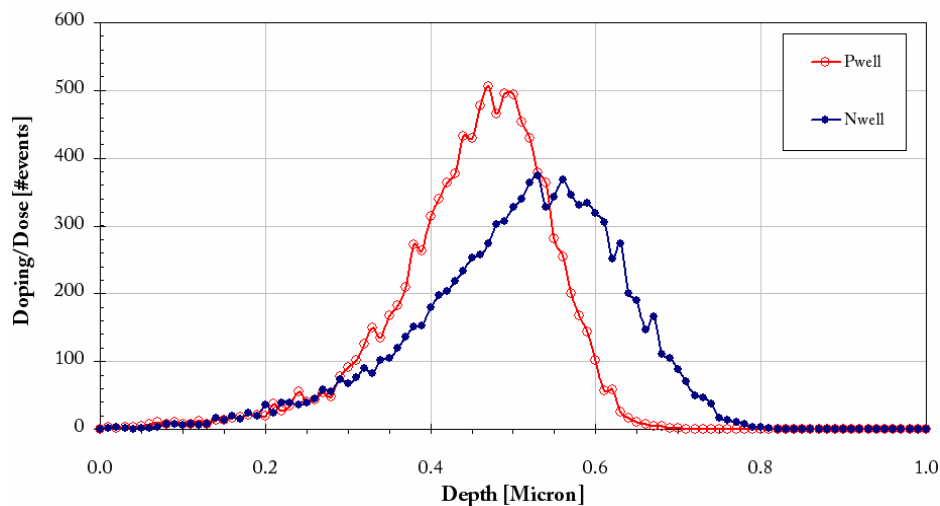


Figure 5-9- Single bit cell





**Figure 5-11- Ion ranges in the CMOS technology.**

Figure 5-11 shows a detailed analysis of the implanted ions ranges in silicon. However it is important to remark that GEANT4 does not allow the use of doping gradients. For that reason, in order to define the GEANT4 Geometry class the following possibilities were discussed.

- I. The implanted layer can be considered as an uniform average doping density for a thickness to be specified, as depicted in figure 5-12 a);
- II. The implanted layer can be considered as a set of sub-layers (daughter volumes) with different doping densities according to the depth and position, as shown in figure 5-12 b).

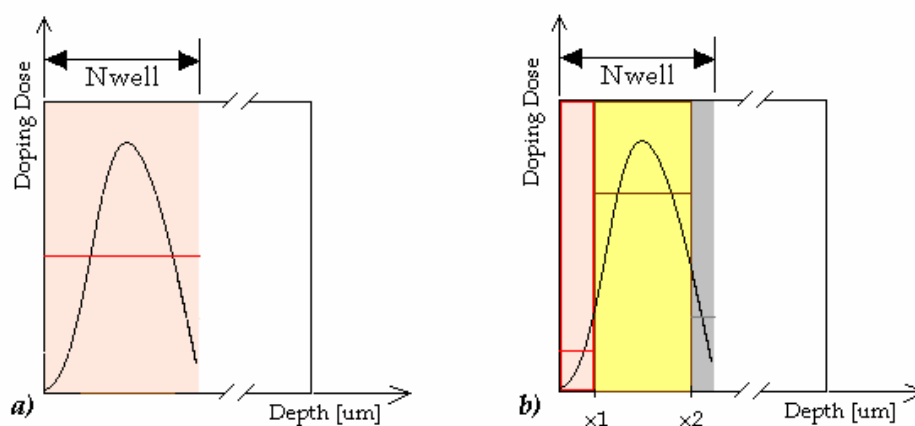


**Figure 5-12- Two possible ways of construct implants geometry into GEANT4.**

#### *5.4. Statistic Approach*

The *statistic approach* works similarly to standard tools such as CREME96. This method considers the sensitive volume as a rectangle parallelepiped (RPP) and inputs the device response functioning given by the fit of irradiation test data with functions, such as Weibull or Bendel [Tylka, 2007].

In particular this module was used to predict proton and neutron-induced Single Event Upsets at the surface of Mars based on the 4-Mbit ATMEL AT60142F SRAM devices comprehensively characterized as part of ESA's SEU reference monitor development activity [Keating, 2006].

From the three different statistic methods described in subsection 5.1.2 the Weibull was found to reproduce better both ion and proton experimental cross-section curves. The following sections will describe in detail fit parameters adjusted to experimental curves and how they were used to predict the SEU rate for 4-Mbit ATMEL SRAM device in the Martian radiation environment.

##### *5.4.1. Reproducing irradiation test data*

A detailed study was carried out in order to identify the parameters set to better adjust SEU response function data obtained for both proton and ion irradiation of the ATMEL AT60142F device.

Figure 5-13 shows ATMEL AT60142F ion irradiation test data and the Weibull function data reproduction.

---

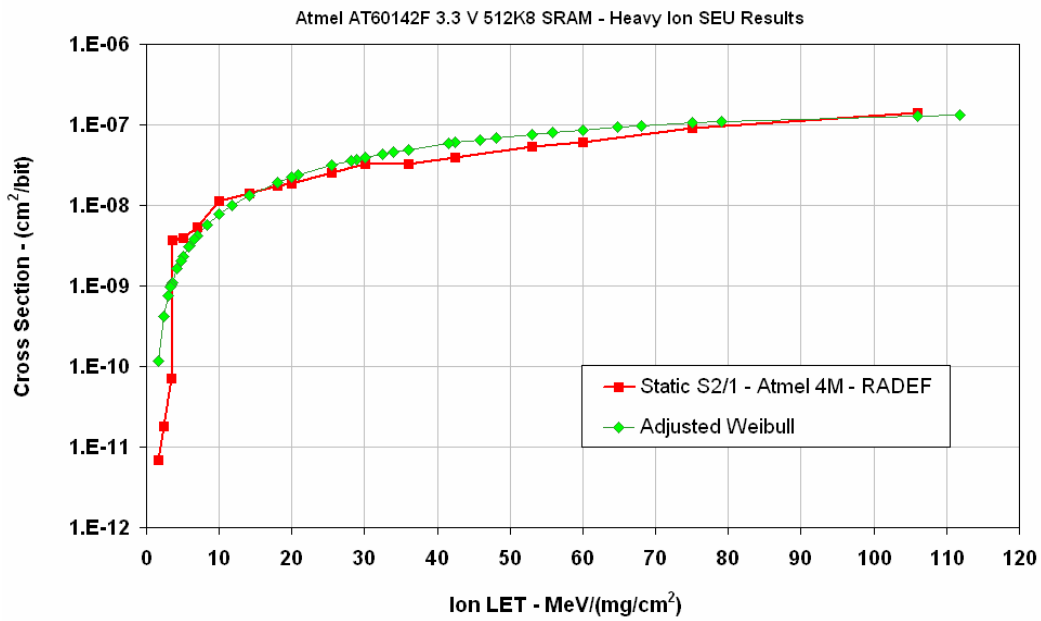


Figure 5-13 - Reproducing experimental data with Weibull response function

Figure 5-14 illustrates ATMEL AT60142F proton irradiation test data and the Weibull function data reproduction.

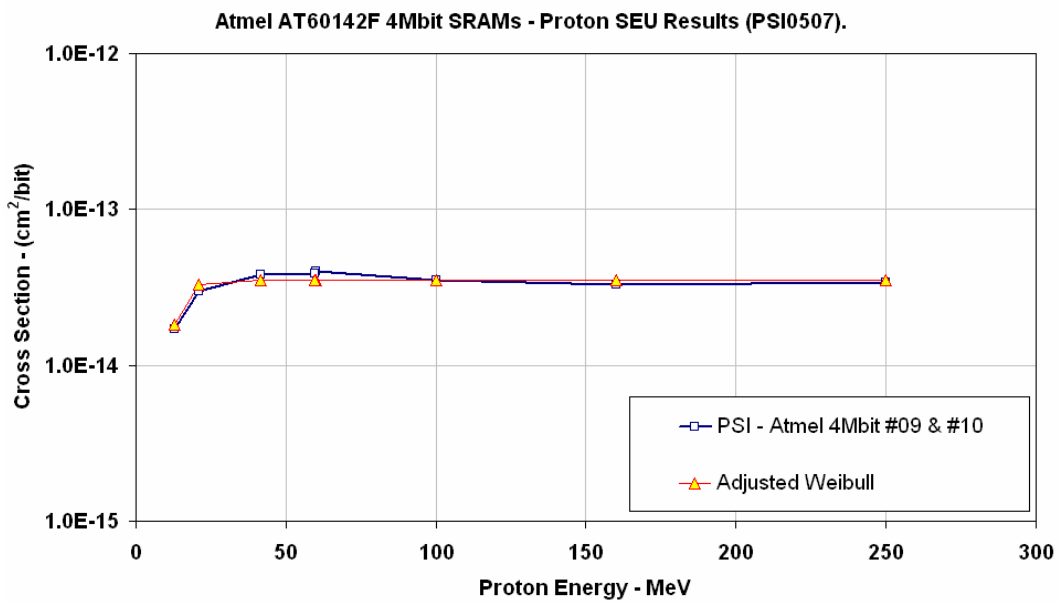


Figure 5-14- Reproducing experimental data with Weibull response function.

Table 5-2 illustrates the sets parameters of the adjusted Weibull functions to ion and protons irradiation data. As previously discussed device response to neutron irradiation is expected to be similar to the response under proton irradiation. Therefore Table 5-2 assumes the Weibull response function for protons can be used to predict and SEE rates for neutrons as well.

Weibull Method Parameters		Ion		Proton/Neutron	
		units		units	
Plateaux	A	15	[ $\mu\text{m}^2/\text{bit}$ ]	0.0353	$\times 10^{-12}[\text{cm}^2/\text{bit}]$
Sensitivity Threshold (LET <sub>c</sub> or E <sub>c</sub> )	x0	1.2	[MeV/(mg/cm <sup>2</sup> )]	10	[MeV]
With	W	65	[MeV/(mg/cm <sup>2</sup> )]	4	[MeV]
Exponent	s	1.47	---	1	---

**Table 5-2- Weibull Fit parameters for ion irradiation test data**

5.4.2. SEU rate predictions

As described by equation 3-19, the upset rate for incident protons or neutrons, N, is given by the integration of the SEU cross-section over the energy spectrum. The SEU cross-section for ions, protons and neutrons are assumed to be given by Weibull functions of Table 5-2, while at the surface of Mars the differential energy spectrum,  $d\Phi/dE$ , is given by environmental module described in Chapter 4.

As illustrated in figure 5-15, the device RPP geometry is implemented in the MarsREC geometry inside the MarsREC Environmental Module (described in Chapter4) [Keating, 2005].

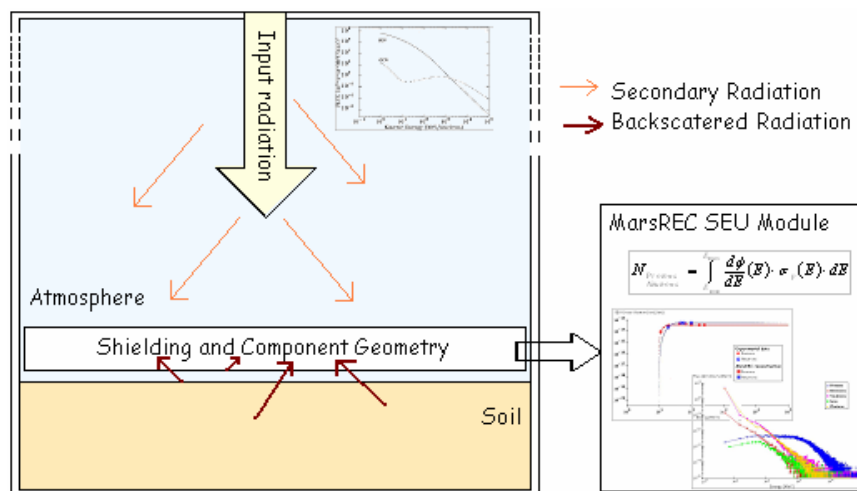


**Figure 5-15 –Simulation set-up scheme**

Results discussed later in this section were obtained by running the GEANT4.7 simulation over  $10^5$  events of GCR and SEP protons with isotropic and perpendicular-to-surface distribution at the top of the Mars atmosphere and through an isotropic 1cm thick aluminum

shielding. The sensitive volume was simulated as a rectangle parallelepiped of 1.5  $\mu\text{m}$  thickness of Silicon [Keating, 2006]. The resulting particles were collected in the Silicon SV.

Figure 5-16 shows the SEU cross-section obtained by the convolution of the shielded spectra at the sensitive volume with the Weibull function, as a function of particle energy for protons and neutrons. Finally it compares the calculated SEU cross-sections with experimental data of figure 5-14 for protons and also with experimental data obtained from neutrons irradiation tests [Sørensen, 2005].

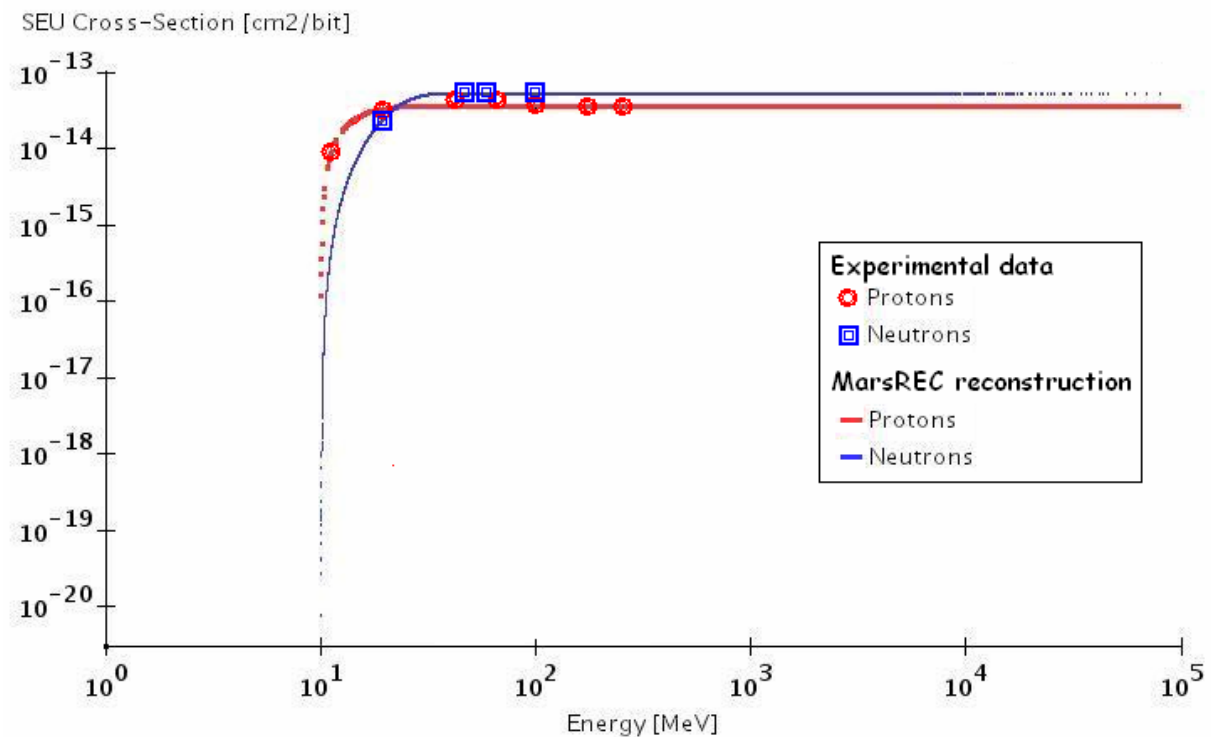


Figure 5-16- SEU cross-sections for protons and neutrons: MarsREC reconstruction and experimental data.

Table 5-3 illustrates the expected dose deposition by electrons, protons and others such as short lived particles (muons and pions) and light ions (tritium, deuterium and alpha particles) in the device.

Particles Species	Dose per year [Rad(SiO <sub>2</sub> )]
All	2.75
Protons	2.08
Electrons	0.30
Other	0.33

Table 5-3 – Deposited dose in the sensitive volume at the Surface of Mars

As discussed in Chapter 4, the radiation environment at the surface of Mars due to proton GCR and SEP did not give significant signature of secondary ions<sup>4</sup>. Therefore SEU rate predictions were explored for protons and secondary neutrons.

MarsREC SEU rate prediction for protons and secondary neutrons due to GCR and SEP protons at the surface of Mars were evaluated and presented in Table 5-4. Note that, as discussed in Chapter 2, GCR input represents a quiet and continuous scenario in time while SEP scenario represents a worst week case of a solar event. Therefore results of Table 5-4 show SEU rates in units of SEUs/device/year for GCR and SEUs/device/week for SEP. It can be seen that in the presence of a solar event the upset rate is in a week almost as higher as during one year of quiet GCR scenario.

PARTICLES	SEU RATES	
	GCR [#/device/year]	SEP [#/device/week]
PROTONS	4.98	3.80
NEUTRONS	2.21	0.48

**Table 5-4 – SEU rates predicted at the surface of Mars due to CGR and SEP protons, secondary protons and neutrons**

#### 5.4.3. Comparisons with CREME96

There are some major differences between the developed statistic method and CREME96. The developed model being based on GEANT4 employs a three-dimensional Monte Carlo simulation, tracking all primary and secondary particles in all directions (section 4.1).

The CREME96 nuclear transport module calculates a numerical solution of the one-dimensional continuity equation, taking into account both ionization energy loss (in the continuous-slowing-down approximation) and nuclear fragmentation. CREME96 incorporates accurate stopping power and range-energy routines, and uses semi-empirical energy-dependent nuclear fragmentation cross-sections [Tylka1 &2, 1997].

---

<sup>4</sup> Simulation work performed with early versions of GEANT4 did not allow tracking of heavy ions. The latest versions in use in the development of CODES already allow the track of primary and secondary generic ions.

Moreover while MarsREC considers slab geometry, CREME96 uses a spherical geometry in which just particles crossing the center of the sphere are considered.

In order to compare predictions from both models, normalization corrections between different models, geometries shall consider the integration in the boundary conditions of the total flux:

$$\Phi_{Mars}^{GCR/SEP} = 2\pi \int_{E1}^{E2} dE \int_0^{\pi/2} \frac{d\phi^{GCR/SEP}(E)}{dE} \cdot \cos\theta \cdot \sin\theta \cdot d\theta \quad (5-9)$$

Finally results were obtained for different locations at the surface of Mars and with CREME96 a shielding layers was simulated with aluminium equivalent thickness to mimic the atmospheric plus device shielding considered in the GEANT4 simulation. Table 5-5 shows the different simulation cases.

Proton Source	Directional Distribution	MarsREC		CREME	
		Particles	Depth [g/cm <sup>2</sup> ]	Particles	Depth [g/cm <sup>2</sup> ]
SEP	Perpendicular	Protons	16.7	Protons	10-23
		Protons + Neutrons			
GCR	Isotropic	Protons	16.7	Protons	10-23
		Protons + Neutrons			
	Perpendicular	Protons	12.3		
		Protons + Neutrons	16.4 20.1		

**Table 5-5 – Simulation cases**

Figure 5-17 illustrates the comparison between SEU rate prediction simulated using the developed GEANT4 based statistic method and CREME96 for SEP protons. Results are presented for Protons (MasREC\_P) and for both protons and secondary neutrons (MARSREC\_P+N) obtained with a perpendicular-to-surface incident beam.

Figure 5-18 shows results obtained with GCR protons and compares with CREME96 predictions. In this case predictions were obtained with perpendicular and isotropic incident beams for Protons (MarsREC\_P) and for both protons and secondary neutrons (MARSREC\_P+N).

Figures 5-17 and 5-18 show that results are in very good agreement with CREME96 predictions under similar geometric conditions.

Moreover it can be seen that results obtained by the GEANT4 based developed statistic method with a perpendicular incident beam are closer to CREME96 results than those simulated with an isotropic incident beam. This result can be easily understood once CREME96 simulates a spherical-concentric geometry. This geometry is comparable, in a first approximation to infinite slab geometry with perpendicular incident beam. On the other hand, for increased depth the difference between perpendicular incidence and CREME96 increases. GEANT4 being a Monte Carlo tool allows the generation of secondary particles in all 3D directions. Therefore increasing the depth, the pass length of all products of interaction is increased by a cosine factor.

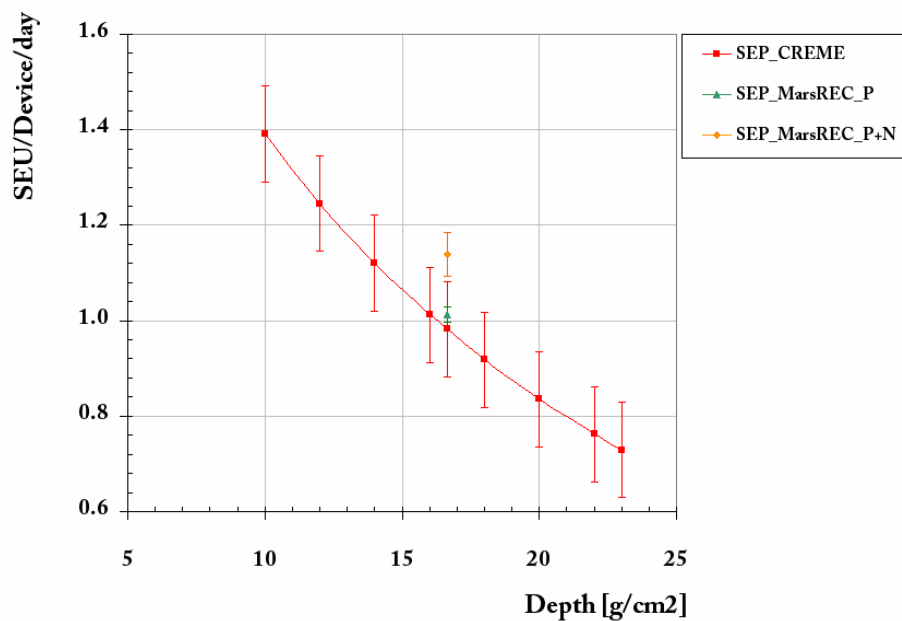


Figure 5-17- SEP- induced simulated SEU rates predictions and CREME96.

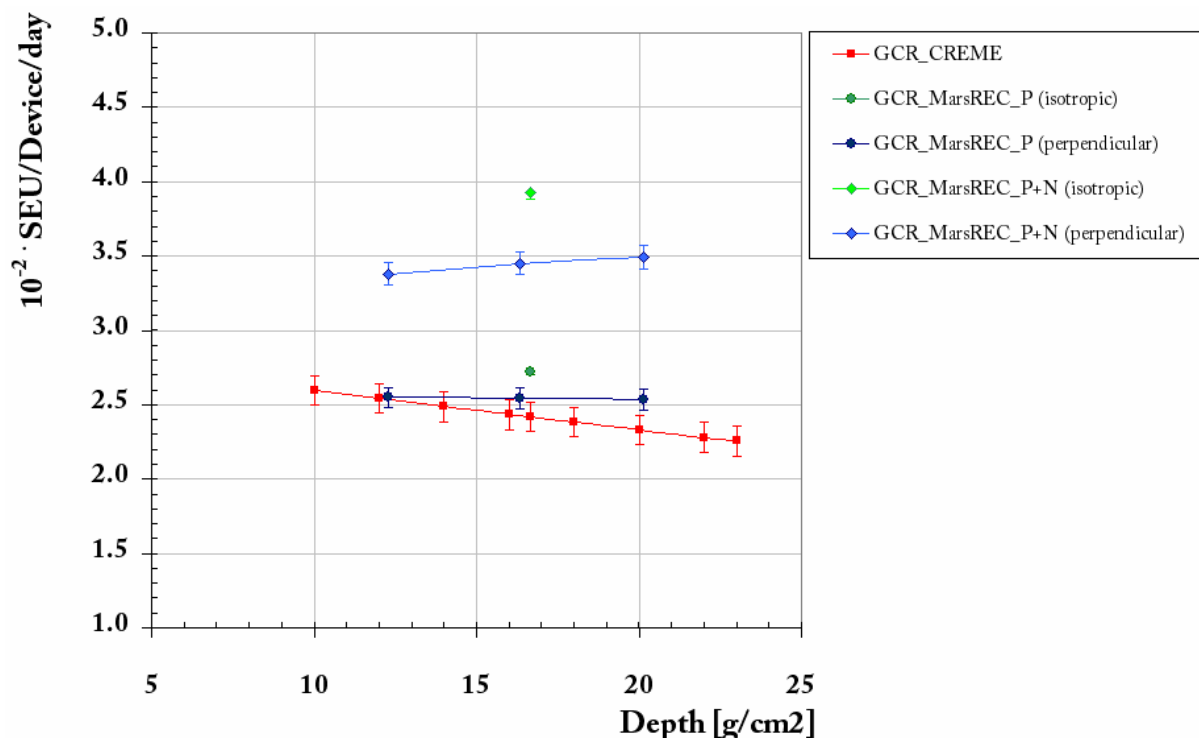


Figure 5-18- GCR- induced simulated SEU rates predictions and CREME 96.

#### 5.4.4. Discussion

The *statistic approach* used in MarsREC provides a comprehensive method to provide SEU Rate prediction for EEE components on Mars also considering secondary particles generated in various shielding configurations, the Martian atmosphere and soil. Results show that the newly developed framework is capable of predicting SEU rates for protons and neutrons. MarsREC results show very good agreement when compared with other software's predictions.

## 5.5. *Microscopic Approach*

This section aims at defining the simulation setup and configurations considered for testing the microscopic approach to the SEU rates calculation in CODES.

### 5.5.1. *Redefinition of Sensitive Volume*

As described in section 5.1.3 CODES assumes the sensitive volume (SV) to be the volume in the device where the charge deposited contributes entirely to prompt charge collection. The sensitive volume shape is not defined or fixed. Instead it will be determined by the interactive fit tool, SV-FIT. However in a first approach CODES assumes the sensitive transversal area of all cells of the device to be fixed (being independent of ions LET), and is given either by vendor technology details or by the ground based irradiation test data saturation cross-section.

### 5.5.2. *Efficiency matrix module*

The Efficiency Matrix is the complete 3D geometry description of the device to process and to output collected charge history. At each unit cell of the matrix corresponds a charge collection efficiency value. In regions where the electric field may contribute to separation of injected carriers and therefore contribute to prompt charge collection, *active regions*, the efficiency is 1. In zones, working as parasitic resistors, that may limit the current flow between active regions, the *passive regions*, the efficiency is 0. In regions where the generated electron-hole pairs have a probability of recombining but are still able to contribute to charge collection, the efficiency values shall be greater than 0 and lower than 1.

However the Efficiency Matrix may be considered as a 2D geometry description if the shape of each sensitive volume is assumed to be known. Sections 5.5.3 and 5.5.4 describe the placement of sensitive volumes and assumed shapes and dimensions, used in the simulations described later in this chapter.

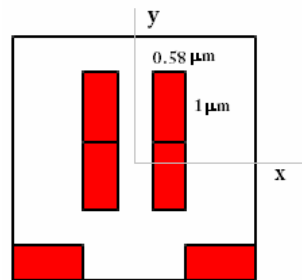
The Efficiency Matrix Module is a class that reads efficiency values in the matrix and associates them to a sensitive volume in the device. The output of the Efficiency Matrix Module is the full placement of the sensitive volumes into the GEANT4 device geometry construction according to the matrix spatial resolution and the association of one efficiency value for charge collection to each volume. The charge collection efficiency is finally passed into the GEANT4 application to the analysis class.

---

### 5.5.3. Placement of Sensitive Volumes

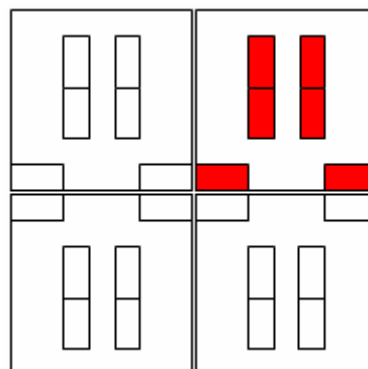
In a first approach sensitive volumes were placed under depletion area of each transistor, according to the analysis of the SRAM unit cell and the electronic circuit.

Figure 5-19 illustrates the dimensions of the sensitive areas and their placement inside a unit cell. The xy dimensions of the cell were estimated based on device geometry details.



**Figure 5-19- Simulated sensitive areas: dimensions and placement**

Finally 4 bit cells were replicated in the simulation as depicted in figure 5-20



**Figure 5-20 – Simulation setup: 4 bit cells with 6 sensitive volumes each.**

The device vertical profile is illustrated in figure 5-21. The whole thickness of the device is 500 $\mu\text{m}$ , including with metallization and epitaxial layers. In the simulation the epitaxial is made of Silicon as well as the sensitive areas, the shielding layer properties are described in section 5.5.3. Shielding is represented in grey on figure 5-21. According to the discussion of subchapter 5.3, the sensitive area was placed 0.1 $\mu\text{m}$  below the top of the silicon device (240 $\mu\text{m}$ )<sup>5</sup> with uniform average density as described in figure 5-12a). Different thicknesses, T, were simulated as described in section 5.5.4.

<sup>5</sup> Note that GEANT4 imports half dimensions.

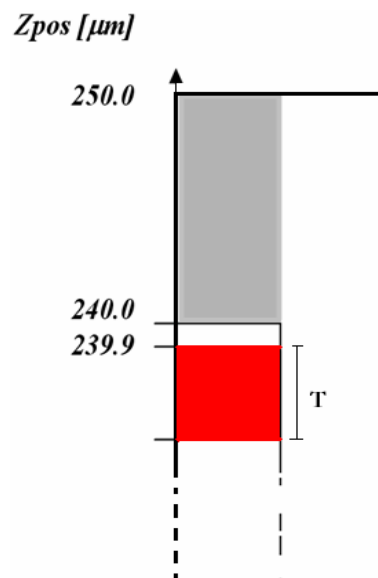


**Figure 5-21- Vertical profile of simulated geometry**

#### 5.5.4. Sensitive volumes thicknesses and shapes

Different geometries were simulated. Initially the SV was constructed as a rectangle parallelepiped with thicknesses of 1, 1.5, 1.7, 2, 3 and 4  $\mu\text{m}$ . Later simulations were performed for different SV shapes and dimensions. Table 5-7 describes the different geometries. The first two values of the transversal area were estimated by the ATMEL device geometry, while the last values were obtained by dividing the maximum SEU cross-section by the number of sensitive volumes simulated, in analogy to the definition of saturation cross-section.

Shape	Thickness [ $\mu\text{m}$ ]	Transversal Area [ $\mu\text{m}^2$ ]
rectangle parallelepiped (RPP)	1, 1.5, 1.7, 2, 3, 4	0.58x1
tetrahedron (TRD)	4	0.58x1 0.81x1
truncated tetrahedron (tTRD)	2	0.81x1

**Table 5-6- Simulated SV shapes and dimensions**

Figure 5-22 depicts the HepRep [Allison, 2008] scheme of the rectangle parallelepiped and tetrahedron SVs.

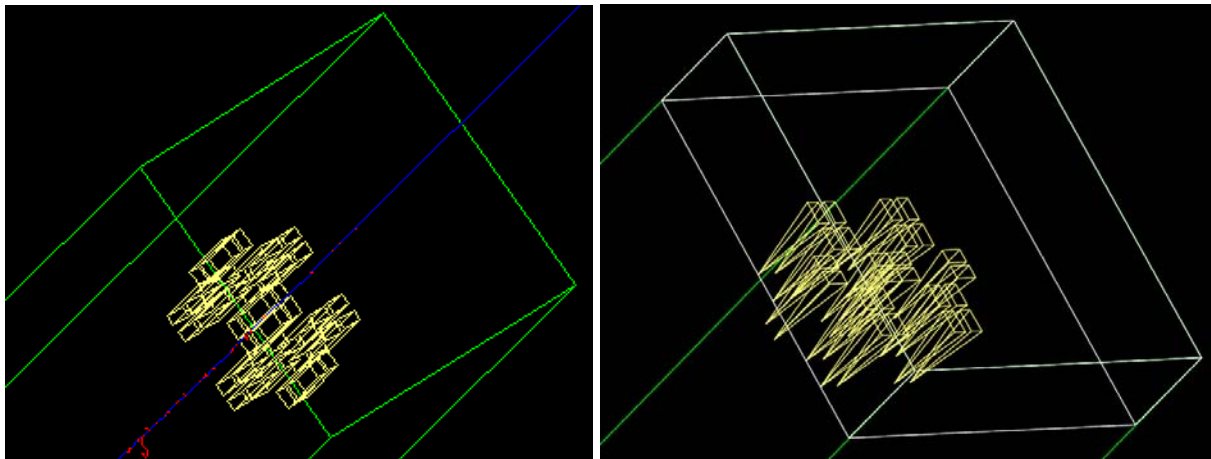


Figure 5-22- Simulation scheme: Rectangle Parallelepiped (left) and Tetrahedron (right).

#### 5.5.5. Shielding

In order to simulate a realistic shielding configuration, the ATMEL technology details were revisited. The final shielding configuration was simulated as illustrated in Table 5-6.

Name	percentage	# layers	composition
Via	41%	3	10% W + 90% SiO <sub>2</sub>
Metal	55%	4	50% AlCu + 50% SiO <sub>2</sub>
Titanium	4%	interfaces	very thin Ti isolation
Final average configuration			
Density	Thickness	Composition	
<i>10.3g/cm<sup>3</sup></i>	4.36 microns	41%(10% W + 90% SiO <sub>2</sub> ) + 55%(50% AlCu + 50% SiO <sub>2</sub> ) 4% Ti	

Table 5-7- Shielding properties

### 5.5.6. Ion Cocktails

As previously referred, the 4-Mbit ATMEL AT60142F SRAM was comprehensively characterized as part of ESA's SEU reference monitor development activity [Sørensen, 2005]. Ion irradiation test data were obtained at Radiation Effects Facility (RADEF), Jyväskylä, Finland. The seven ion species available in the 9.3 MeV/nucleon standard high penetration ion cocktail produced for ESA are described in Table 5-8 [Virtanen, 2007]. In Table 5-8, species' energy, range in silicon simulated with SRIM, range in silicon given at BNL<sup>6</sup>, stopping power simulated with SRIM, and expected LET, are represented.

There are several tools, such as SRIM and BNL, used to calculate the LET caused by ions in a thin surface of silicon, also called surface LET. Depending on the processes they take into account different tools give slightly different results.

GEANT4 simulations were produced for all the ion species of Table 5-10 with the same energy and isotopic number, and ionization state, SEU cross-sections estimated and plotted as function of the LET from BNL.

#	<sup>A</sup> Ion <sup>q+</sup>	E [MeV]	R <sub>SRIM</sub> [μm]	R <sub>BNL</sub> [μm]	St.power [SRIM]	LET [BNL]	Δm/q [%]
1	<sup>15</sup> N <sup>4+</sup>	139	202.1	218.0	1.8	1.7	0.0
2	<sup>20</sup> Ne <sup>6+</sup>	186	145.8	149.0	3.6	3.5	0.0
3	<sup>30</sup> Si <sup>8+</sup>	278	130.1	132.0	6.4	6.0	- 0.9
4	<sup>40</sup> Ar <sup>12+</sup>	372	117.9	117.0	10.2	10.0	- 0.6
5	<sup>56</sup> Fe <sup>15+</sup>	523	97.4	99.0	18.5	18.0	- 5.6
6	<sup>82</sup> Kr <sup>22+</sup>	768	94.0	96.0	32.1	30.0	- 7.1
7	<sup>131</sup> Xe <sup>35+</sup>	1217	89.1	97.0	60.0	53.0	- 2.6

Table 5-8- Standard high penetration ion cocktail produced at RADEF for ESA

<sup>6</sup> Brookhaven National Laboratory Upton, New York [Gardner, 1989] [Lowenstein, 2001].

### 5.5.7. *Angling*

Intermediate LET values were obtained as described in Table 5-9, for the same ion species of Table 5-8 changing the angle of incidence in the device.

LET	Angle of incidence [°]	Ion	Energy
1.7	0	$^{15}\text{N}^{4+}$	139
2.4	45	$^{15}\text{N}^{4+}$	139
3.4	60	$^{15}\text{N}^{4+}$	139
3.5	0	$^{20}\text{Ne}^{6+}$	186
5	45	$^{20}\text{Ne}^{6+}$	186
6	0	$^{30}\text{Si}^{8+}$	278
7	60	$^{20}\text{Ne}^{6+}$	186
10	0	$^{40}\text{Ar}^{12+}$	372
14.1	45	$^{40}\text{Ar}^{12+}$	372
18	0	$^{56}\text{Fe}^{15+}$	523
20	60	$^{40}\text{Ar}^{12+}$	372
25.5	45	$^{56}\text{Fe}^{15+}$	523
30	0	$^{82}\text{Kr}^{22+}$	768
36	60	$^{56}\text{Fe}^{15+}$	523
42.4	45	$^{82}\text{Kr}^{22+}$	768
53	0	$^{131}\text{Xe}^{35+}$	1217
60	60	$^{82}\text{Kr}^{22+}$	768
75	45	$^{131}\text{Xe}^{35+}$	1217
106	60	$^{131}\text{Xe}^{35+}$	1217

**Table 5-9- Angle of incidence**

In this Thesis discussed GEANT4 simulations were obtained with perpendicular ion beams. Further simulations considering 45° and 60° were performed. However the discussion of those results was considered to be outside the scope of this Thesis.

## 5.6. *SV-FIT*

The Sensitive Volume Interactive Fit Tool (SV-FIT) aims at reconstructing the irradiation test data using a GEANT4 based simulation by fitting the device sensitive volume (SV) shape and size. In an iterative process, SV-FIT as described here employs the three modules: the Geometry Description, Efficiency Matrix and Analysis Module to calculate a function for the Sensitive Volume. Results discussed in this subchapter use the efficiency matrix to describe device sensitivity in its simplistic 2D format. The sensitive volumes coincide with the *active regions* where the efficiency is 1 while in the rest of the device is in first order assumed to be *passive* with efficiency 0. Sensitive volume shape was assumed in each iterative step and placed as described in section 5.5.3 and 5.5.4. All the charge deposited in the SVs is considered to be fully collected and contribute to upset the device.

### 5.6.1. *Considerations on AT60142F SRAM Experimental data*

Before starting the discussion of simulation procedures and results it is important to analyse the experimental data. One of the motivations to analyse and simulate irradiation test data of the ATMEL AT60142F SRAM device was the fact that SEU cross-section curve does not exhibit saturation for the tested LET range as theoretically expected. This unexpected effect is comfortably smoothed by the logarithmic scale. The identification of this effect raised an important discussion with ESA expertis that will be considered and described in detail later in this chapter. However this discussion lead the author to assume that ATMEL AT60142F SRAM SEU response function can be defined as a combination of two effects: 1<sup>st</sup> a standard SEU cross-section curve that saturates around  $10\text{MeV}/(\text{mg}/\text{cm}^2)$ , plus an increasing LET-dependent perturbation. According to Mike Xapsos publication in 1993, the solution for the standard SEU cross-section curve is to calculate the shape of the sensitive volume and then the distribution of ion path lengths through the sensitive region [Xapsos, 1993].

Therefore GEANT4 simulation by fitting the SV shape and size is expected to reproduce the first effect while the LET-dependent perturbation shall be included as a correction and optimization of preliminary GEANT4 simulation.

The following sections aim at explaining and discuss the simulation procedures and results.

---

### 5.6.2. Getting RPP Threshold sensitivity from ground based test data

In the beginning of SV-FIT development it was assumed that as in traditional methods SV-FIT should get as input the sensitivity threshold, critical charge or energy (see Chapter 3), and the sensitive volume.

The critical energy was first extracted from experimental results by using the best Weibull function description (section 5.1.2). From equation 3-14 it is clear how to calculate the critical energy in silicon if the critical LET is well known. In Table 5-2 the  $LET_c$  is given as 1.2 [MeV/(mg/cm<sup>2</sup>)]. According to the conversion between charge and energy of equations 3-13, 5-2 and 5-3, the critical energy can be calculated as:

$$E_c = \rho \cdot LET_c \cdot l_{eff} \quad (5-10)$$

In the particular case of perpendicular incidence, the average effective depth,  $l_{eff}$ , is the SV thickness. Table 5-10 shows different critical energy values for different RPP SV thickness considered in the simulation.

SV Thickness [ $\mu\text{m}$ ]	$E_c$ [MeV]
1	0.284
1.5	0.426
1.7	0.483
2	0.568
3	0.852
4	1.136

**Table 5-10 – SV thickness and critical energy**

As previously discussed every time the energy deposited per event exceeds the critical energy an SEU occurs. Based on that principle the SEU cross-section in units of cm<sup>2</sup>/bit is given by:

$$\sigma(LET) = \frac{\text{Number of Evts}(depE > E_c)}{\text{Number of Generated evts}} \cdot \text{Sensitive Area per Bit} \quad (5-11)$$

Consequently the SEU cross-section can be computed using the microdosimetry method of CODES application. Primary ions simulated according to Table 5-8 were tracked through the device as well as the secondary particles produced. Energy deposition per event was computed and finally compared with the critical energy as explained above.

Finally SEU cross-sections for each ion were plotted as function of the LET and compared with experimental values obtained for two different tests as depicted in figure 5-23. The lines in the figure show fits to both experimental and simulation data.

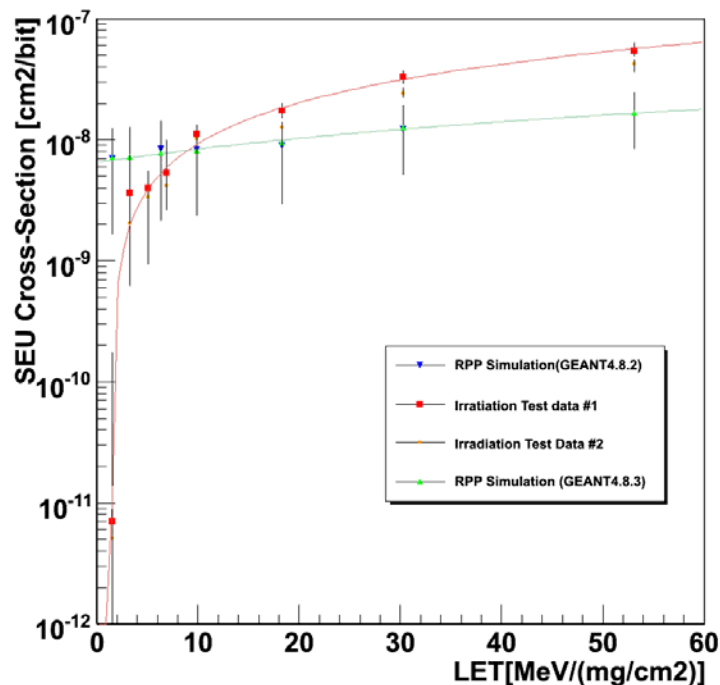


Figure 5-23 – Comparison between GEANT4 RPP simulation irradiation test data

The SEU cross-section obtained by simulation gives a plateau function that barely reproduce experimental results, as illustrated in figure 5-23. The same procedures were used for different SV volume thicknesses for the different ion species according to Table 5-6.

Figure 5-24 shows SEU cross-section as function of the SV thickness for Nitrogen and Xenon. It reveals that it is not possible to establish a dependency function between the SEU cross-section and SV thickness for the ATMEL device.

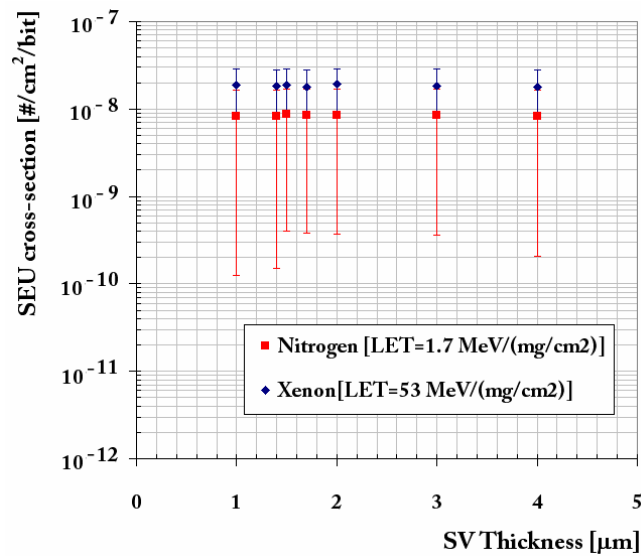


Figure 5-24 – SEU cross-section as function of SV thickness

In a way this result was already expected by traditional RPP models; because they assume the energy deposited to be given by equation 3-13 neglecting scattering effects in the sensitive volume. However this result shows as well that it is not possible to accurately fit the SV based on a method with SV thickness and critical energy as free input parameters. As a consequence it lead to the review of the definition of threshold LET,  $\text{LET}_c$ , and criteria for critical energy calculation as explained in the following section.

### 5.6.3. Redefinition of critical LET

By definition, critical LET is the minimum linear energy transfer from the ion to the target that produces an upset. Therefore instead of using a theoretical description of the experimental curve to extract the highest LET value not producing any upset, the critical LET can be extracted directly from irradiation test data by the lowest LET ion of the cocktail.

This trivial thought raised the following postulates:

- I. The lowest LET ion from the irradiation test cocktail, producing a positive SEU cross-section, is the ion with threshold LET,  $\text{LET}_c$ ;
- II. The critical energy for the simulation modules shall be defined as the energy deposition for which the simulated cross-section reproduces experimental results, as defined in equation 5-12:

$$\sigma(LET_c) = \frac{\text{Number of Evt}(depE > E_c)}{\text{Number of Generated evts}} \cdot \text{Sensitive Area perBit} = \sigma^{\text{experimental}}(LET_c) \quad (5-12)$$

According to Postulate I from Table 5-8 it can be concluded that critical LET of 1.7[MeV/(mg/cm<sup>2</sup>)] is obtained for Nitrogen. figure 5-25 plots the number of events in units of SEU cross-section as function of the energy deposited by Nitrogen in the SV.

The method for calculation of critical energy by analyses based on postulate II is given by equation 5-13 and is depicted in figure 5-25 for the case of 2 $\mu$ m SV.

$$E_c = E[\sigma(LET_c) = \sigma^{\text{experimental}}(LET_c)] \quad (5-13)$$

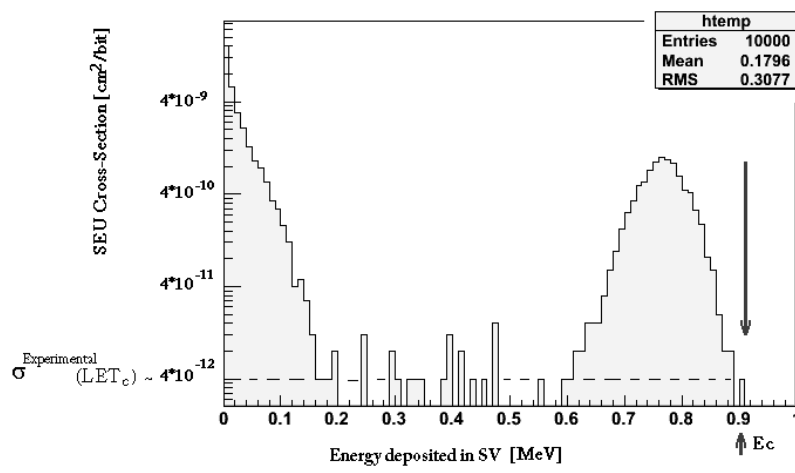


**Figure 5-25– Path length distribution: Assumption critical energy by analyses of Nitrogen deposited Energy distribution for a SV thickness of 2 $\mu$ m**

The path length distribution on the sensitive volume, of figure 5-25, shows that energy deposition has two peaks: one for low energies due to delta ray production and a Gaussian peak at higher energy losses. This higher energy peak is due to the primary particle. Basically it is due to the fact that in each simulation with perpendicular incidence in a RPP SV, the average energy transferred by the primary ions to the SV is the same for all the events corrected by the cosine of the scattering angle that has a random quasi-isotropic distribution, as represented in the scheme of figure 5-26.

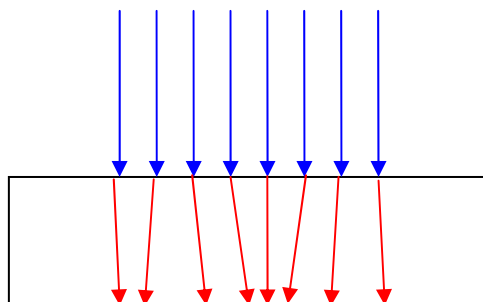


**Figure 5-26- Rpp scheme**

The Gaussian peak due to primary particles shows that ion track scattering may be important in the sensitive volume. This is an important conclusion that reveals that traditional RPP models assumption of the straight line trajectory of the incoming ion is not accurate enough.

Table 5-11 shows the critical energy calculated according to equation 5-13 for different SV thicknesses.

SV Thickness [ $\mu\text{m}$ ]	$E_c$ [MeV]
1	0.46
2	0.90
3	1.33

**Table 5-11 – SV thickness and critical energy according to equation 5-13**

Once the critical energy is calculated, SEU cross-section for higher LET ions can be computed according to equation 5-14.

$$\sigma(LET) = \frac{\text{Number of Evts}(depE > 0.9\text{MeV})}{\text{Number of Generated evts}} \cdot \text{Sensitive Area perBit} \quad (5-14)$$

#### 5.6.4. Fit SV dimensions and shape by microdosimetry calculations

In order to test the redefined critical energy criteria the first shape used for the simulation of the SV was the RPP. Later by evaluating differences between simulation results and experimental irradiation test data new shapes were fitted. Results are discussed in this section.

#### 5.6.4.1. Rectangle Parallelepiped Sensitive Volume

The method previously described was repeated for different SV thicknesses (1, 2 and 3  $\mu\text{m}$ ).

Figure 5-27 shows the SEU cross-section calculated according to this SV-FIT method: the green triangles show the previous result assuming LET<sub>c</sub> to be given by the Weibull description of experimental data (RPP\_weibull), the empty marks show results for different SV thickness using the new LET<sub>c</sub> definition (according to table 5-11) and finally red and orange full squares show irradiation test data.

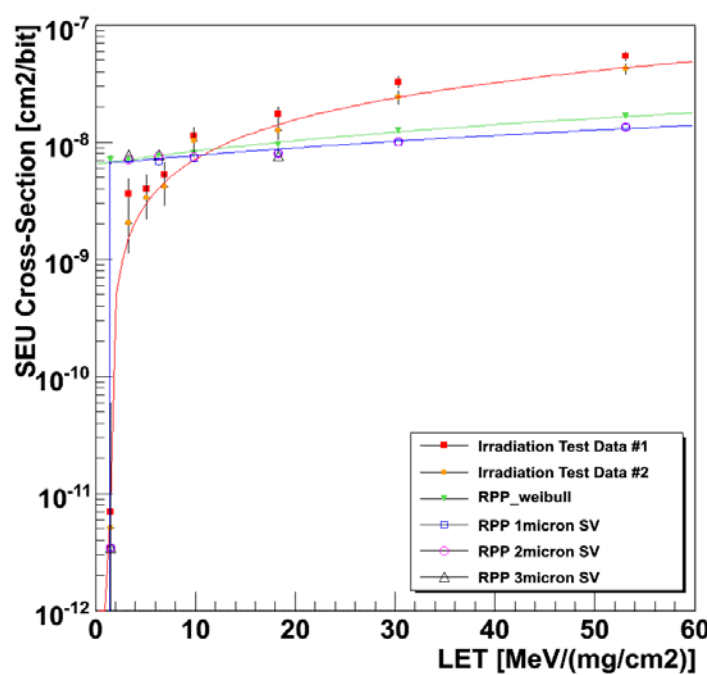


Figure 5-27- SEU cross-section curves: Comparison between experimental data and simulation results

It can be seen that simulations of RPP sensitive volumes give a step function description of experimental data in the same order of magnitude for saturation cross-section. However RPP simulations are not able to fit the knee of the SEU cross-section. Moreover by changing the SV thickness fit curves are not improved, showing inexistent dependence between SEU cross-section and thickness.

In order to understand the reason of such result it is important to investigate the LET path length distribution. Figure 5-28 shows distribution of energy deposited in units of MeV, for Nitrogen and Neon (2<sup>nd</sup> LET), travelling through a device with RPP SV of 1 $\mu\text{m}$  thick. It can be seen that the critical energy was defined by the maximum energy loss that sits in the upper queue of the Gaussian distribution. One other important observation is that high energy

peaks of energy deposition in RPP SV due to consecutive LET ions fall apart from each other. Therefore cutting the energy deposition for Neon (the second LET ion) gives no significant impact when evaluating its SEU cross-section. In other words, cutting deposited energies above the critical energy is just cutting the impact of low energy delta rays. As a consequence all the primary particle events will be taken into account for SEU cross-section calculations, leading to a step function SEU cross-section curve.

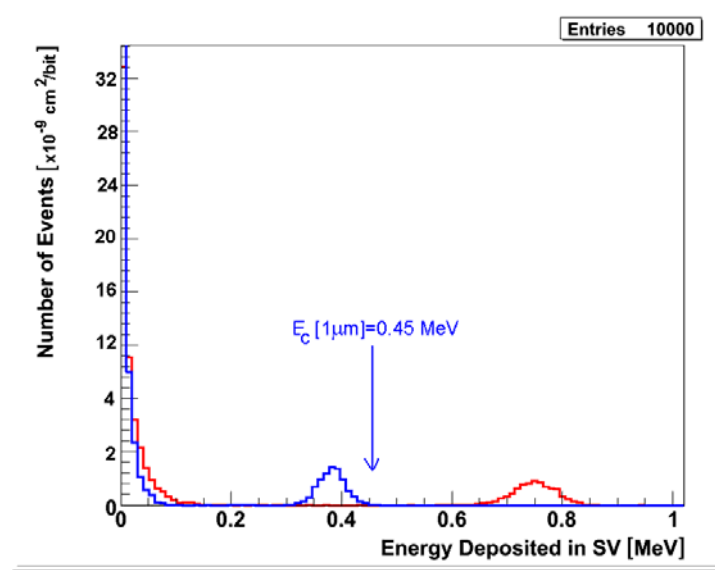


Figure 5-28- Energy deposited in MeV for different Nitrogen and Neon travelling through the device with rpp SV of 1 $\mu$ m thick

The difference between the SV-FIT RPP cross-section estimated for Neon and its experimental cross-section gives the order of the error that should be corrected. This conclusion leads to Postulate III:

- III. The difference between the SV-FIT RPP cross-section estimated for Neon and its experimental cross-section gives a measure of the SV shape modulation. Therefore the energy loss distribution shall be such that:

$$\#Neon_{new\ Geometry}(depE > E_c^{Nitrogen}) = \frac{\sigma^{experimental}(Neon)}{\sigma^{RPP}(Neon)} \times \#Neon_{RPP}(depE > E_c^{Nitrogen}) \quad (5-15)$$

A 2D calculation of the reduction factor  $\sigma^{experimental}(Neon)/\sigma^{RPP}(Neon)$  estimated that the SV shape should be triangular as depicted in figure 5-29.

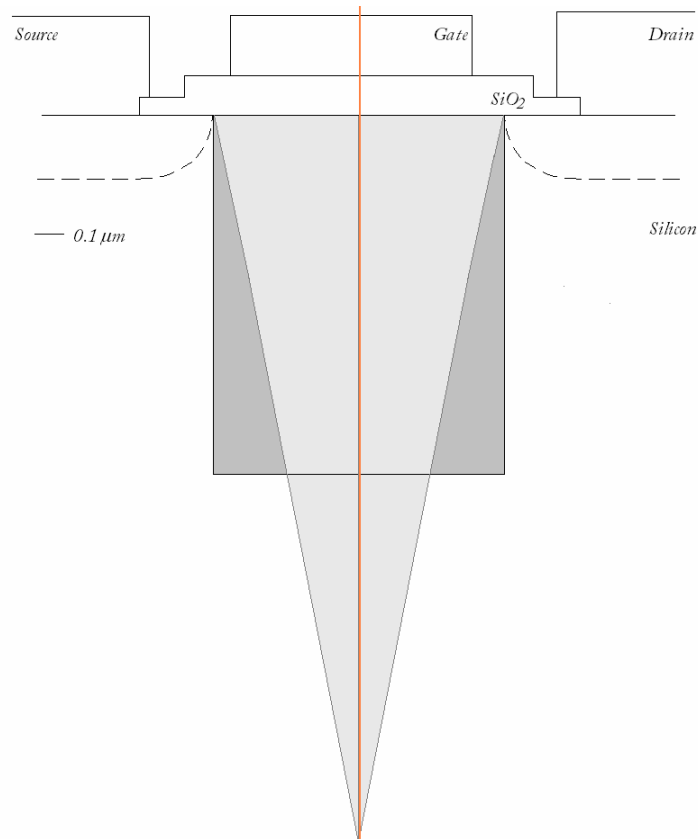


**Figure 5-29 – 2D calculation of SV shape based on reduction postulate III**

#### 5.6.4.2. *Tetrahedron Sensitive Volume*

The tetrahedron (TRD) with dimensions given in Table 5-9 appeared to be the shape to better fulfil condition of Postulate III for the ATMEL device.

Figure 5-30 shows fits of the deposited energy distributions (also called as LET path length distribution) obtained for Nitrogen (black), Neon (orange), Silicon (green), Argon (blue) and Krypton (red) with TRD SV.

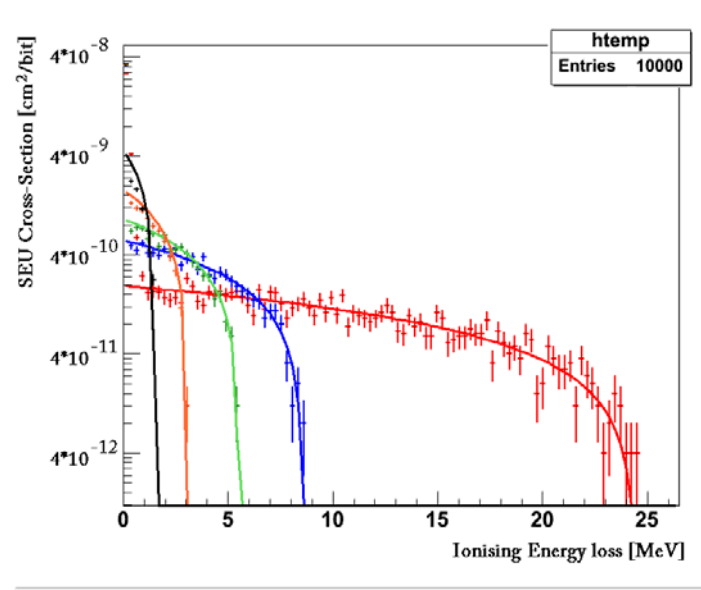


Figure 5-30 - Deposited energy distribution for Nitrogen, Neon, Silicon, Argon and Krypton with the TRD SV

Using Postulates I and II, the critical energy was again calculated according to equations 5-13 and 5-14 and was estimated to be 1.474MeV. Repeating the method, SEU cross-sections were calculated for the five different ions. Figure 5-31 shows the SEU cross-sections calculated for TRD sensitive volume and compares it with RPP sensitive volume and experimental data.

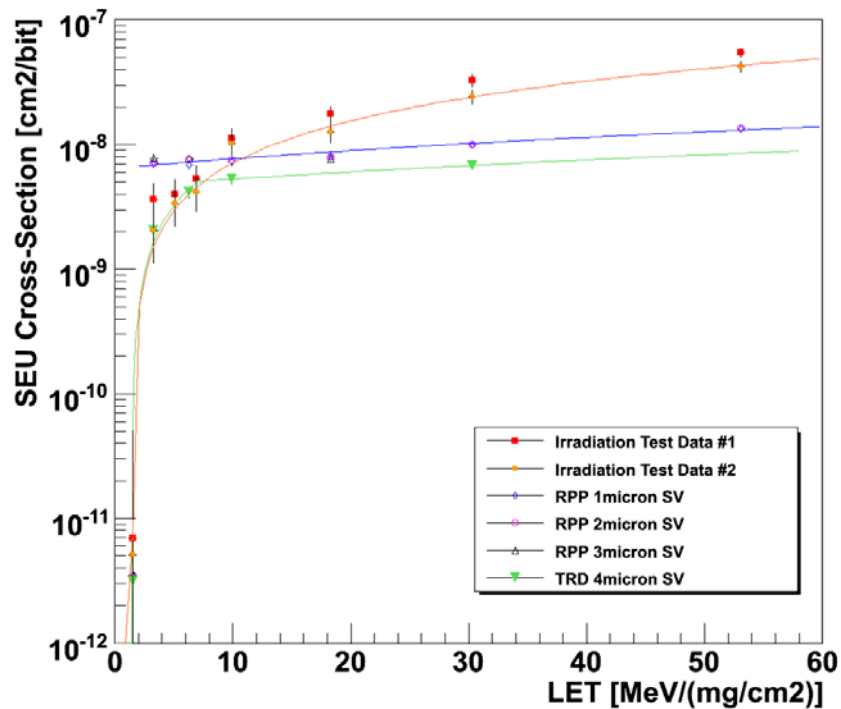


Figure 5-31- SEU cross-section curves: Comparison between experimental data and simulation results

---

TRD simulation significantly improved the results, leading to a very good fit of experimental data in the knee region. However simulated TRD results do not reproduce experimental results for high LET values.

According to the discussion of section 3.7.1 the saturation cross-section,  $\sigma_{\text{sat}}$ , can be assumed to measure the maximum sensitive transversal area of the chip. Although ATMEL AT60142F SRAM does not exhibit saturation for the tested LET range, the SEU cross-section obtained for the highest LET ion can be considered as the maximum transversal area to be sensitive for the considered LET range. This criterion was not taken into account in the geometrical description of the sensitive area. A simple calculation shows that the sensitive transversal area simulated underestimates the maximum sensitive area by 28%. Therefore a correction in the transversal area is expected to improve the fit of experimental data.

#### 5.6.4.3. *Transversal Area correction*

The Tetrahedron volume was revisited. The transversal area of each sensitive volume was recalculated by dividing the maximum SEU cross-section,  $\sigma_{\text{Iron}}$ , by the number of sensitive volumes simulated. The depth of the tetrahedron was kept the same.

According to Postulates I and II, the critical energy was once more calculated according to equations 5-9 and 5-10 and was estimated to be 1.551MeV. Repeating the method SEU cross-sections were calculated for the five ions simulations.

Figure 5-32 illustrates simulation results obtained with the new transversal sensitive area (empty blue triangle) in comparison with previous TRD results (light green triangle) and experimental data (red and orange squares). The area correction shows a significant improvement in the fit of experimental SEU cross-section curves. In particular from low LET values to saturation LET ranges the simulated values reproduce the experimental data within an accuracy of 10%.

However simulated high LET SEU cross-sections are still about 40% below experimental cross-sections. According to the considerations of section 5.5.1, GEANT4 simulations are expected to be able to reproduce standard cross-section curves exhibiting saturation, because the simulation up to now did not include LET dependent effects. This difference will be discussed later in this chapter.

---

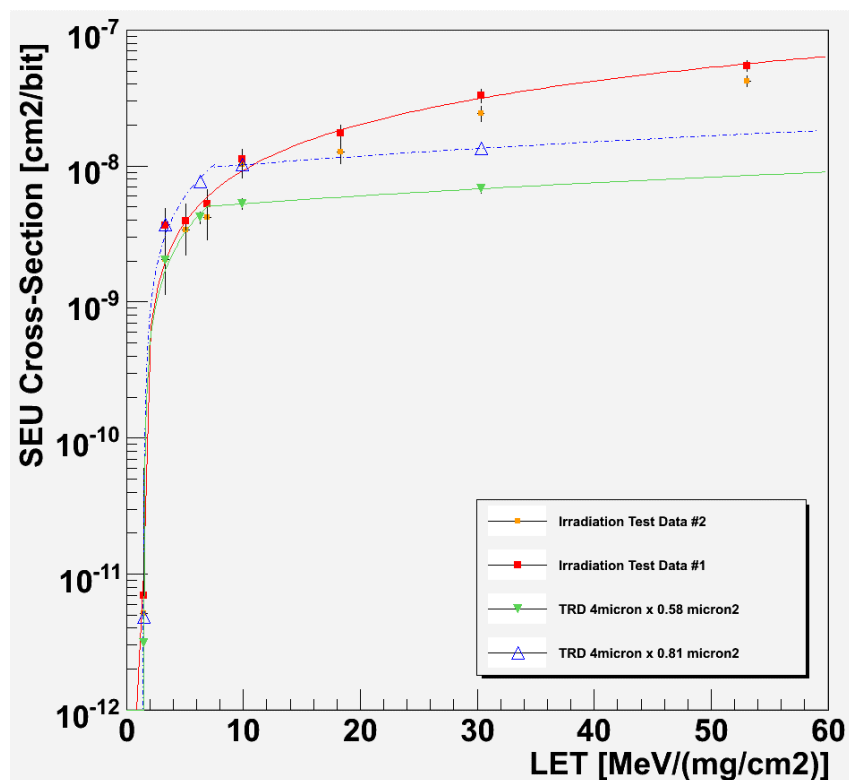


Figure 5-32- SEU cross-section curves: Comparison between experimental data and simulation results

#### 5.6.4.4. Truncated Tetrahedron Sensitive Volume

A cross-checking exercise was performed aiming at verifying if the tetrahedron depth was not over estimated. The same shape of tetrahedron SV was simulated but this time it was truncated (tTRD) with a depth of 2 $\mu$ m (typical SV thickness).

Again following Postulates I and II and equations 5-9 and 5-10, the critical energy was estimated to be of 0.87MeV. Repeating the method SEU cross-sections were calculated for the five ions.

Figure 5-33 shows the SEU cross-sections calculated for tTRD sensitive volume and compares it against TRD sensitive volume and experimental data.

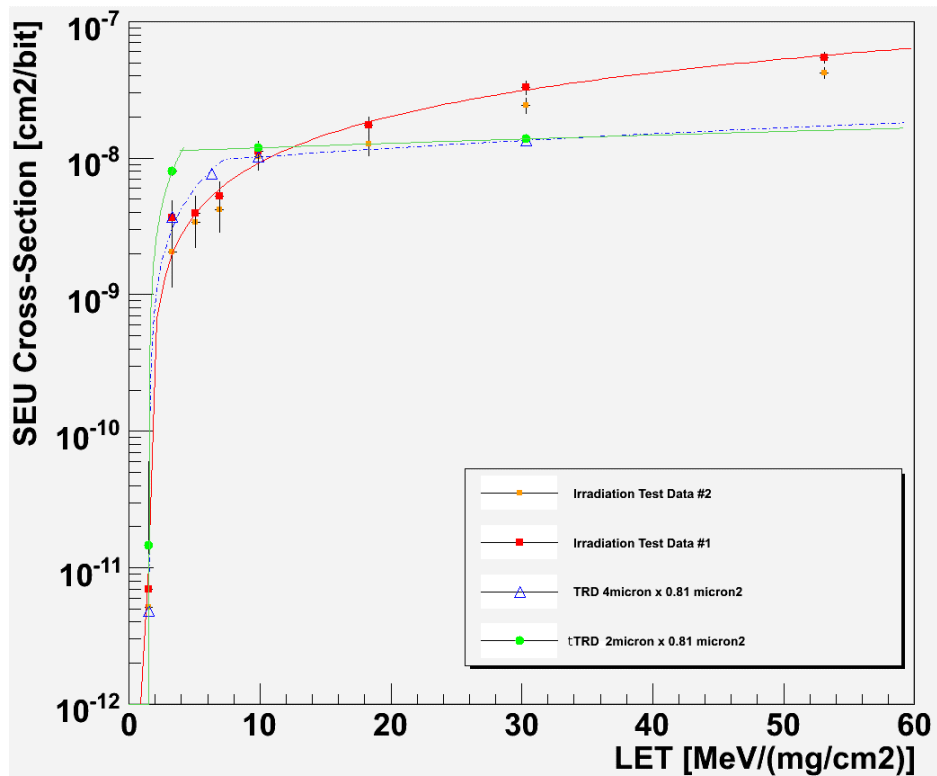


Figure 5-33- SEU cross-section curves: Comparison between experimental data and simulation results TRD and tTRD.

It can be seen that tTRD simulation results reveal the same saturation value as TRD but much worse behaviour in the Knee region.

This test lead to the conclusion that the best fit to the SV as it was defined for CODES application is given by the tetrahedron shape with transversal area given by the saturation experimental cross-section and a depth of  $4\mu\text{m}$ .

From equation 3-11 in Chapter 3 it was concluded that for silicon, electron mobility ranges from 1.5 to 2.5 times higher than holes mobility [Grove, 1967], which means that  $l_F \approx 2.5 \text{ to } 3.5 \cdot l_D / \cos \theta$ . Assuming that traditional RPP Models define the SV to represent the depletion region ranging from 1.5 to  $2\mu\text{m}$  deep for the ATMEL device it would be expected that the funnelling length of the order of  $l_F \approx 4\mu\text{m} / \cos \theta$  which for the particular case of perpendicular incidence previously described would give a similar SV of the type of the TRD  $4\mu\text{m}$  deep.

The concern with the  $4\mu\text{m}$  TRD was due to the fact that ATMEL AT60142F SRAM has a  $6\mu\text{m}$  epitaxial layer. This means that the TRD SV extends  $4\mu\text{m}$  inside the epilayer. According to the literature [Petersen, 1993], smoothly doped epilayers do not limit

funneling. In particular the funneling length is expected to increase with decreasing doping concentrations [Musseau, 1994], [Hsieh, 1981]. Natural limits in funneling length in CMOS technology with epilayers may be encountered when epitaxials are manufactured over heavily doped substrates [Petersen, 1993].

This raises a possible physical explanation for the Fitted SV shape.

#### 5.6.5. Discussion: Drift and Diffusion mechanisms

As shown by the polynomial fit of experimental test data obtained for the ATMEL AT60142F SRAM device, SEU cross-sections do not saturate for the tested LET range. As previously described, discussions with ESA experts lead to the assumption that ATMEL AT60142F SRAM SEU response function can be defined as a combination of two effects, namely *a standard SEU cross-section curve that saturates around 10MeV/(mg/cm<sup>2</sup>)*, plus an *increasing LET-dependent effect*.

Some studies show that this non-saturation effect happens in other technologies such as SOI and other CMOS technologies with different dimensions [Warren, 1999]. In literature this effect is often attributed to the perturbation of several structures in a device by a unique ion charge collected.

In realistic microelectronic devices the regions where the ideal current flows represents only a very small part of the silicon volume. There are other regions where a disabled junction may suddenly be activated by anomalous effects such as a single event effect. These junctions are known as *parasitic transistors*. Figure 5-34 shows an example of a p-n-p-n parasitic effect in a CMOS device.

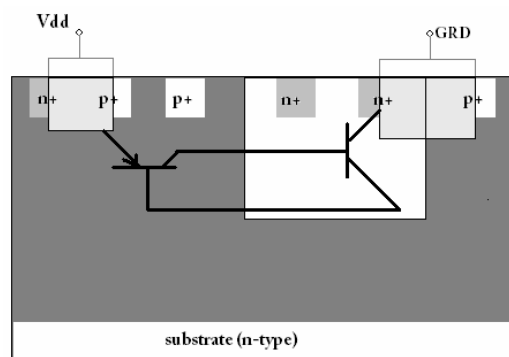


Figure 5-34 – P-n-p-n effects in CMOS device after [Holmes-Siedle, 2006]

---

The n-p-n (or p-n-p) parasitic bipolar transistors consist of pair of closely spaced p-n junctions in a single semiconductor. Under normal operating conditions this structure can be “off”. However a pulse of ionising or non-ionising radiation can trigger it into an “on” state, forcing it into conduction. This can lead to circuit transient upset or to a long-lived and potentially destructive effect, a latch-up.

Those geometric effects involving the perturbation of several structures in a device by a unique ion charge collected by parasitic structures can be of three Types: a) Shunt effect when the ion crosses several depleted regions; b) Grazing angle, when the ion with very high inclinations ( $75^\circ$ - $90^\circ$ ) crosses different sensitive areas; c) Multiple Bit Upset (MBU), when due to limited funnelled charge collection, excess charge is collected by diffusion in several neighbour junctions [Musseau, 1994].

According to Reno Harboe-Sorensen [Sørensen, 2005] the ATMEL AT60142F SRAM is hardened against latch-ups. However this device is not tested against MBU. In the literature, effects such as MBUs are described as being caused by diffusion in the substrate rather than drift.

Bertrand and Renaud [Bertrand, 2007] have shown, for CMOS  $0.18\mu\text{m}$  technology, that transient durations are similar for low LET values. For LET values below  $7\text{MeV}/(\text{mg}/\text{cm}^2)$  transient duration is of the order of  $0.1\text{ns}$ . However for higher LET values transient duration increases. For an LET of  $20\text{MeV}/(\text{mg}/\text{cm}^2)$  duration increases to  $0.3\text{ns}$  while and for  $30\text{MeV}/(\text{mg}/\text{cm}^2)$  it's even higher of the order of  $1\text{ns}$ . For all LET values with impact in the sensitive node the transient is measured by the drain voltage drop from  $1.8\text{V}$  to less than  $0.2\text{V}$ . The transient starts in  $3\text{ps}$  after impact and ends when the drain voltage is restored to its initial value.

In parallel the same authors have studied the influence of the ion impact location on the Drain voltage drop profile (illustrated in figure 5-35). They show that for an LET of  $30\text{MeV}/(\text{mg}/\text{cm}^2)$ , reaching the sensitive node, the transient starts in  $3.8\text{ps}$  after the impact. When increasing the distance from ion impact to the sensitive node to  $1\mu\text{m}$ , the Drain voltage drop is less significant in the first picosecond decreasing to  $1.6\text{V}$  and just  $5\text{ps}$  later a *delayed effect* drops the Drain voltage to around  $0.2\text{V}$ . The same test done with the incoming ion reaching the device at  $2\mu\text{m}$  from the sensitive node showed that there is *no prompt effect* and only a *delayed* voltage drop is felt  $0.15\text{ns}$  after the impact and lasts for  $0.3\text{ns}$ . Finally it can

---

be seen that the pulse is longer for the case of direct impact on the sensitive node, *which means that delayed effects happen during the transient duration.*

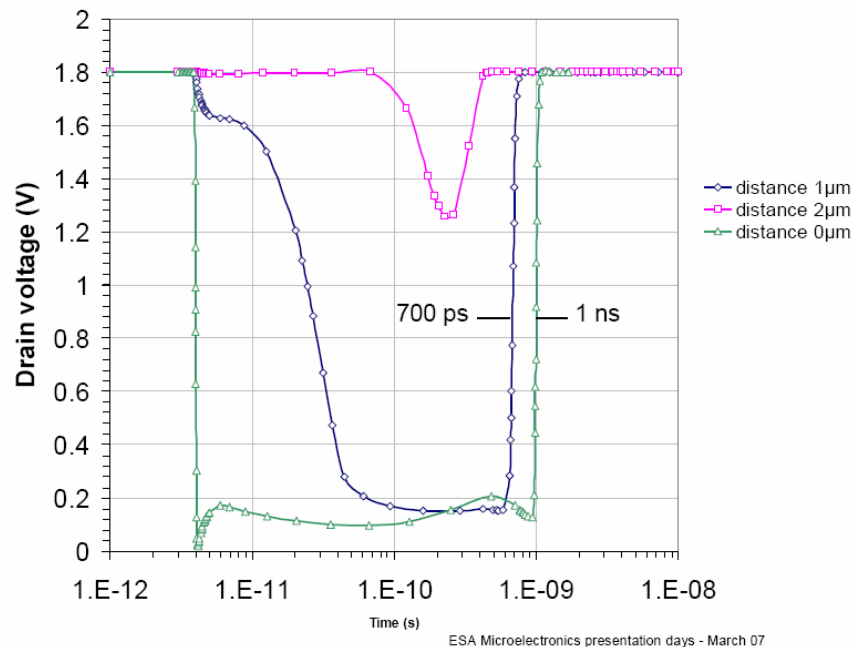


**Figure 5-35 – Influence of ion impact location on transient pulse shape [Bertrand, 2007]**

In the same publication the authors show that the prompt charge starts to be collected in 3.8ps after impact. Its intensity increases with increasing LET, while duration time decreases with increasing LET. From this observation it can be inferred that delayed charge collection happens after prompt collection that the delayed, but during the transient upset.

The analysis of the previous discussed dependences shall be done taking into account the discussions of Chapter 3 on prompt charge, drift and funnelling, delayed charge collection and diffusion.

As defined in Chapter 3 prompt charge collection is due to drift of excess carriers in the funnelled electric field. Prompt charge collection in the 0.5ns immediately after ionization. If the track is long enough (10µm) excess charge generated beyond the funnelling length is left to be transported by diffusion [Hsieh, 1981].

In this context it is reasonable to assume that for LET values higher than 10 or 20MeV/(mg/cm<sup>2</sup>) there is a probability that ions reaching the device at distant positions from the sensitive nodes can still contribute to charge collection by effects of diffusion in the deep

substrate. In other words this effect can be seen as an enhancement of the sensitive transversal area dependent on ion LET.

Similar effects have also been identified for larger technologies differing only by the LET at which an ion reaching the device far away from the sensitive node may still contribute to charge collection.

Moreover as previously referred in this chapter, the solution for the standard SEU cross-section curve reaching saturation is obtained by calculating the shape of the sensitive volume and then the distribution of ion path lengths through the sensitive region [Xapsos, 1993]. Additionally Mike Xapsos and many other authors [Petersen, 1992], state that LET-dependent effects such as enhanced memory cells sensitivity may also contribute to modulate the shape of the SEU cross-section sensitivity.

A final remark goes to the fact that the delayed charge collection due to diffusion may just contribute to upset an SRAM if in the device refreshing time. In the case of the ATMEL AT60142F SRAM, 0.25 $\mu\text{m}$  CMOS, the access time is 15ns. So it is possible that delayed charge collection happening in a few nanoseconds may contribute to upset the device.

Considering the previous discussion, the analysis of SV-FIT results leads to the conclusion that the tool is able to give a good approximation of the funnelled sensitive volume, reproducing the SEU cross-section up to saturation with an accuracy of 10%. SV-FIT by analysing the path length distribution and inferring the best fit sensitive volume shape and size enables a description of ATMEL AT60142F SRAM drift mechanisms.

On the other hand, while simulation results reach a saturation at about 10MeV/(mg/cm<sup>2</sup>), experimental data show an increasing behaviour for high LET values. This effect according to the previous discussion shall be attributed to *diffusion-induced* charge collection. SV-FIT simulation in this first stage did not take into account such effects. In a first approach it was assumed that the transversal area of the sensitive volumes is fixed.

The next step of the simulation improvements consists of including diffusion-induced effect, as a LET-dependent effect. By analysing, testing and quantifying the effect in the ATMEL AT60142F SRAM it is possible to include diffusion effects as a LET-dependent perturbation of the preliminary drift effects already simulated. Finally this perturbation is expected to improve the SEU cross-section curve reconstruction for high LET values.

---

### 5.7. *Future Developments*

As just described the developed SV-FIT tool indicates that GEANT4 simulations based on ground based test data enables a qualitative interpretation of physic mechanism contribution for component damage and space system degradation. However, in order to produce a quantitative analysis of the physical mechanisms, the tool needs further verification and work can still be done at different levels such as: a) experimental quantification and validation; b) generalization and c) further investigation.

#### a) Experimental quantification and validation

All the qualitative discussion on drift and diffusion was based on SV-FIT results and literature survey. However the diffusion effect is not quantified for the ATMEL AT60142F SRAM, 0.25 $\mu$ m CMOS. In order to quantify diffusion mechanisms, it is important to create verification procedures and an experimental verification test program. Some required additional tests already identified include:

- Irradiation testing with different consecutive LET values with the same ions, and different energies
- Extensive cover of the knee region LET values with perpendicular incidence
- Check part –to–part variability
- Evaluate the error of the measure and experimental systematic errors

Therefore irradiation test campaigns shall be planed and performed in order to verify the relation between drift and diffusion mechanisms for specific components.

#### b) Generalization

Additionally the capabilities of the developed component simulation tool shall be generalized to other family of components. Similarities with complex biological systems shall be identified and the application of the tools for prediction of effects on organic materials and systems shall be considered.

A final outcome of this development should enable the calculation of the accuracy of predictions for different simulations as a function of complexity of input parameters.

---

## c) Further Investigation

There are a few other problems regarding traditional methods of evaluation radiation effects on EEE devices that need to be reviewed regarding new technology dimensions and functioning. Traditional assumptions reveal behaviours not compatible with real processes in modern devices. They appear to fail for modern devices with different shielding configurations, complicated SV shapes, several SVs, small features, and consequently depletion sizes. The following list of remaining open questions can be investigated by application of SV-FIT:

- Is the surface LET a good parameter to evaluate SEE damage in modern technologies? To answer this question traditional calculation methods of the linear energy transferred from an ion to the target device shall be investigated and compared with SV-FIT computed LET for the same ions. Additionally simulations considering 45° and 60° shall be analyzed facing differences between surface LET and GEANT4 microdosimetry LET calculations.
  - Which are the dependences between radiation-induced effects with ion penetration depth and the dependence of Destructive effects and ion Bragg peak, for low ranges ions?
  - The developed tools shall be used to investigating the possibility of predicting proton device response based heavy ions test data.
-



## 6. Conclusions

An integrated framework has been developed aiming at characterizing Mars radiation environment and predicting induced effects in EEE components. In particular the complete framework was later derived into two specific main tools. One dedicated to the detailed prediction and analysis of Martian radiation environment with two implementations (MarsREC and dMEREM), and one dedicated to physical interpretation and detailed simulation of radiation effects on EEE components, CODES.

### 6.1. *MarsREC and dMEREM*

MarsREC and later improved dMEREM employ Geant4 particle transport tool and include parameters such as Martian time, detection position, solar longitude, solar cycle modulated cosmic ray and solar particle event spectra, 4-D EMCD atmosphere, geology and MOLA topology. MarsREC results show GCR proton-induced annual fluences at the surface of the order of the  $10^7$  particles/cm<sup>2</sup>. While for SEP fluences are of  $10^8$  particles/cm<sup>2</sup> per event. Above 100MeV, the radiation environment is highly dominated by protons, while at lower energies there is a higher contribution from neutrons and photons. The importance of radiation backscattered at the surface of Mars is verified for both GCR and SEP. For GCR 58% of all particles detected just above the surface are backscattered. This ratio is even more significant for neutrons. Results have shown that 95% of all detected neutrons were produced at the surface and sent back into the atmosphere. For SEP, with lower energy range spectra (<1000MeV), the backscattered component comprises 19% of all particles (51% for neutrons). These results lead to the important conclusion that the Martian atmosphere (with a maximum density equivalent to 5cm of aluminium) works as a very soft attenuator of the primary spectra and increases radiation fluences due to the production of secondary particles. The radiation environment at the surface is dependent on the atmospheric pressure at the surface. However a higher contribution is given from the soil.

An analysis of the Martian soil composition was done based on the GRS data and geologic studies of the surface of Mars. According to the literature, water is expected to exist at the

---

---

surface and subsurface either in the form of hydrated minerals or in the form of ice. MarsREC was used to analyse the impact of different soil compositions on radiation environment. Results show that: a) the presence of water at the surface is the most significant local parameter to affect surface radiation environment, b) changes of 10 to 20% in soil density in the range of  $1 \text{ g/cm}^3$  can give differences of 60% percent on neutron backscattering or 30% on general backscattering radiation, c) the presence of  $\text{CO}_2$  leads to a slightly increased ambient dose equivalent ( $\sim 10\%$ ), d) changes of  $\text{Fe}_2\text{O}_3$  weight percentage also induce 10% changes in neutron ambient dose equivalent. Finally a tool was developed and interfaced with dMEREM in order to describe the Martian soil composition based on the GRS data maps.

The dependence on time was also evaluated at two levels. While diurnal variations are of the order of 1% or lower, seasonal changes are of the order of 10 to 20% between northern summer and northern winter. Seasonal variations were calculated based on surface pressure fluctuation along the Martian year. Similarly altitude effects are expected to be significant for extreme locations at the surface of Mars. For example differences of 35% are expected from Olympus Moons (20km above areoid) to Hellas Basis (8km below the areoid) due to altitude/surface pressure effects. Finally, different dust scenarios lead to important variations of the surface pressure. This effect, taken into account into both MarsREC and dMEREM, may lead to variations of the order of 10%.

Comparisons with other simulation results and with MARIE measurements showed very good agreement proving that the framework is capable of calculating the energy spectra and particle species at any location on Mars with a resolution of  $5^\circ \times 5^\circ$  or  $6.5^\circ \times 3.85^\circ$ .

While the total ionizing dose at the surface is of lesser concern to EEE components, the relative abundance of protons and neutrons may result in Displacement Damage and Single Event Effects. Predictions show that ambient dose equivalents at Mars surface are expected to be of the order of  $10 \text{ cSv/yr}$ , two orders of magnitude higher than that on Earth. Such dose equivalent levels make Mars unsuitable as a human habitat. Therefore the design of manned missions to Mars shall critically consider the severe radiation environment.

---

---

## 6.2. CODES

The *Component Degradation Simulation tool (CODES)* [Keating, 2008] was designed as a general framework in order to predict radiation degradation on EEE components when submitted to different radiation environments. CODES achieves the goal of generality because it interfaces information on the device with Geant4 based Monte Carlo application for tracking primary and secondary particles at component level. Detail simulations are also possible by using the developed interactive tool to fit device sensitivity, *Sensitive Volume interactive Fit Tool (SV-FIT)*, based on ground level irradiation tests.

CODES consists of two different approaches: The *Statistic* and *Microscopic*.

The full development and application of CODES and SV-FIT described were based on the analysis of the 4Mbit ATMEL AT60142F Static Random Access Memory (SRAM) comprehensively characterised as part of ESA's "Reference SEU Monitor" development activity [Sørensen, 2005].

### 6.2.1. *Statistic approach*

The *statistic approach* provides a comprehensive method to predict SEU Rates for EEE components on Mars by convolving radiation environment spectra at component level with a statistical description of SEU test data. It takes into account secondary particles generated in various shielding configurations, Martian atmosphere and soil. Results show that SEU rates for the ATMEL AT60142F SRAM are expected to be of the order of 7 per device per year due to GCR, while for SEP they are expected to be of the order of 5 per device per week of event at the surface of Mars. Results were in very good agreement when compared with other software, showing that the methodology is capable of predicting SEU rates for protons and neutrons.

The statistical approach methodology is adaptable for SEU rate prediction under other radiation environment scenarios. SEU rate can also be predicted under different radiation environment scenarios based on SEU cross-section curve calculations using detailed GEANT4 device simulation as those obtained from SV-FIT.

---

### 6.2.2. *Microscopic approach*

The Microscopic approach is capable of microdosimetry in device sensitive volumes. By using GEANT4 application interfaced with device analysis techniques this method enables the fit of sensitive volume shape and dimensions, as well as the path length distribution. The microscopic approach consists of three main modules to perform SEU rate prediction of memory devices. The three modules are Geometry Description (GD), Efficiency Matrix (EM), and Analysis Module (AM). SV-FIT is an iterative process that by employing the three modules GD, EM and AM, calculates a function for the Sensitive Volume and subsequently calculates the cross-section versus LET curve required to predict SEU rates. SV-FIT Modules employ device geometry data and irradiation test data to generate: path length distributions, SEU cross-section reconstruction, estimate the critical energy, and return the best fit SV shape.

SV-FIT proved that the modulation of path length distribution leads to the understanding of the real sensitive volume shape and size. This result was in fact discussed by other authors [Xapsos, 1993], [Petersen, 1993], [Connell, 1995], that developed models to predict the path length distribution in different conditions. The assumption of the ion track as a straight line through the sensitive volume proves to be a simplification that smoothes real physical mechanisms contributing to the modulation of the sensitive volume shape and size. SV-FIT shows that the convolution of the deposited energy variation due to primary particle scattering with the SV shape, lead to a smoothed knee shape of the SEU cross-section curve.

Results show that the fit of SV shape enables the reconstruction of the experimental effect cross-section curve. In particular initial results of reconstructed cross-section versus LET curves, for the ATMEL device, agree very well with experimental data in the knee region up to saturation (within 5 to 10%) indicating good prediction of the SV. Moreover it shows that best fit to the SV shape for the ATMEL AT60142F SRAM device is given by a tetrahedron with transversal area given by the saturation experimental cross-section and a depth of 4 $\mu\text{m}$ , instead of by the traditional rectangle-parallelepiped. The AT60142F SRAM is a 0.25 $\mu\text{m}$  CMOS technology with 6  $\mu\text{m}$  epilayer, which means that the tetrahedral SV extends 4 $\mu\text{m}$  inside the epilayer. According to the literature [Petersen, 1993], smoothly doped epilayers do not limit funnelling. Funnelling length is just expected to be naturally limited by heavily

doped substrates [Petersen, 1993]. The tetrahedral SV is then believed to be a reproduction of the funnelled volume of the device.

The final outcome of the microscopic approach of CODES is a qualitative analysis of the transport mechanisms of excess charge in the device. According to the analysis the fit of the device sensitive volume gives the description of drift charge collection mechanisms (funnelling), while diffusion mechanisms may reveal themselves as LET-dependent effects. Finally diffusion processes are expected to be evaluated by comparing SV-FIT cross-sections with experimental cross-sections for LETs above saturation.

Future implementation of diffusion effects are expected to improve reproduction of SEU cross-section curves above saturation.

### *6.3. Context and future*

The work described in this thesis aimed at developing scientific and detail simulation tools for Martian radiation environment characterization and understanding of the physical mechanisms of degradation in EEE devices. This goal was successfully achieved.

CODES and SV-FIT development is still in progress. The performance of the tool can be still improved by including diffusion effects as a LET-dependent perturbation, employing the Efficiency Matrix Module in the iterative process of SV-FIT and combining results with laser mapping data. In the near future the full framework is aimed at being verified and tested for other family of devices. Additionally the method will be integrated into a user friendly tool publicly available online.

In parallel the needs of Space Industry require the integration of detailed scientific tools into user friendly engineering tools. With ESA support MarsREM was already developed, integrated and interfaced into user friendly tool available under SPENVIS. It shall be publicly available by July 2008.

Since its first publication the work developed has had a very good acceptance from the scientific community. MarsREC results were used to define specification for the design of EXOMARS mission.

---

Future manned and unmanned missions are being design to Mars. At the moment there is no definite plan for sending a radiation monitor to Mars and radiation environment studies rely merely on simulation work. This work has proved that the radiation hazard on Mars can lead to undesirable effects on EEE components. However simulation work is based on many assumptions that may in fact vary from real conditions. Therefore, it is of fundamental importance to send radiation monitors, to validate the models and the assumed conditions before sending manned missions to Mars.

The author is willing to participate in future collaborations to design and construct radiation monitors for Mars Exploration.

---

---

## 7. Bibliography

- [Abshire, 1999] J.B. Abshire, X. Sun, R.S. Afzal, "Mars Orbiter Laser Altimeter Receiver Model and Performance Analysis", Nasa Goddard Space Flight Center Laser Remote Sensing Branch, Code 924 Greenbelt, Maryland 20711, August 1999 [http://pds-geosciences.wustl.edu/geodata/mgs-m-mola-3-pedr-11a-1/mgsl\\_21xx/document/calib.pdf](http://pds-geosciences.wustl.edu/geodata/mgs-m-mola-3-pedr-11a-1/mgsl_21xx/document/calib.pdf)
- [Adams, 1986] James H. Adams, Jr. "Cosmic Ray Effects on Micro-Electronics (CREME), Part IV", Naval Research Laboratory Memorandum Report 5901, December 31, 1986.
- [Agostinelli, 2003] S Agostinelli et al, "Geant4 – a simulation toolkit," Nucl Instrum Meth Phys Sci, A506, pp.250-303, 2003
- [Ahmad, 1967] S.Ahmad and W.S.Khokley, "Transition Probability of impact ionization in Silicon", J. Phys. Chem. Solids, Vol.28, pp. 2499-2507 (1967)"
- [Allison, 2006] J. Allison et al., "Geant4 Developments and Applications", IEEE Transactions on Nuclear Science 53 No. 1 (2006) 270-278.
- [Allison, 2008] J. Allison, "The Geant4 Visualisation System", Computer Physics Communications, Vol.178, No. 5, pages 331-365, 2008.
- [Anderson, 1972] C.L. Anderson and C.R. Crowell, "The energies for electron-hole pair production by impact ionization in semiconductors", Phys. Rev. B, Vol.5, No. 6, pp. 2267-2272, 1972"
- [Andrews, 2000] D.G. Andrews, "An Introduction to Atmospheric Physics", Cambridge University Press, 2000
- [Ausmann, 1975] G. A. Ausmann and F. B. McLean, "Electron-hole Pair Creation Energy in SiO<sub>2</sub>", Appl. Phys. Lett. 26, 173 (1975)"
- [Balebanov, 1990] V.M.Balebanov, et al.(AMS Proposal), "Alpha Magnetic Spectrometer (AMS) for extraterrestrial Study of Antimatter, matter and Missing Matter on the International Space Station Alpha".
- [Baraff, 1962] G.A.Baraff, "Distribution Functions and ionization rates for hot electrons in semiconductors", Phys. Rev. 128, 2507 (1962)"
- [Barak, 2001] J. Barak, "Analytical Microdosimetry Model for Proton-Induced SEU in Modern Devices", IEEE Transactions on Nuclear Science, Vol.48, No. 6, December 2001.
- [Barbieri, 2004] L. Barbieri and R. Mahmot, "October-November 2003's space weather and operations lessons learnt", Space Weather, Vol. 2, No.9, 2004.
- [Baumann, 2001] Robert C. Baumann, "Silicon Amnesia: Radiation Induced Soft Errors in Commercial Semiconductor Technology", I, Short Course, RADECS 2001.
- [Baumann, 2005] R. Baumann, "Single-Event Effects in Advanced CMOS Technology", Evolving issues for the Application of Microelectronics in Space, Section II, IEEE NSREC short Course 2005.
-

- 
- [Benedetto, 1986] J. M. Benedetto and H.E. Boesch, Jr. , “The Relationship Between  $^{60}\text{Co}$  and 1KeV X-ray Damage in MOS Devices”, IEEE Trans. Nucl. Sci. NS-33, 1318 (1986)
- [Bertrand, 2007] J. Bertrand, N. Renaud, “Single Event Transient characterization of the ATC18RHA ASIC family”, ESA Microelectronics presentation days – March 20 2007
- [Bibring, 2005] J-P Bibring et al, “Mars Surface Diversity as Revealed by the OMEGA/Mars Express Observations”, Science, vol. 307, pp.1576-1581, 11 March 2005.
- [Bibring, 2006] J-P Bibring et al, “Global Mineralogy and Aqueous Mars History Derived from OMEGA/Mars Express data”, Science, vol. 312, pp. 400-404, 21 April 2006.
- [Bieber, 2002] J. W. Bieber, W. Dröge, P. Evenson, R. Pyle, D. Ruffolo, U. Pinsook, P. Tooprakai, M. Rujiwarodom, T. Khumlumlert, and S. Krucker, “Energetic particle observations during 2000 July 14 solar event,” Astrophys. J., vol. 567, pp. 622–634, 2002.
- [Bieber, 2004] J. W. Bieber, W. Dröge, P. Evenson, R. Pyle, D. Ruffolo, M. Rujiwarodom, P. Tooprakai, and T. Khumlumlert, “Spaceship Earth observations of the Easter 2001 solar particle event,” Astrophys. J., vol. 601, pp. L103–L106, 2004.
- [Boezio, 1998] M.Boezio, “Positron and Electrons in the Cosmic Radiation Measured by the CAPRICE94 Experiment”, PhD thesis, 1998.
- [Boyce, 2002] J. M. Boyce, “The Smithsonian Book of Mars”, Smithsonian Institution Press, 2002.
- [Butt, 2007] N.Z. Butt, P. D. Yoder, M.A. Alam, “Soft Error Trends and New Physical Model for Ionizing Dose Effects in Double Gate Z-RAM Cell”, IEEE Transactions on Nuclear Science, 2007, vol.54, no.6, pp.2363-2360.
- [Cane, 2004] H.V.Cane, D.Lario, “CMES and Energetic Particles”, Space Science Reviews, 00, 1-13, 2004.
- [Chaplin, 2007] M. Chaplin, “Phase diagram of water in Water structure and science”. 26 October, 2007. Available: <http://www.lsbu.ac.uk/water/phase.html> "
- [Chugg, 2007] A. M. Chugg, A. J. Burnell, M. J. Moutrie, R. Jones, and R. Harboe-Sørensen, “Laser SEE Sensitivity Mapping of SRAM Cells”, IEEE Transactions on Nuclear Science, 2007, vol. 54, pp.2106-2112.
- [Cleghorn, 2004] T. Cleghorn, “Solar Particle events at Mars seen by MARIE, 2002-2003, COSPAR 2004, <http://www.cosis.net/abstracts/COSPAR04/03500/COSPAR04-A-03500.pdf>
- [Connell, 1995] L.W. Connell, P.J. McDaniel, A.K. Prinja, F.W. Sexton, “Modeling the Heavy Ion Upset Cross-section, IEEE Trans. Nucl. Sci. 42, no 2, 1995, pp. 73-82
- [Cooper, 2003] C.D. Cooper and J.F.Mustard, “New Insights on Mars Low Albedo Regions Composition from Joint Analysis of ISM and TES spectra”, Lunar and Planetary Science XXXIII, 2003
- [Cucinotta, 2003] F.A.Cucinotta, P.B.Saganti, J.W.Wilson, L.C.Simonsen (2003). Model Predictions and Visualization of the Particle Flux on the Surface of Mars. Available: <http://marie.jsc.nasa.gov/Documents/FC-Nara-Paper.pdf>.
-

- 
- [Darnell, 2007] L. R. Darnell, L. Desorgher, J. M. Ward, and A. J. Coates, “Martian sub-surface ionising radiation: biosignatures and geology”, *Biogeosciences Discuss.*, 4, 455–492, 2007.
- [Desorgher, 2008] Planetocosmics web page: <http://cosray.unibe.ch/%7Elaurent/planetocosmics/>
- [DESIRE] Dose Estimation by Simulation of the ISS Radiation Environment (DESIRE):  
<http://gluon.particle.kth.se/desire/>
- [DPMJET, 2000] DPMJET: A Monte Carlo event generator for high-energy hadron-hadron, hadron-nucleus, nucleus-nucleus and photon-nucleus collisions. <http://sroesler.web.cern.ch/sroesler/dpmjet3.html>
- [Duzellier, 2003] Sophie Duzellier, “Radiation engineering methods for space applications -Radiation Effects Analysis: Single Event Effects”, 3-C, Short Course Book, RADECS 2003.
- [ECSS-E-10-04A] ECSS-E-10-04A Standard on Space Environment:  
<http://www.estec.esa.nl/wmwww/wma/standards/ecss/ecss.html>
- [ECSS-E-HB-10-12] ECSS-E-HB-10-12A.v2.0, Space Engineering-Methods for the calculation of radiation received and its effects, and a policy for design margins, 2008. Available:  
<http://www.ecss.nl/forums/ecss/dispatch.cgi/home/showFile/100697/d20080414114318/No/ECSS-E-10-12A%20v0.20Standard.pdf>
- [Edmonds, 1991] L.D. Edmonds, “A simple estimate of funnelling assisted charge collection, *IEEE Trans. Nuc. Sci.* NS-38, 828-833 (1991)
- [Eidelman, 2005] S. Eidelman et al, *Phys. Lett. B* 592, 1 (2004), PDG, Particle Data Group, “Reviews, Tables, and Plots in the 2005 web update of Review of Particle Physics- Cosmic Rays”, 2005 Edition,  
<http://pdg.lbl.gov/2005/reviews/cosmicrayrpp.pdf>
- [Eraker, 1982] J.H.Eraker, “Origin of the low-energy relativistic interplanetary electrons”, *The Astrophysical journal*, 257: 862-880, 15 June 1982.
- [Ersmark , 2006] T. Ersmark, “GEANT4 Monte Carlo Simulations of the International Space Station Radiation Environment”, Doctoral Thesis, Stockholm, Sweden, 2006”
- [ESA, 2005] ESA. (2005, August 4). Aurora Exploration Program. Available:  
[http://www.esa.int/SPECIALS/Aurora/SEM1NVZKQAD\\_0.html](http://www.esa.int/SPECIALS/Aurora/SEM1NVZKQAD_0.html).
- [ESA, 2007] Copyright 2000–2007 © European Space Agency, “Solar Proton Event Archive”, “[http://space-env.esa.int/Data\\_Plots/noaa/events/](http://space-env.esa.int/Data_Plots/noaa/events/)”, June 2007.
- [ESA2, 2005] ESA. (2005, May 31). TOS-EMA Proton Event 26-Oct-2003:18:15. Available:  
[http://www.estec.esa.nl/wmwww/wma/Data\\_Plots/noaa/events/20031026.html](http://www.estec.esa.nl/wmwww/wma/Data_Plots/noaa/events/20031026.html)
- [ESASS, 2008] ESA Space Science web page 2008,  
[http://www.esa.int/esaSC/SEM0KR1VED\\_index\\_0.html](http://www.esa.int/esaSC/SEM0KR1VED_index_0.html)
- [ESAST, 2007] ESA Science & Technology Program. Mars Express Publications. <http://sci.esa.int/science-e/www/area/index.cfm?fareaid=9>, March 2007.
-

- 
- [Feynman, 1993] J. Feynman, G. Spitale, J. Wang, and S. Gabriel, "Interplanetary Proton Fluence Model: JPL 1991", *J. Geophys. Res.* 98, 13281 (1993).
- [Folger, 2004] G. Folger, et al., *Eur. Phys. J. A* 21 (2004) 407.
- [Forget, 2001] F. Forget, Mars Climate Database Documentation, 2001 <http://www-mars.lmd.jussieu.fr/mars/node1.html>.
- [Fortescue, 2001] P. Fortescue, J. Stark, "Spacecraft Systems Engineering", J. Wiley & Sons, 2nd Edition, 2001.
- [G4Phys, 2008] "Reference PhysicsLists," Web page:  
[http://geant4.web.cern.ch/geant4/support/proc\\_mod\\_catalog/physics\\_lists/referencePL.shtml](http://geant4.web.cern.ch/geant4/support/proc_mod_catalog/physics_lists/referencePL.shtml)
- [G4PMan, 2008] "Physics Reference Manual," Web page:  
<http://geant4.web.cern.ch/geant4/UserDocumentation/UsersGuides/PhysicsReferenceManual/html/node144.html>
- [Gardner, 1989] C. Gardner, et al., "Operational experience with heavy ions at BNL: an update", Particle Accelerator Conference, 1989. Accelerator Science and Technology, Proceedings of the 1989 IEEE, vol.3, 20-23 Mar 1989, pp. 1850 – 1852 (10.1109/PAC.1989.72945)"
- [GEANT4, 2008] GEANT4 home page, 2008: <http://geant4.cern.ch/>
- [GEANT4\_SUH] GEANT4 Space Users Home page:  
<http://www.estec.esa.nl/wmwww/WMA/tmp/Geant4Space/>
- [Grove, 1967] A. S. Grove, "Physics and Technology of Semiconductor Devices", J. Wiley & Sons, 1967.
- [GRS, 2006] University of Arizona. Gamma Ray Spectrometer: 2001 Mars Odyssey, Lunar and Planetary Lab Webpage. Available: <http://grs.lpl.arizona.edu/latestresults.jsp>, June 2006.
- [Hall, 1952] R.N.Hall, "Electron-Hole Recombination in Germanium", *Phys. Rev.*, Vol. 87, 387 (1952).
- [Hanlon, 2004] M. Hanlon, "The real Mars: Spirit, Opportunity, Mars Express", 2004.
- [Harland, 2005] D.M. Harland, "Water and the search for life on Mars", Springer, 2005"
- [Hazen, 1978] R.M. Hazen et al, "Effects of compositional variation on absorption spectra from lunar pyroxenes", *Proc. Lunar Planet. Sci. Conf.* 9th 1978, p.2919-2934.
- [Hecht, 1987] E. Hecht, "Optics", Addison - Wesley Publishing Company, Inc. 1987.
- [Heynderickx, 2004] D. Heynderickx, B. Quaghebeur, J. Wera, E. J. Daly, H. D. R. Evans (2004), New radiation environment and effects models in ESA's SPace ENVironment Information System (SPENVIS), *Space Weather*, 2, S10S03, doi:10.1029/2004SW000073.
- [Holmes, 1962] D.K. Holmes, "Terms and Concepts in Radiation Damage Theory", in "Radiation Damage in Solid", Proceedings of the school of Physics Enrico Fermi, course XVIII, Academic Press, New York and London, 1962.
-

- 
- [Holmes-Siedle, 2006] A.Holmes-Siedle, L.Adams, "Handbook of radiation effects", Oxford Science Publications, Second edition, reprinted in 2006.
- [Hsieh, 1981] C.M. Hsieh, P.C. Murley and R.P. O'Brien, "Dynamics of charge collection from alpha-particle tracks in integrated circuits", IEEE/Proc. IRPS, pp. 38-42(1981).
- [Hu, 1982] C. Hu, "Alpha particle induced field and enhanced collection of carriers", IEEE Electron Dev. Lett., EDL-3, 31 (1982)
- [ICRP60, 1991] International Commission on Radiological Protection, 1990 Recommendations of the International Commission on Radiological Protection, ICRP Publication 60, Annals of ICRP, 21(1-3) (1991).
- [ICRP74, 1996] International Commission on Radiological Protection, Conversion Coefficients for use in Radiological Protection Against External Radiation, ICRP Publication 74, Annals of ICRP, 26, No. 3/4 (1996).
- [ICRU39, 1985] International Commission on Radiation Units and Measurements, Determination of Dose Equivalents Resulting from External Radiation Source. ICRU Report 39 (Bethesda, MD: ICRU Publications) (1985).
- [ICRU51, 1993] International Commission on Radiation Units and Measurements, Quantities and Units in Radiation Protection Dosimetry, ICRU Report 51 (Bethesda, MD: ICRU Publications) (1993).
- [ICRU57, 1998] International Commission on Radiation Units and Measurements, Conversion Coefficients for use in Radiological Protection Against External Radiation, ICRU Report 57 (Bethesda, MD: ICRU Publications) (1998).
- [Inguibert, 2004] C. Inguibert and S. Duzellier, SEU Rate Calculation With GEANT4 (Comparison With CREME 86)", IEEE Trans Nuc. Sci., vol.51, No. 5, October 2004
- [Inguibert, 2006] C. Inguibert and R. Gigante, "NEMO: A Code to Compute NIEL of Protons, Neutrons, Electrons, and Heavy Ions", IEEE Transactions on Nuclear Science, 2006, vol.53, no.4, pp.1967-1972.
- [Inguibert, 2007] C. Inguibert, S. Duzellier, T. Nuns, F. Bezerra, "Using Subthreshold Heavy Ion Upset Cross Section to Calculate Proton Sensitivity", IEEE Transactions on Nuclear Science, 2007, vol.54, no.6, pp.2394-2499.
- [ISO 15390:2004(E)] International Organization for Standardization, "International Standard: Space environment (natural and artificial) — Galactic cosmic ray model", ISO 2004.
- [Kahn, 1985] R. Kahn, "The Evolution of CO<sub>2</sub> on Mars", ICARUS 62, pp. 75-190, 1985.
- [Kallenrode, 2001] May-Britt Kallenrode, "Space Physics: an Introduction to Plasmas and Particles in the Heliosphere and Magnetospheres", Second Edition, Springer, 2001.
- [Keating, 2002] A.Keating, "Reconstrução da carga eléctrica de partículas cósmicas no detector RICH da experiência AMS", Master Thesis, May 2002. <https://www.lip.pt/~amswww/AMS.LIP.Thesis.html>.
-

---

[Keating, 2005] A.Keating, A.Mohammadzadeh, P.Nieminen, D. Maia, S.Coutinho, H.Evans, M.Pimenta, J.-P.Huot, and E.Daly, "A Model for Mars Radiation Environment Characterization", IEEE Transactions on Nuclear Science, vol. 52, no. 6, Dec. 2005.

[Keating, 2006] A. Keating, A.Mohammadzadeh, P.Nieminen, M.Pimenta, P.Brogueira, R. Harboe-Sørensen, E.Daly, "Mars Radiation Environment and Effects on Components Tool (MarsREC) and SEU Predictions", RADECS 2006.

[Keating, 2008] A.Keating, A.Mohammadzadez, P. Brogueira, M. Pimenta, P. Gonçalves, S.Valente, R. Harboe-Sorensen, "CODES a SEU Prediction Tool", submitted to NSREC 2008.

[Keating2, 2006] A.Keating et al, Mars Atmosphere Modeling & Observation Workshop, Granada 2006. Available:[http://www-mars.lmd.jussieu.fr/granada2006/abstracts/Keating\\_Granada2006.pdf](http://www-mars.lmd.jussieu.fr/granada2006/abstracts/Keating_Granada2006.pdf)

[Kerra, 2002] M. J. Kerra and A. Cuevas, "General parameterization of Auger recombination in crystalline silicon", Journal Appl. Phys., Vol. 91, No. 4, 2473 (2002).

[Klassen, 2002] A. Klassen, V. Bothmer, G. Mann, M. J. Reiner, S. Krucker, A. Vourlidas, H. Kunow, "Solar energetic electron events and coronal shocks", A&A 385, 1078{1088 (2002).

[Koi, 2003] T. Koi, M. Asai, D. H. Wright, K. Niita, Y. Nara, K. Amako, T. Sasaki, "Interfacing the JQMD and JAM Nuclear Reaction Codes to Geant4", Computing in High Energy and Nuclear Physics (CHEP03), 2003. arXiv:physics/0306115V1

[Koi, 2006] Tatsumi Koi, "Thermal neutron scattering from nuclei within chemically bound atoms in Geant4", Presentation in IEEE 2006 Nuclear Science Symposium and Medical Imaging Conference: <http://geant4hadronics.wikispaces.com/Thermal+Neutron+Scattering+in+Geant4>"

[Kolasinski, 1982] W. A. Kolasinski, R. Koga and J. B. Blake, P. Pandya, E. Petersen, W. Price, "Single Event Upset vulnerability of 4K and 16K CMOS Static RAM's", IEEE Transactions on Nuclear Science, Vol. NS-29, No. 6, December 1982.

[Kramer, 1982] Kramer R., Zankl M., Williams G. and Drexler G. The Calculation of Dose from External Photon Exposure Using Reference Human Phantoms and Monte Carlo Methods. Part I: The Male (ADAM) and Female (EVA) Adult Mathematical Phantoms. Neuherberger, GSF-Forschungszentrum für Umwelt und Gesundheit, GSF-Bericht S885 (1982).

[Krimigis, 1975] S.M.Krimigis, E.T.Sarris, "Observation of quiet-time interplanetary electron enhancements of jovian origin", 14th International Cosmic Ray Conference, Aug.1975.

[Langworthy, 1989] J.B. Langworthy, "Depletion Region Geometry Analysis Applied to Single Event Sensitivity", IEEE Transactions on Nuclear Science, 1989, vol. 36, no.6, pp.2427-2434.

[Lepping, 1995] Lepping, Ronald P., "Characteristics of the magnetopauses of the magnetized planets", in Physics of the Magnetopause, B.U.O.Sonnerup and P. Song, editors, p. 61-70, Amer. Geophys. Union, Washington, D.C. 1995.

---

- 
- [Lewis, 1999] S.R.Lewis, M.Collins, and P.L.Read, "A climate database for Mars", *Journal of Geophysical Research-Planets*, vol. 104, no. E10, pages 24,177-24,194 (1999).
- [Lintunen, 2004] J. Lintunen and R. Vainio, "Solar energetic particle event onset as analysed from simulated data," *Astron. Astrophys.*, vol. 420, pp. 343-350, 2004.
- [Lopate, 1991] C. Lopate, "Jovian and Galactic Electrons (2-30MeV) in the Heliosphere from 1 to 50 Au", 22nd International Cosmic Ray Conference, Aug.1991.
- [Lowenstein, 2001] D.I. Lowenstein, BNL Accelerator-Based Radiobiology Facilities, *Physica Medica - Vol. XVII, Supplement 1*, 2001.
- [Ma, 1989] T.P.Ma and P.V.Dressendorfer, "Ionizing Radiation Effects in MOS devices and circuits", J. Wiley and Sons, 1989.
- [Maclennan, 2001] Maclennan, C.G.; Lanzerotti, L.J. ; Lagg,a., "Hot plasma heavy ions abundance in the inner Jovian Magnetosphere", in *Planet. and Space Sci.*, 49, p. 275-282, 2001.
- [Makoto, 2005] A. Makoto, R.A. Reed, R.A. Weller, "GEANT4 applications for NASA Space Missions", 10th ICATPP Conference on Astroparticle, Particle, Space Physics, Detectors and Medical Physics Applications, 2005. Available:  
[http://villaolmo.mib.infn.it/ICATPP9th\\_2005/GEANT4%20and%20SW%20Applications/ASAI.pdf](http://villaolmo.mib.infn.it/ICATPP9th_2005/GEANT4%20and%20SW%20Applications/ASAI.pdf)
- [MARIE, 2003] F.A. Cucinotta, C. Dardano(27th October 2003) , "MARIE, Mars Radiation Environment Experiment: References and Documents", online: <http://marie.jsc.nasa.gov/Documents/Index.html>
- [MarsOdyssey, 2006] Mars Odyssey (2006) <http://grs.lpl.arizona.edu/latestresults.jsp>.
- [MCD, 2008] Mars Climate Database , 2008 <http://johnson.lmd.jussieu.fr:8080/las/servlets/dataset>
- [McKay, 1953] McKay and McAfee, "Electron Multiplication in Silicon and Germanium", *Phys. Rev.* 91, 1079 (1953)
- [Melosh , 1989] H. J. Melosh & A. M. Vickery, "Impact erosion of the primordial atmosphere of Mars", *Nature* 338, 487 - 489 (06 April 1989); doi:10.1038/338487a0
- [Mewaldt, 1975] R.A. Mewaldt, E.C. Stone, R.E. Vogt, "Observations of low energy interplanetary electrons", 14th International Cosmic Ray Conference, Aug.1975.
- [Miley, 2006] G.K. Miley et al., "The Spiderweb Galaxy: A Forming Massive Cluster Galaxy at  $z \sim 2$ ", *Astrophysical Journal Letters*, Vol: 650, Issue: 1, pp. L29-L32, 2006.
- [Mitrofanov, 2003] I.G. Mitrofanov et al, "CO<sub>2</sub> Snow Depth and Subsurface Water-ice Abundance in the Northern Hemisphere of Mars", *Science*, vol. 300, pp.2081-2084, 27 June 2003
- [Murley, 1996] P. C. Murley, G. R. Srinivasan, "Soft-Error Monte- Carlo Modeling program, SEMM", *IBM J. Res. Develop.* vol. 40, no. 1, pp- 109-118, January 1996.
- [Musseau, 1994] O.Musseau, "Charge collection and SEU Mechanisms", *Radiat. Phys. Chem.*, Vol.43, No.1/2, pp.151-163, 1994.
-

- 
- [Mustard, 2005] J.F. Mustard et al, "Olivine and Pyroxene diversity in the Crust of Mars", *Science*, vol. 307, pp.1594-1597, 11 March 2005.
- [NASA, 2006] NASA. Mars Exploration Programme. Available: <http://mars.jpl.nasa.gov/missions/>, March 2006
- [NASA, 2007] NASA, Marshall Space Flight Center, "Solar Physics", Last update: May 2007, <http://solarscience.msfc.nasa.gov/>.
- [Nichols, 1988] D.K. Nichols, M.A. Huebner, W.E. Price, L.S. Smith, J.R. Coss, "Heavy Ion Induced Single Event Phenomena (SEP) Data for Semiconductor Devices from Engineering Testing", JPL Publication 88-17, July 1988.
- [Nieminen, 1997] P. Nieminen, "Neutrons from the 15 June 1991 Solar Flare", PhD Thesis, Bern University, 1997.
- [Normand, 1993] E. Normand and T.J. Baker, "Altitude and Latitude Variations in Avionics SEU and Atmospheric Neutrons Flux", *IEEE Transactions on Nuclear Science*, 1993, vol. 40, No.6, pp. 1484-1490.
- [Normand, 2004] E. Normand, "Extension of the FOM Method- Proton SEL and Atmospheric Neutrons SEU", *IEEE Transactions on Nuclear Science*, 2004 vol. 52, No.6, pp. 3494-3504.
- [Noyola, 2008] E. Noyola et al., "Gemini and Hubble Space Telescope Evidence for an Intermediate-Mass Black Hole in omega Centauri", *ApJ* doi:10.1086/529002, 2008.
- [Nymmik, 1992] R.A. Nymmik, M.I. Panasyuk, T.I. Pervaja, and A.A. Suslov, "A Model of Galactic Cosmic Ray Fluxes", *Nuclear Tracks and Radiation Measurements*, 1992, vol. 20, pp. 427-429.
- [Nymmik, 2006] R.A. Nymmik, "Initial conditions for radiation analysis: Models of galactic cosmic rays and solar particle events", *Advances in Space Research* 38 (2006) 1182-1190.
- [Pelliccioni, 1999] Pelliccioni, M. Radiation Weighting Factors and Conversion Coefficients for High- Energy Radiation, SATIF-4, Workshop Proceedings Knoxville, 17-18 September 1998, 179-192, OECD (1999).
- [Pelliccioni, 2000] Pelliccioni, M. Overview of Fluence-to-Effective Dose and Fluence-to-Ambient Dose Equivalent Conversion Coefficients for High Energy Radiation Calculated Using the FLUKA Code, *Radiat. Prot. Dosim.* 88(4), 279-297 (2000)
- [Pelliccioni, 2003] M. Pelliccioni, "Conversion coefficients for high-energy radiation calculated using the FLUKA Code", [Online] G. Battistoni (2003-05-09) <http://www.mi.infn.it/~battist/DoseCoeff/node3.html>
- [Petersen, 1992] E. L. Petersen, J. C. Pickel, J. H. Adams, Jr., E. C. Smith, "Rate prediction for Single Event Effects—a Critique", *IEEE Trans Nuc. Sci.*, vol. 39, no. 6, December 1992
- [Petersen, 1993] E.L. Petersen, J.C. Pickel, E.C. Smith, P.J. Rudeck, J.R. Letaw, "Geometrical factors in SEE Rate Calculations", *IEEE Trans. Nucl. Sci.* 40, no 6, 1993, pp. 1888-1909
- [Petersen, 1998] E. L. Petersen, "The SEU Figure of Merit and Proton Upset Rate Calculations", *IEEE Transactions on Nuclear Science*, 1998, vol.45, no.6, pp.2550-2562.
-

- 
- [Philips, 2003] Tony Phillips, "The Sun Goes Haywire- Solar maximum is years past, yet the sun has been remarkably active lately. Is the sunspot cycle broken?" *Science@Nasa*, 12 Nov. 2003.
- [Poulet, 2003] F. Poulet and S. Erard, "The surface Compositions of Martian Low Albedo Regions Revisited", *Lunar and Planetary Science XXXVI*, 2003
- [Ptuskin, 2001] V. S. Ptuskin, "Cosmic Rays: origin, propagation, and interaction", *Proceedings of the Third International Workshop on New Worlds in astroparticle Physics*, pp.46-65, World Scientific Publishing, 2001.
- [Ranft, 2008] Prof Johannes Ranft web-site for DPMJET-II.5, <http://cip-lxw.physik.uni-siegen.de/kolloquium/dpmjet/>, correct at March 2008.
- [REAT] Radiation Effects Analysis Tools (REAT): [http://reat.space.qinetiq.com/Reat/reat\\_mn.html](http://reat.space.qinetiq.com/Reat/reat_mn.html)
- [Rosenqvist, 2003] Rosenqvist, L., and A. Hilgers (2003), Sensitivity of a statistical solar proton fluence model to the size of the event data set, *Geophys. Res. Lett.*, 30(16), 1865, doi:10.1029/2003GL017038.
- [Ruffolo, 1995] D. Ruffolo "Effect of adiabatic deceleration on the focused transport of solar cosmic rays", *The Astrophysical Journal*, Vol. 442, pp 861-874, 1 April, 1995.
- [Ruffolo, 1998] D. Ruffolo, T. Khumlumert, and W. Younfddee, "Deconvolution of interplanetary transport of solar energetic particles", *Journal of Geophysical Research*, Vol. 103, No A9, pp 20591-20602, 1 Sept. 1998.
- [Russell, 1987] C.T. Russell, "The Magnetosphere", In *The Solar Wind and the Earth*, edited by S. -I. Akasofu and Y. Kamide, pp 73-100, Terra Scientific Publishing Company (TERRAPUB), Tokyo, 1987.
- [Santin, 2005] G. Santin, V. Ivanchenko, H. Evans, P. Nieminen, E. Daly, "GRAS: A general-purpose 3-D modular simulation tool for space environment effects analysis", *IEEE Trans. Nucl. Sci.* 52, Issue 6, 2005, pp 2294 – 2299.
- [Schneider, 2005] Schneider, I. (2005). Characterization of the radiation on the surface of Mars and its astrobiological implications. *Eos Trans. AGU*, 86(52), Fall Meet. Suppl., abstract P51D-0954.
- [Seltzer, 1979] S.M.Seltzer, "Electron, Electron-Bremsstrahlung and proton depth-dose data for space-shielding applications", *IEEE Transactions on Nuclear Science*, Dec. 1979, vol. NS-26.
- [SEPTIMESS] SEPTIMESS web page: <http://reat.space.qinetiq.com/septimess/>
- [Shima, 1979] M. Shima et al, "Chemical Composition, Petrography and Minerals of the Shibayama Chondrite found in Shibayama-Machi, Sanbu-gun, Chiba-ken, Japan", *Meteoritics*, Vol. 14, No. 3, pp. 317-330, September 1979.
- [Shockley, 1952] W. Shockley and W.T. Read, Jr., "Statistics of the Recombination of Holes and Electrons", *Phys. Review*, Vol. 87, No.5, 835 (1952)"
- [Shockley, 1961] W. Shockley, "Problems related to p-n junctions in Silicon", *Solid State Electron.* 2, 35 (1961)
- [SIDC, 2007] R. A. M. Van der Linden and the SIDC team, "Online catalogue of the sunspot index", <http://www.sidc.be/>
-

- 
- [Sizemore, 2005] H.G. Sizemore and M.T. Mellon, "Effects of Rock on Martian Ground Ice and Neutron Flux", *Lunar and Planetary Science XXXVI*, 2005
- [Sørensen, 2005] R. Harboe-Sørensen, F.-X. Guerre and A. Roseng, "Design, Testing and Calibration of Reference SEU Monitor System", proceedings, RADECS 2005.
- [Spohn, 1998] T. Spohn et al, "Mars", *Astron Astrophys Rev* (1998) 8 : 181-236.
- [Swain, 2008] M.R. Swain et al., "Methane present in an extrasolar planet atmosphere", *Nature*, Vol. 452, Issue 7185, pp. 329-331, 2008.
- [Sze, 1981] S. M. Sze, "Physics of Semiconductor Devices", J. Wiley & Sons, 2nd Edition, 1981.
- [Tassara, 2005] A. Tassara, "Three Factors Controlling the Crustal Density Structure Underneath Active Continental Margins with implications for their Evolution", Paper accepted for publication in *Geochemistry, Geophysics, Geosystems*, 20th September 2005.
- [Torsti, 2001] J. Torsti, L. Kocharov, D. E. Innes, J. Laivola, and T. Sahla, "Injection of energetic protons during solar eruption on 1999 May 9: Effect of flare and coronal mass ejection", in *Astronomy & Astrophysics*, 365, p. 198-203, 2001.
- [Truscott, 2008] P. Truscott, F. Lei, A. Keating, S. Valente, P. Gonçalves, L. Desorgher, D. Heynderickx, N. Crosby, H. de Witte, G. Degreef, P. Nieminen and G. Santin, "The Mars Energetic Radiation Environment Models", accepted to NSREC 2008 (submitted to IEEE TNS December 2008).
- [Tylka, 2007] A.J.Tylka (2007), CREME96 Home Page. Available: <https://creme96.nrl.navy.mil/>.
- [Tylka1, 1997] A.J. Tylka, W.F. Dietrich, and P.R. Boberg, "Probability Distributions of High-Energy Solar-Heavy-Ion Fluxes from IMP-8: 1973-1996", *IEEE Transactions on Nuclear Science*, 44, 2140-2149 (1997).
- [Tylka2, 1997] A.J. Tylka, J.H. Adams, P.R. Boberg, B. Brownstein, W.F. Dietrich, E.O. Flueckiger, E.L. Petersen, M.A. Shea, D.F. Smart, E.C. Smith, "CREME96: A revision of the Cosmic Ray Effects on Micro-Electronics Code", *IEEE Transactions on Nuclear Science*, 1997, vol. 44, pp.2150-2160.
- [Underwood, 1996] Craig Ian Underwood, "Single Event Effects in commercial memory devices in the space radiation environment", PhD Thesis, University of Surrey, Aug. 1996.
- [Virtanen, 2007] A. Virtanen, "Linear Energy Transfer Measurements of Heavy Ions in Silicon", TEC-QCA Presentations Day, 2007. Available: <https://escies.org/ReadArticle?docId=702>
- [Warren, 1999] K. Warren, L. Massengill, R. Schrimpf, H. Barnaby, "Analysis of the Influence of MOS Device Geometry on Predicted SEU Cross Sections", *IEEE Trans. Nucl. Sci.* 46, no 6, 1999, pp. 1363-1369.
- [Warren, 2006] K. M. Warren, R. A. Weller, B. Sierawski, R. A. Reed, M.H. Mendenhall, R. D. Schrimpf, L. W. Massengill, Mark Porter, J. Wilkinson, K. A. LaBel and J. Adams, "Application of RADSAFE to Model Single Event Upset Response of a 0.25  $\mu\text{m}$  CMOS SRAM", A-6 RADECS Workshop, Greece 2006.
-

[Weller, 2004] R.A. Weller, M.H. Mendenhall, D.M. Fleetwood, "Screened Coulomb Scattering Module for Displacement Damage Computations in Geant4", IEEE Transactions on Nuclear Science, 2004, vol.51, no.6, pp. 3669-3678.

[Weller, 2006] R.A. Weller, R.A. Reed, "Overview: Physically- Based Simulation of Single-Event Effects", MURI Review - Vanderbilt - 13-14/Jun/2006.

[Wilson, 1997] J.W.Wilson, J.Miller, A.Konradi and F.A. Cucinotta,"Shielding Strategies for Human Space Exploration", NASA Conference Publication 3360, December 1997.

[Wolff, 1954] P.A.Wolff, "Theory of electron multiplication in Silicon and Germanium", Phys.Rev.95, 1415 (1954)

[Xapsos, 2006] Janet Barth, Mike Xapsos, Jean-Marie Lauenstein, Ray Ladbury, "Radiation Environment Modelling for Spacecraft Design: New Models Development", RADECS Workshop, 28 September 2006, Athens, Greece

[Xapsos, 1993] M.A. Xapsos, "The shape of heavy ion upset cross section curves", IEEE Transactions on Nuclear Science, Vol.40, No. 6, December 1993.

[Ziegler, 2006] J.F. Ziegler, "The Stopping and Range of Ions in Matter", SRIM Home Page, Available: <http://www.srim.org/#SRIM>.

---



## Appendix I:

### Fluence-to-ambient dose equivalent conversion coefficients

The procedures described in this Appendix were obtained from literature [Pelliccioni, 2003] FLUKA webpage (<http://www.fluka.org/pickup/DoseCoeff/>).

According to the definition of ambient dose equivalent discussed in Chapter 4, the geometry of the problem considered in FLUKA conversions from fluence to ambient dose equivalent coefficients consists of a 30 cm diameter sphere of unit density tissue and composition as specified by ICRU (H, 10.1%; C, 11.1%; N, 2.6%; O, 76.2%; %-compositions are given by weight). This tissue equivalent geometry was exposed to a parallel particle beam uniformly expanded over its front surface. The density of such tissue is 1.371g/cm<sup>3</sup> according to SRIM. The medium between the source and the ICRU sphere was assumed to be vacuum.

The determination of the dose equivalents takes into account quality factors dependent on the linear energy transfer, LET. Therefore the energies deposited per unit mass are directly multiplied by the quality factor appropriate to the LET of the charged particle imparting energy to the matter.

The values of the ambient dose equivalent have been averaged over the depth 0.95-1.05 cm or 0.9-1.1 cm according to the incident energy.

Once the ambient dose equivalent,  $H^*(E)$ , as a function of particle energy for various kinds of radiation was computed, the fluence-to-ambient dose equivalent conversion coefficients,  $f_{H^*(E)}$ , are given in terms of ambient dose equivalent per unit of fluence (Sv.cm<sup>2</sup>) by:

$$f_{H^*(E)} = \frac{H^*(E)}{\Phi(E)} \quad (1)$$

where  $\Phi(E)$  is the fluence of primary particle of energy  $E$ .

Tables 1 to 4 show the calculation results.

---

PROTONS		
ENERGY (GeV)	CONVERSION (SV.CM2)	% STANDARD DEVIATION
5.00E-02	2.97E-09	1.39E-02
1.00E-01	1.52E-09	1.70E-02
2.00E-01	9.99E-10	1.76E-02
5.00E-01	7.86E-10	9.51E-02
1.00E+00	6.41E-10	4.63E-02
5.00E+00	7.65E-10	3.31E-02
1.00E+01	8.39E-10	5.13E-02
1.00E+02	8.22E-10	4.77E-02
1.00E+03	9.96E-10	1.01E-01
1.00E+04	1.20E-09	9.18E-02

---

**Table 1**

NEUTRONS		
ENERGY (GeV)	CONVERSION (SV.CM2)	% STANDARD DEVIATION
2.50E-11	1.04E-11	4.30E-02
1.00E-06	8.62E-12	4.28E-02
1.00E-04	1.08E-10	1.23E-02
1.00E-03	4.92E-10	1.59E-02
5.00E-03	4.26E-10	2.54E-02
1.00E-02	4.63E-10	3.44E-02
1.50E-02	5.08E-10	2.75E-02
1.90E-02	5.56E-10	1.38E-02
2.00E-02	5.26E-10	1.74E-02
5.00E-02	3.59E-10	2.79E-02
1.00E-01	2.62E-10	2.31E-02
2.00E-01	2.21E-10	2.22E-02
5.00E-01	2.90E-10	3.45E-02
1.00E+00	3.77E-10	4.57E-02
5.00E+00	4.92E-10	3.29E-02
1.00E+01	5.23E-10	7.56E-02
1.00E+02	4.99E-10	6.14E-02
1.00E+03	7.17E-10	8.57E-02
1.00E+04	1.16E-09	8.31E-02

---

**Table 2**

---

ELECTRONS		
ENERGY (GEV)	CONVERSION (SV.CM2)	% STANDARD DEVIATION
2.50E-03	1.60E-10	8.50E-03
3.00E-03	3.33E-10	9.20E-03
4.00E-03	4.44E-10	8.90E-03
5.00E-03	4.21E-10	7.40E-03
7.00E-03	3.60E-10	8.40E-03
1.00E-02	3.25E-10	1.30E-02
2.00E-02	3.27E-10	2.80E-02
3.00E-02	3.18E-10	1.10E-02
4.00E-02	3.06E-10	1.20E-02
5.00E-02	3.10E-10	1.00E-02
7.00E-02	3.19E-10	1.30E-02
1.00E-01	3.15E-10	1.30E-02
2.00E-01	3.23E-10	1.40E-02
5.00E-01	3.18E-10	1.50E-02
1.00E+00	3.08E-10	3.50E-02
2.00E+00	3.17E-10	2.20E-02
5.00E+00	3.14E-10	1.30E-02
1.00E+01	3.28E-10	2.00E-02

---

**Table 3**

PHOTONS		
ENERGY (GEV)	CONVERSION (SV.CM2)	% STANDARD DEVIATION
1.00E-05	8.34E-14	7.40E-03
1.50E-05	8.53E-13	5.40E-03
2.00E-05	1.05E-12	7.70E-03
3.00E-05	7.95E-13	6.00E-03
4.00E-05	6.24E-13	1.20E-02
5.00E-05	5.24E-13	1.10E-02
6.00E-05	5.15E-13	2.40E-02
8.00E-05	5.56E-13	1.40E-02
1.00E-04	6.22E-13	3.00E-02
1.50E-04	8.70E-13	1.60E-02
2.00E-04	1.23E-12	1.10E-02
3.00E-04	1.81E-12	1.40E-02
4.00E-04	2.36E-12	2.10E-02
5.00E-04	2.78E-12	9.80E-03
6.00E-04	3.46E-12	2.00E-02
8.00E-04	4.29E-12	1.40E-02
1.00E-03	5.18E-12	1.50E-02
1.50E-03	6.92E-12	1.50E-02
2.00E-03	8.25E-12	1.30E-02
3.00E-03	1.05E-11	2.00E-02
4.00E-03	1.08E-11	2.50E-02
5.00E-03	1.04E-11	1.60E-02
6.00E-03	9.58E-12	9.40E-03
8.00E-03	9.10E-12	1.70E-02
1.00E-02	8.76E-12	2.50E-02
2.00E-02	8.29E-12	2.00E-02
3.00E-02	8.23E-12	2.00E-02
4.00E-02	8.26E-12	1.80E-02
5.00E-02	8.64E-12	2.00E-02
1.00E-01	9.00E-12	5.90E-02
2.00E-01	1.02E-11	5.60E-02
5.00E-01	1.18E-11	4.00E-02
1.00E+00	1.17E-11	3.90E-02
2.00E+00	1.15E-11	3.40E-02
5.00E+00	1.33E-11	5.00E-02
1.00E+01	1.22E-11	4.00E-02

Table 4



